MONASH University

CHARGE TRANSPORT LAYER AND INTERFACE ENGINEERING IN PEROVSKITE SOLAR CELLS

Jingsong Sun
M.E.

A thesis submitted for the degree of *Doctor of Philosophy* at
Monash University in 2019
Department of Materials Science and Engineering

Copyright notice

Abstract

Organo-lead halide perovskite solar cells have sparked considerable attention as one of the most promising next generation solar cells. Such devices have the merits of high efficiency, low-cost processing, easy fabrication, and compatibility with flexible plastic substrates for large-area production. However, it is well known that perovskite solar cells exhibit electrical hysteresis, chemical instability and are difficult to scale. Overcoming these challenges will require the development of novel perovskite compositions, highly efficient charge transport layers and optimised interfaces between the electrodes, charge transport layers and the perovskites. Of these, this thesis focuses on the development of effective charge transporting layers and their interfaces with the perovskite layer. For the former, we have selectively studied the formation of compact and meso-structured NiO and TiO_2 layers as hole and electron transport layers, respectively. Under optimal compositions, it was found that meso-porous structures across both of these layers provided improved charge extraction capabilities, which enabled higher device efficiencies to be obtained. These studies focussed on developing conducive bottom electrode configurations for inverted and standard perovskite devices. To compliment these efforts, we further focussed on the top electrode through interface engineering of the perovskite layers using molecular additive modification of 2D perovskites capping layers. This strategy was found to enhance charge extraction from the perovskite to the hole transporting layer, passivate the defects on the perovskite surface to reduce the charge recombination, improve device stability and enhance device efficiencies to more than 20%. Collectively, the results presented in this thesis show the inter-dependent importance of structural and compositional control of charge transport layers and their interfaces to enable high performance perovskite devices. These work provide important steps forward towards realising scalable fabrication and high-performance of perovskite solar cells.

Declaration

This thesis is an original work of my research and contains no material which has been accepted for the award of any other degree or diploma at any university or equivalent institution and that, to the best of my knowledge and belief, this thesis contains no material previously published or written by another person, except where due reference is made in the text of the thesis.

Signature:

Print Name:

Date: …….

Publications during enrolment

1. **Jingsong Sun**, Alexander R. Pascoe, Steffen Meyer, Qijie Wu, Enrico Della Gaspera, Sonia R. Raga, Tian Zhang, Andrew Nattestad, Udo Bach, Yi Bing Cheng, Jacek J. Jasieniak, Ultrasonic spray deposition of TiO_2 electron transport layers for reproducible and high efficiency hybrid perovskite solar cells, *Solar Energy*, **2019**,188, 697-705

2. **Jingsong Sun**, Jianfeng Lu, Bin Li, Liangcong Jiang, Anthony S. R. Chesman, Andrew D. Scully, Thomas R. Gengenbach, YiBing Cheng, Jacek J. Jasieniak* Inverted perovskite solar cells with high fill-factors featuring chemical bath deposited mesoporous NiO hole transporting layers, *Nano Energy*, **2018**, 49, 163-171

3. **Jingsong Sun**, Jacek J. Jasieniak* Semi-transparent solar cells, *Journal of Physics D: Applied Physics*, **2017**, 50, 9

4. Jian-Feng Lu, Xiongfeng Lin, Xuechen Jiao, Thomas R. Gengenbach, Andrew D Scully, Liangcong Jiang, Boer Tan, **Jingsong Sun**, Bin Li, Narendra Pai, Udo Bach, Alexandr N Simonov* and Yi-Bing Cheng*, Interfacial benzenethiol modification facilitates charge transfer and improves stability of cm-sized metal halide perovskite solar cells with up to 20 % efficiency, *Energy & Environmental Science*, **2018**,11, 1880-1889

5. Liangcong Jiang, Jianfeng Lu, Sonia R.Raga, Jingsong Sun, Xiongfeng Lin, Wenchao Huang, Fuzhi Huang, Udo Bach, Yi-Bing Cheng.* Fatigue stability of $CH_3NH_3PbI_3$ based perovskite solar cells in day/night cycling, *Nano Energy*, **2019**, 58, 687-694

6. **Jingsong Sun**, Naresh Chandrasekaran, Chang Liu, Andrew D. Scully, Wenping Yin, Chun Kiu Ng and Jacek J. Jasieniak*. 3D/2D Perovskite Solar Cells using F4TCNQ as an Additive in the 2D Perovskite Layer. Under review

Thesis including published works declaration

I hereby declare that this thesis contains no material which has been accepted for the award of any other degree or diploma at any university or equivalent institution and that, to the best of my knowledge and belief, this thesis contains no material previously published or written by another person, except where due reference is made in the text of the thesis.

This thesis includes (2) original papers published in peer reviewed journals. The core theme of the thesis is an understanding of the charge transporting layer design and interface engineering of perovskite solar cells. The ideas, development and writing up of all the papers in the thesis were the principal responsibility of myself, the student, working within the Materials Science Engineering, Monash University under the supervision of Professor Jacek Jasieniak.

The inclusion of co-authors reflects the fact that the work came from active collaboration between researchers and acknowledges input into team-based research.

In the case of *(***Chapter 3 and 4**) my contribution to the work involved the following:

Thesis Chapter	Publication Title	Status *(published, in press, accepted or returned for revision)*	Nature and % of student contribution	Co-author name(s) Nature and % of Co-author's contribution*	Co-author(s), Monash student Y/N*
3	Inverted perovskite solar cells with high fill-factors featuring chemical bath deposited mesoporous NiO_x hole transporting layers	Published	60%. Concept and collecting data and writing first draft	1) Jianfeng Lu, data analysis, input into manuscript 5% 2) Bin Li, FIB-SEM measurement, input into manuscript 5% 3) Liangcong Jiang, photovoltage decay measurement, input into manuscript 5% 4) Anthony S. R. Chesman, UV-Vis spectra measurement, input into manuscript 5% 5) Andrew D. Scully, TRPL and PL intensity measurement, input into manuscript 2% 6) Thomas R. Gengenbach, UPS and XPS measurement, input into manuscript 2% 7) Yibing Cheng, data analysis 1% 8) Jacek J. Jasieniak, supervision 15%	No Yes Yes No No No No No
4	Ultrasonic spray deposition of TiO_2 electron transport layers for reproducible and high efficiency hybrid perovskite solar cells	Published	60%. Concept and collecting data and writing first draft	1) Alexander R. Pascoe, System optimization, contribution to 15% of the work 2) Steffen Meyer, MAI synthesis, contribution to 5% of the work 3) Qijie Wu, Andrew Nattestad, Enrico Della Gaspera, data analysis, input into manuscript 5% 4) Sonia R. Raga, Tian Zhang, measurement of IPCE and Ellipsometry,	No No No No

				input into manuscript 3%. 5) Udo Bach, Yibing Cheng, data analysis 2% 6) Jacek J. Jasieniak, supervision 10%	 No No

**If no co-authors, leave fields blank*

I have not renumbered sections of submitted or published papers in order to generate a consistent presentation within the thesis.

Student signature: *()* **Date:**

The undersigned hereby certify that the above declaration correctly reflects the nature and extent of the student's and co-authors' contributions to this work. In instances where I am not the responsible author, I have consulted with the responsible author to agree on the respective contributions of the authors.

Main Supervisor signature: ***()*** **Date:**

Acknowledgements

I have experienced a fantastic learning and life style in the four years, and I really appreciate the experience. Here, I would like to acknowledge many people who helped me a lot in this thesis. I have to say that I cannot gain any progress and achievement without your supporting.

First of all, I would like to thank my supervisor, Prof. Jacek Jasieniak for his constant support on my research and study. In each of my work, he was patient enough to explain the intricacies of knowledge, teach me to improve the research capability and help me to point out the scientific problems. All his help made me improve the work competence and inspired me on the search for knowledge. Moreover, his enthusiasm for science and life made me become more optimistic and have a positive attitude towards any problems.

Then I would also like to thank all my co-workers in my group and in the renewable energy lab. Thanks for their responsible work to guarantee us the good research atmosphere in this big family. Especially, thanks Dr. Alexander R. Pascoe for his help on establishing the ultrasonic spray system, which helped me to finish the work on charge transporting layers. Thanks Dr. Jianfeng Lu, Dr. Naresh Chandrasekaran, and Dr. Sonia Ruiz Raga for their help on characterizations and analysis in my work. In addition, I would really appreciate that Dr. Anthony S. R. Chesman and Dr. Andrew D. Scully from CSIRO supported me on my research. I will always remember the time we work together, and I understand that my work cannot be finished without your help.

To my parents, I would like to say thank you for your inspiration for me to study on scientific research. It has been more than ten years since my first day to leave my hometown and go to the university. In these years, I can always feel your care and encouragement, which reminds me to be working hard. Your unconditional love is the most important support to my research, to my study and most importantly to my life. Finally, I also would like to say thank you to my partner Chang, thanks for your support and encouragement for my life.

Abbreviations

a-Si	Monocrystalline Silicon
BA	Butylammonium
BCP	Bathocuproine
BIPV	Building-integrated Photovoltaic
CBD	Chemical Bath Deposition
CIGS	Cu-In-Ga-Se
DMSO	Dimethyl Sulfoxide
DOSC	DSO-X 3032A Digital Oscilloscope
DSSC	Dye Sensitized Solar Cell
EIS	Electrochemical Impedance Spectroscopy
ETL	Electron Transporting Layer
ETM	Electron Transporting Material
F4TCNQ	2,3,5,6-Tetrafluoro-7,7,8,8-tetracyanoquinodimethane
FA	Formamidinium
FF	Fill Factor
FTIR	Fourier-transform Infrared Spectroscopy
FTO	Fluorine Doped Tin Oxide
GA-FTIR	Grazing Angle Fourier-transform Infrared Spectroscopy
GIWAX	Grazing-Incidence Wide-Angle X-ray Scattering
HOMO	Highest Occupied Molecular Orbital
HTL	Hole Transporting Layer
HTM	Hole Transporting Material

IE	Ionization Energy
IPA	Isopropanol
IPCE	Incident Photon to Current Conversion Efficiency
J-V	Photocurrent Density-voltage
J_{sc}	Short-Circuit Current Density
LUMO	Lowest Unoccupied Molecular Orbital
MA	Methylammonium
m-Si	Monocrystalline Silicon
MCEM	Monash Centre for Electron Microscopy
MXP	Monash X-ray Platform
OSC	Organic Solar Cell
P3HT	Poly(3-hexylthiophene)
PCBM	Phenyl-C61-butyric Acid Methyl Ester
PCE	Power Conversion Efficiency
PEDOT: PSS	Poly(3,4-ethylenedioxythiophene) Polystyrene Sulfonate
PET	Poly (ethylene terephthalate)
PID	Proportional–integral–derivative
PL	Photoluminescence
ppm	parts per million
PSC	Perovskite Solar Cell
poly-Si	Polycrystalline Silicon
PTAA	Poly[bis(4-phenyl)(2,4,6-trimethylphenyl)amine
QD	Quantum Dot
rGO	Reduced Graphene Oxide
RH	Relative Humidity

R_s	Series Resistance
R_{sh}	Shunt Resistance
SEM	Scanning Electron Microscope
Spiro-OMeTAD	2,2′,7,7′-Tetrakis[N,N-di(4-methoxyphenyl)amino]-9,9′-spirobifluorene
TAA	bis(isopropoxide)-bis(acetylacetonate) titanium
TCO	Transparent Conductive Oxide
TEM	Transmission Electron Microscope
TPC	Transient Photocurrent
TPV	Transient Photovoltage
TRPL	Time-Resolved Photoluminescence
XRD	X-ray Powder Diffraction
XPS	X-ray Photoelectron Spectroscopy
UPS	Ultraviolet Photoelectron Spectroscopy
V_{oc}	Open Circuit Voltage

Contents

Content of Figures

Contents of Tables

Chapter 1.
Introduction

Today's global society faces two imminent energy issues: (i) the need to address escalating environmental pollution and (ii) overcoming the widespread energy poverty in developing nations.[1, 2] Fossil fuels based on coal, oil and natural gas are the dominant sources of energy today, representing ~ 80% of the total global energy use.[3, 4] However, these energy resources inherently suffer from their non-renewable and environmentally polluting characteristics. Emerging from progressive societal viewpoints concerning our environmental sustainability, the concept of sustainable human progress has been proposed. It is defined as "... to ensure that it (sustainable development) meets the needs of the present without compromising the ability of future generations to meet their own needs".[5] Thus, the urge of the challenge is underlined by limited resources and the need to change the fundamental energy construction on which our planet is operated on. To achieve sustainable energy development and environmental improvement, on the one hand, we need to develop new energy solutions that harness solar energy, wind energy and nuclear energy to replace fossil fuels, while on the other hand, we need to concurrently apply energy conservation and emission reduction innovation to existing infrastructure to achieve increased energy efficiency measures. While these two pathways are equally important, this thesis is focussed on the former by specifically looking at progressing solar cell technologies to ensure that our planet has reliable access to low-cost and renewable electricity.

1.1 Overview of Solar Cells

Solar cells are one of the most promising technologies to supersede traditional fuels that are used to produce electricity. This arises because, firstly, solar energy is proverbially inexhaustible. It has been calculated that the solar energy received on the earth surface is around 85,000 TW every year, which is 5000 times more than our present energy consumption.[6] This number is even far more than all of the other sustainable energy sources (wind, tidal, geothermal etc.) combined.[7] Secondly, since sunlight is available everywhere on our planet, it can be used to provide electricity power in remote and special needs area without major power losses induced by long-distance transmission. Moreover, with existing silicon technologies providing high reliability and small operational and maintenance costs, as well as modularity, it provides a convenient and cost-effective energy solution across many parts of the world.[8] Finally, solar cells convert light energy into electrical energy with no pollution at

the point of conversion. As a result, these devices create clean, renewable power from the sun without the generation of noise, moving parts, emissions, nor the use of fuels or water. Thus, the shift from fossil fuels toward such a near-infinite, ubiquitous and clean energy source promises to bring profound changes to people's real life and virtually every industry.

The use of solar energy is an age-old concept, but it was limited by the conversion from solar energy into heat energy until 1839. In that year, Becquerel discovered the photovoltaic effect when he inserted platinum electrodes into an ionically conductive solution containing silver halide salts that were exposed to light.[9] This effect can be more accurately defined as the generation of a potential difference between two layers of semiconductor or metal under incidence of a light stream. It was many years after this initial discovery that, what we now term as solar cells, were first demonstrated at Bell Lab in 1954.[10] The first solar cell used silicon as the light absorbing medium, exhibiting a power conversion efficiency (PCE) of 6%. Early research on solar cells mainly focused on developing monocrystalline silicon devices, due to its relatively mature purification process. In the 1970s, solar cell technologies were extended to polycrystalline and amorphous silicon devices.[11, 12] The lower price points of these technologies enabled them to rapidly dominate the photovoltaic market share, with polycrystalline being the market leader today.[11, 13] Through progressive developments in device architecture and manufacturing since that time, silicon solar cells have continued to reduce in cost per produced Watt, reaching current values of 0.3 USD/W,[14] which is already cost competitive to traditional fossil fuel sources. Meanwhile, from an environmental point of view, this CO_2-free technology is widely encouraged today because it helps alleviate the greenhouse effect.

There is no doubt that silicon paved the way for the development of a global photovoltaic market. However, as an indirect gap semiconductor, silicon is a poor absorber of light, which limits its further improvement. Thus, to better use solar energy, research on new materials and fabrication process of next-generation solar cells is required. Among the emerging candidates, thin film solar cells using vapour deposited multi-component materials, such as CdTe[15] and Cu-In-Ga-Se (CIGS)[16] have been historically the most promising. Currently, 5% of the global solar cell market share is CdTe, while CIGS is slowly gaining traction through advances in manufacturing.[17] From the 1990s, solar cell technologies were undergoing a third evolution due to the development of organic semiconductors and dyes. These new materials possessed the advantages of high light absorption coefficients and the potential to be processed using low cost deposition methods. More importantly, solar cells based on these could be made by solution processing at relatively low temperature, which simplified the fabrication process and paved the way for large scale fabrication.

1.2 Classification of Solar Cells

Solar cells fundamentally operate on the principle of efficient electron and hole creation in the absorbing material, then extraction of these charge carriers through the electrodes. Various types of device configurations can achieve these operational principles with promising PCEs (**Figure 1.1**). On this basis, photovoltaic solar cells have traditionally been categorized into three generations of devices, which are now described.

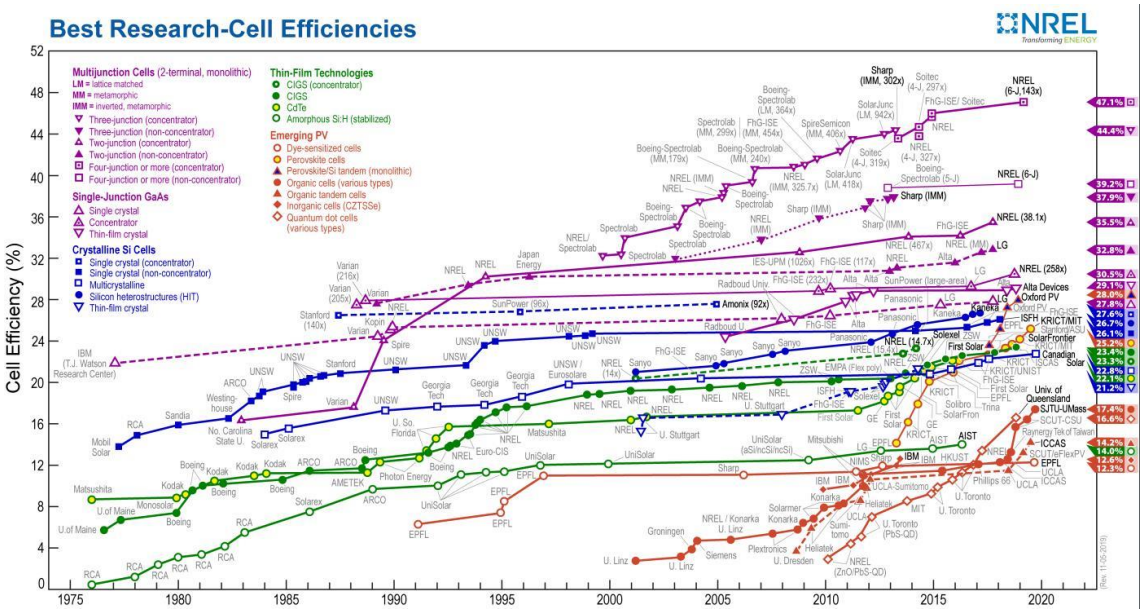

Figure 1.1 Record PCEs for different cell technologies.[18]

1.2.1 First Generation Solar Cell—Silicon Solar Cells

As the name indicates, the main materials in these solar cells are different types of silicon, including m-Si (monocrystalline silicon), poly-Si (polycrystalline silicon) and a-Si (amorphous silicon) (**Figure 1.2**). The m-Si solar cell, with a current top PCE record of ~27%,[19] is based on a p-n junction made by m-Si with high purity, which is fabricated by the tedious Czochralski process.[20] In this process, the Si crystals are sliced from big sized ingots and recrystallized, which results in high cost (more than half cost of the whole solar cell devices). In contrast, the poly-Si solar cell cost much less, being produced by simply cooling a graphite mould filled with molten silicon. Although the highest record PCE based on these materials is less than that of m-Si solar cell at ~20% up to now,[13, 19] the outstanding cost performance makes it occupy the largest market share of the global solar cell market.[17] Noteworthy, most leading firms fabricate both m-Si and poly-Si solar cells for their panels. The a-Si devices use silicon that lacks long-range order of the silicon atoms in the lattice giving it a

non-crystalline structure.[11] This breaking of structural symmetry means a-Si possesses a higher absorption coefficient compared to crystalline silicon forms, which enables it to be successfully used in solar cells as a very thin layer deposited onto a backing substrate, such as metal, glass or even plastic. As such, a-Si devices are fundamentally different from those based on both m- and poly- Si materials, with many also considering a-Si to be a second-generation solar cell candidate. While possessing a low purity requirement, a-Si is comparatively cheaper than other silicon devices, but it suffers the problem of poor and unstable performance, with the highest certified record PCE of around 10%.[19]

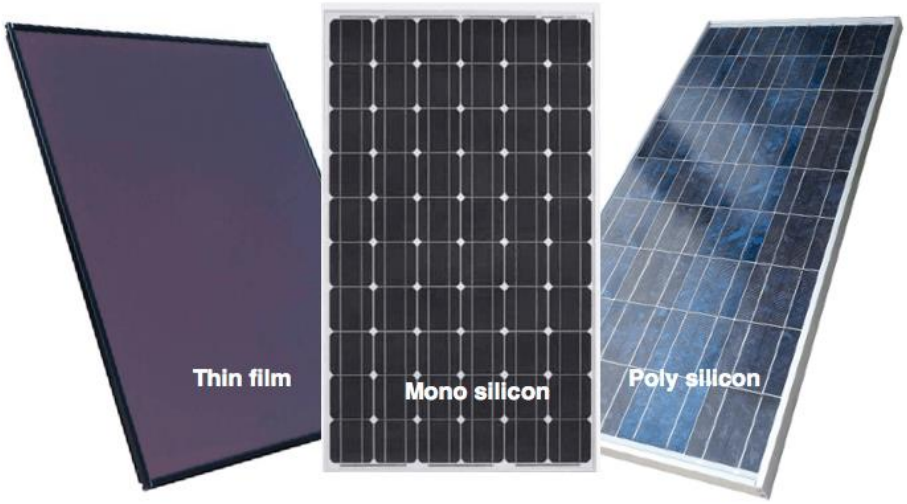

Figure 1.2 Digital photos of the three different types of solar panels.[21]

1.2.2 Second Generation Solar Cells—Thin Film Solar Cells

To lower the cost of solar cells, simplified device architectures that are based on inorganic semiconducting thin-film absorbers have been developed. The most successful of these have harnessed CdTe and $Cu(In_{1-x}Ga_x)Se_2$ (CIGS) absorbing layers.[22] Notably, the maximum efficiency of a single-junction solar cell as a function of the absorber material band-gap can be predicted by the Shockley-Queisser model (Figure 3A).[23] Based on this model, CdTe and CIGS materials can achieve high solar cell efficiencies that are comparable to Si devices. Alternative candidates, such as Cu_2ZnSnS_4 (CZTS) have also started to emerge, however these continue to remain far less developed in terms of their performance. One of the driving factors for such thin film technologies is that they dramatically reduce the material needs by thinning the absorbing layers compared to silicon. As is seen in **Figure 1.3B**, this is enabled by major gains in absorption coefficients across these thin-film

candidates.[24] As a result, thin-film solar cells have absorbing layers of ~0.5 to 5 µm in thickness, while crystalline silicon devices require silicon with 100's µm in thickness.

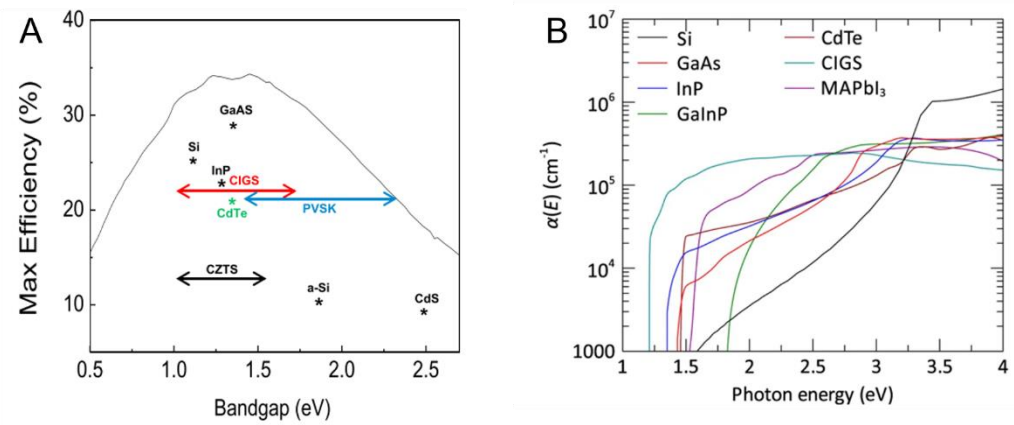

Figure 1.3 Optoelectrical properties of various materials for solar absorbers.[24]

CdTe Solar Cells

CdTe solar cells are the only commercially competitive technology to silicon on the market place today.[17] These devices are fabricated using a fluorine doped tin oxide (FTO) electrode on glass with an n-type CdS layer. The CdTe layer is vacuum deposited onto these substrates through a process called close-space sublimation, then re-crystallised in the presence of $CdCl_2$ to induce favourable doping and interfacial alloying. The back contact is typically a p-ZnTe or p-CuTe layer with a carbon electrode (**Figure 1.4A**). Record device efficiencies are now at >22%, with First Solar being the commercial supplier of these.[25] Notably, because Cd is toxic and, as a result, highly regulated, and Te is elementally scarce in terms of abundance, the viability of CdTe as a scalable photovoltaic technology in the future remains under question.

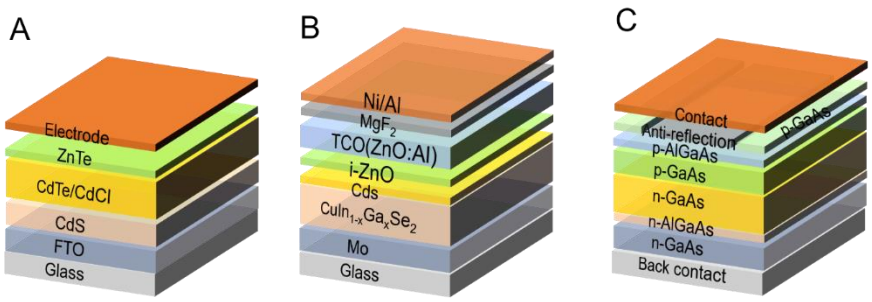

Figure 1.4 Schematic cross section of CdTe (A), GIGS (B) and GaAs (C) thin film solar cells.[22]

CIGS Solar Cells

CIGS is a promising technology as a non-toxic alternative to CdTe solar cell. CIGS is a direct-gap semiconductor with a tuneable bandgap across 1.04 to 1.67 eV and has high absorption coefficients across the visible ($>10^5$ cm^{-1}). Through gradual bulk and interfacial optimisation, record PCEs for CIGS solar cells are already at >23%, with steady progress in recent years being demonstrated.[17] CIGS solar cells are fabricated on soda lime glass with a molybdenum metal electrode. This contacts the p-type $Cu(InGa)Se_2$ which has an n-type CdS buffer layer, an intrinsic zinc oxide layer an n-type ZnO:Al, an anti-reflective film and finally a metal gate electrode (**Figure 1.4B**). This technology is highly promising in terms of efficiency, but its complex deposition process and the use of indium place major scaling restrictions in going forward.[24]

GaAs Solar Cells

GaAs solar cells were first demonstrated by IBM using a AlGaAs/GaAs device architecture that achieved 18–20% efficiency in 1972.[26] These devices have now emerged with world record efficiencies across all single-junction solar cells at a value of 28.8%.[19] However, GaAs is an expensive solar cell technology. While they use thin films of GaAs material, this is typically deposited onto a GaAs wafer and then delaminated from the wafer, which is reused (**Figure 1.4C**). This creates major disadvantages in terms of processing times and scalability, both of which increase their cost.[27] Given their high efficiency and high costs, GaAs solar cells are widely used in aerospace and military applications, where high efficiency is desirable and cost is not a limiting constraint.

1.2.3 Third Generation Solar Cells—New Concept Solar Cells

The Carnot limit of sunlight conversion to electricity yields a theoretical efficiency of 95%, which is almost three times the theoretical upper limit for a single junction standard solar cell.[28] Going beyond the existing Shockley–Queisser limit is one of the key focal point for third generation devices. Enhancing the practical application of solar cells beyond those offered by traditional solar cells through novel functionality creates the second focal point. Finally, developing ultra-low cost solar cells is other underlying focal point of these device types. Towards achieving these goals, investigations into new material and device configuration have yielded major advances towards developing high-efficiency third generation solar cells. These have largely been in quantum dots solar cells (QDSCs), organic solar cells (OSCs), dye sensitized solar cells (DSSCs) and perovskite solar

cells (PSCs). A common link across all these technologies is their ability to be processed through scalable printing or simple thermal evaporation approaches.

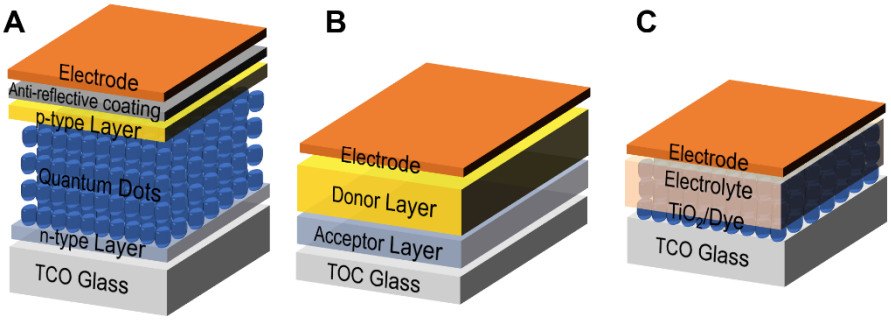

Figure 1.5 Schematic cross section of QDSCs (A),[29] OSCs (B)[30] and DSSCs (C).[31]

Quantum Dot Solar Cells

Quantum dots (QDs) are nanoparticles with a size that is smaller than their excitonic Bohr radius. Due to quantum confinement, they exhibit size-tuneable absorption and fluorescence properties. Typically, QDs are synthesised by wet-chemistry methods, which requires the use of long aliphatic chained stabilising ligands to achieve colloidal stability. A key challenge for QDs is that these ligands need to be displaced to successfully harness them within optoelectronic applications. As such, while bandgap tuneability makes QD solar cells appealing to more effectively harness sunlight,[29] gentle sintering to grow these particles is typically found to yield devices with much higher efficiencies.[32] Operationally, such materials are incorporated into solar cell architectures that mimic those of conventional thin-film device geometries (**Figure 1.5A**). A record PCE for such devices of 16.6% has been achieved by Wang's group from the University of Queensland based on metal halide perovskites.[33] Such perovskite QDs have been reported to possess better phase stability compared with their bulk counterparts, providing a strategy for improving the lifetime of perovskite solar cells.[34] In comparison to bulk perovskite films (*vide infra*) and other types of inorganic semiconductors, the ubiquitously lower PCE values of equivalent materials in nanocrystalline versus those in bulk forms raise question on the comparative viability of QDs and, more generally, nanocrystalline based solar cells to their bulk counterparts.

Organic Solar Cells

OSCs are a type of photovoltaic device that use organic semiconductors. Most of these are based on semiconducting polymers, for which Heeger, MacDiarmid and Shirakawa won the 2000 Nobel Prize

in Chemistry. Typically, high performance OSCs use a combination of a nanoscale blend of polymer donor and a fullerene or non-fullerene acceptor as the absorbing layer, named bulk heterojunction, which is sandwiched between two electrodes (**Figure 1.5B**).[35] The energetic difference between the lowest unoccupied molecular orbital (LUMO) and the highest occupied molecular orbital (HOMO) of the acceptors and donors induces exciton dissociation. Subsequent conduction of these isolated electrons and holes through the acceptor and donor materials, respectively, and their collection at the electrodes produces the electrical current. Since organic materials can be structurally highly flexible, organic solar cells pave the way to the promise of flexible solar cells, including those integrated within textiles and fabrics.[36] Over the past 25 years, tremendous efforts in OSCs have seen myriad new materials and device architecture being developed to yield devices that now reach record PCE of 16.4%.[30] The development of new materials, particularly acceptors, that reduce the intrinsic voltage losses across the donor-acceptor heterojunction remains one of the biggest current challenges for these devices.

Beyond efficiency, achieving high stability has been another key problem that has hindered the application of OSCs. The instability of devices mainly results from simultaneous diffusion of oxygen and water into the OSCs.[37] Oxygen takes part in the various photo-oxidation reactions of active materials and enhances their hole concentration, which results in an increase of traps in the active layer.[38, 39] Meanwhile, water leads to phase separation and decreases the donor/acceptor interfaces, which is harmful to exciton dissociation in the active layer.[39] Although these drawbacks can be alleviate by encapsulation technology,[40] stable active materials have to be explored to resolve the stability issue at a fundamental level.

Dye-Sensitised Solar Cells

DSSCs are also named Grätzel solar cells because they were first reported by the group of Michael Grätzel in 1991.[41] These devices consist of four basic components: (i) a semiconductor electrode (n-type TiO_2 and p-type NiO) deposited on FTO; (ii) a dye sensitizer; (iii) a liquid or solid-state redox mediator; and (iv) a counter electrode (carbon or Pt) deposited on FTO (**Figure 1.5C**). These devices operate through light absorption in the sensitiser, which then acts to inject a charge into the sensitized semiconductor and undergo a neutralising redox reaction with the redox couple. Charge balance is maintained through a counter electrode redox process. The semi-transparent nature of DSSCs was a major driver for this technology, largely due to its potential application in building-integrated photovoltaics (BIPV), as shown in **Figure 1.6**. While offering the promise of low-cost production, the PCE of DSSCs has reached an upper limit of only 13% after nearly 30 years of intense research.[42]

Beyond limited efficiency, the use of liquid electrolytes in these devices has caused major scaling and operation problems. While solid electrolytes have been investigated, such devices still have suffered from high degradation during continued operation.[43] The development of higher-efficiency and solid-state perovskite solar cells has seen many of the leading DSSC groups transition away from this type of device architecture over the past 10 years.[44]

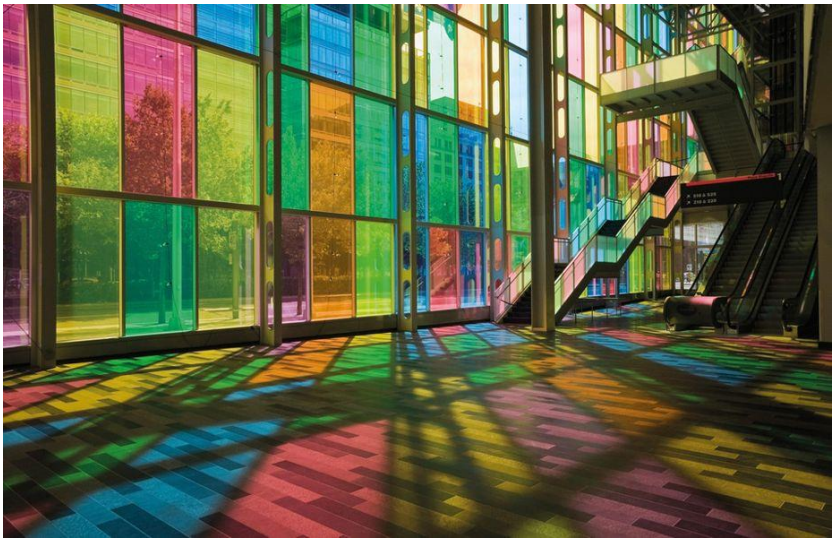

Figure 1.6 The striking coloured DSSC used as BIPV facade of the Palais des Congrès in Montreal.[45]

Perovskite Solar Cells

With modest origins as a failed sensitiser for DSSC,[44] metal halide perovskites have over the past decade become the hottest solar cell material candidate in the world. Such perovskites have the chemical form $A^{(1+)}B^{(2+)}X^{(1-)}_3$, where A represents large monovalent cations (e.g. $CH_3NH_4^+$, $HC(NH_2)_2^+$ or Cs^+), B are large divalent metal ions (e.g. Pb^{2+} or Sn^{2+}) and C being a monovalent halide anion (e.g. Cl^-, Br^-, I^-). Their first true promise as solar cell candidates arose when the Snaith and Miyasaka groups collaborated to place methyl ammonium lead iodide between FTO/(n-)TiO_2 and (p-)spiro-OMeTAD/Au to develop a solid-state "superstrate" PSC configuration, which achieved a PCE of 9.7%.[46] Tremendous research efforts into perovskites have since ensued, which have yielded certified PCEs of 25.2%.[19] This degree of success can be ascribed directly to their composition-dependent tuneable and direct optical bandgaps, large light absorption coefficients, high carrier mobilities and long carrier diffusion lengths.[47] Despite these successes in increasing PCE, the instability of current metal halide perovskites towards moisture and the toxicity from Pb^{2+} or Sn^{2+} place significant uncertainty on the future viability of metal halides perovskites commercially.[48] Significant research efforts are currently underway into the development of novel lead and lead-free

perovskite compositions, with various stabilisation mechanisms, to reduce the extent of these two factors.[49, 50] Equally important is the synergistic role of the charge transport layers and the associated interfaces towards enabling efficient charge extraction, reducing interfacial recombination and enhancing intrinsic and environmental stability factors. These form the key thematic areas that are explored in this thesis.

1.3 Working Principles of Solar Cells

1.3.1 Fundamental Principle of Solar Cells:

A solar cell is a device that converts optical energy to electric energy through the photovoltaic effect. This can be understood based on four stages of operation (**Figure 1.7**). To demonstrate this concept, we will use an n-i-p thin film solar cell architecture due to its functional relevance to perovskite solar cells, which are the focus of this thesis.

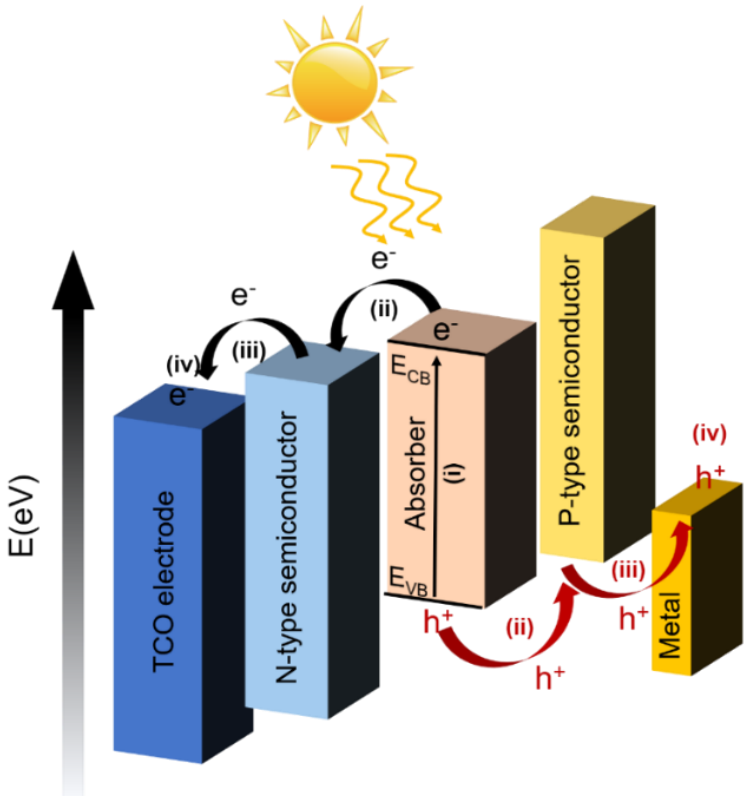

Figure 1.7 Schematic of working principle of solar cells.

(i) Generation of light-induced carriers. In an ideal semiconductor, the valence band maximum (VBM) is the highest range of electron energies in which electrons are normally present at absolute

zero temperature and the conduction band minimum (CBM) is the lowest range of vacant electronic states. There is a bandgap between these, E_g=E_{CBM}-E_{VBM}, where limited electronic states exist. When a material absorbs incident photons, the incident photon energy causes an excitation of electrons from E_{VBM} to E_{CBM}. The electron can only jump when the incident energy is higher than E_g. The excited electron leaves a hole in E_{VB}, which is physically treated as a positive charge. Thus, photoexcitation in the simplest sense create electrons and holes in a material following absorption. At low temperatures, the Coulomb interaction between these forms exciton states, while at room temperature, the thermal energy is typically sufficient to ionise these largely into free photo-induced carriers.

(ii) Separation and transport of light-generated carriers. In isolated semiconductors, the generated electrons and holes will ultimately recombine through the release of photons or lattice vibrations (i.e. heat). To minimise these recombination processes, solar cells use electric field gradients generated through doping (i.e. p-n junction) or through charge selective heterojunctions (i.e. n-i-p thin film configurations) to create an electric field across the light absorbing layer to transport the charges away from each other. For the latter, these charge selective layers are known as charge transport layers, although ideally, they also provide selective charge blocking properties of the counter charged carrier. For charges to be successfully collected it is a fundamental requirement that the lifetime of the charge carriers is longer than the charge extraction time. The charge extraction rate (k_{ex}) in a device is approximated as:[51]

$$k_{ex} = \frac{2\mu V_{int}}{L^2} \quad \textbf{(1.1)}$$

where L is the active layer's thickness, μ is charge mobility and V_{int} is the internal voltage developed across the absorber layer. Notably, this is an approximate equation to calculate k_{ex} value as it is confined in a simplified situation: (I) the device possesses a uniform absorption across the active layer and constant electron and hole mobility; (II) the active layer is thinner than 300 nm, so that including an optical profile in the modelling of the device does not significantly change the results; and (III) on average, electrons have to travel half the active layer thickness to reach the cathode. For n-i-p structures, the latter is approximated as the difference in the Fermi energy of the electron and hole charge transport layers, although they are fundamentally limited to the difference is quasi-Fermi energy splitting between the valence and conduction bands. It is evident that high charge mobilities or large electric field strengths are key parameters to permit this condition in the general sense. With the electric field strength being equivalent to the voltage difference across the device, V, divided by the L of the absorbing layer, it is evident that maximising voltage and minimising thickness will induce a higher electric field strength.

Notably, charge transport in solar cells arises from both drift and diffusion processes, with the latter being dominant when devices are operating under nearly zero-field conditions, i.e. close to the open circuit voltage. As such, in addition to high charge mobility, it is equally important to have large charge diffusion coefficients in good solar cell material candidates.

(iii) Charge extraction of photocarriers. Charges that reach the selective interfaces in the solar cells need to be efficiently transported through these layers into the electrodes. As such, interfaces need to be engineered to reduce interfacial trap states.[52] In addition, the overall resistance contribution for charges being transported across the individual layers needs to be minimised.[53] This is achieved by balancing the thickness of these layers relative to their layer resistivities. Given that typical layers have resistivity values of > 200 Ohm cm, thicknesses of 10 – 500 nm for such layers are typical, with lower thicknesses being needed for more poorly conducting transport layers.[54, 55]

(iv) Charge collection of photocarriers. To realise electrical power, an external circuit is established to collect these carriers by minimising any resistance contributions arising from the electrodes and electrical wiring connections across the circuit. As is typical in a photochemical cell, the electrons flow through the electrical circuit from the anode to the cathode, with holes flowing in the opposite direction.

1.3.2 Device Characterization of Solar Cells:

The equivalent circuit model of solar cells is shown in **Figure 1.8**, where J_{ph} is the photo generated current density, R_s is the series resistance arising from contact resistances between different layers and electrodes, and R_{sh} is the shunt resistance from the current leakage. J_0 is the dark saturation current density of the solar cell.

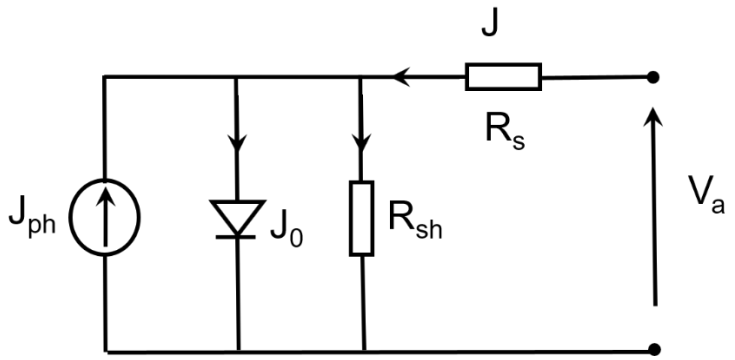

Figure 1.8 Equivalent circuit for practical solar cells.

When a solar cell is measured in the electrical network under dark condition, the net current density flowing through the load under applied voltage J(V_a) is determined as:

$$J(V_a) = J_{rec}(V_a) - J_{gen}(V_a) \quad \textbf{(1.2)}$$

where J_{rec} is the recombination current resulting from the recombination of diffusing minority carriers with the majority carriers, and is dependent to the applied voltage:

$$J_{\text{rec}}(V_a) = J_{\text{rec}}(V_a = 0)\, exp(\frac{eV_a}{kT}) \quad \textbf{(1.3)}$$

J_{gen} is the thermal generation current density that is caused by the drift of minority carriers, and is almost independent of the potential barrier across the junction and is determined by the availability of the thermally-generated minority carriers:

$$J_{\text{gen}}(V_a) \approx J_{\text{gen}}(V_a = 0) \quad \textbf{(1.4)}$$

When there is no applied voltage:

$$J(V_a = 0) = J_{rec}(V_a = 0) - J_{gen}(V_a = 0) = 0 \quad \textbf{(1.5)}$$

Thus, the external current density can be expressed as:

$$J(V_a) = J_{rec}(V_a) - J_{gen}(V_a) = J_0 \left[exp\left(\frac{qV_a}{kT}\right) - 1\right] \quad \textbf{(1.6)}$$

Where J_0 is the dark saturated current density that is given by:

$$J_0 = J_{gen}(V_a = 0) \quad \textbf{(1.7)}$$

On the other hand, the dark saturated current density J_0 of the solar cell is expressed as:

$$J_0 = \text{e}n_i^2(\frac{D_N}{L_N N_A} + \frac{D_P}{L_P N_D}) \quad \textbf{(1.8)}$$

D_N and D_P are the electron and hole diffusion coefficients, respectively. L_N and L_P are minority-carrier diffusion length for electrons in a p-type material and for holes in an n-type material, especially. N_D and N_A are the concentration of donor and acceptor atoms, respectively.

Under illumination, J_{ph} is related to the generation rate, the minority-carrier-diffusion length:

$$J_{ph} = \text{e}G(L_n + L_p) \quad \textbf{(1.9)}$$

In this case, the net current is the sum of the photo- and thermal generation currents and the recombination current.

$$J(V_a) = J_0 \left[exp(\frac{eV_a}{nkT}) - 1\right] - J_{\text{ph}} \quad \textbf{(1.10)}$$

It should be noted that in practical solar cells, the dark diode current does not obey the Boltzmann approximation, so the Boltzmann factor used should be modified by an ideality factor *n*. The ideality factor is a measure of the junction quality and the type of recombination in a solar cell. *n*=1 represents that the carrier recombination in the depletion region is zero (or negligible) and a diffusion current is dominant in the device, while strong bimolecular recombination in the bulk or interface is represented by values of *n*=2 or higher. In practice, an ideally factor of between 1 and 2 is observed.

J-V Curve:

The performance of solar cells can be characterised by the measurement of the current density (J) as a function of the variable bias voltage (V) under light irradiation, which is named the J-V curve. A representative J-V curve is shown in **Figure 1.9**. Below, we discuss each of the main components that enable the J-V curve to be used to assess solar cell performance. Notably, in this figure we show the current density in the positive quadrant as a way of convention. As is seen from **Equation 1.2**, strictly speaking the photocurrent is negative in sign.

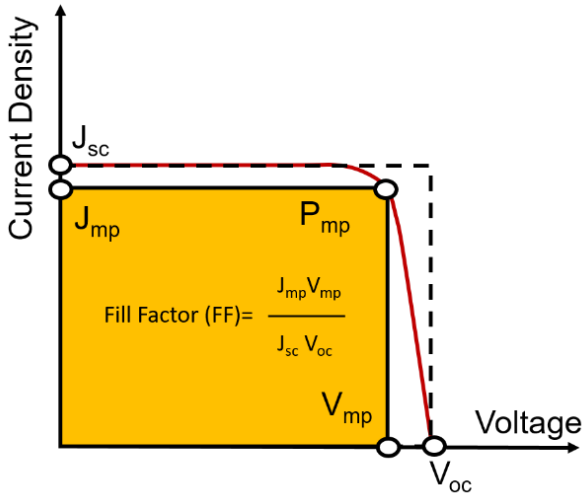

Figure 1.9 Typical J-V characteristics for dark and light current in a solar cell illustrating the important parameters for such devices.

Short-circuit Current Density:

The short-circuit current density (J_{sc}) is the photocurrent of a solar cell when the voltage is zero. As seen from **Equation 1.9**, the photocurrent depends strongly on the charge generation rate and the carrier diffusion lengths. Evidently, the generation rate is directly related to the overlap of the absorption profile and the incident light spectrum, as well as the photon flux incident on the solar cell. To realise photocurrent, the transported carriers also have to be collected at the electrodes, which necessitates low recombination rates compared to the extraction dynamics.

Open-circuit Voltage:

The open-circuit voltage (V_{oc}) is the voltage at which a solar cell delivers zero photocurrent. In general, this value is related to the splitting of electron and hole quasi-Fermi energy levels actuated by light illumination and is directly related to the electrical bandgap of an absorbed material. Under open circuit conditions, from the modified Shockley equation, V_{oc} can be approximated as:

$$V_{oc} = \frac{nkT}{e} ln(\frac{J_{sc}}{J_0} + 1) \quad (\mathbf{1.11})$$

As J_0 depends on recombination in the solar cell, the V_{oc} is a comparative measure of recombination in the device relative to the radiative bandgap of an absorbing material.[56] For solar cells with the same absorber, the V_{oc} is mainly determined by the amount of interface charge recombination, the electronic nature of trap states and incident light intensity.

Fill Factor:

The fill factor (FF*)* is the ratio of the maximum obtainable power (P_{max}) per unit working area (the product of J_{mp} and V_{mp}) to the product of V_{oc} and J_{sc} in **Figure 1.9**.

$$FF = \frac{J_{mp}V_{mp}}{J_{sc}V_{oc}} \quad (\mathbf{1.12})$$

The FF characterizes the shape of J–V curves and represents how "difficult" or how "easy" the photo-generated carriers can be extracted out of a photovoltaic device. It can be influenced by many factors that interplay with each other intricately, but the main influence factors on FF are the R_s and R_{sh} and the intrinsic properties of the diode materials, such as the charge mobility, exciton dissocation and interfacial and bulk recombination (**Figure 1.10**). The R_s and the R_{sh} show the effects on the shape of J–V curve around V_{oc} and J_{sc}, respectively. The properties of the diode determine the curvature of the J–V curve around the maximum power point.[57] For example, charge accumulation in devices (in active layers or relative interfaces) can lead to S-shape J-V curve due to the formation of redistribution of internal electric fields. Thus, in fabrication of solar cells, factors such as contact resistance, current leakage, charge transport, interface quality, crystallinity and composition of materials all need to be considered to realize high FFs.

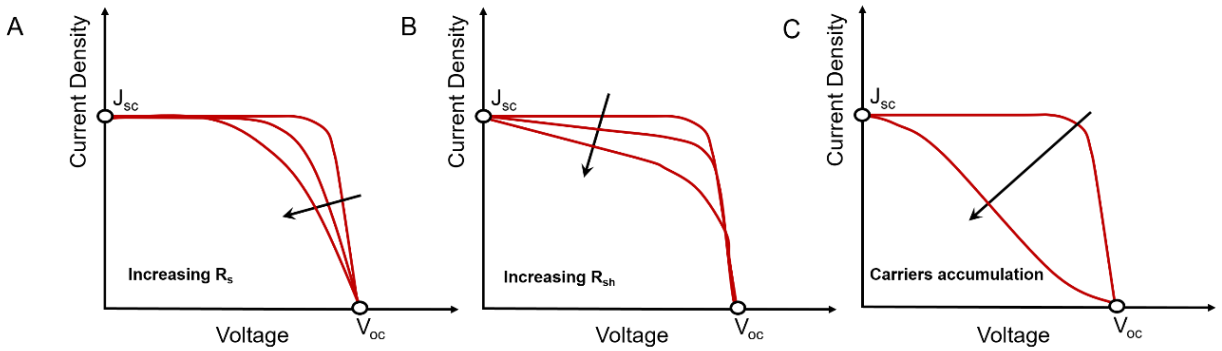

Figure 1.10 J-V curves with different FFs, which are influenced by R_s, R_{sh} and diode properties.

Power Conversion Efficiency

The PCE is calculated as the ratio between the maximal generated power and the incident power from the light source. Based on the above equations, it can be readily shown that this simply equated to:

$$PCE = \frac{J_{sc} V_{oc} FF}{P_{solar}} \quad (\mathbf{1.13})$$

The certified PCE is measured by standard condition as follow:

(I) Air mass 1.5 spectrum (AM1.5) for terrestrial cells and Air Mass 0 (AM0) for space cells.

(II) Intensity of 100 mW cm^{-2} (1 kW m^{-2}, also known as one-sun of illumination)

(III) Cell temperature of 25 ℃.

(IV) Four-point probe to remove the effect of probe/cell contact resistance

1.4 Perovskite Solar Cells

1.4.1 Structure of Perovskite

Perovskites form a group of materials with the crystal structure similar to naturally occurring $CaTiO_3$, which was discovered in metamorphic rocks from the Ural Mountains by Gustav Rose in 1839,[58] and then named by L.A.Perovski. In later years, it was found that perovskite compounds commonly exist in undersaturated alkaline rocks, and increasingly paid attention to these materials due to their unique properties of thermoelectricity, dielectricity, and semi-conduct nature.[59] The typical structural formula of perovskite is ABX_3 where A are 1^+ ions, B are 2^+ or 4^+ metal cations and X can be O, C, N or halides anion. The perovskite structure is symmetric, where X-anions hold the octahedral corner coordinates, while B-cations hold the octahedral holes in the 3-D structure, as shown in **Figure 1.11**. Idealised perovskites are generally cubic crystals. The B-cation and the adjacent 6 X-anions form a

network of corner-sharing BX_6^- octahedra, and the A-cation is selected to neutralize the total charge and form a cuboctahedron with the adjacent 12 X anions.

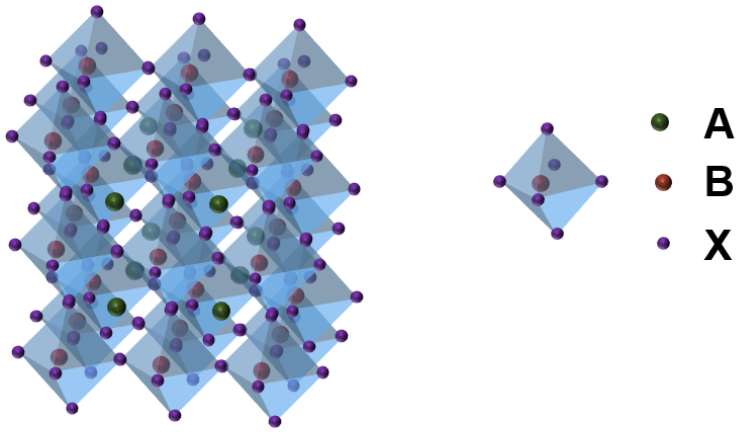

Figure 1.11 The basic ABX_3 perovskite structure.

The size of the elements in perovskites requires certain conditions to stabilize the structure. At the most basic level, the Goldschmidt tolerance factor, t, provides this gauging as defined from the relation:[60]

$$（R_A + R_X） = t\sqrt{2}(R_B + R_X) \quad \textbf{(1.14)}$$

where R_A, R_B, and R_X are the ionic radius of the corresponding A, B and X elements, respectively. By changing these radii, the t can be varied, but only in a restrict range of values around unity to have a stable, even distorted, three-dimensional perovskite structure (t = 1 corresponds to a perfectly packed perovskite, and $0.9 < t < 1.0$ supports a cubic perovskite).[61] Generally, B is a metal ion in the form of Cu, Ti, Ni, Co, Fe, Mn, Cr, Pd, Cd, Ge, Sn, Pb, Eu, Yb etc., and is smaller than A, which is typically Ca, K, Na, Sr, Cs, some rare earth metals or some organic molecules, such as (CH_3-NH_3^+, NH_2-CH=NH_2^+).[62]

When A represents organic ions, such perovskite compounds are named hybrid organo-metal perovskite. Organic compounds, which typically interact through weaker interactions (van der Waals or hydrogen bonding), offer the potential of high luminescence efficiency, large polarizability, plastic mechanical properties, and in some case exhibit conducting properties.[63] In these perovskite compounds, if the A is too small, an orthorhombic phase or tetragonal phase is observed, while if it is too large, a 2-D structure is typical. $(RNH_3)_2A_{n-1}B_nX_{3n+1}$ is used to summarize the dimension of perovskite, where n=1 corresponds pure 2D perovskite structure, and $n \rightarrow \infty$ represents the 3D perovskite structure. In contrast to 3D halide perovskites, 2D halide perovskites are well known to be

more resistant to humidity when hydrophobic alkylamines are used in their layered structures. However, they are poor light absorbers due to their higher bandgaps, poor carrier mobilities, and low absorption coefficients. Thus, mixed dimensional perovskites, so-called quasi-2D perovskites, have been developed to improve the performance of solar cells as they combine the excellent air stability of 2D perovskites with the enhanced electronic properties of 3D perovskites.[64]

1.4.2 Configurations of Perovskite Solar Cells.

The device structures of PSCs can be broadly categorized into either mesoscopic or planar geometries within conventional or inverted configurations, as **Figure 1.12** shows. Conventional configuration PSCs consist of a transparent bottom electrode made of a transparent conductive oxide (TCO) for electron collection, an n-type electron transporting layer (ETL), a perovskite photoactive layer, an upper p-type hole transporting layer (HTL) that extracts holes, and a top metal electrode for hole collection. For the inverted configuration, hole and electron transporting layers are swapped relative to each other and the role of the transparent bottom electrode and top metal electrode are reversed. Within each of these classes of device, mesoporous architectures are those where a metal oxide mesoporous scaffold is introduced within the perovskite layer, while when the scaffold is absent the devices are termed planar PSCs.

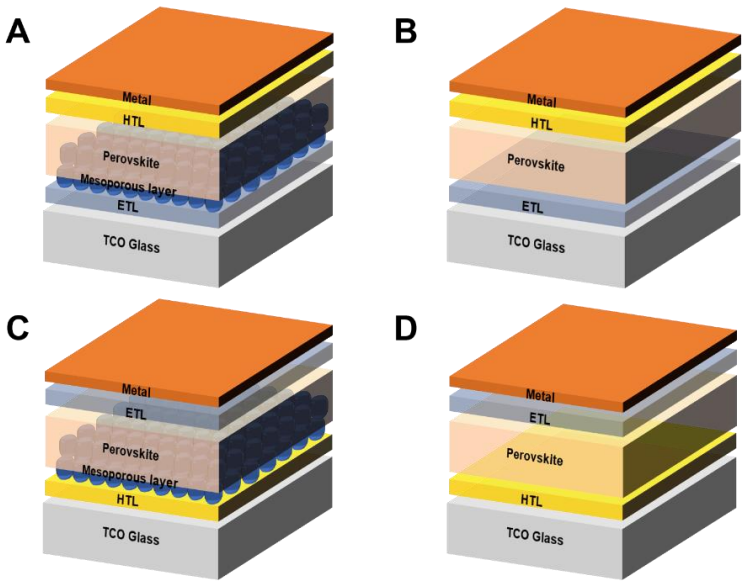

Figure 1.12 Device structures of (A) conventional mesoporous, (B) conventional planar, (C) inverted mesoporous and (D) inverted planar perovskite solar cells.[65]

The structural differences across the different PSC devices present fundamental variations to their processing limits. If the underlying substrate is glass, then the processing ceiling temperature for the bottom HTL is limited by the TCO and glass layer limits. This is typically 400 °C for ITO/glass and 500 °C for FTO/glass.[66, 67] Lower temperature limits exist for flexible solar cells deposited on plastic substrates, such as Poly (ethylene terephthalate) (PET). Meanwhile, for layers deposited on the perovskite, these present ceiling temperatures that vary with the perovskite formulations. To gauge this trend, the processing temperature for $MAPbI_3$,[68] $FAPbI_3$,[69] and $CsPbI_3$[70] are 100 ℃, 175 ℃ and 210 ℃, respectively. Evidently, these create the necessity for low-temperature processing of the top layers. This fundamentally restricts the type of charge transporting layer (CTL) and electrode that can be used.

Across the different device structures, CTLs establish the work function at the interfaces to maximise the built-in electric field across the device, reduce the recombination of electrons and holes, and improve the stability of the perovskite layer. For many high-performance PSCs, their configuration consists a mesoporous layer (typically TiO_2) that is infiltrated by a perovskite precursor solution before annealing to form solid a perovskite film. This not only facilitates the collection and transportation of charges from within the photoactive layer to guarantee high V_{oc} and J_{sc}, as well as low hysteresis,[71] but also improves the device FF by eliminating capacitive charges.[72] Each of these factors makes the investigation of materials and methodology, as well as relative interface engineering of CTLs, of paramount importance towards developing high efficiency perovskite solar cells.

1.4.3 Charge Transporting Layers

Despite promising PCEs, PSCs exhibit problems involving the stability,[73] as well as reproducibility and scalability,[74] which hinder their progress to commercial arenas. To a large part, these issues can be isolated to the underlying perovskite layer, but cannot be decoupled from the charge transport layers and their interfaces with the perovskite layer itself. Therefore, exploration of device architectures that use alternative semiconductors is of great importance towards achieving high-performance and stable PSCs in going forward.

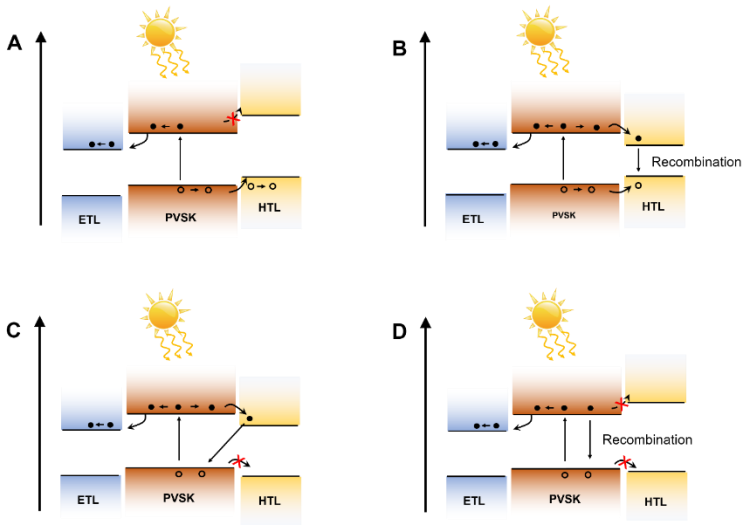

Figure 1.13 Schematic diagrams of potential energy level alignments at perovskite/HTM contacts when the ETL is correctly aligned.[75]

One of the most important factors to consider for a CTL is their energy alignment in PSC architecture. The energy alignment between the charge transport layer and the perovskite layer determines the energetic feasibility for charge transfer across their interface. To schematically demonstrate this, we take configurations of the perovskite layer sandwiched between a correctly aligned ETL and various HTLs as examples here to explain the charge transfer at perovskite and HTL interface in **Figure 1.13**, where figures from (A) to (D) demonstrate staggered heterointerface between an HTL with higher HOMO than the VBM of perovskite layer, straddling heterointerface between an HTL with higher HOMO than the VBM of perovskite layer, staggered-gap heterointerface between an HTL with lower HOMO than the VBM of perovskite layer and straddling heterointerface between an HTL with lower HOMO than the VBM of perovskite layer, respectively. Here we assume that the HTL has good hole charge transport properties compared to the electron. Critical to the successful charge transfer of a hole from the perovskite to the HTL is an energetically staggered heterojunction interface (**Figure 1.13A**). Under this condition, an electronic barrier exists to prevent electron transfer, which renders the layer also an electron blocking layer. For a straddling-gap heterojunction interface (**Figure 1.13B**) both electron and hole transfer are permitted. As a result, electron-hole recombination in the charge transport layer will occur to reduce the achievable photocurrent and voltage. For HTLs with a deep-lying bandgap configuration level relative to the perovskite (**Figure 1.13C**), the energy barrier for hole extraction results in hole accumulation in perovskite and the conducive energy alignment for electron transfer. However, with the p-type HTL (typically) exhibiting relatively poor electron transport properties, electrons injected into the HTL rapidly recombine with the accumulated holes at the perovskite/HTL interface. Finally, when a large bandgap charge transport layer is energetically

misaligned to exhibit energetic barriers for both electrons and holes (**Figure 1.13D**), this layer can be considered as a purely dielectric resistor, which is not conducive for extraction of either carrier from the perovskite.[65] Thus, appropriate energy levels of CTLs is the key to achieve high PCE PSCs. **Figure 1.14** summarizes the typical charge transporting materials (CTMs) with appropriate energy levels.[76-89]

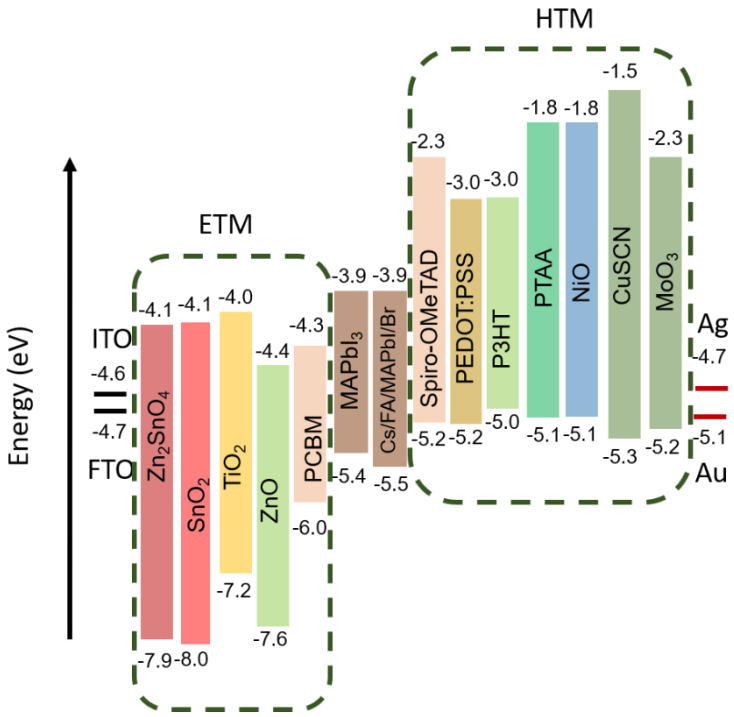

Figure 1.14 Summarized energy level diagram of typical ETMs and HTMs. Energy levels of two perovskites in our work in this thesis are also shown in this diagram.

Electron Transporting Materials

Myriad n-type electron transporting materials (ETMs) have been investigated for use in conventional PSCs, with TiO_2,[68] SnO_2,[79] and ZnO[81] being the most common. Across these, TiO_2 is the most widely used ETM due to its high chemical stability, large optical bandgap of 3.2 eV and appropriate conduction band energy of -4.2 eV vs. vacuum for minimizing voltage losses. Its successful use has been demonstrated across all high efficiency planar,[90, 91] meso-porous [46, 92, 93] and sensitized [94] PSC architectures. Moreover, TiO_2 deposition has been demonstrated using spin coating,[92, 95] atomic-layer deposition,[96, 97] spray pyrolysis,[93, 98, 99] electrodeposition,[100, 101] sputtering [102] and thermal oxidation.[103, 104] Among these, spray deposition is the most commonly employed approach owing to its simplicity, although uniformity and reproducibility remain as issues for the commonly used air-

brush spray approach. In **Chapter 4**, we introduce an ultrasonic spray pyrolysis protocol for TiO_2 compact layers that overcomes these challenges, paving the way for the fabrication of large area ETLs suitable for PSCs.

However, TiO_2 suffers from the problem of low electron mobility (~ 1 $cm^2\ V^{-1}\ S^{-1}$), which limits the extraction of electrons from the perovskite within solar cell devices.[105] In addition, in the view of low temperature fabrication process, crystallization of TiO_2 at a low temperature is difficult. This has promoted the exploration of other n-type semi-conductors as ETMs. SnO_2 and ZnO have emerged as promising candidates to replace TiO_2 in perovskite solar cells due to their higher electron mobility (>200 $cm^2\ V^{-1}\ S^{-1}$).[105] However, it was quickly realised that the electrochemical instability exists between ZnO and perovskite layers,[106] which has resulted in SnO_2 being the most preferred TiO_2 alternative ETM in recent years.[107] This has arisen because SnO_2 possesses better optical and electric properties, and stability than the traditional TiO_2.[107] In addition, owing to its low temperature processability, it is a more versatile ETM, having also been successfully used in tandem solar cells.[108]

Compared with inorganic ETMs, as discussed above, organic ETMs are more promising in terms of tailored structure, solubility engineering and flexibility.[109] However, such ETMs routinely possess poor electronic mobility (~$10^{-3}\ cm^2\ V^{-1}\ s^{-1}$) and low conductivities, making them usable only as very thin layers.[110] In inverted PSCs, the ETL plays a critical role in achieving high device stability because it provides a protection role to the underlying perovskite layer. The ETL on top of perovskite layers are normally solution-processed or evaporated fullerene-based materials with buffer layers such as bathocuproine (BCP), [111] poly [9,9-bis(30-(N,N-dimethylamino)propyl)-2,7-fluorene-alt-2,7-(9,9-dioctylfluorene)] (PFN),[112] and LiF.[82] These layers should ideally help to chemically protect the perovskite layer, but also help to form ohmic contacts with the metal electrode. However, fullerene derivatives, such as PCBM, have been shown to lead to degradation of hybrid perovskite films, possibly because (i) they tend to absorb water and oxygen in ambient conditions, with perovskites being particularly susceptible to moisture, and (ii) they form discontinuous layers on perovskite films, which is insufficient to provide protection during the deposition of the top metal electrode and/or further exposure to the ambient environment.[113]

To combat these issues, n-type inorganic semiconductors that are chemically stable, possess a controllable morphology and can be deposited at low-temperatures have been explored to replace fullerene derivatives in inverted devices. Unlike sol-gel made ZnO or spray pyrolysis made TiO_2 in conventional PSCs, both of which are prepared on chemically and temperature stable doped oxide

electrodes, the deposition of ETLs should avoid destroying the underlying perovskite layer and form a continuous film. Thus, homogeneous nanoparticle inks with volatile solvent that cannot dissolve the underlying perovskite film have been introduced to replace C_{60} derivatives in inverted devices. For example, Yang's group firstly spin-coated ready-made ZnO nanoparticles on top of perovskite layer as ETL and fabricated an organic-free inverted PSC with a PCE of 14.6 ± 1.5%.[113] Through the replacement of PCBM with ZnO in an ITO/PEDOT: PSS/perovskite/ZnO/Al device structure, the stability was well improved, preserving 90% of the initial PCE for 2 months. [113] Very recently, Zhu et al. exploited SnO_2 nanocrystals to serve as ETLs in inverted PSCs, with SnO_2 showing higher mobility, wider bandgap and lower trap density compared with ZnO and TiO_2.[114] A high PCE of 18.8% was achieved and the device retained over 90% of its initial PCE in a moist environment for 30 days. Compared with the typical PEDOT:PSS (HTL)/PCBM (ETL) configuration, which show PCEs of ~12% and totally degrade in 10 days, the inorganic ETLs are particularly important to simultaneously improve the performance and the stability of the devices. Small molecules such as diketopyrrolopyrrole-based molecules[115] and polymers such as naphthalene diimide (NDI)-based polymer[116] have been reported, but their device PCEs remain comparatively poor.

Another strategy to stabilize the ETL is to partially introduce an inorganic n-type semiconductor layer on fullerene derivatives. For example, Chen et al. introduced a thin layer of Nb doped TiO_x between PCBM and Ag top electrode by hydrolysis and condensation of titanium alkoxides with 5% Nb precursor at low temperature, where the n-doping of Nb dramatically improved the conductivity of amorphous TiO_x by orders of magnitude.[117] The inorganic buffer layer boosted the device PCE from 10.2% (without buffer layer) to 18.3% (with $Ti(Nb)O_x$ layer) and protected the device from degradation for 7 days with 95% performance of its initial PCE. Although advantageous, such approaches do require hydrolysis steps, which can be detrimental to the underlying perovskite layers. Developing non-hydrolytic approaches towards such approaches would provide a feasible way to overcome this challenge.

Hole Transporting Materials:

In comparison to ETLs, fewer hole transporting material **(**HTM) candidates exist, particularly for depositing on top of the perovskite layer for which processing ceiling temperatures create challenges. Most of the HTMs used in PSCs are organic molecules owing to their milder processing conditions compatible with perovskites. Spiro-OMeTAD and its derivatives are one of the best candidates for high-performance conventional PSCs.[79, 118] However, pristine Spiro-OMeTAD suffers from low hole mobility (~10^{-4} cm^2 V^{-1} s^{-1}), which leads to poor hole transport in devices.[119, 120] While offering doped

conductivities of > 10^3 S/cm and appropriate electronic structure, the use of hygroscopic dopants (Li-TFSI) makes these materials highly unstable under long term use.[120] As such, the quest for fabricating high-efficiency Spiro-OMeTAD-free devices has been a long-standing issue. These efforts have seen the development of a number of promising Spiro-OMeTAD alternatives.

Molecular HTMs, especially dopant-free varieties, have become an important development direction for PSCs that exhibit high PCE and high stability simultaneously. Towards this goal, engineering of their energy levels, hydrophobicity and film morphology has been widely explored.[121] For example, Cheng's group developed a series of acceptor-donor-acceptor small molecules with an electron rich phenoxazine core as HTMs in PSCs. The hole mobility of these molecules was shown to be 10-fold higher than that of Spiro-OMeTAD. As a result, a PCE of 12.8% was achieved in related devices. More recently, 2,8-bis(4-(bis(4-methoxyphenyl)amino)phenyl)-5-octyl-4Hdithieno[3,2-c:2′,3′-e]azepine-4,6(5H)-dione and N2,N2,N7,N7-tetra-ptolylspiro[fluorene-9,20-[1,3]dioxolane]-2,7-diamine were reported to as HTMs for inverted PSCs. These molecules helped to achieve devices with high PCEs of more than 20% and high stability.[122, 123] However, for conventional PSCs, the development of dopant-free small molecular HTMs is still required to achieve PSCs with high PCE that are comparable with doped Spiro-OMeTAD counterparts.

In addition, polymers such as Poly[bis(4-phenyl)(2,4,6-trimethylphenyl)amine (PTAA) and Poly(3-hexylthiophene (P3HT) possess respective hole mobilities of 5×10^{-3} cm^2 V^{-1} s^{-1} and 0.2 cm^2 V^{-1} s^{-1},[124] which are higher than for Spiro-OMeTAD. However, the poor contact between such HTMs and neat perovskite surfaces hinder hole extraction.[125] Thus, these require appropriate interface engineering to mitigate defect formation between the HTLs and perovskite.[84] Recently, researchers have made a great headway on P3HT HTM and achieved a PCE as high as 22.8% by using a wide-bandgap halide modified perovskite absorber.[84]

In comparison to organic candidates, inorganic p-type semiconductors possess superior hole mobilities, e.g. CuO (> 1 cm^2 V^{-1} s^{-1}),[126] CuSCN (0.01–0.1 cm^2 V^{-1} s^{-1})[127] and doped NiO (>0.1 cm^2 V^{-1} s^{-1}).[128] In addition, their outstanding transparency throughout the visible-near infrared spectrum and good chemical stability make them very promising alternatives. However, the deposition of such HTLs on the perovskite layer has remained challenging owing to the need for stabilisation within suitable nanoparticle inks[129] and the need for interface modification.[88] To date, the highest PCE of conventional PSC with inorganic HTL (20.4%) was achieved by the Gratzel's group, who used a configuration of FTO coated glass/TiO_2/perovskite/CuSCN/Au with a reduced graphene oxide (rGO)

spacer layer between HTL and electrode. The inorganic HTLs provided outstanding stability with > 95% of their initial efficiency being retained after aging for 1000 hours.

For HTL in inverted PSCs, PEDOT:PSS and p-type NiO are the most successfully used HTLs in such devices, with the latter presenting better stability and electron blocking properties. Various approaches have been used to fabricate NiO HTLs for inverted PSCs, including sol-gel deposition,[130] nanoparticle inks,[131] and spray pyrolysis.[117] Yang's group was the first to introduce a sol–gel–processed NiO nanocrystals HTL in PSCs, achieving a PCE of 9%.[130] Recent progress has seen a further improvement to more than 15% via a monolayer molecular modification.[132] Meanwhile, Choy's group reported a solution processed HTL made with a NiO nanoparticle ink that gave an inverted PSCs with PCEs of ~16%.[131] The most successfully deployed NiO HTL was deposited through spray deposition, relying on Li^{+}/Mg^{2+} co-doping to control oxygen deficiency and conductivity. The PCE of inverted PSCs using this doped NiO was 18.3%.[117]

In each of these devices, NiO has advantageously provided a matching energy alignment with the perovskite, resulting in a high photovoltage. However, all of these NiO based devices displayed low FF. This can be ascribed to the modified crystallinity of the perovskite and the poor contact developed between the NiO and perovskite layers. In addition, the low conductivity of NiO (~ 10^{-4} S cm^{-1}) requires very thin layers to avoid reducing the FF due to a high series resistance contribution.[117] To address these factors, additional mesoporous layers and molecular surface modification strategies have been successfully deployed to improve the FFs and, consequently, PCEs of inverted PSCs.[133, 134] Unfortunately, these additional processing steps introduce further complications that impact fabrication times, scalability and reliability. Developing a simple, one-step and efficient approach to deposit NiO that is suitable for inverted PSCs with both high FFs and PCEs remains an unresolved scientific challenge. To address this, in **Chapter 3** we introduce a facile one-step method to realise a compact-mesoporous NiO bilayer that can be used as an HTL in inverted PSCs with high PCEs of ~ 17% and FFs up to 85%.

Continual improvements of CTLs tailored towards specific perovskites remains a key point to develop perovskite solar cells with improved efficiency and stability. To explore efficient materials as CTMs, many factors have to be fully considered. On the one hand, the material properties, i.e. film formation, conductivity (charge mobility) and transparency, are the first priorities to be understood. On the other hand, the compatibility of CTMs in devices involves the formation of a contact interface, which influences interfacial recombination and charge extraction dynamics, both of which affect the

resulting device performance. Towards achieving this factor, interface engineering forms a critical aspect of developing a high performing perovskite/CTL interface.

1.4.4 Interface Engineering

As noted in **Section 1.3**, achieving high efficiency in PSCs requires an optimisation across a multi-step process that involves the separation and collection of photocarrier in a circuit. At the simplest level, this involves the development of perovskite and charge transporting materials with appropriate electrical and energy level properties. At a deeper level, this also necessitates the consideration of the interfacial properties between the perovskite/ETL and perovskite/HTL to ensure that photocarriers are collected as efficiently as possible with minimal voltage and current losses across the device.[52] Engineering of such interfaces can be considered across three main optimisation pathways:

(1) Optimization of Energy Level Alignment:

Appropriate energy level alignment as shown in **Figure 1.14** provides a thermodynamically favourable condition for charge transfer from the perovskite to the charge transporting layers. To make high performance PSCs, it has been reported that the optimal energy alignment between the perovskite layer and the charge transport layers requires minimal energy mis-match within 0.3 eV.[135] Under this condition, charge extraction with minimal energy loss and an ensuing reduction in carrier recombination can permit for high performance PSCs. As a simple example of this, Qiu et.al. demonstrated that PSC using an anatase TiO_2 ETL (CBM=3.85 eV) showed a higher V_{oc} than that using an amorphous TiO_2 ETL (CBM=-4.07 eV) because it is closer to the CBM of perovskite layer (-3.73 eV).[136]

In this thesis, engineering of energy alignment is only focused on ETL/perovskite and HTL/perovskite interfaces, with the interfaces between the CTLs and the electrodes not being considered. The most widely used strategy to optimize the energy level of inorganic CTLs is through compositional engineering. This can act to modify any energy levels through composition changes or interfacial dipoles.[117, 132, 137] Moreover, it can improve the conductivity of the CTLs through electrical doping. As an example for HTLs, Han's group reported using Li/Mg co-doped NiO to control the VBM and achieve a "perfect" energy alignment in an inverted PSC.[117] As a result, the negligible difference between the VBM of the charge transporting and perovskite materials facilitated a high V_{oc} of 1.07 V. For ETLs, Gratzel's group demonstrated TiO_2 with a Li-rich surface by spin-coating a Li salt solution on top of TiO_2 mesoporous layer then post-annealing at high temperature (500 °C).[71]

The lowered CBM of TiO_2 facilitated improved electron extraction in the mesoporous TiO_2, thus the V_{oc} of was enhanced from 1.038 V to 1.114 V.

Introducing or converting an intermediate layer between the perovskite layer and the charge transporting layer is another approach to reduce the energy loss at the perovskite/CTL interface. As an example, Liu's group has reported a gradient energy-level modification of perovskite in inorganic PSCs.[138] This architecture consisted of FTO coated glass/TiO_2/3D/2D/0D perovskite/PTAA/Au, and was realized by solution processing of 2D perovskite nanosheets (NSs) and 0D quantum dots (QDs) on 3D bulk perovskite before deposition of a PTAA HTL. The graded configuration showed a gradual increase in perovskite VBM energies of -5.2 eV (3D), -5.17 eV (2D) and -5.15 eV (QD), which progressively approached the E_{HOMO} of the PTAA HTL (5.14 eV), achieving a very high V_{oc} of 1.19 V in PSCs.

Evidently, appropriate energy level alignment across CTL/perovskite interfaces is critical to optimize charge collection efficiency and V_{oc}. In **Chapter 6**, we will discuss the use of 2D perovskite capping layer with a VBM of -5.45 eV to reduce the offset between 3D perovskite (E_{VBM} = -5.5 eV) and Spiro-OMeTAD HTL (E_{HOMO} = -5.2 eV), and thus help to reduce the charge recombination of 3D/2D PSCs.

(2) Surface passivation:

Surface passivation refers to either chemical passivation, which reduces the trap states in order to optimize the charge transfer between interfaces, or physical passivation, which isolates certain functional layers from the external environment to avoid degradation of the device.[139] For PSCs, although their low-processing temperature makes them show promising potential for low-cost fabrication and thus commercialization, defects can be easily generated due to their low formation energies (**Figure 1.15A**).[140] When defect states occur at a perovskite surface adjacent to the CTLs, electrons and holes can be captured and recombine. This forms an unfavourable band alignment due to Fermi-level pinning by these defects. However, appropriate passivation can reduce such defects, which prevents pinning of the Fermi levels to enable the formation of a more traditional n-i-p device configuration (**Figure 1.15B**). Therefore, passivating the defects in PSCs is crucial to improve the device PCE and stability simultaneously.

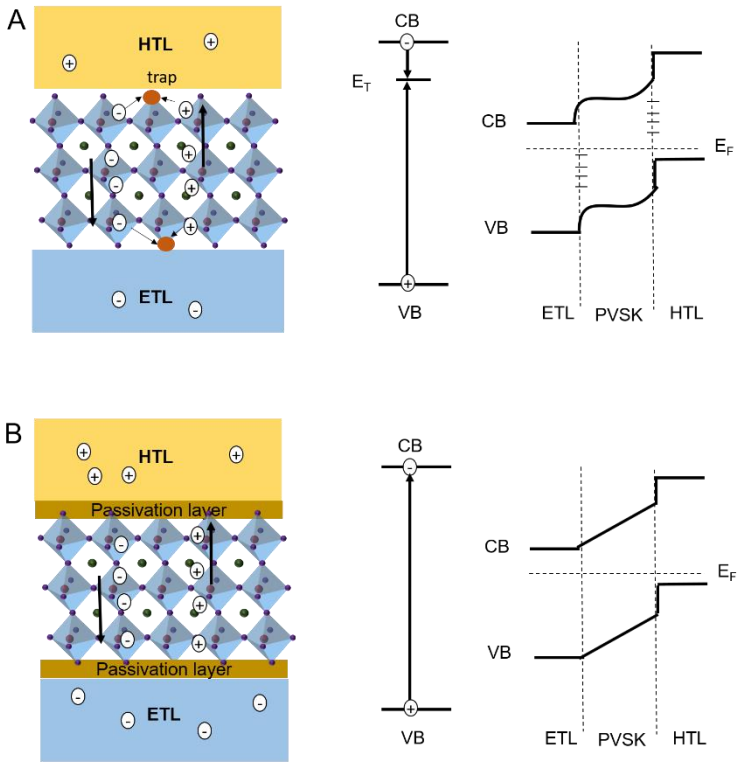

Figure 1.15 Schematic of the effect that hole and electron capture by a recombination centre in a trap-assisted recombination in perovskite (A) and the schematic that the trapes are passivated (B).

Similar to the perovskite surface, the passivation of the CTLs is equally important. A number of reports have focussed on the archetypal TiO_2, despite it possessing an abundance of surface trap states, which are known to limit the photovoltaic performance of the resulting PSCs.[141, 142] Cl-passivated TiO_2 has been reported to dramatically improve the PSC performance by Sargent's group.[80] It was suggested that the chlorine not only passivated the TiO_2 surface traps, but also suppressed deep trap states at the perovskite interface to considerably reduce interface recombination at the TiO_2/perovskite contact. Moreover, such passivation also protected the perovskite from decomposition, with TiO_2 being a well-known photocatalyst under UV light. It has been reported that UV light induces holes in TiO_2, which interact with halides in perovskite.[143] Thus, Snaith's group demonstrated that CsBr modified TiO_2 ETL improves the stabilized PCE by reducing the recombination arising from defects on the TiO_2 surface and protects the perovskite from high level UV light exposure.

Passivation of the perovskite layer is more complicated than for charge transporting layers as perovskites are more chemically sensitive. It has been reported that perovskites are highly dependent on their substrates,[144] deposition method[145] and environment,[146] which readily induces defects at interfaces that lead to charge recombination.[147] In addition, ionic defect movement also induces hysteresis and material instability in perovskites.[148] These intrinsic instabilities have been harnessed to shown self-induced passivation of grain boundaries and surfaces.[149] By controlling the perovskite annealing time, the perovskite structure at the surface and grain boundaries can partially convert back to PbI_2 and form such a surface passivation layer, which reduces recombination in the device. Beyond this approach, many passivation materials have been introduced into or onto the perovskite layer to reduce the interfacial recombination and enhance charge extraction.[149] Beyond direct passivation, Huang's group showed that introducing polystyrene tunnelling layers between the perovskite and ETL in inverted PSC leads to dramatic improvements in device performance by decoupling the electronic states of the CTLs and the perovskite layer.[111] Noteworthy, as the polystyrene is hydrophobic, this approach is not only favourable in terms of device performance by suppressing interfacial carrier recombination, but also reduced the extent of perovskite degradation caused by exposure to moisture.[139]

More recently, reduced-dimensionality perovskites have become more attractive in PSCs.[150] In contrast to normal bulk perovskites, large ammonium cations (RNH_3^+) are induced between the PbI_2 octahedral planes and thus forms a layered structure with the general chemical form $(RNH_3)_2A_{n-1}B_nX_{3n+1}$ (n=1,2,3,4…∞),[151] where n is an integer that represents the number of perovskite sheets.[152] In general, structures having smaller values of n are considered to be 2D or quasi-2D perovskites, with 3D-like perovskite structure developing with increasing values of n. The existence of the larger spacer cations in the 2D sheet structures makes them more hydrophobic than their 3D analogues, facilitating an improved environmental stability.[153] Initial reports of 2D-perovskite solar cells in 2014 exhibited poor PCE of < 5% due to the poor charge mobility.[150] However, through the introduction of a 2D passivation layer treatment on a 3D perovskite, dramatic improvements in PCEs to 21.7% were demonstrated.[154] In addition to efficiency, the hydrophobic nature of such 2D layers translated to unencapsulated passivated–treated devices stored under humid (75 ± 20% relative humidity (RH)) ambient conditions showing excellent moisture resistance, sustaining over 87% of the initial PCE during 38 days of testing. Critical to these developments was the engineering of passivation layer composition by using a combination of FAI and iso-butylammonium iodide (i-BAI) as cations in the 2D perovskite layer. Further developments towards achieving structurally and electronically tailored 2D intermediate interfaces remain as the next set of challenges for such hybridised perovskite devices.

Towards these, in **Chapter 6**, we introduce a facile approach to modify the 2D perovskite layer using a molecular additive to simultaneously passivate the 3D perovskite and enhance charge extraction across the 2D perovskite layer in 3D/2D PSCs.

(3) Morphology Design:

It is well known that the structural and chemical properties of the layers on which a perovskite is grown influence the crystallization of the perovskite layer itself.[155-159] A comparison of perovskite films formed on a planar and mesoporous TiO_2 ETL exemplifies these factors. For planar substrates, the dense ETL layers ensure that perovskite nucleation during deposition is structurally unconstrained and occurs largely homogeneously throughout the film. However, for mesoporous substrates, the perovskite solution infiltrates into the scaffold, which provides a structural constraint during annealing. As the perovskite morphology is highly dependent on the nuclei density, more voids in the ETL lead to greater nuclei at the start of annealing, resulting in smaller grains and a less textured surface.[156, 159] As a result, the deposition of perovskites onto charge transporting layers with varying structure, but equally surface chemistry, will influence the perovskite quality and the charge extraction properties in the resulting device.

Initial research on morphology of charge transporting layers has mainly focused on thickness and particle size control of the mesoporous layer. It has been shown that thick mesoporous layers result in enhanced recombination of the injected electron in the TiO_2 conduction band with holes in perovskite,[160] while thin mesoporous layers lead to differences in efficiency between the forward and reverse scans, i.e. hysteresis, due to the imbalanced in charge extraction.[161, 162] In comparison, few reports have actively studied the morphologic structuring to achieve efficient and facile modification on the mesoporous layer for high performance PSCs. Across these reported work, most have been focused on the impact of TiO_2 ETLs with various morphology on the performance of PSCs.

The conventionally used mesoporous TiO_2 nanoparticles have numerous grain boundaries and surface defects that hinder electron transport, thus leading to charge recombination.[141] Thanks to the abundant synthetic libraries for this material, 0D nanoparticles, 1D nanowires and 2D nanosheets have been widely investigated as ETLs in PSCs.[156, 159, 163] Among these, 1D TiO_2 nanostructures, especially nanorods, can be considered the most promising ETMs due to the direct pathway for charge transport and enhanced light harvesting by light scattering.[155, 156] It has been reported that electron mobility in rutile TiO_2 nanorods is much higher than that in nanoparticulate TiO_2, which facilitates a faster and more balanced charge extraction in devices.[164] However, to date, the highest PCE that has been

achieved using 1D TiO_2 ETL is only ~16% by Wu et, al.[156] A number of alternative ETLs that exhibit large-surface-areas to maximise charge extraction have also been investigated, including inverse-opal-like TiO_2,[165] nanohelical TiO_2 arrays,[166] and TiO_2-WO_3 nanowires and nanosheets.[167] However, the PCEs of PSCs with such ETLs are still not comparable to normal mesoporous PSCs. This can be ascribed to challenges in the fabrication of such layers and the potentially non-favourable perovskite growth conditions which they impart.

Given the importance of meso-structured CTLs for perovskite solar cells, in **Chapter 3** we will report on the impact of a facile chemical bath deposition (CBD) approach towards achieving NiO layers, and in **Chapter 6** we will report on using a chemical additive to induced meso-structuring of TiO_2 mesoporous layers, and their influence on inverted and normal PSCs, respectively.

1.5 Thesis Outline

The rapid evolution of metal halide perovskites has seen an explosion in research efforts across perovskite composition and device engineering efforts. As we have outlined in this chapter, the development of low-cost and scalable charge transport layers for such devices exhibits many knowledge gaps that need to be addressed. Moreover, the interfaces of perovskites, particularly with the charge transport layers remain poorly understood. This thesis addresses these shortcomings by focussing on the development of structurally controlled charge transport layers and interfaces that enable optimal charge extraction properties to achieve high-efficiency PSCs. To do so, research into meso-structured NiO_x and TiO_2 films, as well as 3D/2D perovskite interfaces has been carried out. The results and drawing conclusions from these are presented across the following chapters.

Chapter 2: Experimental Methods and Instrumentation

In this Chapter, an outline of the experimental methods and instrumentation used will be introduced.

Chapter 3: Inverted Perovskite Solar Cells with High Fill-factors Featuring Chemical Bath Deposited Mesoporous NiO_x Hole Transporting Layers

In this work, we employed a thin mesoporous NiO scaffold formed via chemical bath deposition as the hole transporting layer. This hole transporting material is found to dramatically improve the performance of inverted mixed cation and anion PSCs by enhancing their light harvesting and charge transporting efficiencies. Optimized devices achieve efficiencies of up to 16.7% with fill factors as

high as 85%. These values are significantly higher than PSCs using conventionally spray-deposited planar NiO hole transport layers, which exhibit efficiencies up to 14.5% and fill factors of only 73%.

Chapter 4: Spray Pyrolysis of Planar TiO_2 Film as Electron Transporting Layers in Perovskite Solar Cells

The fabrication of high efficiency hybrid perovskites at larger scales will rely on the optimized deposition conditions of every layer using scalable methodologies. Most current perovskite devices that employ the archetypal TiO_2 hole blocking layer utilise a simple air-brush approach. This approach is not scalable as it results in significant layer inhomogeneity across larger devices areas. To overcome this inherent limitation, in this work we use ultrasonic spray deposition as an alternative approach for the TiO_2 deposition. Focusing on identical reaction chemistries as for air-brush, namely bis(isopropoxide)-bis(acetylacetonate) titanium (IV) based solutions, we find that under optimized conditions smooth TiO_2 layers can be readily deposited over scalable areas on fluorine doped tin oxide (FTO). These are found to serve as highly effective blocking layers, with photovoltaic devices readily possessing highest efficiencies of >16%. Importantly, the mean batch efficiency of devices fabricated using the ultrasonic spray deposition method is significantly improved and the standard deviation is drastically narrowed.

Chapter 5: Enhanced Performance of Perovskite Solar Cells by Micro-structuring the Mesoporous TiO_2 Layer

In this chapter, we report a facile method to develop high-efficiency PSCs by micro-structuring a mesoporous TiO_2 layer formed from directly from a TiO_2 nanoparticle dispersion. The micro-structuring is achieved through the controlled crystallization of additives in the dispersion, which are subsequently thermolized following coating. This micro-structure enables for a more efficient charge extraction, achieving current densities and fill factors some 5% higher than for pristine meso-porous TiO_2 layers. The PSCs using this modified TiO_2 mesoporous layer show the highest PCE of ~19% for the controls of ~18%. These results highlight that achieving high-performance PSCs relies not only on the nanoscale structure of charge extraction layers, but also their extended microstructure.

Chapter 6: Enhanced Performance of Perovskite Solar Cells by Introducing a Modified 2D Perovskite Layer

In this chapter, we report a facile method to develop high-efficiency PSCs by introducing a molecule modified 2D-3D perovskite stacking-layered architecture. The modified 2D perovskite layer is formed via in situ growth of BA_2PbI_4 capping layer with molecular dopant on top of 3D Cs/MA/FA mixed perovskite film. In contrast with devices with pristine 2D perovskite layer, devices with modified 2D layers show improved charge transfer and reduced defect states. The PSCs using this modified 2D perovskite layer show the highest PCE of 20.3% compared to 17.1% for the controls. This work provides an efficient and facile strategy to achieving high-performance PSCs.

Chapter 7 Conclusions and Outlook

In this chapter, we summarise how the work presented has led to perovskite solar cells with higher PCE and stability. We also outline the key challenges in going forward, particularly around the need to develop an improved understanding of the charge extraction and charge transport related to perovskite layer, as well as the development of low-temperature processable materials that are amendable to printing processes.

References

1. González-Eguino, M., Energy Poverty: An Overview. *Renewable and Sustainable Energy Reviews* **2015,** *47*, 377-385.
2. Bildiric, M. E.; Gökmenoğlu, S. M., Environmental Pollution, Hydropower Energy Consumption and Economic Growth: Evidence from G7 Countries. *Renewable and Sustainable Energy Reviews* **2017,** *75*, 68-85.
3. Energy, B. W., BP Statistical Review of World Energy, 2019.
4. Thornton, K. *Clean Energy Australia Report 2019*; Australian Clean Energy Council: 2019.
5. *Our Common Future*. Oxford University Press: Oxford/New York, 1987.
6. Liu, X.; Xuan, Y., Defects-assisted Solar Absorption of Plasmonic Nanoshell-based Nanofluids. *Solar Energy* **2017,** *146*, 503-510.
7. Winston, R.; Minano, J. C.; Benitez, P. G., Nonimaging Optics. **2005**.
8. Zeman, M., *Solar Cells*. Delft University of Technology: Netherlands, 2006.
9. Becquerel, E., The Becquerel Effect in the Presence of Dyestuffs and the Action of Light on Dyes. *Compt Rend Acad Science Paris* **1839,** *9*, 561.
10. Chapin, D. M.; Fuller, C. S.; Pearson, G. L., A New Silicon p‐n Junction Photocell for Converting Solar Radiation into Electrical Power. *Journal of Applied Physics* **1954,** *25* (5), 676-677.
11. Carlson, D. E.; Wronski, C. R., Amorphous Silicon Solar Cell. *Applied Physics Letters* **1976,** *28* (11), 671-673.
12. Brandhorst, H. W. In *Current Status of Silicon Solar Cell Technology*, 1975 International Electron Devices Meeting, Washington, D. C., IEEE: Washington, D. C., 1975.
13. Redfield, D., Multiple‐pass Thin‐film Silicon Solar Cell. *Applied Physics Letters* **1974,** *25* (11), 647-648.
14. Mariusz, M.; Leon, J. I.; Abu-Rub, H., Photovoltaic Energy Systems. In *Power Electronics in Renewable Energy Systems and Smart Grid: Technology and Applications*, Bose, B. K., Ed. John Wiley & Sons, Inc.: 2019; p 356.
15. Shockley, W.; Queisser, H. J., Detailed Balance Limit of Efficiency of p‐n Junction Solar Cells. *Journal of Applied Physics* **1961,** *32* (3), 510-519.
16. Sharma, S.; Jain, K. K.; Sharma, A., Solar Cells: In Research and Applications—A Review. *Materials Sciences and Applications* **2015,** *06* (12), 1145-1155.
17. ISE, F., Photovoltaics-Report. **2019**.
18. NREL, Best Research-Cell Efficiency Chart. 2019.
19. Green, M. A.; Hishikawa, Y.; Dunlop, E. D.; Levi, D. H.; Hohl-Ebinger, J.; Ho-Baillie, A. W. Y., Solar Cell Efficiency Tables (Version 52). *Progress in Photovoltaics: Research and Applications* **2018,** *26* (7), 427-436.
20. http://www.top-alternative-energy-sources.com/.
21. https://www.newsouthernenergy.com/.
22. Lee, T. D.; Ebong, A. U., A Review of Thin Film Solar Cell Technologies and Challenges. *Renewable and Sustainable Energy Reviews* **2017,** *70*, 1286-1297.
23. Munday, J. N., The Effect of Photonic Bandgap Materials on the Shockley-Queisser Limit. *Journal of Applied Physics* **2012,** *112*, 064501.
24. Bae, S.-H.; Zhao, H.; Hsieh, Y.-T.; Zuo, L.; De Marco, N.; Rim, You S.; Li, G.; Yang, Y., Printable Solar Cells from Advanced Solution-Processible Materials. *Chem* **2016,** *1* (2), 197-219.
25. Green, M. A.; Hishikawa, Y.; Dunlop, E. D.; Levi, D. H.; Hohl-Ebinger, J.; Yoshita, M.; Ho-Baillie, A. W. Y., Solar Cell Efficiency Tables (Version 53). *Progress in Photovoltaics: Research and Applications* **2019,** *27* (1), 3-12.
26. Woodall, J. M.; Hovel, H. J., High‐efficiency $Ga_{1-x}Al_xAs$–GaAs Solar Cells. *Applied Physics Letters* **1972,** *21* (8), 379-381.

27. https://www.ossila.com/.
28. Green, M. A., Third Generation Photovoltaics Solar Cells for 2020 and Beyond. *Physica E: Low-dimensional Systems and Nanostructures* **2002,** *14* (1-2), 65–70.
29. Pan, Z.; Rao, H.; Mora-Sero, I.; Bisquert, J.; Zhong, X., Quantum dot-sensitized Solar Cells. *Chemical Society Reviews* **2018,** *47* (20), 7659-7702.
30. Dong, S.; Zhang, K.; Xie, B.; Xiao, J.; Yip, H.-L.; Yan, H.; Huang, F.; Cao, Y., High-Performance Large-Area Organic Solar Cells Enabled by Sequential Bilayer Processing via Nonhalogenated Solvents. *Advanced Energy Materials* **2019,** *9* (1), 1802832.
31. Bach, U.; Lupo, D.; Comte, P.; Moser, J. E.; Weissortel, F.; Salbeck, J.; Spreitzer, H.; Gratzel, M., Solid-state Dye-sensitized Mesoporous TiO_2 Solar Cells with High Photon-to-electron Conversion Efficiencies. *Nature* **1998,** *395*, 583-585.
32. MacDonald, B. I.; Gengenbach, T. R.; Watkins, S. E.; Mulvaney, P.; Jasieniak, J. J., Solution-processing of Ultra-thin CdTe/ZnO Nanocrystal Solar Cells. *Thin Solid Films* **2014,** *558*, 365-373.
33. Hao, M.; Bai, Y.; Zeiske, S.; Ren, L.; Liu, J.; Yuan, Y.; Zarrabi, N.; Cheng, N.; Ghasemi, M.; Chen, P.; Lyu, M.; He, D.; Yun, J.-H.; Du, Y.; Wang, Y.; Ding, S.; Armin, A.; Meredith, P.; Liu, G.; Cheng, H.-M.; Wang, L., Ligand-assisted Cation-exchange Engineering for High-efficiency Colloidal $Cs_{1-x}FA_xPbI_3$ Quantum Dot Solar Cells with Reduced Phase Segregation. *Nature Energy* **2020,** *5*, 79–88.
34. Zhen Li, M. Y., Ji-Sang Park, Su-Huai Wei, Joseph J. Berry, and Kai Zhu, Stabilizing Perovskite Structures by Tuning Tolerance Factor: Formation of Formamidinium and Cesium Lead Iodide Solid-State Alloys. *Chemistry of Materials* **2016,** *28*, 284-292.
35. Brabec, C. J.; Gowrisanker, S.; Halls, J. J.; Laird, D.; Jia, S.; Williams, S. P., Polymer-fullerene Bulk-heterojunction Solar Cells. *Advanced Materials* **2010,** *22* (34), 3839-3856.
36. Yeh, N.; Yeh, P., Organic Solar Cells: Their Developments and Potentials. *Renewable and Sustainable Energy Reviews* **2013,** *21*, 421-431.
37. Cheng, P.; Zhan, X., Stability of Organic Solar Cells: Challenges and Strategies. *Chemical Society Reviews* **2016,** *45*, 2544-2582.
38. Schafferhans, J.; Baumann, A.; Wagenpfahl, A.; Deibel, C.; Dyakonov, V., Oxygen Doping of P3HT:PCBM Blends: Influence on Trap States, Charge Carrier Mobility and Solar Cell Performance. *Organic Electronics* **2010,** *11*, 1693-1700.
39. Reese, M. O.; Nardes, A.; Benjamin, M.; Rupert, L.; Larsen, R. E.; Olson, D. C.; Lloyd, M. T.; Shaheen, S. E.; Ginley, D. S.; Rumbles, G.; Kopidakis, N., Photoinduced Degradation of Polymer and Polymer–Fullerene Active Layers: Experiment and Theory. *Advanced Functional Materials* **2020,** *20*, 3476–3483.
40. Burlingame, Q.; Zanotti, G.; Ciammaruchi, L.; Katz, E. A.; Forrest, S. R., Outdoor Operation of Small-molecule Organic Photovoltaics. *Organic Electronics* **2016,** *41*, 274-279.
41. O'Regan, B.; Gratze, M., A Low-cost, High-efficiency Solar Cell based on Dye-sensitized Colloidal TiO_2 Films. *Nature* **1991,** *353*, 737-740.
42. Cao, Y.; Liu, Y.; Zakeeruddin, S. M.; Hagfeldt, A.; Grätzel, M., Direct Contact of Selective Charge Extraction Layers Enables High-Efficiency Molecular Photovoltaics. *Joule* **2018,** *2* (6), 1108-1117.
43. Mehmood, U.; Al-Ahmed, A.; Al-Sulaiman, F. A.; Malik, M. I.; Shehzad, F.; Khan, A. U. H., Effect of Temperature on the Photovoltaic Performance and Stability of Solid-state Dye-sensitized Solar Cells: A Review. *Renewable and Sustainable Energy Reviews* **2017,** *79*, 946-959.
44. Kojima, A.; Teshima, K.; Shirai, Y.; Miyasaka, T., Organometal Halide Perovskites as Visible-Light Sensitizers for Photovoltaic Cells. *Journal of the American Chemical Society* **2009,** *131*, 6050-6051.
45. Debije, M., Better Luminescent Solar Panels in Prospect. *Nature* **2015,** *519*, 298-299.

46. Kim, H. S.; Lee, C. R.; Im, J. H.; Lee, K. B.; Moehl, T.; Marchioro, A.; Moon, S.-J.; Humphry-Baker, R.; Yum, J.-H.; Moser, J. E.; Grätzel, M.; Park, N.-G., Lead Iodide Perovskite Sensitized All-solid-state Submicron Thin Film Mesoscopic Solar Cell with Efficiency Exceeding 9%. *Science Reports* **2012,** ***2***, 591.
47. Hussain, I.; Tran, H. P.; Jaksik, J.; Moore, J.; Islam, N.; Uddin, M. J., Functional Materials, Device Architecture, and Flexibility of Perovskite Solar Cell. *Emergent Materials* **2018,** *1* (3-4), 133-154.
48. Sun, J.; Jasieniak, J. J., Semi-transparent Solar Cells. *Journal of Physics D: Applied Physics* **2017,** *50* (9), 093001.
49. Park, N. G.; Grätzel, M.; Miyasaka, T., *Organic-Inorganic Halide Perovskite Photovoltaics: From Fundamentals to Device Architectures*. Springer: 2016; Vol. Cham.
50. Ke, W.; Kanatzidis, M. G., Prospects for Low-toxicity Lead-free Perovskite Solar Cells. *Nature Communications* **2019,** *10* (1), 965.
51. Bartesaghi, D.; Perez Idel, C.; Kniepert, J.; Roland, S.; Turbiez, M.; Neher, D.; Koster, L. J., Competition between Recombination and Extraction of Free Charges Determines the Fill Factor of Organic Solar Cells. *Nature Communications* **2015,** *6*, 7083.
52. Zhou, H.; Chen, Q.; Li, G.; Luo, S.; Song, T. B.; Duan, H. S.; Hong, Z.; You, J.; Liu, Y.; Yang, Y., Interface Engineering of Highly Efficient Perovskite Solar Cells. *Science* **2014,** *345* (6196), 542-546.
53. Shi, J.; Li, Y.; Li, Y.; Li, D.; Luo, Y.; Wu, H.; Meng, Q., From Ultrafast to Ultraslow: Charge-Carrier Dynamics of Perovskite Solar Cells. *Joule* **2018,** *2* (5), 879-901.
54. Shalan, A. E.; Narra, S.; Oshikiri, T.; Ueno, K.; Shi, X.; Wu, H.-P.; Elshanawany, Mahmoud M.; Wei-Guang Diau, E.; Misawa, H., Optimization of a Compact Layer of TiO_2 via Atomic-layer Deposition for High-performance Perovskite Solar Cells. *Sustainable Energy & Fuels* **2017,** *1* (7), 1533-1540.
55. Sun, J.; Lu, J.; Li, B.; Jiang, L.; Chesman, A. S. R.; Scully, A. D.; Gengenbach, T. R.; Cheng, Y.-B.; Jasieniak, J. J., Inverted Perovskite Solar Cells with High Fill-factors Featuring Chemical Bath Deposited Mesoporous NiO Hole Transporting Layers. *Nano Energy* **2018,** *49*, 163-171.
56. Elumalai, N. K.; Uddin, A., Open Circuit Voltage of Organic Solar Cells: an in-depth Review. *Energy & Environmental Science* **2016,** *9* (2), 391-410.
57. Qi, B.; Wang, J., Fill Factor in Organic Solar Cells. *Physical Chemistry Chemical Physics* **2013,** *15* (23), 8972-8982.
58. Gustav, R., Beschreibung Einiger Neuen Mineralien Urals. *Annalen der Physik* **1839,** *124* (12), 551-573.
59. Mitchell, R. H., Perovskites: a Revised Classification Scheme for an Important Rare Earth Element Host in Alkaline Rocks. In *Rare Earth Minerals Chemistry, origin and ore deposites*, Adrian P. Jones, F. W., C.Terry Willams, Ed. Chapman&Hall: 1996; p 41.
60. Goldschmidt, V. M., Die Gesetze der Krystallochemie. *Die Naturwissenschaften* **1926,** *21*, 477-485.
61. Li, Z.; Yang, M.; Park, J.-S.; Wei, S.-H.; Berry, J. J.; Zhu, K., Stabilizing Perovskite Structures by Tuning Tolerance Factor: Formation of Formamidinium and Cesium Lead Iodide Solid-State Alloys. *Chemistry of Materials* **2015,** *28* (1), 284-292.
62. Kieslich, G.; Sun, S.; Cheetham, A. K., An extended Tolerance Factor Approach for Organic-inorganic Perovskites. *Chemical Science* **2015,** *6* (6), 3430-3433.
63. Borriello, I.; Cantele, G.; Ninno, D., Ab Initioinvestigation of Hybrid Organic-inorganic Perovskites based on Tin Halides. *Physical Review B* **2008,** *77* (23), 235214.
64. Kim, H.; Han, J. S.; Choi, J.; Kim, S. Y.; Jang, H. W., Halide Perovskites for Applications beyond Photovoltaics. *Small Methods* **2018,** *2* (3), 1700310.

65. Li, M.-H.; Shen, P.-S.; Wang, K.-C.; Guo, T.-F.; Chen, P., Inorganic p-type Contact Materials for Perovskite-based Solar Cells. *Journal of Materials Chemistry A* **2015,** *3* (17), 9011-9019.
66. Paeng, S.-H.; Park, M.-W.; Sung, Y.-M., Transparent Conductive Characteristics of Ti:ITO Films Deposited by RF Magnetron Sputtering at Low Substrate Temperature. *Surface and Coatings Technology* **2010,** *205*, 210-215.
67. Yang, J. K.; Liang, B.; Zhao, M. J.; Gao, Y.; Zhang, F. C.; Zhao, H. L., Reference of Temperature and Time During Tempering Process for non-stoichiometric FTO Films. *Scientific Reports* **2015,** *5*, 15001.
68. Sun, J.; Pascoe, A. R.; Meyer, S.; Wu, Q.; Della Gaspera, E.; Raga, S. R.; Zhang, T.; Nattestad, A.; Bach, U.; Cheng, Y. B.; Jasieniak, J. J., Ultrasonic Spray Deposition of TiO_2 Electron Transport Layers for Reproducible and High Efficiency Hybrid Perovskite Solar Cells. *Solar Energy* **2019,** *188*, 697-705.
69. Wu, C.; Wang, D.; Zhang, Y.; Gu, F.; Liu, G.; Zhu, N.; Luo, W.; Han, D.; Guo, X.; Qu, B.; Wang, S.; Bian, Z.; Chen, Z.; Xiao, L., FAPbI3 Flexible Solar Cells with a Record Efficiency of 19.38% Fabricated in Air via Ligand and Additive Synergetic Process. *Advanced Functional Materials* **2019,** *29* (34), 1902974.
70. Wang, Y.; Dar, M. I.; Ono, L. K.; Zhang, T.; Kan, M.; Li, Y.; Zhang, L.; Wang, X.; Yang, Y.; Gao, X.; Qi, Y.; Grätzel, M.; Zhao, Y., Thermodynamically Stabilized β-$CsPbI_3$–based Perovskite Solar Cells with Efficiencies >18%. *Science* **2019,** *365*, 591-595.
71. Giordano, F.; Abate, A.; Baena, J. P. C.; Saliba, M.; Matsui, T.; Im, S. H.; Zakeeruddin, S. M.; Nazeeruddin, M. K.; Hagfeldt, A.; Graetzel, M., Enhanced Electronic Properties in Mesoporous TiO_2 via Lithium Doping for High-efficiency Perovskite Solar Cells. *Nature Communications* **2016,** *7*, 10379.
72. Kim, H. S.; Park, N. G., Parameters Affecting I-V Hysteresis of CH3NH3PbI3 Perovskite Solar Cells: Effects of Perovskite Crystal Size and Mesoporous TiO_2 Layer. *The Journal of Physical Chemistry Letters* **2014,** *5* (17), 2927-2934.
73. Niu, G.; Guo, X.; Wang, L., Review of Recent Progress in Chemical Stability of Perovskite Solar Cells. *Journal of Materials Chemistry A* **2015,** *3*, 8970-8980.
74. Li, Z.; Klein, T. R.; Kim, D. H.; Yang, M.; Berry, J. J.; van Hest, M. F. A. M.; Zhu, K., Scalable Fabrication of Perovskite Solar Cells. *Nature Reviews Materials* **2018,** *3* (4), 18017.
75. Wang, Q.-K.; Wang, R.-B.; Shen, P.-F.; Li, C.; Li, Y.-Q.; Liu, L.-J.; Duhm, S.; Tang, J.-X., Energy Level Offsets at Lead Halide Perovskite/Organic Hybrid Interfaces and Their Impacts on Charge Separation. *Advanced Materials Interfaces* **2015,** *2* (3), 1400528.
76. Ye, M.; He, C.; Iocozzia, J.; Liu, X.; Cui, X.; Meng, X.; Rager, M.; Hong, X.; Liu, X.; Lin, Z., Recent Advances in Interfacial Engineering of Perovskite Solar Cells. *Journal of Physics D: Applied Physics* **2017,** *50* (37), 373002.
77. Dou, J.; Zhang, Y.; Wang, Q.; Abate, A.; Li, Y.; Wei, M., Highly Efficient Zn_2SnO_4 Perovskite Solar Cells through Band Alignment Engineering. *Chemical Communications* **2019,** *55*, 14673-14676.
78. Zhou, H.; Chen, Q.; Li, G.; Luo, S.; Song, T. B.; Duan, H. S.; Hong, Z.; You, J.; Liu, Y.; Yang, Y., Photovoltaics Interface Engineering of Highly Efficient Perovskite Solar Cells. *Science* **2014,** *345* (6196), 542-546.
79. Yang, D.; Yang, R.; Wang, K.; Wu, C.; Zhu, X.; Feng, J.; Ren, X.; Fang, G.; Priya, S.; Liu, S. F., High Efficiency Planar-type Perovskite Solar Cells with Negligible Hysteresis Using EDTA-complexed SnO_2. *Nature Communications* **2018,** *9* (1), 3239.
80. Tan, H.; Jain, A.; Voznyy, O.; Lan, X.; Pelayo, F.; Fan, J.; Quintero-Bermudez, R.; Yuan, M.; Zhang, B.; Zhao, Y.; Fan, F.; Li, P.; Quan, L.; Zhao, Y.; Lu, Z.; Yang, Z.; Hoogland, S.; Sargent, E., Efficient and Stable Solution-processed Planar Perovskite Solar Cells via Contact Passivation. *Science* **2017,** *355*, 722-726.

81. Mahmud, M. A.; Elumalai, N. K.; Upama, M. B.; Wang, D.; Chan, K. H.; Wright, M.; Xu, C.; Haque, F.; Uddin, A., Low Temperature Processed ZnO Thin Film as Electron Transport Layer for Efficient Perovskite Solar Cells. *Solar Energy Materials and Solar Cells* **2017,** *159*, 251-264.
82. Seo, J.; Park, S.; Chan Kim, Y.; Jeon, N. J.; Noh, J. H.; Yoon, S. C.; Seok, S. I., Benefits of Very Thin PCBM and LiF Layers for Solution-processed p–i–n Perovskite Solar Cells. *Energy & Environmental Science.* **2014,** *7* (8), 2642-2646.
83. Hu, L.; Li, M.; Yang, K.; Xiong, Z.; Yang, B.; Wang, M.; Tang, X.; Zang, Z.; Liu, X.; Li, B.; Xiao, Z.; Lu, S.; Gong, H.; Ouyang, J.; Sun, K., PEDOT:PSS Monolayers to Enhance the Hole Etraction and Stability of Perovskite Solar Cells. *Journal of Materials Chemistry A* **2018,** *6* (34), 16583-16589.
84. Jung, E. H.; Jeon, N. J.; Park, E. Y.; Moon, C. S.; Shin, T. J.; Yang, T. Y.; Noh, J. H.; Seo, J., Efficient, Stable and Scalable Perovskite Solar Cells Using Poly(3-hexylthiophene). *Nature* **2019,** *567* (7749), 511-515.
85. Hou, Y.; Du, X.; Scheiner, S.; McMeekin, D. P.; Wang, Z.; Li, N.; Killian, M. S.; Chen, H.; Richter, M.; Levchuk, I.; Schrenker, N.; Spiecker, E.; Stubhan, T.; Luechinger, N. A.; Hirsch, A.; Schmuki, P.; Steinrück, H.-P.; RFink, a. H.; Halik, M.; Snaith, H. J.; Brabec, C. J., A Generic Interface to Reduce the Efficiency-stability-cost Gap of Perovskite Solar Cells. *Science* **2017,** *358*, 1192-1197.
86. Khadka, D. B.; Shirai, Y.; Yanagida, M.; Ryan, J. W.; Miyano, K., Exploring the Effects of Interfacial Carrier Transport Layers on Device Performance and Optoelectronic Properties of Planar Perovskite Solar Cells. *Journal of Materials Chemistry C* **2017,** *5* (34), 8819-8827.
87. Toroker, M. C.; Kanan, D. K.; Alidoust, N.; Isseroff, L. Y.; Liao, P.; Carter, E. A., First Principles Scheme to Evaluate Band Edge Positions in Potential Transition Metal Oxide Photocatalysts and Photoelectrodes. *Physical Chemistry Chemical Physics* **2011,** *13* (37), 16644-16654.
88. Arora, N.; Dar, M. I.; Hinderhofer, A.; Pellet, N.; Schreiber, F.; Zakeeruddin, S. M.; Grätzel, M., Perovskite Solar Cells with CuSCN Hole Extraction Layers Yield Stabilized Efficiencies Greater than 20%. *Science* **2017,** *358*, 768-771.
89. Tseng, Z.-L.; Chen, L.-C.; Chiang, C.-H.; Chang, S.-H.; Chen, C.-C.; Wu, C.-G., Efficient Inverted-type Perovskite Solar Cells Using UV-ozone Treated MoO_x and WO_x as Hole Transporting Layers. *Solar Energy* **2016,** *139*, 484-488.
90. Docampo, P.; Ball, J. M.; Darwich, M.; Eperon, G. E.; Snaith, H. J., Efficient Organometal Trihalide Perovskite Planar-heterojunction Solar Cells on Flexible Polymer Substrates. *Nature Communications* **2013,** *4*, 2761.
91. Liu, M.; Johnston, M. B.; Snaith, H. J., Efficient Planar Heterojunction Perovskite Solar Cells by Vapour Deposition. *Nature* **2013,** *501*, 395-398.
92. Ball, J. M.; Lee, M. M.; Hey, A.; Snaith, H. J., Low-temperature Processed Meso-superstructured to Thin-film Perovskite Solar Cells. *Energy & Environmental Science* **2013,** *6*, 1739–1743.
93. Lee, M. M.; Teuscher, J.; Miyasaka, T.; Murakami, T. N.; Snaith, H. J., Efficient Hybrid Solar Cells Based on Meso-superstructured Organometal Halide Perovskites. *Science* **2012,** *338*, 643-647.
94. Chung, I.; Lee, B.; He, J.; Chang, R. P.; Kanatzidis, M. G., All-solid-state Dye-sensitized Solar Cells with High Efficiency. *Nature* **2012,** *485*, 486-489.
95. Moehl, T.; Im, J. H.; Lee, Y. H.; Domanski, K.; Giordano, F.; Zakeeruddin, S. M.; Dar, M. I.; Heiniger, L. P.; Nazeeruddin, M. K.; Park, N. G.; Gratzel, M., Strong Photocurrent Amplification in Perovskite Solar Cells with a Porous TiO_2 Blocking Layer under Reverse Bias. *The Journal of Physical Chemistry Letters* **2014,** *5*, 3931-3936.

96. Chandiran, A. K.; Yella, A.; Mayer, M. T.; Gao, P.; Nazeeruddin, M. K.; Gratzel, M., Sub-nanometer Conformal TiO_2 Blocking Layer for High Efficiency Solid-state Perovskite Absorber Solar Cells. *Advanced Materials* **2014,** *26*, 4309-4312.
97. Hu, H.; Dong, B.; Hu, H.; Chen, F.; Kong, M.; Zhang, Q.; Luo, T.; Zhao, L.; Guo, Z.; Li, J.; Xu, Z.; Wang, S.; Eder, D.; Wan, L., Atomic Layer Deposition of TiO_2 for a High-efficiency Hole-blocking Layer in Hole-conductor-free Perovskite Solar Cells Processed in Ambient Air. *ACS Applied Materials Interfaces* **2016,** *8*, 17999-18005.
98. Kavan, L.; Grätzel, M., Highly Efficient Semiconducting TiO2 Photoelectrodes Prepared by Aerosol Pyrolysis. *Electrochimica Acta* **1995,** *40*, 643-652.
99. Supasai, T.; Henjongchom, N.; Tang, I. M.; Deng, F.; Rujisamphan, N., Compact Nanostructured TiO_2 Deposited by Aerosol Spray Pyrolysis for the Hole-blocking Layer in a $CH_3NH_3PbI_3$ Perovskite Solar Cell. *Solar Energy* **2016,** *136*, 515-524.
100. Kavan, L.; O'Regan, B.; Kay, A.; Grätzel, M., Preparation of TiO_2 (anatase) Films on Electrodes by Anodic Oxidative Hydrolysis of $TiCl_3$. *Journal of Electroanalytical Chemistry* **1993,** *346*, 291-307.
101. Kim, M. C.; Kim, B. J.; Yoon, J.; Lee, J. W.; Suh, D.; Park, N. G.; Choi, M.; Jung, H. S., Electro-spray Deposition of a Mesoporous TiO_2 Charge Collection Layer: toward Large Scale and Continuous Production of High Efficiency Perovskite Solar Cells. *Nanoscale* **2015,** *7*, 20725-20733.
102. Braga, A.; Baratto, C.; Colombi, P.; Bontempi, E.; Salvinelli, G.; Drera, G.; Sangaletti, L., An Ultrathin TiO_2 Blocking Layer on Cd Stannate as Highly Efficient Front Contact for Dye-sensitized Solar Cells. *Physical Chemistry Chemical Physics* **2013,** *15*, 16812-16818.
103. Ke, W.; Fang, G.; Wang, J.; Qin, P.; Tao, H.; Lei, H.; Liu, Q.; Dai, X.; Zhao, X., Perovskite Solar Cell with an Efficient TiO_2 Compact Film. *ACS Applied Materials & Interfaces* **2014,** *6*, 15959-15965.
104. Xia, J.; Masaki, N.; Jiang, K.; Yanagida, S., Deposition of a Thin Film of TiO_x from a Titanium Metal Target as Novel Blocking Layers at Conducting Glass/TiO_2 Interfaces in Ionic Liquid Mesoscopic TiO_2 Dye-Sensitized Solar Cells. *The Journal of Physical Chemistry B* **2006,** *110*, 25222-25228.
105. Leijtens, T.; Stranks, S. D.; Eperon, G., E. ; Lindblad, R.; Johansson, E. M. J.; Ian, J. M.; Håkan, R.; Ball, J. M.; Lee, M. M.; Snaith, H. J., Electronic Properties of Meso-Superstructured and Planar Organometal Halide Perovskite Films: Charge Trapping, Photodoping, and Carrier Mobility and Planar Organometal Halide Perovskite Films: Charge Trapping, Photodoping, and Carrier Mobility. *ACS Nano* **2014,** *8*, 7147-7155.
106. Dkhissi, Y.; Meyer, S.; Chen, D.; Weerasinghe, H. C.; Spiccia, L.; Cheng, Y. B.; Caruso, R. A., Stability Comparison of Perovskite Solar Cells Based on Zinc Oxide and Titania on Polymer Substrates. *ChemSusChem* **2016,** *9* (7), 687-695.
107. Xiong, L.; Guo, Y.; Wen, J.; Liu, H.; Yang, G.; Qin, P.; Fang, G., Review on the Application of SnO_2 in Perovskite Solar Cells. *Advanced Functional Materials* **2018,** *28* (35), 1802757.
108. Bush, K. A.; Palmstrom, A. F.; Yu, Z. J.; Boccard, M.; Cheacharoen, R.; Mailoa, J. P.; McMeekin, D. P.; Hoye, R. L. Z.; Bailie, C. D.; Leijtens, T.; Peters, I. M.; Minichetti, M. C.; Rolston, N.; Prasanna, R.; Sofia, S.; Harwood, D.; Ma, W.; Moghadam, F.; Snaith, H. J.; Buonassisi, T.; Holman, Z. C.; Bent, S. F.; McGehee, M. D., 23.6%-efficient Monolithic Perovskite/silicon tandem solar cells with improved stability. *Nature Energy* **2017,** *2* (4), 17009.
109. Lee, J.; Kim, J.; Lee, C.-L.; Kim, G.; Kim, T. K.; Back, H.; Jung, S.; Yu, K.; Hong, S.; Lee, S.; Kim, S.; Jeong, S.; Kang, H.; Lee, K., A Printable Organic Electron Transport Layer for Low-Temperature-Processed, Hysteresis-Free, and Stable Planar Perovskite Solar Cells. *Advanced Energy Materials* **2017,** *7* (15), 1700226.

110. Mihailetchi, V. D.; Duren, J. K. J. v.; Blom, P. W. M.; Hummelen, J. C.; Janssen, R. A. J.; Kroon, J. M.; Rispens, M. T.; Verhees, W. J. H.; Wienk, M. M., Electron Transport in a Methanofullerene. *Advanced Functional Materials* **2003,** *13* (1), 43-46.
111. Wang, Q.; Dong, Q.; Li, T.; Gruverman, A.; Huang, J., Thin Insulating Tunneling Contacts for Efficient and Water-Resistant Perovskite Solar Cells. *Advanced Materials* **2016,** *28* (31), 6734-6739.
112. Lee, J.; Kang, H.; Kim, G.; Back, H.; Kim, J.; Hong, S.; Park, B.; Lee, E.; Lee, K., Achieving Large-Area Planar Perovskite Solar Cells by Introducing an Interfacial Compatibilizer. *Advanced Materials* **2017,** *29* (22), 1606363.
113. You, J.; Meng, L.; Song, T. B.; Guo, T. F.; Yang, Y. M.; Chang, W. H.; Hong, Z.; Chen, H.; Zhou, H.; Chen, Q.; Liu, Y.; De Marco, N.; Yang, Y., Improved Air Stability of Perovskite Solar Cells via Solution-processed Metal Oxide Transport Layers. *Nature Nanotechnology* **2016,** *11* (1), 75-81.
114. Zhu, Z.; Bai, Y.; Liu, X.; Chueh, C. C.; Yang, S.; Jen, A. K., Enhanced Efficiency and Stability of Inverted Perovskite Solar Cells Using Highly Crystalline SnO_2 Nanocrystals as the Robust Electron-Transporting Layer. *Advanced Materials* **2016,** *28* (30), 6478-6484.
115. Sharma, S.; Sakai, N.; Ray, S.; Senanayak, S. P.; Sirringhaus, H.; Snaith, H. J.; Patil, S., Inverted Perovskite Solar Cells with Air Stable Diketopyrrolopyrrole-based Electron Transport Layer. *Solar Energy* **2019,** *186*, 9-16.
116. Kim, H. I.; Kim, M.-J.; Choi, K.; Lim, C.; Kim, Y.-H.; Kwon, S.-K.; Park, T., Improving the Performance and Stability of Inverted Planar Flexible Perovskite Solar Cells Employing a Novel NDI-Based Polymer as the Electron Transport Layer. *Advanced Energy Materials* **2018,** *8* (16), 1702872.
117. Chen, W.; Wu, Y.; Yue, Y.; Liu, J.; Zhang, W.; Yang, X.; Chen, H.; Bi, E.; Ashraful, I.; Grätzel, M.; Han, L., Efficient and Stable Large-area Perovskite Solar Cells with Inorganic Charge Extraction Layers. *Science* **2015,** *350* (6263), 944-948.
118. Jeon, N. J.; Na, H.; Jung, E. H.; Yang, T. Y.; Lee, Y. G.; Kim, G.; Shin, H. W.; Il Seok, S.; Lee, J.; Seo, J., A Fluorene-terminated Hole-transporting Material for Highly Efficient and Stable Perovskite Solar Cells. *Nature Energy* **2018,** *3* (8), 682-689.
119. Hawash, Z.; Ono, L. K.; Qi, Y., Recent Advances in Spiro-OMeTAD Hole Transport Material and Its Applications in Organic-Inorganic Halide Perovskite Solar Cells. *Advanced Materials Interfaces* **2018,** *5* (1), 1700623.
120. Snaith, H. J.; Grätzel, M., Enhanced Charge Mobility in a Molecular Hole Transporter via Addition of Redox Inactive Ionic Dopant: Implication to Dye-sensitized Solar Cells. *Applied Physics Letters* **2006,** *89* (26), 262114.
121. Schloemer, T. H.; Christians, J. A.; Luther, J. M.; Sellinger, A., Doping Strategies for Small Molecule Organic Hole-Transport Materials: Impacts on Perovskite Solar Cell Performance and Stability. *Chemical Science* **2019,** *10*, 1904-1935.
122. Cao, Y.; Li, Y.; Morrissey, T.; Lam, B.; Patrick, B. O.; Dvorak, D. J.; Xia, Z.; Kelly, T. L.; Berlinguette, C. P., Dopant-free Molecular Hole Transport Material that Mediates a 20% Power Conversion Efficiency in a Perovskite Solar Cell. *Energy & Environmental Science* **2019,** *12*, 3502-3507.
123. Wang, Y.; Chen, W.; Wang, L.; Tu, B.; Chen, T.; Liu, B.; Yang, K.; Koh, C. W.; Zhang, X.; Sun, H.; Chen, G.; Feng, X.; Woo, H. Y.; Djurišic, A. B.; He, Z.; Guo, X., Dopant‐Free Small‐Molecule Hole‐Transporting Material for Inverted Perovskite Solar Cells with Efficiency Exceeding 21%. *Advanced Materials* **2019,** *26*, 1902781
124. Yu, Z.; Sun, L., Recent Progress on Hole-Transporting Materials for Emerging Organometal Halide Perovskite Solar Cells. *Advanced Energy Materials* **2015,** *5* (12), 1500213.
125. Brauer, J. C.; Lee, Y. H.; Nazeeruddin, M. K.; Banerji, N., Charge Transfer Dynamics from Organometal Halide Perovskite to Polymeric Hole Transport Materials in Hybrid Solar Cells. *The Journal of Physical Chemistry Letters* **2015,** *6* (18), 3675-3681.

126. Fortunato, E.; Figueiredo, V.; Barquinha, P.; Elamurugu, E.; Barros, R.; Gonçalves, G.; Park, S.-H. K.; Hwang, C.-S.; Martins, R., Thin-film Transistors Based on P-type Cu_2O Thin Films Produced at Room Temperature. *Applied Physics Letters* **2010,** *96* (19), 192102.
127. Pattanasattayavong, P.; Ndjawa, G. O.; Zhao, K.; Chou, K. W.; Yaacobi-Gross, N.; O'Regan, B. C.; Amassian, A.; Anthopoulos, T. D., Electric Field-induced Hole Transport in Copper(I) Thiocyanate (CuSCN) Thin-films Processed from Solution at Room Temperature. *Chemical Communications* **2013,** *49* (39), 4154-4156.
128. Liu, S.; Liu, R.; Chen, Y.; Ho, S.; Kim, J. H.; So, F., Nickel Oxide Hole Injection/Transport Layers for Efficient Solution-Processed Organic Light-Emitting Diodes. *Chemistry of Materials* **2014,** *26* (15), 4528-4534.
129. Tirado, J.; Vásquez-Montoya, M.; Roldán-Carmona, C.; Ralaiarisoa, M.; Koch, N.; Nazeeruddin, M. K.; Jaramillo, F., Air-Stable n–i–p Planar Perovskite Solar Cells Using Nickel Oxide Nanocrystals as Sole Hole-Transporting Material. *ACS Applied Energy Materials* **2019,** *2* (7), 4890-4899.
130. Zhu, Z.; Bai, Y.; Zhang, T.; Liu, Z.; Long, X.; Wei, Z.; Wang, Z.; Zhang, L.; Wang, J.; Yan, F.; Yang, S., High-performance Hole-extraction Layer of Sol-gel-processed NiO Nanocrystals for Inverted Planar Perovskite Solar Cells. *Angewandte Chemie International Edition* **2014,** *53* (46), 12571-12575.
131. Jiang, F.; Choy, W. C.; Li, X.; Zhang, D.; Cheng, J., Post-treatment-Free Solution-Processed Non-stoichiometric NiO_x Nanoparticles for Efficient Hole-Transport Layers of Organic Optoelectronic Devices. *Advanced Materials* **2015,** *27* (18), 2930-2937.
132. Bai, Y.; Chen, H.; Xiao, S.; Xue, Q.; Zhang, T.; Zhu, Z.; Li, Q.; Hu, C.; Yang, Y.; Hu, Z.; Huang, F.; Wong, K.; Yip, H.; Yang, S., Effects of a Molecular Monolayer Modification of NiO Nanocrystal Layer Surfaces on Perovskite Crystallization and Interface Contact toward Faster Hole Extraction and Higher Photovoltaic Performance. *Advanced Functional Materials* **2016,** *26* (17), 2950-2958.
133. Bai, Y.; Chen, H.; Xiao, S.; Xue, Q.; Zhang, T.; Zhu, Z.; Li, Q.; Hu, C.; Yang, Y.; Hu, Z.; Huang, F.; Wong, K.; Yip, H.; Yang, S., Effects of a Molecular Monolayer Modification of NiO Nanocrystal Layer Surfaces on Perovskite Crystallization and Interface Contact toward Faster Hole Extraction and Higher Photovoltaic Performance. *Adv. Funct. Mater.* **2016,** ***26*** (17), 2950-2958.
134. Chen, W.; Wu, Y.; Liu, J.; Qin, C.; Yang, X.; Islam, A.; Cheng, Y.-B.; Han, L., Hybrid Interfacial Layer Leads to Solid Performance Improvement of Inverted Perovskite Solar Cells. *Energy & Environment Science* **2015,** ***8*** (2), 629-640.
135. Minemoto, T.; Murata, M., Theoretical Analysis on Effect of Band Offsets in Perovskite Solar Cells. *Solar Energy Materials and Solar Cells* **2015,** *133*, 8-14.
136. Qiu, L.; Ono, L. K.; Jiang, Y.; Leyden, M. R.; Raga, S. R.; Wang, S.; Qi, Y., Engineering Interface Structure to Improve Efficiency and Stability of Organometal Halide Perovskite Solar Cells. *The Journal of Chemical Physics B* **2018,** *122* (2), 511-520.
137. Liu, C.; Huang, Z.; Hu, X.; Meng, X.; Huang, L.; Xiong, J.; Tan, L.; Chen, Y., Grain Boundary Modification via F4TCNQ To Reduce Defects of Perovskite Solar Cells with Excellent Device Performance. *ACS Applied Materials & Interfaces* **2018,** *10* (2), 1909-1916.
138. Zhang, J.; Bai, D.; Jin, Z.; Bian, H.; Wang, K.; Sun, J.; Wang, Q.; Liu, S. F., 3D-2D-0D Interface Profiling for Record Efficiency All-Inorganic $CsPbBrI_2$ Perovskite Solar Cells with Superior Stability. *Advanced Energy Materials* **2018,** *8* (15), 1703246.
139. Zhao, P.; Kim, B. J.; Jung, H. S., Passivation in Perovskite Solar Cells: A Review. *Materials Today Energy* **2018,** *7*, 267-286.
140. Buin, A.; Pietsch, P.; Xu, J.; Voznyy, O.; Ip, A. H.; Comin, R.; Sargent, E. H., Materials Processing Routes to Trap-free Halide Perovskites. *Nano Letters* **2014,** *14* (11), 6281-6286.

141. Ho, Y.-C.; Hoque, M. N. F.; Stoneham, E.; Warzywoda, J.; Dallas, T.; Fan, Z., Reduction of Oxygen Vacancy Related Traps in TiO_2 and the Impacts on Hybrid Perovskite Solar Cells. *The Journal of Physical Chemistry C* **2017,** *121* (43), 23939-23946.
142. Ma, J.; Chang, J.; Lin, Z.; Guo, X.; Zhou, L.; Liu, Z.; Xi, H.; Chen, D.; Zhang, C.; Hao, Y., Elucidating the Roles of $TiCl_4$ and PCBM Fullerene Treatment on TiO_2 Electron Transporting Layer for Highly Efficient Planar Perovskite Solar Cells. *The Journal of Physical Chemistry C* **2018,** *122* (2), 1044-1053.
143. Li, W.; Zhang, W.; Van Reenen, S.; Sutton, J.; Fan, J.; Haghighirad, A.; Johnston, M.; Wang, L.; Snaith, H., Enhanced UV-light Stability of Planar Heterojunction Perovskite Solar Cells with Caesium Bromide Interface Modification. *Energy & Environment Science* **2016,** ***9*** (2), 490-498.
144. Schulz, P.; Whittaker-Brooks, L. L.; MacLeod, B. A.; Olson, D. C.; Loo, Y.-L.; Kahn, A., Electronic Level Alignment in Inverted Organometal Perovskite Solar Cells. *Advanced Materials Interfaces* **2015,** *2* (7), 1400532.
145. Wang, Q.; Shao, Y.; Xie, H.; Lyu, L.; Liu, X.; Gao, Y.; Huang, J., Qualifying Composition Dependent P and N Self-doping in $CH_3NH_3PbI_3$. *Applied Physics Letters* **2014,** *105* (16), 163508.
146. Gong, X.; Li, M.; Shi, X.-B.; Ma, H.; Wang, Z.-K.; Liao, L.-S., Controllable Perovskite Crystallization by Water Additive for High-Performance Solar Cells. *Advanced Functional Materials* **2015,** *25* (42), 6671-6678.
147. Peng, J.; Wu, Y.; Ye, W.; Jacobs, D. A.; Shen, H.; Fu, X.; Wan, Y.; Duong, T.; Wu, N.; Barugkin, C.; Nguyen, H. T.; Zhong, D.; Li, J.; Lu, T.; Liu, Y.; Lockrey, M. N.; Weber, K. J.; Catchpole, K. R.; White, T. P., Interface Passivation Using Ultrathin Polymer–fullerene Films for High-efficiency Perovskite Solar Cells with Negligible Hysteresis. *Energy & Environmental Science* **2017,** *10* (8), 1792-1800.
148. Yun, J. S.; Kim, J.; Young, T.; Patterson, R. J.; Kim, D.; Seidel, J.; Lim, S.; Green, M. A.; Huang, S.; Ho-Baillie, A., Humidity-Induced Degradation via Grain Boundaries of $HC(NH_2)_2PbI_3$ Planar Perovskite Solar Cells. *Advanced Functional Materials* **2018,** *28* (11), 1705363.
149. Chen, Q.; Zhou, H.; Song, T. B.; Luo, S.; Hong, Z.; Duan, H. S.; Dou, L.; Liu, Y.; Yang, Y., Controllable Self-induced Passivation of Hybrid Lead Iodide Perovskites toward High Performance Solar Cells. *Nano Letters* **2014,** *14* (7), 4158-4163.
150. Smith, I. C.; Hoke, E. T.; Solis-Ibarra, D.; McGehee, M. D.; Karunadasa, H. I., A Layered Hybrid Perovskite Solar-cell Absorber with Enhanced Moisture Stability. *Angewandte Chemie International Edition* **2014,** *53* (42), 11232-11235.
151. David, B. M., *Synthesis, Structure, and Properties of Organic-Inorganic Perovskites and Related Materials*. John Wiley & Sons, Inc.: **1999**; Vol. 48, p 246.
152. Yan, J.; Qiu, W.; Wu, G.; Heremans, P.; Chen, H., Recent Progress in 2D/quasi-2D Layered Metal Halide Perovskites for Solar Cells. *Journal of Materials Chemistry A* **2018,** *6* (24), 11063-11077.
153. Chen, P.; Bai, Y.; Wang, S.; Lyu, M.; Yun, J.; Wang, L., In Situ Growth of 2D Perovskite Capping Layer for Stable and Efficient Perovskite Solar Cells. *Advanced Functional Materials* **2018,** *28* (17), 1706923.
154. Cho, Y.; Soufiani, A. M.; Yun, J. S.; Kim, J.; Lee, D. S.; Seidel, J.; Deng, X.; Green, M. A.; Huang, S.; Ho-Baillie, A. W. Y., Mixed 3D-2D Passivation Treatment for Mixed-Cation Lead Mixed-Halide Perovskite Solar Cells for Higher Efficiency and Better Stability. *Advanced Energy Materials* **2018,** *8* (20), 1703392.
155. Thakur, U. K.; Askar, A. M.; Kisslinger, R.; Wiltshire, B. D.; Kar, P.; Shankar, K., Halide Perovskite Solar Cells Using Monocrystalline TiO_2 Nanorod Arrays as Electron Transport Layers: Impact of Nanorod Morphology. *Nanotechnology* **2017,** *28* (27), 274001.

156. Wu, W.-Q.; Huang, F.; Chen, D.; Cheng, Y.-B.; Caruso, R. A., Thin Films of Dendritic Anatase Titania Nanowires Enable Effective Hole-Blocking and Efficient Light-Harvesting for High-Performance Mesoscopic Perovskite Solar Cells. *Advanced Functional Materials* **2015,** *25* (21), 3264-3272.
157. Bi, C.; Wang, Q.; Shao, Y.; Yuan, Y.; Xiao, Z.; Huang, J., Non-wetting Surface-driven High-aspect-ratio Crystalline Grain Growth for Efficient Hybrid Perovskite Solar Cells. *Nature Communications* **2015,** *6*, 7747.
158. Nie, W.; Tsai, H.; Blancon, J. C.; Liu, F.; Stoumpos, C. C.; Traore, B.; Kepenekian, M.; Durand, O.; Katan, C.; Tretiak, S.; Crochet, J.; Ajayan, P. M.; Kanatzidis, M.; Even, J.; Mohite, A. D., Critical Role of Interface and Crystallinity on the Performance and Photostability of Perovskite Solar Cell on Nickel Oxide. *Advanced Materials* **2018,** *30* (5), 1703879.
159. Wu, W.-Q.; Chen, D.; Caruso, R. A.; Cheng, Y.-B., Recent Progress in Hybrid Perovskite Solar Cells Based on N-type Materials. *Journal of Materials Chemistry A* **2017,** *5* (21), 10092-10109.
160. Huangfu, M.; Shen, Y.; Zhu, G.; Xu, K.; Cao, M.; Gu, F.; Wang, L., Copper Iodide as Inorganic Hole Conductor for Perovskite Solar Cells with Different Thickness of Mesoporous Layer and Hole Transport Layer. *Applied Surface Science* **2015,** *357*, 2234-2240.
161. Yin, J.; Cao, J.; He, X.; Yuan, S.; Sun, S.; Li, J.; Zheng, N.; Lin, L., Improved Stability of Perovskite Solar Cells in Ambient Air by Controlling the Mesoporous Layer. *Journal of Materials Chemistry A* **2015,** *3* (32), 16860-16866.
162. Jeon, N. J.; Noh, J. H.; Kim, Y. C.; Yang, W. S.; Ryu, S.; Seok, S. I., Solvent Engineering for High-performance Inorganic-organic Hybrid Perovskite Solar Cells. *Nature Materials* **2014,** *13* (9), 897-903.
163. Huang, F.; Pascoe, A. R.; Wu, W. Q.; Ku, Z.; Peng, Y.; Zhong, J.; Caruso, R. A.; Cheng, Y. B., Effect of the Microstructure of the Functional Layers on the Efficiency of Perovskite Solar Cells. *Advanced Materials* **2017,** *29* (20), 1601715.
164. Kim, H. S.; Lee, J. W.; Yantara, N.; Boix, P. P.; Kulkarni, S. A.; Mhaisalkar, S.; Gratzel, M.; Park, N. G., High Efficiency Solid-state Sensitized Solar Cell-based on Submicrometer Rutile TiO_2 Nanorod and $CH_3NH_3PbI_3$ perovskite sensitizer. *Nano Letters* **2013,** *13* (6), 2412-2417.
165. Chen, X.; Yang, S.; Zheng, Y. C.; Chen, Y.; Hou, Y.; Yang, X. H.; Yang, H. G., Multifunctional Inverse Opal-Like TiO_2 Electron Transport Layer for Efficient Hybrid Perovskite Solar Cells. *Advanced Science* **2015,** *2* (9), 1500105.
166. Lee, J.-W.; Lee, S. H.; Ko, H.-S.; Kwon, J.; Park, J. H.; Kang, S. M.; Ahn, N.; Choi, M.; Kim, J. K.; Park, N.-G., Opto-electronic Properties of TiO_2 Nanohelices with Embedded $HC(NH_2)_2PbI_3$ Perovskite Solar Cells. *Journal of Materials Chemistry A* **2015,** *3* (17), 9179-9186.
167. Mahmood, K.; Swain, B. S.; Kirmani, A. R.; Amassian, A., Highly Efficient Perovskite Solar Cells Based on a Nanostructured WO_3–TiO_2 Core–shell Electron Transporting Material. *Journal of Materials Chemistry A* **2015,** *3* (17), 9051-9057.

Chapter 2.

Experimental Methods and Instrumentation

2.1 Introduction

A brief overview of the materials, experimental methods and characterization approaches that are overarching across the different Chapters of this Thesis are provided here. This includes the description of the keys steps towards the fabrication of PSCs, which involves patterning of electrodes and the deposition of the charge transporting layers, perovskite and top electrode. Specific experimental details and analysis relevant to only a single Chapter, has been detailed in that Chapter.

2.2 Materials

Patterned and non-patterned FTO/glass substrates were purchased from Latech Scientific Supply and Zhuhai Kaivo Optoelectronic Technology Co., Ltd, respectively, and they were used after cleaning using a three-stage sonication process in hellmanex, water and ethanol. n-butylammonium iodide (BAI), formamidinium iodide (FAI), methylammonium bromide (MABr), TiO_2 nanoparticle paste (NR30) were purchased from Greatcellsolar; lead iodide (PbI_2), lead bromide ($PbBr_2$), and nickel sulphate ($NiSO_4 \cdot 6H_2O$) were purchased from Alfa Aesar; 2,3,5,6-Tetrafluoro-7,7,8,8-tetracyanoquinodimethane (F4TCNQ) and Spiro-OMeTAD were purchased from Lumtech. Unless otherwise stated, all other materials were purchased from Sigma Aldrich, and used as received.

2.3 Fabrication Tools and Facilities

Ultrasonic Cleaner: An S300H Elmasonic ultrasonic bath from Invitro Technologies (**Figure 2.1**) was used to clean the FTO substrates. Substrates have to be cleaned by ultrasonic cleaner with 2% Helmanex solution (10 min), deionized water (10 min), and ethanol (10 min), successively. FTO coated glass substrates were vertically put in a home-made plastic holder (in the ultrasonic bath) during ultrasonic cleaning.

Figure 2.1 The digital photograph of the ultrasonic cleaner.

Plasma Cleaner: The Harrick PDC plasma cleaner (**Figure 2.2**) was used to treat the FTO substrate and HTL substrate to eliminate surface impurities and contaminants. All substrates were plasma treated by 10 min before use.

Figure 2.2 The digital photograph of the plasma cleaner.

Spin Coater: WS-650HZ-23NPP/UD2 Spin Coaters from Laurell Technologies (**Figure 2.3**) was used to deposit the mesoporous TiO_2 mesoporous layers, perovskite layers and charge transporting

layers on top of perovskite layers. Details about spin-coating program will be reported in the device fabrication section.

Figure 2.3 The digital photograph of the spin coater.

Titanium Hot Plate: HOP-2820-TIT-C titanium hotplates with the proportional–integral–derivative (PID) temperature programmer from MRClab (**Figure 2.4**) were used to calcine TiO_2 mesoporous layer and anneal perovskite layer. Details about heating treatment temperature and annealing time will be reported in the device fabrication section.

Figure 2.4 The digital photograph of the titanium hot plate with a PID temperature controller.

Ultrasonic Spray System: The ultrasonic spray system is a homemade system featuring a Sonotek Vortex nozzle operating at 120 kHz controlled by a Zaber Computer-controlled positioner (**Figure 2.5**). The precursor was sprayed onto a heated substrate with a spray rate of 0.5 mL/min and a 200 kPa shaping pressure to facilitate the precipitation spray droplets. The distance between the spray needle tip and the substrate was 23.5 cm. The rest of detailed spray parameters for NiO and TiO_2 compact films on FTO substrates will be reported in device fabrication section and **Chapter 4**.

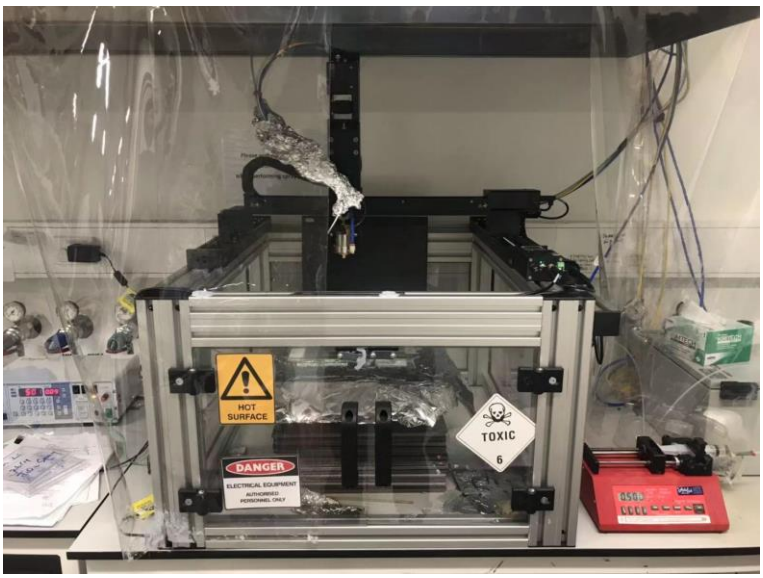

Figure 2.5 The digital photograph of the ultrasonic spray system.

Glovebox: The Korea Kiyon glove box **(Figure 2.6)** was used to fabricate the PSCs. The concentration of O_2 and H_2O were well controlled to be ≤ 10 ppm and ~0.1 ppm, respectively.

Figure 2.6 The digital photograph of the glovebox.

Thermal Evaporator: The thermal evaporator from Korea Kiyon (**Figure 2.7**) was set in the Korea Kiyon glovebox and used to deposit the metal electrodes of PSCs. Electrodes were performed with an evaporation rate of 2 Å/s under a vacuum of 2×10^{-6} Pa.

Figure 2.7 The digital photograph of the thermal evaporator.

2.4 Device Fabrication

In this thesis, we studied both of inverted and conventional perovskite solar cell device configurations. Thus, to clarify this experimental section, we will demonstrate the device fabrication process in the order of the electrode substrate (FTO), CTL underneath of the perovskite layer, the perovskite layer, the CTL on top of perovskite and finally the top electrode.

FTO Substrates: The as received FTO coated glass substrates patterned for four devices with separated cathode and anode were bought from Latech Scientific Supply (**Figure 2.8)**. Before use, substrates have to be cleaned by ultrasonic cleaner with 2% Helmanex solution (10 min), deionized water (10 min), and ethanol (10 min), successively. Then the cleaned substrates were treated by the plasma cleaner for 10 min to further eliminate impurities and contaminants on their surfaces.

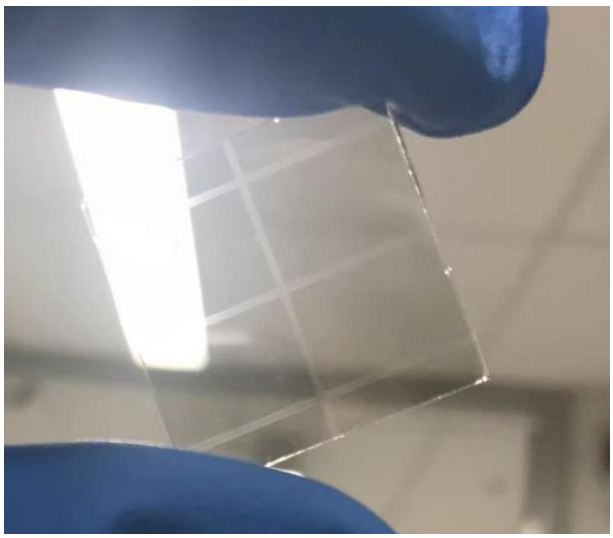

Figure 2.8 The digital photograph of the FTO coated glass from Latech Scientific Supply.

CTLs on FTO: CTLs were deposited by CBD for mesoporous NiO films and ultrasonic spray pyrolysis for planar NiO and TiO_2 films.

CBD NiO film: Mesoporous NiO films were made by CBD as shown in **Figure 2.9A**. CBD is a simple method that involves controllable deposition of oxide solid from liquid precursor to yield uniform films with good reproducibility. The product films are highly dependent on the deposition temperature, pH value of precursor and surface energy of the substrate. Our mesoporous NiO films were deposited on oxygen plasma treated FTO-coated glass. Firstly, the back (glass) side of the substrate was covered by 3M scotch tape to make sure only the FTO side was coated. The substrate was then vertically loaded into a beaker with an aqueous ammoniacal precursor solution containing 0.2 M $NiSO_4$ and 37.5 mM $K_2S_2O_8$ at room temperature (pH=11) for 2 to 10 mins to achieve different thicknesses. The substrate was dried with nitrogen gun and then annealed at 500 ℃ on the Ti hotplate for 1 hour in air. Examples of final Glass/FTO/NiO films achieved by different deposition time are shown in **Figure 2.9B**.

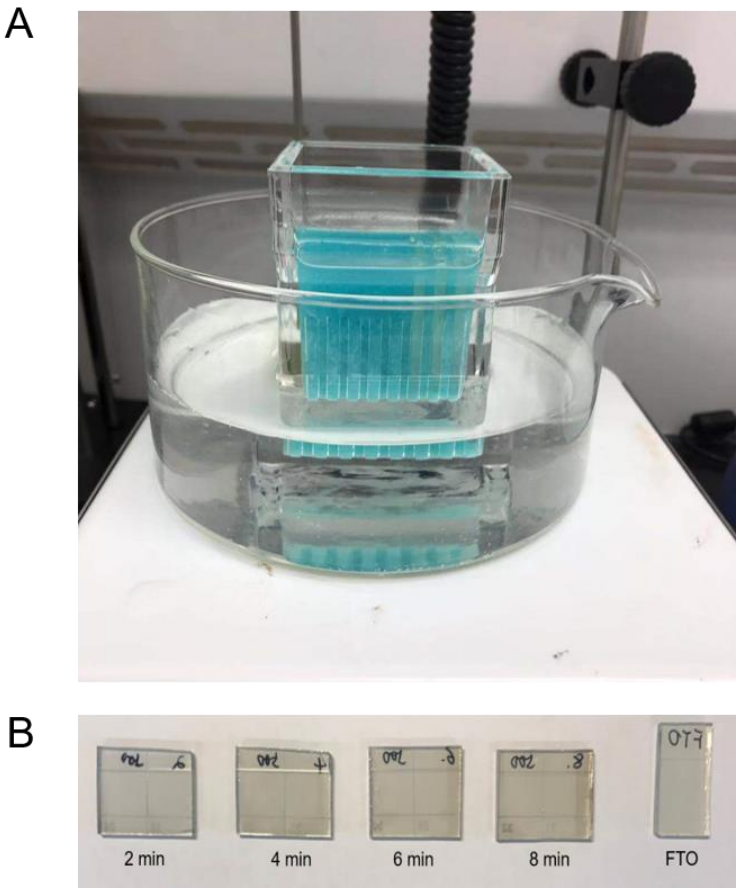

Figure 2.9 Digital photographs of the reaction setup used for CBD NiO films on FTO substrates (A) and as deposited Glass/FTO/NiO films achieved by different deposition time.

Ultrasonic Spray Deposition of NiO: Planar NiO films as HTLs for inverted PSCs and planar TiO_2 films as ETLs for conventional PSCs were deposited using ultrasonic spray. For the NiO film, 20 mL of a 0.04M Ni acetylacetonate ($Ni(acac)_2$) in acetonitrile solution was sprayed by the ultrasonic spray system onto the FTO-coated glass substrate at 500 ℃ in air. The spray conditions were optimized to provide 10 individual coating passes (~10 mL solution) across the substrate and to give a total NiO thickness of ~10 nm. This was followed by 30 min of annealing at 500 ℃ before being cooled down to room temperature.

Ultrasonic Spray Deposition of Compact TiO_2: The dense TiO_2 blocking layer was formed by the ultrasonic spray pyrolysis of a bis(isopropoxide)-bis(acetylacetonate)titanium(IV) (TAA) solution at 500 °C. This solution was formed by diluting TAA in isopropanol (1:19 vol) and sprayed on to the FTO coated glass substrates at 500 ℃ in air. The sprayed samples were annealing for 10 mins at 500 ℃ in air after 4 spray cycle (~4 mL solution), before being cooled down to room temperature.

Deposition of meso-TiO_2: An 18nm TiO_2 nanoparticle paste was diluted in ethanol (1:6 vol) prior to spin-coating on the dense TiO_2 blocking layer at 4000 rpm for 20 s in air and then annealed at 500 ℃ for 30 mins. In **Chapter 4**, we will demonstrate the study on ultrasonic spray of TiO_2 ETL and show its high reproducibility.

Perovskite Deposition: Perovskite deposition was carried out in the glovebox. In this thesis, we used gas-assistance deposition[1] and anti-solvent deposition[2] to achieve $MAPbI_3$ perovskite and Cs/FA/MA tri-cation perovskite, respectively (**Figure 2.10**).

For gas-assistance method to make $MAPbI_3$ perovskite: The perovskite precursor solution was formed by mixing stoichiometric amounts of CH_3NH_3I and PbI_2 in a combination of dimethyl sulfoxide (DMSO) and N-methyl-2-pyrrolidone (NMP) (7:3 vol) to form a (46 wt%) concentration solution. 30 μL of the perovskite precursor solution was applied to the surface of the substrate prior to spin-coating. The films were spin-coated using a two-stage process: 1000 rpm for 5 s using an acceleration of 200 rpm/s, then 6000 rpm for 50 s using an acceleration of 6000 rpm/s. A nitrogen gas flow was introduced after 20 s of the second spin-coating step and sustained for a further 20 s. The perovskite films were then annealed on a hot-plate at 100 °C for a duration of 10 mins.

For anti-solvent method to make $Cs_{0.05}FA_{0.81}MA_{0.14}PbI_{2.55}Br_{0.45}$: precursor solution (1.2 M) was prepared with molar ratios of PbI_2/$PbBr_2$ and FAI/MABr both fixed at 0.85:0.15, molar ratio of CsI/(FAI+MABr)=0.05:0.95, and the molar ratio of (FAI+MABr+CsI)/(PbI_2+$PbBr_2$) being fixed at 1:1. The perovskite films were deposited onto the TiO_2 substrates with a two-step spin coating procedures. The first step involved 1000 rpm for 5 s with an acceleration of 200 rpm/s. The second step was conducted at 6000 rpm for 20 s with a ramp-up of 1000 rpm/s. Chlorobenzene (200 μL) was deposited on the spinning substrate during the second spin-coating step at 5 s before the end of the procedure. The substrate was then immediately transferred to a hotplate and heated at 100 °C for 40 min. To grow the 2D perovskite layer, 100 μL of BAI (5mg mL^{-1}) isopropanol (IPA) solution with various concentration of F4TCNQ was prepared and then shaken or stirred for 24h. The solution was spin-casted on ready-made 3D perovskite substrates when it is spinning at 6000 rpm for 20s and then annealed at 100 °C for 10 min.

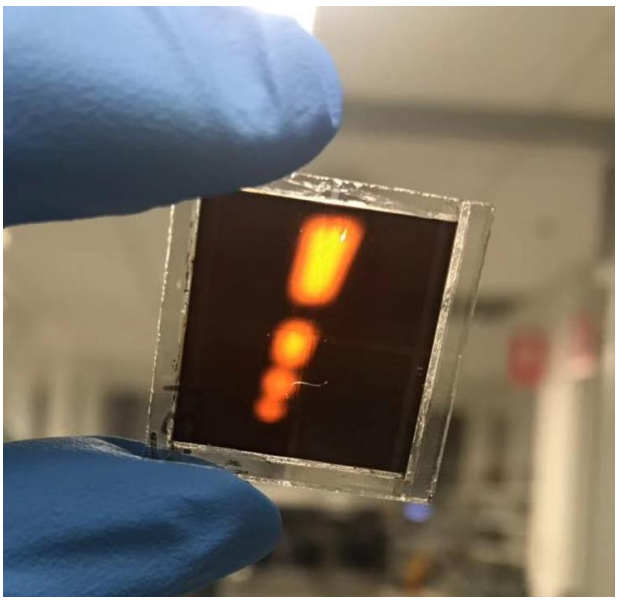

Figure 2.10 Digital photographs of the A perovskite film deposited on a Glass/FTO/CTL substrate.

CTLs on Top of Perovskite: For conventional PSCs, a Spiro-OMeTAD layer was deposited on top of the perovskite layer as the HTL. Spiro-OMeTAD was well dissolved in chlorobenzene (70 mM) by shaking the solution for a few minutes at room temperature. Then, appropriate volumes of FK209 and LiTFSI stock solutions and tBP were added (**Table 2.1**).[3] The solution was spin-coated on the perovskite film at 3000 rpm for 30 s.

Table 2.1 Spiro-OMeTAD additives stock solutions and the composition of the final solution

Stock Solutions	Mw (g/mol)	Solvent	M (mol/L)	($mol_{additive}$/ $mol_{spiro\text{-}OMeTAD}$)
FK209	1503.18	Acetonitrile	0.25	0.03
LiTFSI	287.09	Acetonitrile	1.8	0.50
tBP	135.21			3.30

For inverted PSCs, The ETL was deposited from a 20 mg/ml chlorobenzene solution of PCBM that was spin-coated at a rotation speed of 1800 rpm for 30s. Onto the PCBM layer, 25 µL of a BCP saturated IPA solution was spin coated without any post treatment.

Metal Electrode Deposition: To benefit the energy alignment, we used Au and Ag as electrodes in conventional and inverted PSCs, respectively. Before the thermal deposition, the devices without electrodes were masked as shown in **Figure 2.11A** to avoid the connection of anode and cathode. The

films were placed under a vacuum of 2 $\times 10^{-6}$ Pa, and then 80 nm Au and Ag films were evaporated using an evaporation rate of 2 Å/s on to Glass/FTO/TiO_2/Perovskite/Spiro-OMeTAD films for conventional PSCs and Glass/FTO/NiO/Perovskite/PCBM/BCP films for inverted PSCs, respectively. **Figure 2.11** shows the masked semi-finished products (Glass/ETL/perovskite/HTL films as an example) before and after deposition of Au electrodes.

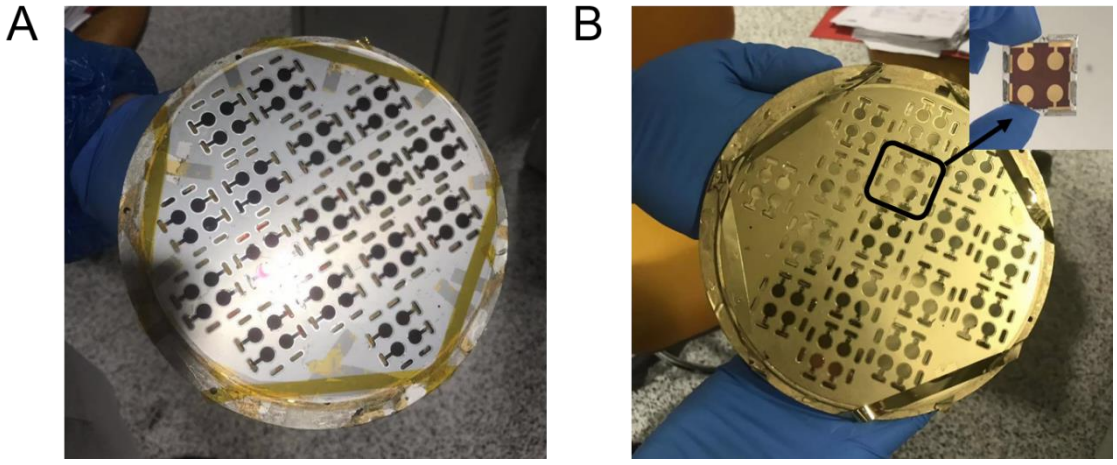

Figure 2.11 Digital photographs of the masked Glass/FTO/ETL/perovskite/HTL substrates before (A) and after (B) thermal deposition of Au top electrodes. The inset photograph is an individual product with 4 separated PSCs.

2.5 Characterization

Absorption, Transmittance and Reflection Measurements: Optical absorption, transmittance and reflection Measurements spectra were characterized by a Perkin Elmer Lambda 1050 UV/VIS/NIR spectrophotometer using an attached integrating sphere.

Steady-State Photoluminescence (PL): Steady-state photoluminescence measurements were performed using an Fluoromax4 Spectro fluorometer. Samples were illuminated using a 465.8 nm excitation source. Slit widths were set to 1.2 nm and the samples were excited for a duration of 1 μs.

Transient Photoluminescence (TRPL): TRPL decay measurements were performed using an Edinburgh Instruments Ltd. FLSP920 time correlated single-photon counting spectrometer equipped with a 465.8 nm pulsed diode laser excitation source (EPL-475, Edinburgh Instruments Ltd.) with ca 100 ps pulse width and a peak laser excitation density of ca 0.2 nJ cm^{-2}. Luminescence was collected using a grating monochromator. Samples were prepared on glass microscope slides of 1 cm × 1 cm

films and encapsulated. Noteworthy, excitation and luminescence collection were performed on the glass side.

Scanning Electron Microscope (SEM): Top-view and the cross-section morphology of films were characterized by an FEI Nova Nano SEM operating at a 5kV voltage. Cross-section samples were sputter coated by ~2nm Iridium before characterizing.

X-ray Powder Diffraction (XRD): XRD patterns were recorded using a D2 phaser X-ray diffractometer with Cu Kα X-ray tube at 40 kV and 40 mA and with a step size of 0.02° and 0.5 s per step.

Spectroscopic Ellipsometry: Ellipsometry measurements were carried out on J.A.Woollam M-2000DI Spectroscopic ellipsometer with TiO_2 samples being deposited on polished silicon wafers with a natural oxide layer. Atomic Force Microscopy (AFM) measurements were performed on a Dimension Icon (Veeco).

X-ray photoelectron spectroscopy (XPS) and Ultraviolet Photoelectron Spectroscopy (UPS): XPS and UPS photoelectron spectroscopy analysis was performed using an AXIS Ultra DLD spectrometer (Kratos Analytical Inc., Manchester, U.K.) with a monochromate Al K X-ray source (1486.6 eV) and a He discharge lamp (He I radiation at 21.22 eV), respectively. The XPS survey spectra were acquired with the hemispherical analyser set to a pass energy of 160 eV, while the high-resolution narrow scans were made using a 40 eV pass energy (resolution ca. 0.75 eV FWHM). UPS data were recorded at 5 eV pass energy (resolution ca. 0.1 eV). The standard analyser slot aperture was used, resulting in an area of approximately 0.7 mm × 0.3 mm being analysed on the sample.

Current-Voltage Analysis: The J–V curve characteristics of completed solar cell devices were recorded using a Keithley 2400 Source Meter. The devices were illuminated using a Xenon lamp provided by an Oriel solar simulator with an AM1.5G filter that was set to 100 mW cm^{-2} using a calibrated Si-photodiode. A non-reflective mask with an aperture of 0.16 cm^2 was used to keep the irradiation area constant.

Incident Photon to Current Conversion Efficiency (IPCE): IPCE spectra were recorded using a Keithley 2400 Source Meter under 300 W xenon lamp irradiation with an Oriel Corner-stone 260¼ m monochromator and white light bias from light-emitting diode (LED; Thorlabs MWWHL3) light source. The monochromatic photon flux was quantified through a calibrated silicon cell.

Transient photocurrent decay (TPC) measurements: TPCs of devices were performed by illuminating devices with a constant background intensity high-power white LED (Thorlabs MWWHL3). A small light perturbation was provided by a Kingbright L-7104VGC-H green LED (465 nm wavelength) driven by a function generator (Agilent 33533A). A pulse width of 2 μs was chosen for the small perturbation with the rise and fall times of the LED to be <100 ns measured using a Thorlabs DET10A/M Si photodetector. The transient response of the cell under test was recorded on an Agilent Technologies InfiniiVision DSO-X 3032A digital oscilloscope (DOSC). The device was connected to the DOSC with a 50 Ω termination to achieve a short-circuit condition.

Transient photovoltage decay (TPD) measurements: For open-circuit photovoltage decay measurements, devices were illuminated with a 630 nm LED source with a switch-off response time of ≈20 μs. Voltage transients measured using NI-DAQMX USB-6212 data acquisition card. During the measurements of the transient photovoltage measurements, a termination of 1 MΩ was used by connecting the cells to the DOSC to achieve the open circuit condition.

References

1. Huang, F.; Dkhissi, Y.; Huang, W.; Xiao, M.; Benesperi, I.; Rubanov, S.; Zhu, Y.; Lin, X.; Jiang, L.; Zhou, Y.; Gray-Weale, A.; Etheridge, J.; McNeill, C. R.; Caruso, R. A.; Bach, U.; Spiccia, L.; Cheng, Y.-B., Gas-assisted Preparation of Lead Iodide Perovskite Films Consisting of a Monolayer of Single Crystalline Grains for High Efficiency Planar Solar Cells. Nano Energy 2014, 10, 10-18.
2. Paek, S.; Schouwink, P.; Athanasopoulou, E. N.; Cho, K. T.; Grancini, G.; Lee, Y.; Zhang, Y.; Stellacci, F.; Nazeeruddin, M. K.; Gao, P., From Nano- to Micrometer Scale: The Role of Antisolvent Treatment on High Performance Perovskite Solar Cells. Chemistry of Materials 2017, 29 (8), 3490-3498.
3. Saliba, M.; Correa-Baena, J. P.; Wolff, C. M.; Stolterfoht, M.; Phung, N.; Albrecht, S.; Neher, D.; Abate, A., How to Make over 20% Efficient Perovskite Solar Cells in Regular (n–i–p) and Inverted (p–i–n) Architectures. Chemistry of Materials 2018, 30 (13), 4193-4201.

Chapter 3.

Inverted Perovskite Solar Cells with High Fill-factors Featuring Chemical Bath Deposited Mesoporous NiO Hole Transporting Layers

Synopsis:

PCEs of PSCs have rapidly achieved record values of more than 25%. All of the reported high PCE devices have been achieved within a conventional PSC configuration, which has been suggested to possess lower stabilities over time. Inverted device structures can potentially overcome this limitation; however, due to existing challenges in controlling perovskite microstructure and charge extraction at the electrodes, the reported PCEs of such devices remain lower compared to the conventional device architectures. In this work we undertake interfacial engineering between NiO, the archetypal p-type layer used in inverted PSCs, and mixed cation and halide perovskites to improve charge extraction and reduce interfacial recombination losses in these devices. This is achieved through the introduction of a facile meso-structured NiO scaffold as the hole-transporting layer. Through the optimisation of these scaffolds, PSCs with efficiencies of up to 16.5% can be readily fabricated. Importantly, these devices show exceptional fill factors of up to 85% due to the excellent light harvesting and charge transporting efficiencies. In comparison, devices fabricated using the conventionally spray-deposited planar NiO transporting layers exhibited PCEs of up to 14.5% and fill factors of around 70%.

This paper has been published in Nano Energy (2018, V49, 163-171, 10.1016/j.nanoen.2018.04.026)

Nano Energy 49 (2018) 163–171

Contents lists available at ScienceDirect

Nano Energy

journal homepage: www.elsevier.com/locate/nanoen

Full paper

Inverted perovskite solar cells with high fill-factors featuring chemical bath deposited mesoporous NiO hole transporting layers

Jingsong Sun[a,b], Jianfeng Lu[a,b], Bin Li[a,b], Liangcong Jiang[a,b], Anthony S.R. Chesman[b,c], Andrew D. Scully[c], Thomas R. Gengenbach[c], Yi-Bing Cheng[a,b,d], Jacek J. Jasieniak[a,b,*]

[a] Department of Materials Science and Engineering, Monash University, Clayton, Victoria 3800, Australia
[b] ARC Centre of Excellence in Exciton Science, Australia
[c] CSIRO Manufacturing, Research Way, Clayton, Victoria 3168, Australia
[d] State Key Laboratory of Advanced Technology for Materials Synthesis and Processing, Wuhan University of Technology, Wuhan, 430070 China

ARTICLE INFO

Keywords:
NiO
Chemical bath deposition
Mesoporous
Hole transporting layer
Perovskite solar cells

ABSTRACT

The development of hole transporting layers that optimize charge extraction and minimize interfacial recombination losses offer an important route for further enhancement in the performance of inverted perovskite solar cells (PSCs). NiO is a widely adopted hole transporting material in such devices, possessing a reasonably high hole mobility and suitable energy level positions to provide high efficiency solar cells. However, its use in inverted PSCs has typically resulted in relatively low fill factors, which arises from underlying contact issues between the perovskite and NiO layers. In this work, we address this issue by employing a thin mesoporous NiO scaffold formed via chemical bath deposition as the hole transporting layer. This hole transporting material is found to dramatically improve the performance of inverted mixed cation and anion PSCs by enhancing their light harvesting and charge transporting efficiencies. Optimized devices achieve efficiencies of up to 16.7% and fill factors as high as 85%. These values are significantly higher than PSCs using conventionally spray-deposited planar NiO hole transport layers, which exhibit efficiencies of up to 14.5% and fill factors of only 73%.

1. Introduction

Hybrid organic-inorganic lead halide perovskite solar cells (PSCs) are attracting increasing attention due to their low-cost, facile fabrication opportunities, and outstanding optoelectronic properties [1]. The power conversion efficiency (PCE) of these devices has increased rapidly to more than 22.1% [2]. This is comparable to all other thin film and polycrystalline silicon photovoltaics. With a theoretical PCE of up to 31% being predicted based on detailed balance modelling [3], it is evident that through further progress in materials and device engineering, the PCEs of PSCs will be further enhanced [4].

To date, most high-efficiency PSCs have been achieved with a so-called conventional configuration in which the perovskite layer is deposited on top of an electron transporting layer (ETL), followed by a hole transporting layer (HTL) to form a n-i-p type device [5]. However, the n-i-p configuration suffers from serious hysteresis and high cost, as well as thermal instability, associated with the use of (2,2′,7,7′-tetrakis (N,N-di-pmethoxyphenyl-amine)9,9′-spirobifluorene) (spiroOMeTAD) as an HTL material. These factors have created significant interest in inverted device configurations, which swap the relative positions of the HTL and ETL in the device to reverse the direction of charge extraction and form an p-i-n type configuration [6]. While attractive, such inverted PSCs currently possess inferior PCEs compared to their conventional counterparts, with certified record efficiencies being 20.6% and 22.1%, respectively [7,8]. An important strategy aimed at improving the performance of inverted devices has involved tailoring the HTLs to achieve higher optical transparencies and more favourable interfacial band alignments [9]. At present, poly(3,4-ethylenedioxythiophene): poly(styrene-sulfonate) (PEDOT: PSS) and p-type NiO are the HTLs which have been employed with the greatest success, with the latter presenting better stability and electron blocking properties [10].

Various approaches have been used to fabricate NiO HTLs for inverted PSCs, including sol-gel deposition [11], nanoparticle inks [12], and spray pyrolysis [13]. Yang's group was the first to introduce a sol–gel-processed NiO nanoparticle HTL in PSCs, achieving a PCE of 9% [11]. Recent progress has seen a further improvement to more than 15% via a monolayer molecular modification [14]. Meanwhile, Choy's group reported a solution processed HTL made with a NiO nanoparticle ink that gave inverted PSCs with PCEs of ~16% [12]. The most successfully deployed NiO HTL was deposited through spray deposition,

* Corresponding author at: Department of Materials Science and Engineering, Monash University, Clayton, Victoria 3800, Australia.
E-mail address: jacek.jasieniak@monash.edu (J.J. Jasieniak).

https://doi.org/10.1016/j.nanoen.2018.04.026
Received 8 January 2018; Received in revised form 12 March 2018; Accepted 9 April 2018
Available online 12 April 2018

relying on Li^+/Mg^{2+} co-doping to control oxygen deficiency and conductivity. The PCE of the inverted PSCs using this doped NiO was 18.3% [15].

In each of these devices, NiO has advantageously provided a matching energy alignment with the perovskite, resulting in a high photovoltage. However, all of these NiO based devices displayed low fill factors (FF). This can be ascribed to the modified crystallinity of the perovskite and the poor contact formed between the NiO and perovskite layers [14]. In addition, the low conductivity of NiO ($\sim 10^{-4}$ S cm^{-1}) can also reduce the FF due to a high series resistance contribution [15]. To address these factors, additional mesoporous layers and molecular surface modification strategies have been successfully deployed to improve the FFs and, consequently, PCEs of inverted PSCs [11,13]. Unfortunately, these additional processing steps introduce further complications that impact fabrication times, scalability and reliability. Developing a simple, one-step approach to deposit NiO that is suitable for inverted PSCs with both high FFs and PCEs remains an unresolved scientific challenge.

Herein, we address this challenge by harnessing chemical bath deposition (CBD) to form a mesoporous NiO scaffold in a single processing step that is suitable for use in inverted PSCs. The approach utilises a persulphate salt to modify the chemical bath conditions of the NiO to drive the formation of a mesoporous NiO scaffold that consists of a bilayer structure. In this structure, a compact layer is formed on the surface of our fluorine-doped tin oxide (FTO) transparent conducting electrode (TCE), and a ridge-like mesoporous structure develops on top. The vertical and continuous flakes in this upper layer act as anchors to improve the contact between NiO and perovskite layers. Consequently, inverted PSCs with a PCE and FF of up to 16.7% and 85%, respectively, can be achieved, a marked improvement compared to reference devices fabricated using spray-deposited NiO HTLs.

2. Results and discussion

2.1. CBD of mesoporous NiO HTLs

CBD is a low cost and low temperature approach for depositing thin coatings at laboratory and industrial scales [16]. The beauty of this approach lies in its simplicity, involving the immersion of FTO-coated glass into an aqueous solution containing nickel sulfate, potassium persulfate and ammonia, with a pH value of ~11, for only several minutes (Fig. 1**A**). Scanning electron micrographs (SEM) of NiO films deposited using this approach on FTO-coated glass as a function of CBD reaction time and after thermal annealing at 500 °C are shown in Fig. 1**B-E**. For simplicity, from hereon we define the CBD samples deposited on FTO-coated glass (Fig. S1) for different durations as CBDx, where x denotes the number of minutes the CBD was carried out for. It is found that a 2 min deposition (CBD2) yields a thin coating of NiO nano-flakes on the FTO surface (Fig. 1**B**). Prolonging the deposition time from 4 to 8 min induces the formation of a 3D mesoporous scaffold that consists of interconnected flakes protruding from the surface (CBD4–8, Fig. 1**C-E**). It is found that the scaffold becomes gradually denser and more interconnected during this process, with the thickness of these mesoporous films concurrently increasing from < 10 nm for CBD2 through to 200 nm for CBD8 (Fig. S2). Notably, for CBD conducted with no potassium persulfate present in the reaction solution (as shown in Fig. S3), only planar films were deposited; highlighting the importance of potassium persulfate as a determinant in the formation of the 3D mesoporous layer.

The overall reaction mechanism in our CBD can be described by a series of steps that involve precipitation, oxidation, and dehydration [16,17].

$$|Ni(H_2O)_{6-x}(NH_3)_x|^{2+}(aq) + 2OH^-(aq) \rightarrow Ni(OH)_2(s)\downarrow + (6-x)H_2O(l) + xNH_3(g)\uparrow \quad (1)$$

$$2Ni(OH)_2(s) + S_2O_8^{2-}(aq) + 2OH^-(aq) \rightarrow 2NiOOH(s) + 2SO_4^{2-}(aq) + 2H_2O(l) \quad (2)$$

$$6NiOOH(s) + 2NH_3{\cdot}H_2O(l) \rightarrow 6Ni(OH)_2(s) + N_2(g)\uparrow + 2H_2O(g)\uparrow \quad (3)$$

$$Ni(OH)_2(s) \rightarrow NiO(s) + H_2O(g)\uparrow \quad (4)$$

Evidently, in this reaction mechanism the persulfate salt induces Ni^{2+} oxidation to generate Ni^{3+} species within the deposited films (Eq. (2)). The subsequent reduction of these species back into Ni^{2+} has been suggested to occur through the oxidation of ammonia (Eq. (3)) [18], with a subsequent dehydration step yielding NiO (Eq. (4)).

It is well known that Ni^{3+} centers in NiOOH are highly light absorbing across the visible spectrum and are the light absorbing component in "darkened" $Ni(OH)_2$ electrochromic windows [16]. With charge transporting layers for photovoltaics requiring maximized optical transmittance across the visible spectral region, the effective conversion of NiOOH into NiO is important. Our as-deposited CBD NiO films on FTO-coated glass were all a dark-brown colour, consistent with the presence of NiOOH. At annealing temperatures of > 300 °C the coatings became transparent, indicating the thermally-induced reduction of Ni^{3+} to Ni^{2+} in the film (Eq. (2)). In Fig. 2**A** we show the transmittance of our CBD NiO films deposited on FTO-coated glass after heat treatment at 500 °C as measured through ultraviolet visible (UV–Vis) spectroscopy. These measurements indicate that the mesoporous NiO films on the FTO-coated glass possess transmittance values of more than 75% across the visible spectrum, with a progressively decreasing transmission of 2–5% being observed at longer deposition times compared to neat FTO-coated glass. While NiO has a high optical bandgap of approximately 3.6 eV [13], it commonly exhibits absorption within the visible range due to intrinsic oxygen deficiencies [19]. This phenomenon, coupled with the additional scattering contributions arising from the scaffold, are likely to be responsible for these transmission trends. Despite these moderate losses, our NiO films possess a sufficiently high transmission to be a conducive HTL within PSCs, particularly at lower deposition times.

Probing the structural evolution using X-ray diffraction (XRD) (see Fig. 2**B**) shows that the as-deposited CBD films using potassium persulfate additives crystallize as both β-$Ni(OH)_2$ (peaks at 33.8°, 36.8°, 60.5° and 63.1° 2θ according to JCPDS 14-0117 file) and γ-NiOOH (peaks at 23.7° and 41.5° 2θ according to JCPDS 06-0075 file). Conversion of these nickel oxy-hydroxide species to NiO, occurs at temperatures as low as 200 °C [17], with higher annealing temperatures improving the crystallinity of the nickel oxide film. This is evidenced by more pronounced cubic NiO diffraction peaks at 37.4°, 43.6° and 62.7° 2θ (according to JCPDS 04-0835 file) being observed at these elevated temperatures. It is worth noting that as-deposited CBD films made without potassium persulfate were predominantly $Ni(OH)_2$, with poor crystallinity (see Fig. S4). This ultimately yielded NiO with significantly poorer crystallinity after annealing at 500 °C compared to CBD that used the potassium persulfate, thus confirming its importance in achieving meso-structuring, as well as high crystallinity of the NiO films.

Ultraviolet photoelectron spectroscopy (UPS) has been carried out to determine the band positions of our mesoporous NiO layers formed using the persulfate salt at various deposition times (Fig. 2**C**). All of the CBD NiO films display a Fermi energy of −4.7 eV (vs vacuum) and a valence band maximum (VBM) energy of −5.45 eV. This is consistent with the p-type character of NiO. As a comparison, we also determined the ionization potential of samples using photoelectron spectroscopy in air (PESA). With the assumption that the ionization potential approximates the VBMs in these semiconductors [20], the VBM energy positions were determined to be approximately −5.57 eV for our CBD NiO films (Fig. S5). The discrepancy of 0.1 eV between PESA and UPS is consistent with what has been observed for other semiconducting

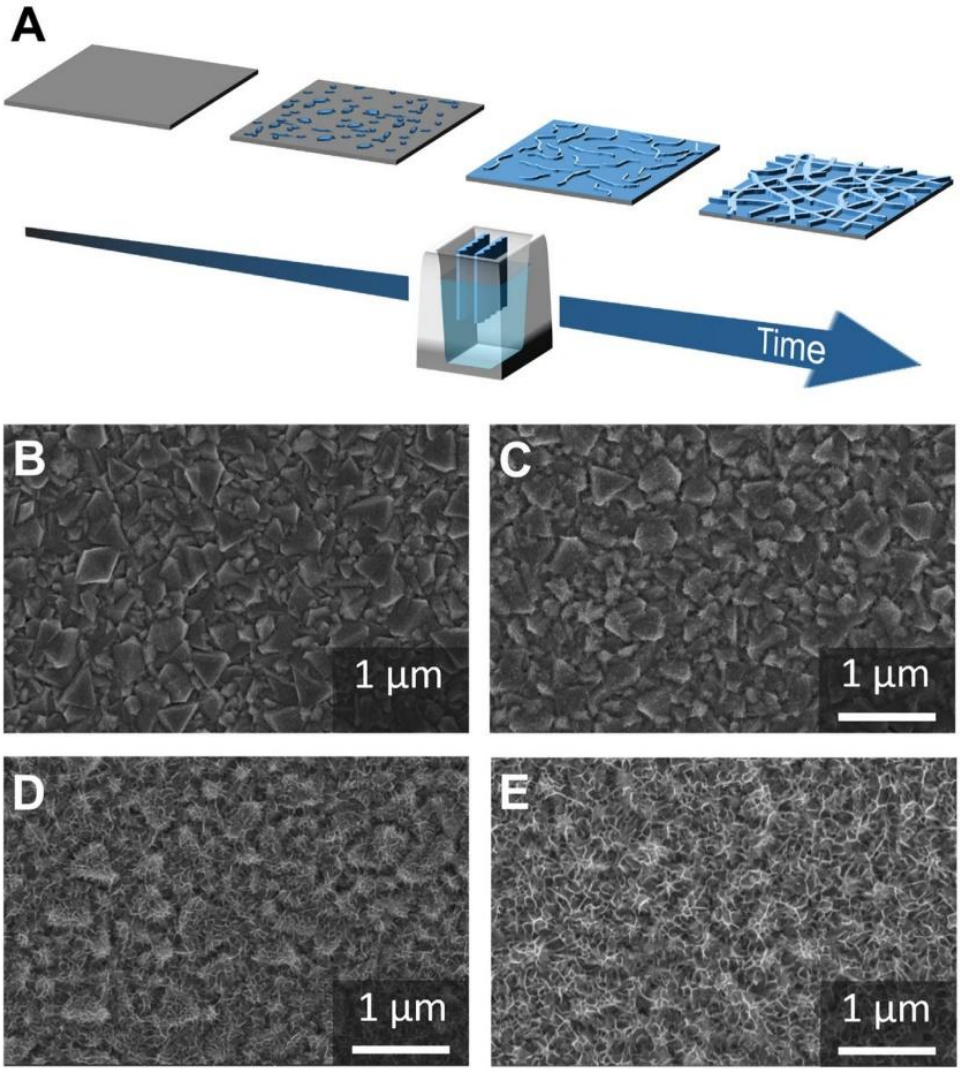

Fig. 1. A) Schematic illustration of the chemical bath process for depositing mesoporous Ni hydroxide/oxy-hydroxide films on FTO-coated glass before dehydration. The digital images show the chemical bath solutions as a function of deposition time, clearly indicating the progressive formation of the colored Ni oxyhydroxide species, which govern the formation of the scaffolded films on the FTO. Subsequent conversion of these films to cubic NiO is achieved through thermal annealing at 500 °C in air. B-E) Top-view SEM images of CBD NiO-coated films deposited on FTO substrates with deposition time of B) 2 min, C) 4 min, D) 6 min and E) 8 min.

materials [21]. Considering that NiO has a direct optical bandgap of 3.6 eV [13], we can approximate the conduction band minimum (CBM) energy to be −1.9 to −2.0 eV. These energy levels are suitably matched for HTLs with Ohmic contacts to perovskites, for which the VBM range has been reported to between −5.4 eV and −5.6 eV [14,15]. Consistent with these studies, in this work we selectively used the $Cs_{0.05}FA_{0.81}MA_{0.14}PbI_{2.55}Br_{0.45}$ ($FA^+ = CH(NH_2)_2^+$, $MA^+ = CH_3NH_3^+$) cation and anion mixed perovskite, which was found to possess a VBM of − 5.4 eV as measured by UPS (see Fig. S6).

To investigate the chemical composition of our CBD NiO films annealed at 500 °C, we have used X-ray photoelectron spectroscopy (XPS). Survey scans of NiO films made by CBD using potassium persulfate showed almost stoichiometric quantities of nickel: oxygen 1.00:1.05. As a comparison, samples prepared with no persulfate showed a higher nickel: oxygen ratio of 1:2.3. These samples also contained 11.4% of tin, suggesting an additional contribution from the FTO substrate, likely due to an inhomogeneous coating (see Fig. 2**D**). Both samples showed trace amounts of sulfur (4–7% vs Ni) resulting from residual nickel sulfate and persulfate precursor materials.

To further probe the chemical nature of these films we performed high resolution scans of the Ni $2p_{3/2}$ and O 1s regions (see Fig. 2**E** and **F**). The interpretation of the Ni 2p spectra is notoriously difficult because of its complex, extended multiplet, shake-up and plasmon loss structures. As such, here we restrict ourselves to a qualitative discussion based on a publication by Biesinger et al. who reported the results of a detailed and thorough investigation of a series of Ni compounds [21]. Both Ni $2p_{3/2}$ peaks display a similar peak shape, with the main component at lower binding energy (BE) consisting of two contributions (ca. 855 eV and 857 eV) and a broad shake-up peak centered at approx. 862 eV. These can be interpreted as a combination of contributions from NiO, NiOOH and $Ni(OH)_2$. Pure NiO displays a strong, narrow peak at 855 eV and a weaker peak at 857 eV, while for $Ni(OH)_2$ the latter is the dominant peak and the former is only detectable as a weak low BE shoulder [21,22]. In the case of CBD NiO prepared with persulfate (Fig. 2**E**) the spectrum is very similar to that of pure NiO, (i.e. Ni^{2+} in the standard Ni-O octahedral bonding configuration of cubic rock-salt NiO [10]), but likely has some additional hydroxide contributions. In comparison, samples prepared without persulfate salts (Fig. 2**F**) exhibited significantly higher relative contributions of the higher binding energy peak (862 eV). This is consistent with a higher level of Ni-hydroxide being present, although the precise quantification of its relative contribution to Ni-O is not possible.

The corresponding high resolution O 1s scans shown in Fig. 2**E** and **F** also feature multiple contributions, with a narrow peak at a lower BE

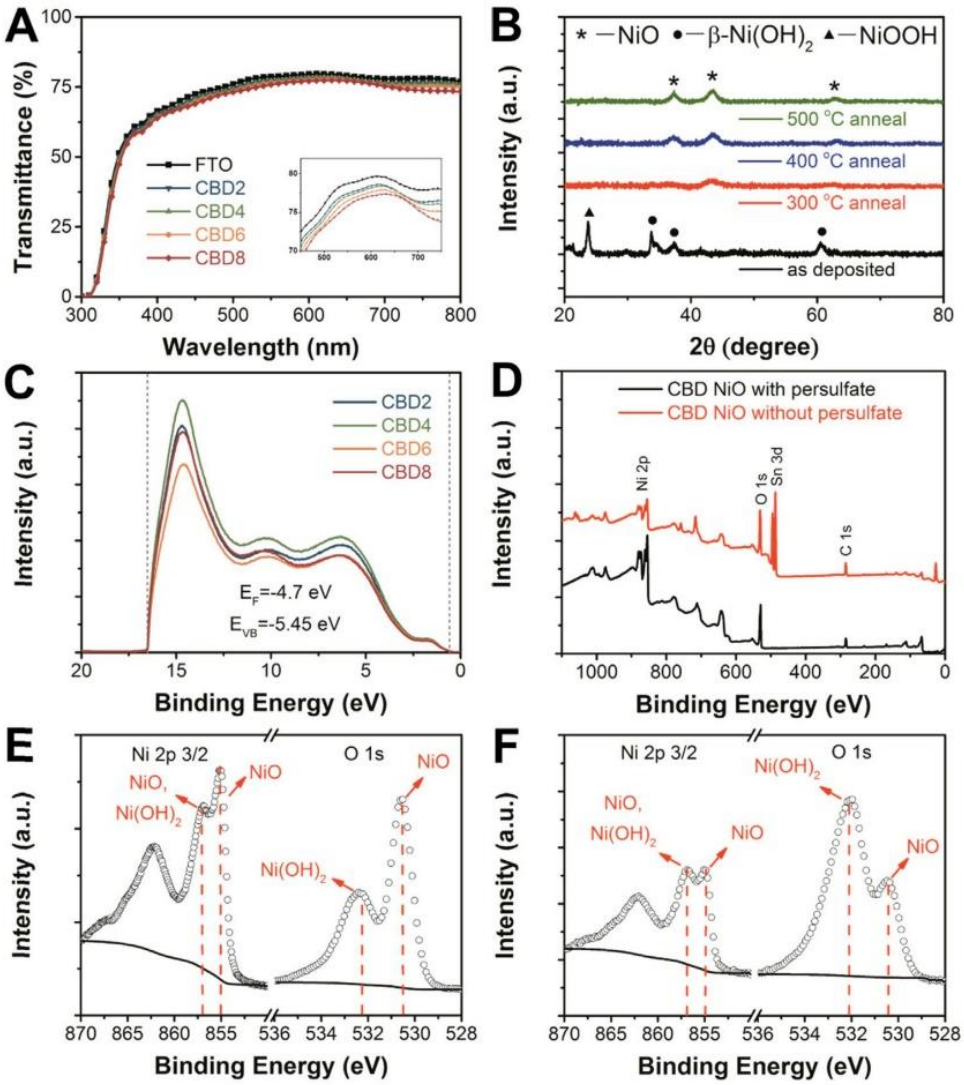

Fig. 2. (A) UV–Vis spectra (transmittance) of FTO-coated glass and CBD 2–8 min NiO films on FTO-coated glass; (B) XRD patterns of the NiO crystals that were scratched down from FTO-coated glass; (C) UPS spectra of CBD2 to CBD8 on FTO glass substrates; (D) Full range XPS survey spectra of CBD6 films prepared with and without persulfate during the synthesis; and (E, F) Ni 2p 3/2 and O 1 s high resolution spectra of CBD6 films prepared with and without persulfate during the synthesis, respectively. The dominant NiO and $Ni(OH)_2$ peaks are labeled in both high resolution spectra.

of ~530 eV that arises from NiO, a broader component at ~532 eV, which likely originates from defect sites within the NiO crystal lattice, hydroxide species, or organic oxygen, and a broad high BE contribution at ~533–534 eV arising from adsorbed water or oxygen [21]. While a quantitative evaluation of the O 1 s spectra is not possible because of the presence of multiple, overlapping contributions, qualitatively they confirm the interpretation of the Ni 2p spectra presented above. From a comparison of the XPS data of samples grown with and without persulfate salts, it is evident that the use of persulfate in the CBD induces greater NiO crystallinity and a less defective and/or less Ni-OH rich network. These findings are consistent with our XRD findings.

2.2. Mixed cation and anion lead halide perovskites on mesoporous NiO HTLs

A top view SEM image of a well-crystallized perovskite layer on a CBD6 NiO film is shown in Fig. 3**A**. The perovskite film has a compact morphology without pinholes and with a grain size of ~100–200 nm. In addition, although the mesoporous NiO films possess different morphologies due to the variable deposition times, the surface profiles of the perovskite layers on top of CBD2 to CBD6 are comparable (see Fig. S7**A-D**). XRD measurements show that all of the deposited films are cubic perovskite in structure without any obvious impurity phases, such as PbI_2 at ~12.6° (see Fig. 3**B**) [23]. These measurements confirm that the microstructural differences of the NiO films deposited using our CBD compared to more planar charge transport layers do not negatively influence the crystallization of the perovskite layer.

With optimized charge extraction dynamics being critical for high performance solar cells, we have investigated the steady-state photoluminescence (PL) and time-resolved photoluminescence (TRPL) characteristics of the perovskites on our CBD NiO films. Although possessing the same composition, the CBD NiO HTLs from CBD2 to CBD8 show increasingly stronger steady-state luminescence quenching of the perovskite luminescence (Fig. 3**C**). Compared to neat perovskites on glass, these NiO films show progressively stronger relative PL quenching of up to ~ 90% with longer CBD deposition time. These trends are consistent with improved hole extraction stemming from an enhanced interface area between the HTL and perovskite [24].

A similar trend has also been observed in the PL decay curves (Fig. 3**D**), with progressively decreasing decay lifetimes being observed. It has been reported that perovskite materials in contact with transporting layers show a short lifetime component (τ_1) due to charge

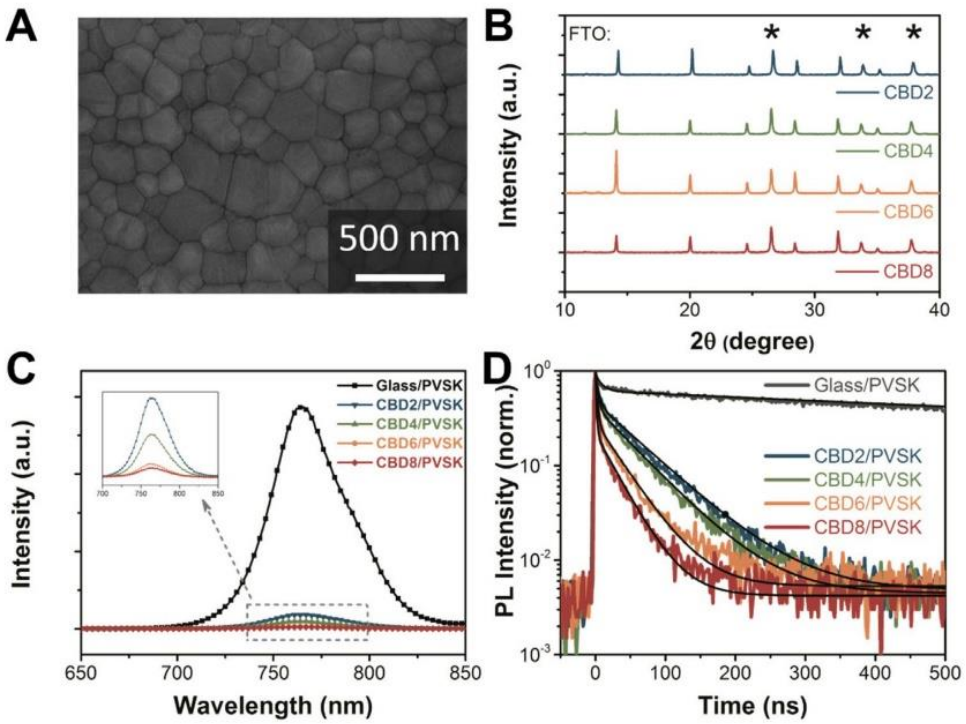

Fig. 3. (A) SEM image of a perovskite film deposited on top of CBD6 NiO HTL; (B) XRD patterns of perovskite films on top of CBD2, 4, 6, 8 NiO HTL, respectively; (C, D) PL (excitation wavelength 465.8 nm) spectra and normalized time-resolved PL decay profiles measured at an emission wavelength 765nm (logarithmic plot) of perovskite (PVSK) layers on the mesoporous NiO/FTO substrates with different deposition times. Excitation and luminescence detection was performed from NiO side.

injection and a longer PL lifetime component (τ_2) from charges that directly recombine within the film before reaching the quenching interface [25]. To quantify these characteristics, the PL decay curves have been fitted using the following bi-exponential decay function [26]:

$$Y = A_1 \exp\left(\frac{-t}{\tau_1}\right) + A_2 \exp\left(\frac{-t}{\tau_2}\right) + A_0 \quad (5)$$

where A and τ are the best-fit amplitudes and PL decay times, respectively. The TRPL curves and the extracted parameters that are summarized in Table S1 show an increasing (decreasing) amplitude of τ_1 (τ_2) contributions as the CBD deposition time is increased. This is indicative of a more efficient charge quenching process at longer deposition times. Consistent with this observation, both τ_1 and τ_2 of the perovskite on CBD2–8 films decrease to yield a reduced average PL decay lifetimes.

2.3. Inverted PSCs with mesoporous NiO HTLs

The mesoporous NiO scaffolds have been assessed as HTLs within an inverted PSC device configuration consisting of glass/FTO/NiO/perovskite/phenyl-C61-butyric acid methyl ester ($PC_{61}BM$)/bathocuproine (BCP)/Ag (see Fig. 4**A**). Based on the above mentioned UPS results and literature values [13], the energy level diagram (versus vacuum) for the components in these devices is shown in Fig. 4**B**. It can be seen that an appropriate energetic landscape exists to facilitate suitable charge blocking and maximise voltage, with the notable anomaly of BCP, for which charge transport is predominantly trap-mediated and through a lower energy transport band than its lowest unoccupied molecular orbit level [27].

The dark and light current-voltage (J-V) curves of the PSC devices fabricated using CBD NiO at various deposition times are shown in Fig. 4**C**, with the extracted device characteristics included in Table 1 and Fig. S8. The dark onset voltages of devices with no HTL (CBD0) is only ~0.4 V, which is consistent with a non-selective electrode contact [13]. The onset voltages increases to 0.8–0.9 V for devices with CBD4~8 NiO HTLs, highlighting the more appropriate HTL formation. Notably, the CBD2 sample shows a slightly lower onset voltage of ~0.6 V, implying that shunting pathways are still present at low NiO deposition times. These trends are also consistent across the light J-V curves measured under forward scan (short-circuit (SC) to forward-bias (FB) scan) conditions, which show poor device performance for CBD0 and CBD2, largely due to shunting ($R_{sh} < 200\ \Omega\ cm^2$) causing low open circuit voltages (V_{oc}). At longer NiO deposition times the device characteristics improve significantly, with CBD6 yielding the highest average performance metrics, including: a short-circuit current (J_{sc}) of 20.0 mA cm^{-2}, V_{oc} of 1.0 V and FF of 0.80. Devices with a FF of 0.85 were achieved under these conditions (see Fig. S9), indicating nearly perfect extraction of available charge carriers.

Devices featuring CBD8 possessed reduced photocurrent and V_{oc}, resulting in slightly inferior device performance compared to CBD6. We believe that this arises due to the more extended (~200 nm) NiO scaffold present in CBD8, which induces less efficient charge extraction and consequently greater recombination of carriers because of the poorly conducting NiO ($< 10^{-3}$ S cm^{-1}). The corresponding incident photon-to-current conversion efficiency (IPCE) of the samples is shown in Fig. 4**D**. These measurements confirm the electronic bandgap of our perovskites is ~770 nm (1.61 eV) and clearly highlight the superior spectral conversion of the CBD6 sample. We note that the integrated IPCEs with the AM1.5 G spectrum is consistent with our measured J_{sc} values.

2.4. Comparison of PSCs with chemical bath and spray-deposited NiO HTLs

As a comparison to our CBD NiO HTLs, analogous devices were prepared using the more conventional spray-deposited NiO [13]. SEM images of the planar NiO films on FTO show a dense NiO nanoparticle coating with a thickness of 10–20 nm (see Fig. S10), contrasting the mesoporous scaffold obtained through CBD. J–V curves of both CBD and spray-deposited NiO PSC devices are shown in Fig. 5**A** under forward and reverse scan conditions. Both of these devices exhibit a higher forward scan performance compared to their reverse direction, which is contrary to most PSCs reported [28], but is consistent with a number of NiO HTL devices [13]. To date, no clear explanation has been provided as to the origin of this hysteresis difference. The CBD6 NiO devices present a champion PCE of 16.7% (V_{oc} = 1.02 V, J_{sc} = 20.8 mA cm^{-2} and FF = 0.80) under forward scan, while the sprayed NiO counterpart

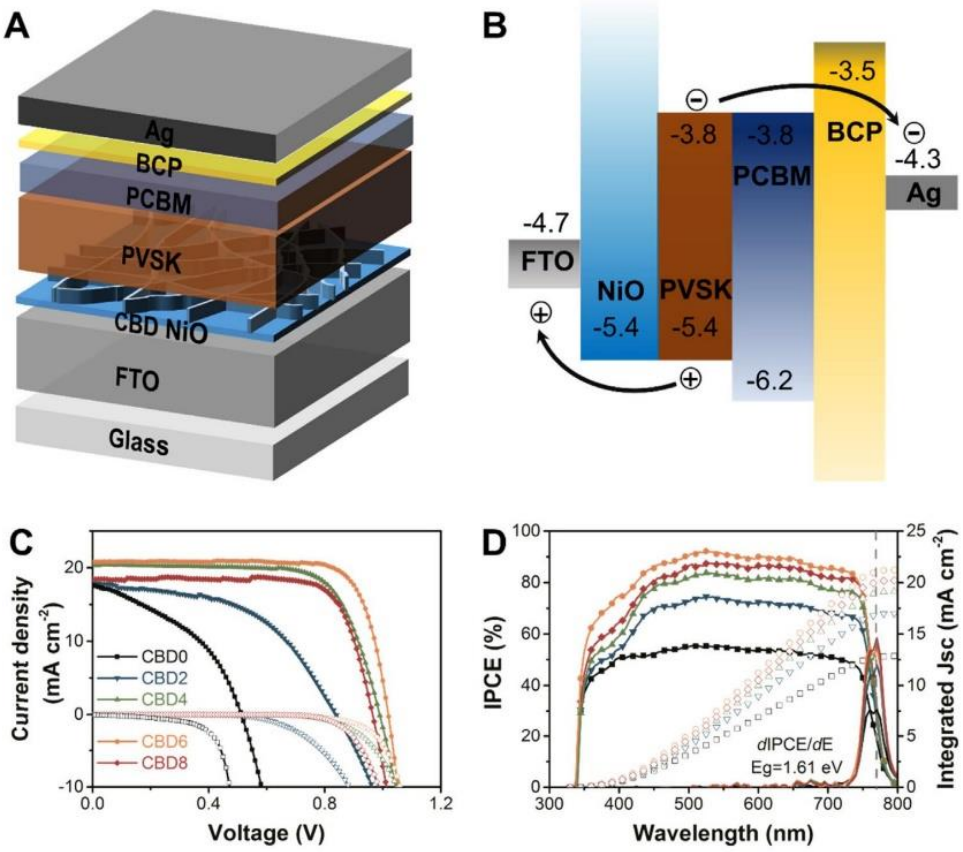

Fig. 4. (A) Overall device structure, consisting of glass/FTO/NiO/perovskite/PCBM/BCP/Ag; (B) the corresponding energy band alignment; (C) J-V curves of inverted PSCs with CBD0-8 HTLs under light and dark conditions; (D) IPCE and integrated current density.

shows a PCE of 14.5% (V_{oc} = 1.02 V, J_{sc} = 19.4 mA cm^{-2} and FF = 0.73). Evidently, the main differences arise from an enhanced J_{sc} and FF for the CBD NiO devices, which increased device efficiency.

To determine the output stability of these devices, we have carried out steady-state current density measurements at a constant potential defined at the maximum power point of 0.85 V and 0.84 V for CBD NiO and sprayed NiO devices, respectively (Fig. 5**B**). The current density for CBD NiO is maintained at 19 mA cm^{-2}, while for the sprayed NiO device it is slightly lower at 16.5 mA cm^{-2}. These values correspond to PCEs of 16.2% and 13.9%, respectively, which are consistent with their averaged performance measurement from forward and reverse scans.

To better understand the origin of the device performance differences, we firstly compared the conductivity of CBD6 and sprayed NiO films (Fig. S11). The CBD6 NiO films were found to possess a minimum conductivity of 6.64 × 10^{-4} S cm^{-1}, which is about 5 times larger than for sprayed NiO at 1.40 × 10^{-4} S cm^{-1}. This may partly explain the higher FF in the CBD devices. In addition, we have also investigated the cross-sectional microstructure of both types of PSC as prepared through focused ion beam (FIB) milling (see Fig. 5**C**). The perovskite layers on both HTLs have a thickness of ~440 nm and possess a comparable bulk microstructure. However, it is evident that the mesoporous NiO network induces a more adherent interface formation with the perovskite layer compared to the planar NiO structure. This suggests that the high-surface area mesoporous layer acts as an anchor at this interface to improve interfacial adhesion.

We have also compared the CBD and sprayed deposited NiO through TRPL of neat perovskite layers and open-circuit voltage decay (OCVD) of completed devices. The TRPL measurements show that both films exhibit similar PL decay trends, indicating comparable diffusion lengths and quenching dynamics (see Fig. S12**A**). However, the CBD NiO does

Table 1
Champion and average photovoltaic parameters of PSC devices (0.16 cm^2 aperture) with CBD0~8 HTLs under 1 sun simulated irradiation.

Solar cells		V_{oc} (V)	J_{sc} (mA cm^2)	FF	PCE (%)	R_s (Ω cm^2)	R_{sh} (Ω cm^2)	J_0 (mA/cm^2)
CBD0	Champion[a]	0.53	17.4	0.45	4.0	9.5	84	2.7 × 10^{-4}
	Average[b]	0.40 ± 0.17	16.2 ± 1.2	0.35 ± 0.08	2.6 ± 1.4			
CBD2	Champion[a]	0.97	17.9	0.65	10.5	8.7	200	6.9 × 10^{-6}
	Average[b]	0.88 ± 0.07	17.5 ± 1.5	0.53 ± 0.07	7.6 ± 3.0			
CBD4	Champion[a]	1.03	20.3	0.80	14.5	7.6	1067	1.0 × 10^{-9}
	Average[b]	1.01 ± 0.02	18.6 ± 0.9	0.72 ± 0.03	13.6 ± 0.8			
CBD6	Champion[a]	1.02	21.0	0.85	16.7	5.5	2000	2.9 × 10^{-12}
	Average[b]	1.00 ± 0.03	20.0 ± 0.6	0.80 ± 0.02	15.9 ± 0.5			
CBD8	Champion[a]	1.05	19.8	0.81	14.0	8.9	1230	2.6 × 10^{-6}
	Average[b]	0.96 ± 0.07	17.9 ± 1.1	0.75 ± 0.02	12.9 ± 0.9			

[a] Best performance for each parameter.
[b] Mean values and one standard deviation calculated from the values obtained for 10 independent devices.

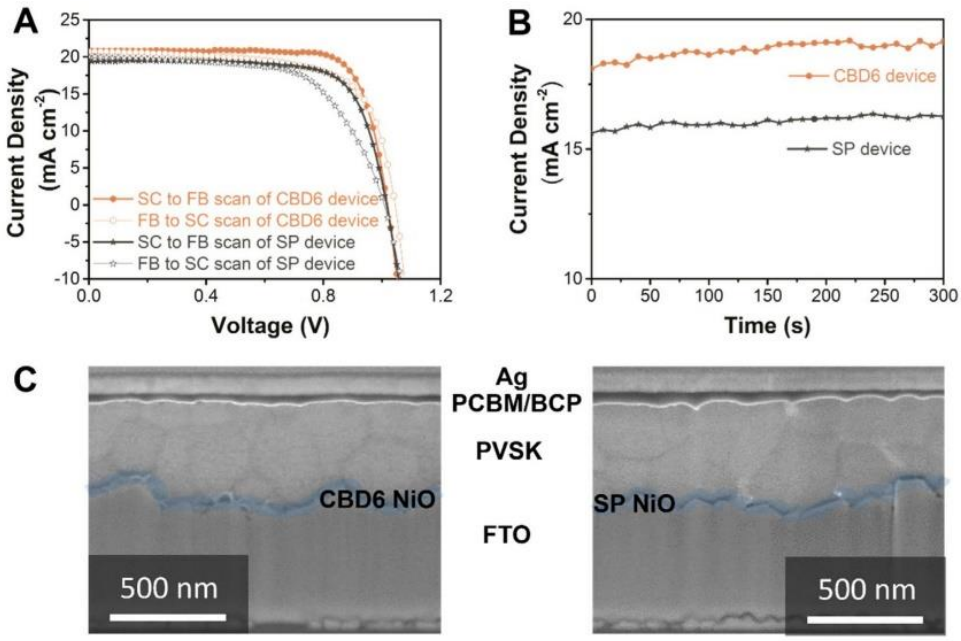

Fig. 5. (A) Short-circuit (SC) to forward-bias (FB) scan and backward FB to SC scan J–V curves of the devices based on CBD6 and sprayed NiO HTLs. (B) Time profiles of photocurrent density applied by holding the potential at about the maximum output power point (0.85V and 0.84V for CBD NiO and sprayed NiO devices, respectively) and (C) FIB-SEM image of cross-section in perovskite devices with CBD6 NiO HTL (left) and sprayed NiO planar HTL (right).

exhibit differences in the OCVD, which is a measure of the recombination dynamics of residual charges remaining in the device, inherently reflecting the polarization of the perovskite material and the trapping of charges at the perovskite/contacts interfaces [29]. The OCVD charge-recombination lifetimes for the CBD and sprayed NiO were measured as 267 μs and 59 μs, respectively (see Fig. S12**B**). These results indicate that the CBD NiO exhibits markedly slower interfacial charge recombination compared to spray deposited NiO. With the OCVD recombination dynamics being reflective of the processes around zero-field conditions, the slower recombination lifetime is suggested to be the major reason for the enhancement of the FF in these devices [30]. The origins of this phenomenon can be related to both the enhanced conductivity and improved interfacial properties identified above.

3. Experimental section materials

FTO-coated glass, formamidinium iodide (FAI), methylammonium bromide (MABr) were purchased from Dyesol; PbI_2, $PbBr_2$, and $NiSO_4{\cdot}6H_2O$ were purchased from Alfa Aesar; bathocuproine (BCP), CsI, dimethyl sulphoxide (DMSO), isopropanol (IPA), and $NH_3{\cdot}H_2O$ were purchased from Sigma-Aldrich; $K_2S_2O_8$ was purchased from Merck. All of chemicals were used as received without any further purification.

3.1. Fabrication of NiO films

FTO-coated glass was laser engraved to separate the cathode and anode, and then cleaned by ultra-sonication in 1% Helmanex solution, deionized water, and ethanol, successively. Mesoporous NiO films were deposited by a CBD method. Briefly, the back side of the FTO-coated glass was covered by 3 M scotch tape to ensure only a single side was coated. The FTO-coated substrate was then vertically loaded into a beaker with an aqueous ammoniacal precursor solution containing 0.2 M $NiSO_4$ and 37.5 mM $K_2S_2O_8$ at room temperature (pH = 11). The substrate was dried with a nitrogen gun and then annealed at 500 °C on a Ti hotplate for 1 h in air. Planar NiO films were deposited using ultrasonic spray deposition according to the approach previously reported [13]. Typically, 20 mL of a 0.04 M Ni acetylacetonate ($Ni(acac)_2$) in acetonitrile solution was sprayed by a homemade ultrasonic spray system featuring a Sonotek Vortex nozel operating at 120 kHz onto the FTO-coated glass substrate at 500 °C in air. This was followed by 30 min of annealing. The spray conditions were optimized to provide 4 individual coating passes across the substrate and to give a total NiO thickness of ~10 nm.

3.2. Fabrication of PSC devices

The NiO HTL on FTO was transferred into a N_2 purged glovebox for the deposition of the perovskite layer using a modified method to that reported in literature [23]. The $Cs_{0.05}FA_{0.81}MA_{0.14}PbI_{2.55}Br_{0.45}$ precursor solution (1.2 M) was prepared with molar ratios of $PbI_2/PbBr_2$ and FAI/MABr both fixed at 0.85:0.15, the molar ratio of CsI/(FAI + MABr) = 0.05:0.95, and the molar ratio of (FAI + MABr + CsI)/(PbI_2 + $PbBr_2$) being fixed at 1:1. The perovskite films were deposited onto the NiO substrates with a two-step spin coating procedure. The first step involved 1000 rpm for 10 s with an acceleration of 200 rpm/s. The second step was conducted at 4000 rpm for 30 s with a ramp-up of 1000 rpm/s. Chlorobenzene (200 μL) was deposited on the spinning substrate during the second spin-coating step at 10 s before the end of the procedure. The substrate was then immediately transferred to a hotplate and heated at 100 °C for 10 min. The ETL was deposited from a 20 mg/mL chlorobenzene solution of PCBM that was spin-coated at a rotation speed of 1800 rpm for 30 s. Onto the PCBM, 25 μL of a BCP saturated IPA solution was spin coated without any post treatment. The Glass/FTO/HTL/Perovskite/ETL films were placed under a vacuum of 2×10^{-6} Pa, then a 100 nm thick Ag film was evaporated using an evaporation rate of 2 Å/s as the anode.

3.3. Characterization

Transmittance and reflection spectra were characterized by a Perkin Elmer Lambda 1050 UV/VIS/NIR spectrophotometer. Top-view and the cross section morphology were characterized by an FEI Nova Nano SEM. XRD patterns were recorded using a Bruker D2 Phaser X-ray diffractometer with Cu Kα radiation.

X-ray (XPS) and ultraviolet (UPS) photoelectron spectroscopy analysis was performed using an AXIS Ultra DLD spectrometer (Kratos Analytical Inc., Manchester, U.K.) with a monochromated Al Kα X-ray source (1486.6 eV) and a He discharge lamp (He I radiation at 21.22 eV), respectively. The XPS survey spectra were acquired with the hemispherical analyser set to a pass energy of 160 eV, while the high resolution narrow scans were made using a 40 eV pass energy

(resolution ca. 0.75 eV FWHM). UPS data were recorded at 5 eV pass energy (resolution ca. 0.1 eV). The standard analyser slot aperture was used, resulting in an area of approximately 0.7 mm x 0.3 mm being analysed on the sample.

Steady-state photoluminescence measurements were performed using a Fluoromax4 Spectro fluorometer. Samples were illuminated using a 465.8 nm excitation source. Slit widths were set to 1.2 nm and the samples were excited for a duration of 1 μs.

Transient photoluminescence decay measurements were performed using an Edinburgh Instruments Ltd. FLSP920 time correlated single-photon counting spectrometer equipped with a 465.8 nm pulsed diode laser excitation source (EPL-475, Edinburgh Instruments Ltd.) with ca 100 ps pulse width and a peak laser excitation density of ca 0.2 nJ cm^{-2}. Luminescence was collected using a grating monochromator. Samples were prepared on glass microscope slides of 1 cm × 1 cm films and encapsulated. Noteworthy, excitation and luminescence collection was performed on the NiO side.

The J–V curve characteristics of completed solar cell devices were recorded using a Keithley 2400 Source Meter. The devices were illuminated using a Xenon lamp source (100 mW cm^{-2}) provided by an Oriel solar simulator with an AM1.5G filter. A non-reflective mask with an aperture of 0.16 cm^2 was used to keep the irradiation area constant.

Incident photon to current conversion efficiency (IPCE) spectra were recorded using a Keithley 2400 Source Meter under 300 W xenon lamp irradiation with an Oriel Corner-stone 260¼ m monochromator. The monochromatic photon flux was quantified through a calibrated silicon cell. For open-circuit voltage decay measurements, devices were illuminated with a 630 nm LED source with a switch-off response time of ≈ 20 μs. Voltage transients were measured using an NI-DAQMX USB-6212 data acquisition card.

4. Conclusion

In this work we have used chemical bath deposition to form mesoporous nickel oxyhydroxide films on fluorine doped tin oxide glass. These could be readily converted into 3D meso-structured cubic NiO scaffolds following thermal annealing at temperatures up to 500 °C. Such scaffolds were explored as hole-transport layers within inverted hybrid mixed cation and anion perovskite solar cells, delivering device efficiencies of over 16% and with nearly ideal fill-factors as high as 0.85. In comparison, spray-deposited devices with a planar NiO layer were found to exhibit markedly lower efficiencies of 14.5% and fill-factors of only 0.73. The significant improvements in devices prepared using chemical bath deposited NiO were shown to arise from improved interfacial adhesion between the perovskite and NiO layers, as well as reduced charge recombination dynamics. It is envisaged that further improvements to the device characteristics reported here will be realized through further engineering of the NiO to enhance its electrical properties and tailoring of its interfacial chemistry.

Acknowledgements

JS acknowledges funding support through the Monash Graduate Scholarship and Monash International Postgraduate Research Scholarship programs. The authors acknowledge funding support through the Australian Research Council under the grant CE170100026. The authors acknowledge the use of the facilities at the Monash Centre for Electron Microscopy (MCEM). The authors acknowledge use of facilities within the Monash X-ray Platform. This research used equipment funded by Australian Research Council grant LE130100072.

Appendix A. Supporting information

Supplementary data associated with this article can be found in the online version at http://dx.doi.org/10.1016/j.nanoen.2018.04.026.

References

[1] L. Pazos-Outón, M. Szumilo, R. Lamboll, J. Richter, M. Crespo-Quesada, M. Abdi-Jalebi, H. Beeson, M. Vrućinić, M. Alsari, H. Snaith, B. Ehrler, R. Friend, F. Deschler, Photon recycling in lead iodide perovskite solar cells, Science 351 (2016) 1430–1433.
[2] NREL, ⟨www.nrel.gov/pv/assets/images/efficiency-chart.png⟩.
[3] W. Sha, X. Ren, L. Chen, W. Choy, The efficiency limit of CH3NH3PbI3 perovskite solar cells, Appl. Phys. Lett. 106 (2015) 221104.
[4] S. Shin, E. Yeom, W. Yang, S. Hur, M. Kim, J. Im, J. Seo, J. Noh, S. Seok, Colloidally prepared La-doped BaSnO3 electrodes for efficient, photostable perovskite solar cells, Science 356 (2017) 167–171.
[5] S. Kim, C. Lee, J. Im, K. Lee, T. Moehl, A. Marchioro, S. Moon, R. Humphry-Baker, J. Yum, J. Moser, M. Gratzel, N. Park, Lead Iodide Perovskite Sensitized all-solid-state submicron thin film mesoscopic solar cell with efficiency exceeding 9%, Sci. Rep. 2 (2012) 591.
[6] J. Jeng, Y. Chiang, M. Lee, S. Peng, T. Guo, P. Chen, T. Wen, CH3NH3PbI3 perovskite/fullerene planar-heterojunction hybrid solar cells, Adv. Mater. 25 (2013) 3727–3732.
[7] F. Xie, C. Chen, Y. Wu, X. Li, M. Cai, X. Liu, X. Yang, L. Han, Vertical recrystallization for highly efficient and stable formamidinium-based inverted-structure perovskite solar cells, Energy Environ. Sci. 10 (2017) 1942–1949.
[8] W. Yang, B. Park, E. Jung, N. Jeon, Y. Kim, D. Lee, S. Shin, J. Seo, E. Kim, J. Noh, S. Seok, Iodide management in formamidinium-lead-halide-based perovskite layers for efficient solar cells, Science 356 (2017) 1376–1379.
[9] L. Meng, J. You, T. Guo, Y. Yang, Recent advances in the inverted planar structure of perovskite solar cells, Acc. Chem. Res. 49 (2016) 155–165.
[10] Z. Bakr, Q. Wali, A. Fakharuddin, L. Schmidt-Mende, T. Brown, R. Jose, Advances in hole transport materials engineering for stable and effcient perovskiet solar, Nano Energy 34 (2017) 271–305.
[11] Z. Zhu, Y. Bai, T. Zhang, Z. Liu, X. Long, Z. Wei, Z. Wang, L. Zhang, J. Wang, F. Yan, S. Yang, High-performance hole-extraction layer of sol–gel-processed NiO nanocrystals for inverted planar perovskite solar cells, Angew. Chem. 126 (2014) 12779–12783.
[12] H. Zhang, J. Cheng, F. Lin, H. He, J. Mao, K. Wong, A. Jen, W. Choy, Pinhole-free and surface-nanostructured NiOx film by room-temperature solution process for high-performance flexible perovskite solar cells with good stability and reproducibility, ACS Nano 10 (2016) 1503–1511.
[13] W. Chen, Y. Wu, J. Liu, C. Qin, X. Yang, A. Islam, Y. Cheng, L. Han, Hybrid interfacial layer leads to solid performance improvement of inverted perovskite solar cells, Energy Environ. Sci. 8 (2015) 629–640.
[14] Y. Bai, H. Chen, S. Xiao, Q. Xue, T. Zhang, Z. Zhu, Q. Li, C. Hu, Y. Yang, Z. Hu, F. Huang, K. Wong, H. Yip, S. Yang, Effects of a molecular monolayer modification of NiO nanocrystal layer surfaces on perovskite crystallization and interface contact toward faster hole extraction and higher photovoltaic performance, Adv. Funct. Mater. 26 (2016) 2950–2958.
[15] W. Chen, Y. Wu, Y. Yue, J. Liu, W. Zhang, X. Yang, H. Chen, E. Bi, I. Ashraful, M. Grätzel, L. Han, Efficient and stable large-area perovskite solar cells with inorganic charge extraction layers, Science 350 (2015) 944–948.
[16] X. Xia, J. Tu, Zhang, X. Wang, W. Zhang, H. Huang, Electrochromic properties of porous NiO thin films prepared by a chemical bath deposition, Sol. Energy Mater. Sol. Cells 92 (2008) 628–633.
[17] S. Han, D. Lee, Y. Chang, S. Ryu, T. Lee, C. Chang, The growth mechanism of nickel oxide thin films by room-temperature chemical bath deposition, J. Electrochem. Soc. 153 (2006) (C382-Ce86).
[18] P. Pmmonik, S. Bhattacharya, A chemical method for the deposition of nickel oxide thin films, J. Electrochem. Soc. 137 (1990) 3869–3870.
[19] M. Warasawa, Y. Watanabe, J. Ishida, Y. Murata, S. Chichibu, M. Sugiyama, Fabrication of visible-light-transparent solar cells using p-type NiO films by low oxygen fraction reactive RF sputtering deposition, Jpn. J. Appl. Phys. 52 (2013) 021102.
[20] J. Jasieniak, M. Califano, S. Watkins, Size-dependent valence and conduction band-edge energies of semiconductor nanocrystals, ACS Nano 5 (2011) 5888–5902.
[21] M. Abulikemu, S. Ould-Chikh, X. Miao, E. Alarousu, B. Murali, G. Ndjawa, J. Barbé, A. El, A. Amassian, S. Del, Optoelectronic and photovoltaic properties of the air-stable organohalide semiconductor $(CH_3NH_3)3Bi_2I_9$, J. Mater. Chem. A 4 (2016) 12504–12515.
[22] M. Biesinger, B. Payne, L. Lau, A. Gerson, R. Smart, X-ray photoelectron spectroscopic chemical state quantification of mixed nickelmetal, oxide and hydroxide systems, Surf. Interface Anal. 41 (2009) 324–332.
[23] H. Tan, A. Jain, O. Voznyy, X. Lan, F. Pelayo, J. Fan, R. Quintero-Bermudez, M. Yuan, B. Zhang, Y. Zhao, F. Fan, P. Li, L. Quan, Y. Zhao, Z. Lu, Z. Yang, S. Hoogland, E. Sargent, Efficient and stable solution-processed planar perovskite solar cells via contact passivation, Science 355 (2017) 722–726.
[24] W. Li, W. Zhang, S. Van Reenen, J. Sutton, J. Fan, A. Haghighirad, M. Johnston, L. Wang, H. Snaith, Enhanced UV-light stability of planar heterojunction perovskite solar cells with caesium bromide interface modification, Energy Environ. Sci. 9 (2016) 490–498.
[25] B. Park, B. Philippe, S. Jain, X. Zhang, T. Edvinsson, H. Rensmo, B. Zietz, G. Boschloo, Chemical engineering of methylammonium lead iodide/bromide perovskites: tuning of opto- electronic properties and photovoltaic performance, J. Mater. Chem. A 3 (2015) 21760–21771.
[26] T. Jacobsson, J. Correa-Baena, E. Halvani Anaraki, B. Philippe, S. Stranks, M. Bouduban, W. Tress, K. Schenk, J. Teuscher, J. Moser, H. Rensmo, A. Hagfeldt, Unreacted PbI2 as a double-edged sword for enhancing the performance of

perovskite solar cells, J. Am. Chem. Soc. 138 (2016) 10331–10343.
[27] J. Lee, S. Park, Y. Lee, H. Kim, D. Shin, J. Jeong, K. Jeong, S. Cho, H. Lee, Y. Yi, Electron transport mechanism of bathocuproine exciton blocking layer in organic photovoltaics, Phys. Chem. Chem. Phys. 18 (2016) 5444–5452.
[28] H. Shen, D. Jacobs, Y. Wu, T. Duong, J. Peng, X. Wen, X. Fu, S. Karuturi, T. White, K. Weber, K. Catchpole, Inverted hysteresis in CH3NH3PbI3 solar cells: role of stoichiometry and band alignment, J. Phys. Chem. Lett. 8 (2017) 2672–2680.
[29] G. Sepalage, S. Meyer, A. Pascoe, A. Scully, U. Bach, Y. Cheng, L. Spiccia, A facile deposition method for CuSCN: exploring the influence of CuSCN on J-V hysteresis in planar perovskite solar cells, Nano Energy 32 (2017) 310–319.
[30] H. Yan, J. Manion, M. Yuan, F. Garcia de Arquer, G. McKeown, S. Beaupre, M. Leclerc, E. Sargent, D. Seferos, Increasing polymer solar cell fill factor by trap-filling with F4-TCNQ at parts per thousand concentration, Adv. Mater. 28 (2016) 6491–6496.

Jingsong Sun received his B.S and M.S degrees in Applied Chemistry from Beijing University of Chemical Technology in 2011 and 2014, respectively. He is currently a PhD student in the Department of Materials Science and Engineering at Monash University. His current research activities are focused on the development of novel charge transport materials for efficient perovskite solar cells.

Jianfeng Lu received his B.S. and PhD from Huazhong University of Science and Technology in 2010 and 2015. From 2015, he works as a post-doc in Monash University, Australia. His research interests include novel organic materials synthesis, development of new strategy for improving the efficiency and stability of perovskite solar cell.

Bin Li is a Ph.D. candidate in Monash University, Australia. He received his B.S. degree in Wuhan Institute of Technology, China. Now he is in Associate Prof. Jacek Jasieniak's group working on perovskite solar cells. Currently, his work focuses on the microstructure control and ions exchange in perovskite films by two-step sequential deposition.

Liangcong Jiang received his B.S degree in Material Engineering from the Monash University in 2014. He is currently taking his PhD degree in Material Science and Engineering from Monash University and will finish at 2018. His research interests in thin film perovskite solar cells.

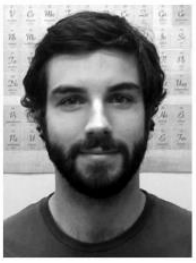

Anthony Chesman is a Senior Research Scientist at the Commonwealth Scientific and Industrial Research Organisation (CSIRO) and is the Team Leader of the Nanomaterials and Devices Team. Anthony is also a Partner Investigator in the Australian Research Council's Centre of Excellence in Exciton Science and is a Technology Fellow Ambassador at the Melbourne Centre for Nanofabrication (MCN). Anthony's research interests focus on the use of nanostructured materials for novel photocatalysts and new electrode structures for perovskite solar cells.

Andrew Scully completed a Ph.D. at the University of Melbourne investigating ultra-fast optical spectroscopy of polymer stabilizers, and subsequently held post-doctoral positions at Kyoto Institute of Technology, University of Melbourne, and Imperial College/Rutherford Appleton Laboratory. He is a Principal Research Scientist at CSIRO where he has led teams developing polymer-based active packaging, biopolymer composites, and optical features for document security. He currently leads CSIRO's research into encapsulation of printed photovoltaic modules, and characterization of their photo-physical and optoelectronic performance.

Thomas Gengenbach is a Senior Research Scientist and the X-ray Photoelectron Spectroscopy (XPS) Specialist in the Biophysics Group of CSIRO Manufacturing (Clayton, Melbourne). His background and main expertise is in the areas of modification and characterization of polymeric surfaces for biomedical applications, aimed at understanding the interactions of biomaterial surfaces with biological media (proteins, cells etc.). Dr. Gengenbach now specialises in using a combination of complementary characterization techniques to elucidate the complex chemical structure of materials surfaces generally.

Yi-Bing Cheng Yi-Bing Cheng is a Thousand Talents professor at Wuhan University of Technology, China and an Adjunct professor in the Faculty of Engineering, Monash University, Australia. He completed his undergraduate (1978) and Master (1983) studies at WuhanUniversity of Technology, China and received a PhD degree from University of Newcastle-upon- Tyne, U.K. in 1989. He was an academic staff at Monash University between October 1991 and March 2018. He specialises in inorganic materials. Perovskite solar cell is his current research interest.

Jacek Jasieniak is an Associate Professor in the Department of Materials Science and Engineering at Monash University. He completed his PhD from the University of Melbourne (2008) and then undertook post-doctoral work at the Commonwealth Scientific and Industrial Research Organisation (CSIRO). In 2011 he moved to the University of California Santa Barbara to study with Prof. Alan Heeger as a Fulbright Fellow. In 2012 he returned to CSIRO, progressing to a Senior Research Scientist and then Group Leader, before moving to Monash in 2015. Jacek is also currently the Director of the Monash Energy Materials and Systems Institute.

Supplemental Information

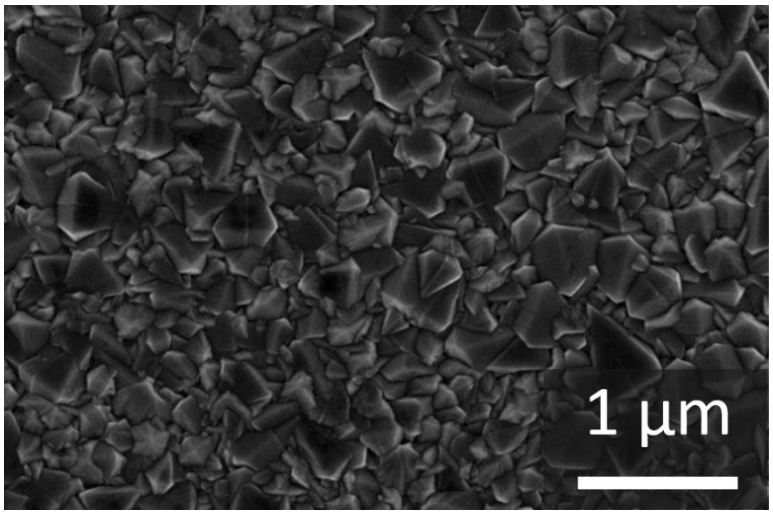

Figure 3S 1 Top-view SEM image of FTO-coated glass.

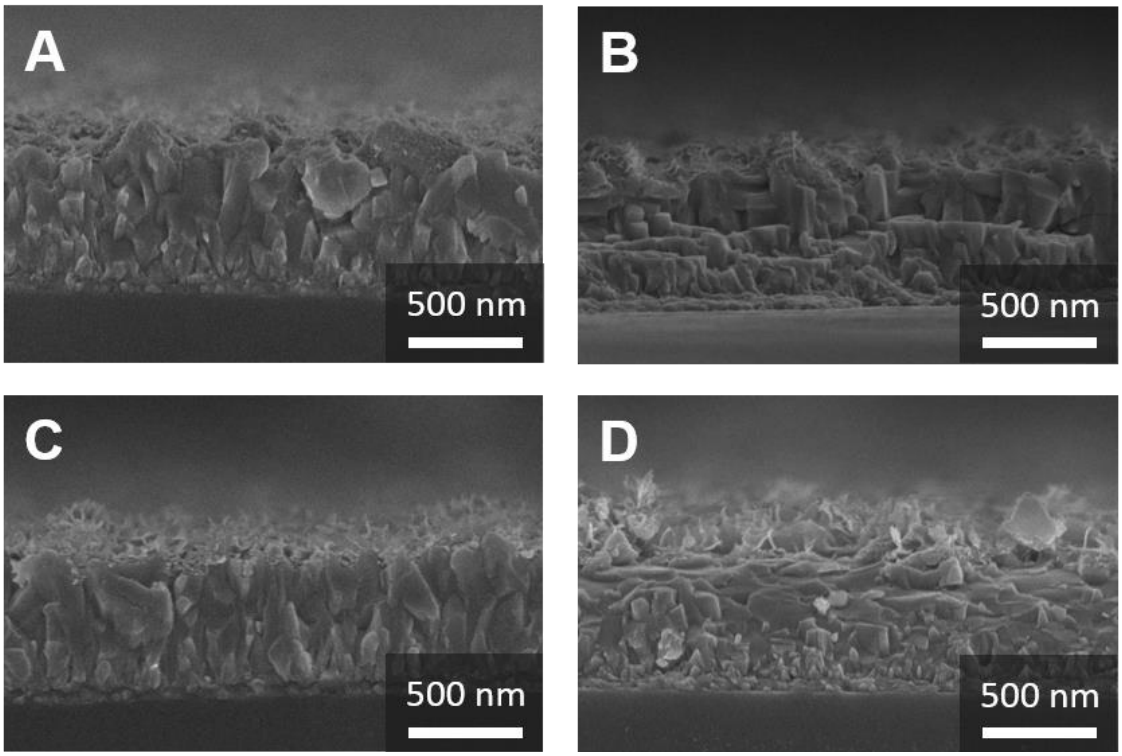

Figure 3S 2 Cross-section SEM images of CBD2, 4, 6 and 8 NiO films on FTO-coated glass, respectively.

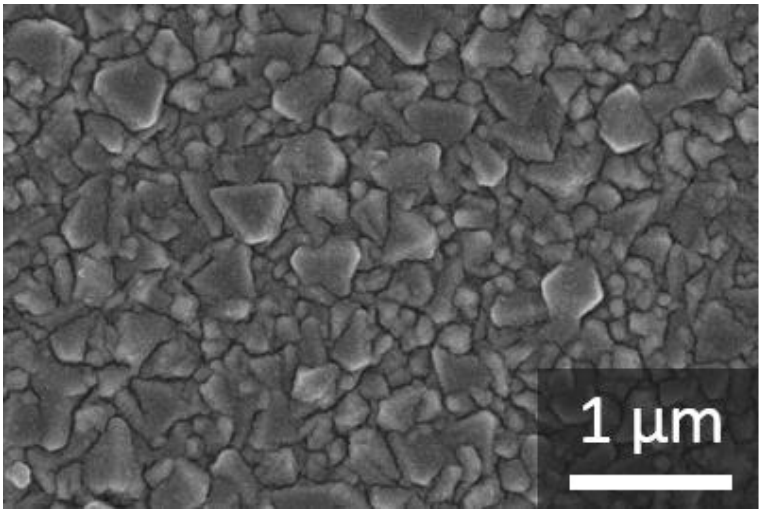

Figure 3S 3 Top-view SEM image of CBD6 NiO film without persulfate salt additive in reaction solution.

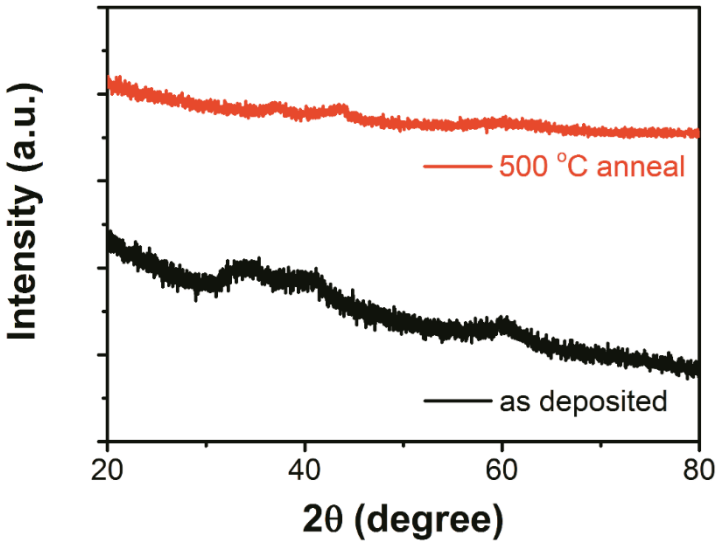

Figure 3S 4 XRD patterns of as-deposited NiO and the annealed products.

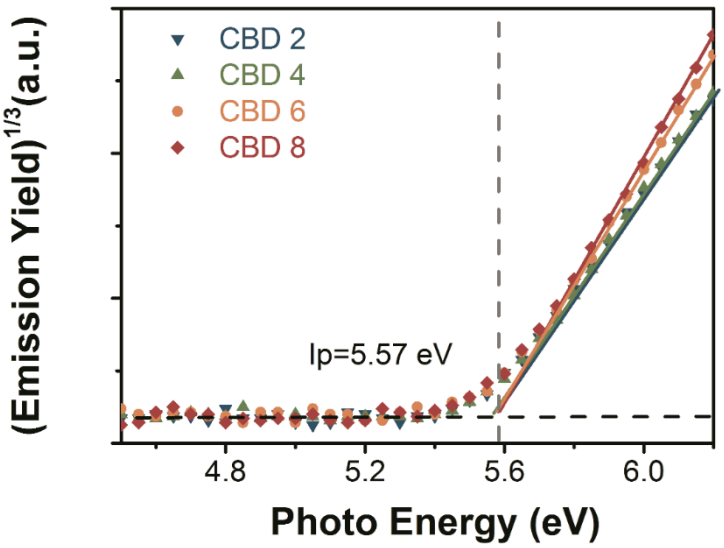

Figure 3S 5 PESA spectra of perovskite film on top of CBD NiO HTLs.

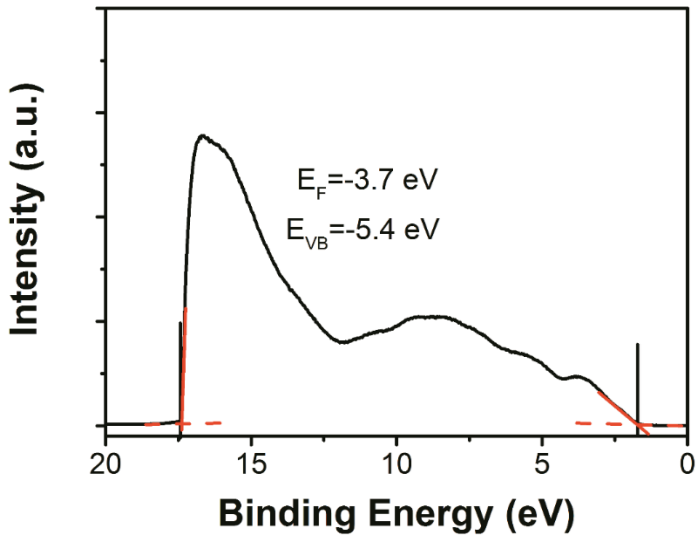

Figure 3S 6 UPS spectrum of a perovskite film on top of a NiO HTL.

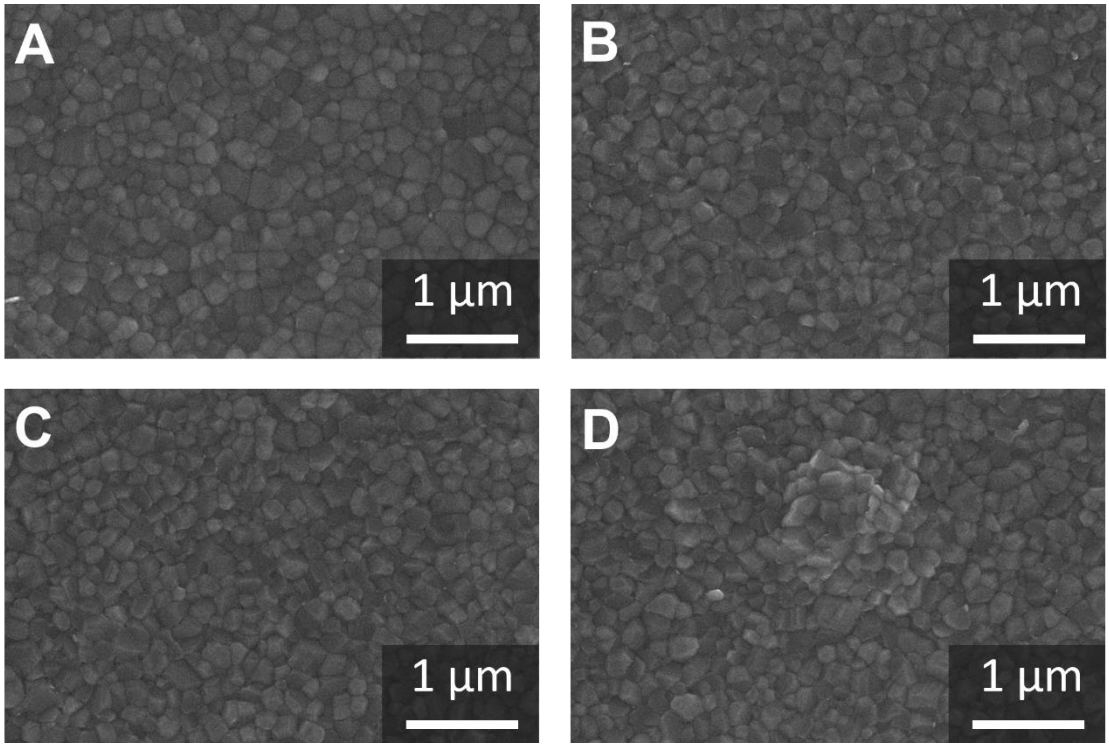

Figure 3S 7 Top view SEM images of perovskite films deposited on top of CBD2, 4, 6 and 8, respectively.

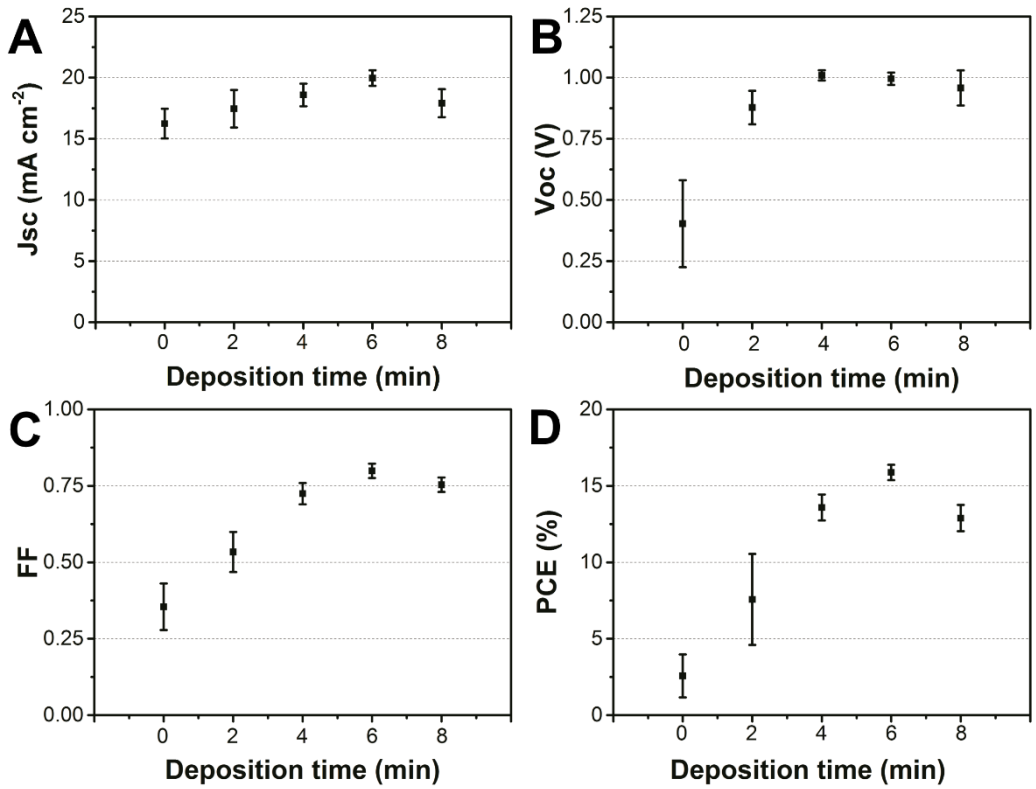

Figure 3S 8 Dependence of photovoltaic parameters of PSC devices with CBD0~8 NiO HTLs.

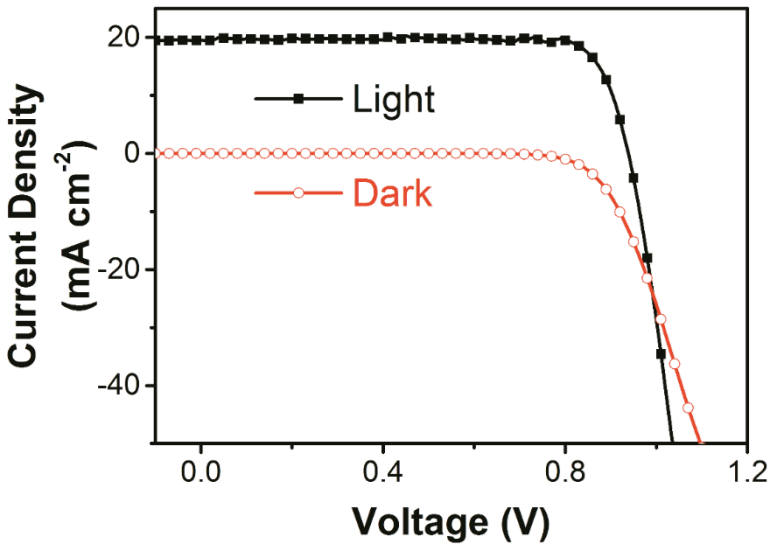

Figure 3S 9 Forward (SC to FB) scan J–V curves of the CBD6 PSC device with a J_{sc} of 19.5 mA cm^{-2}, V_{oc} of 0.94 V and FF of 0.85V.

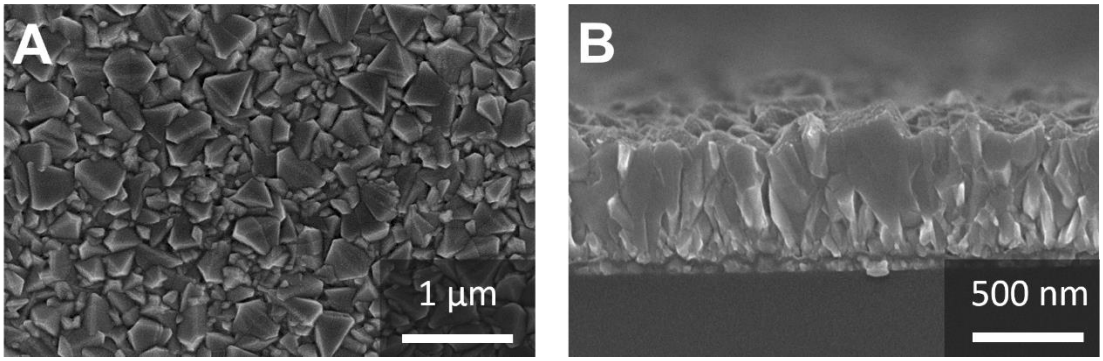

Figure 3S 10 (A) Top view and (B) cross section SEM images of sprayed NiO on top of FTO substrate.

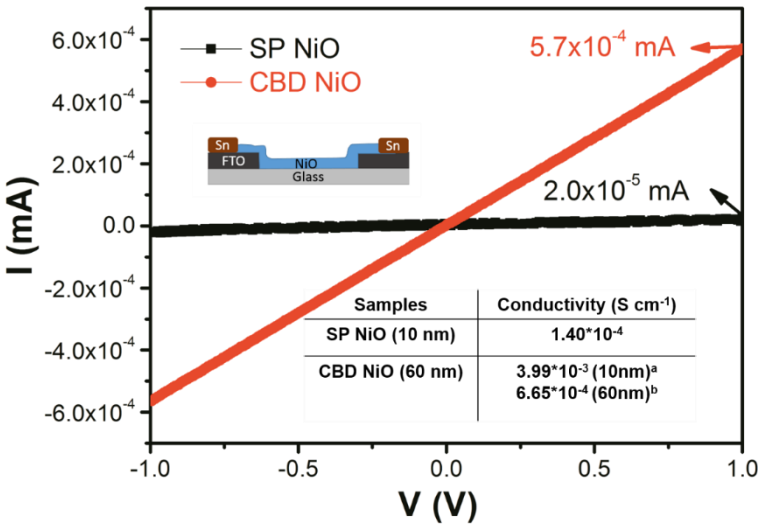

Figure 3S 11 Comparison of the I-V curves of sprayed and CBD NiO films with calculated conductivity inset.

The thickness of the CBD NiO film is hard to define due to the mesoporous structure. Thus, we gave an approximate thickness range of 10 nm [a] to 60 nm [b], which are for the compact layer and the whole layer thicknesses in the CBD NiO film, respectively.

* For this measurement we patterned an insulating gap line (l=70 µm) on the FTO substrate (w=1 cm) with a laser cutter before the deposition of NiO onto the entire substrate, including the gap. We then soldered tin to the FTO on either side of the insulating gap line to provide a low-resistance connection for electrical measurements. To this geometry a voltage from -1 V to 1 V was applied at the electrodes to measure the current. From this current-voltage plot, the conductivity (σ) could be determined through:

$$\sigma = \frac{I \times l}{U \times t \times w}$$

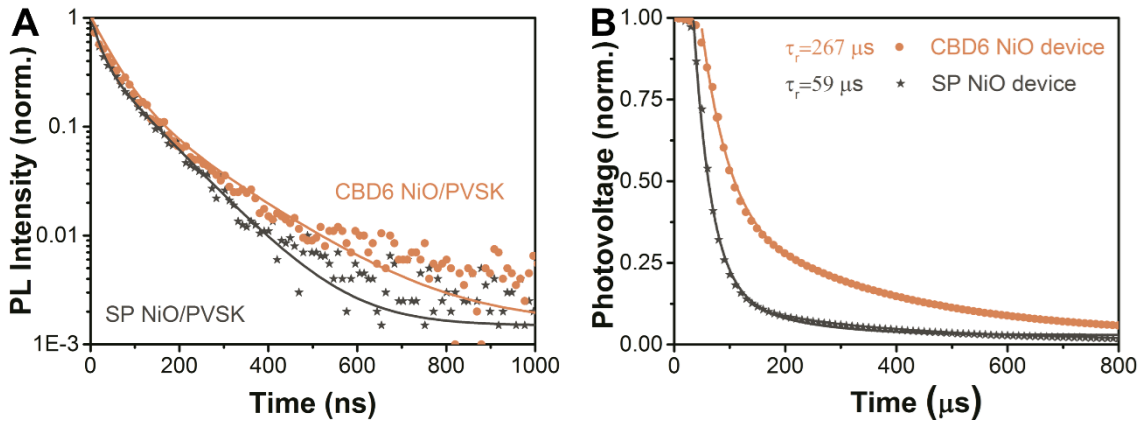

Figure 3S 12 (A) Normalized transient PL decay profiles (logarithmic plot) of perovskite layers on the mesoporous CBD NiO and planar sprayed NiO HTLs. (B) Photovoltage decay of devices with mesoporous CBD NiO and planar sprayed NiO HTLs.

Fittings were performed with the bi-exponential function in Equation (5).

Table 3S.1 Parameters used to fit Equation (5) (main text) to TPRL curves measured for perovskite films with different CBD NiO HTL substrates.

The average lifetime $<\tau>= \sum \alpha_i \tau_i$, where $\alpha_i = A_i\tau_i / \sum A_i\tau_i$

Device	A_1	τ_1(ns)	τ_1(%)	A_2	τ_2(ns)	τ_2(%)	τ_{avg}(ns)
Glass/PVSK	1695	672	76.4	193.3	1820	23.6	943
CBD2/PVSK	1514	4.6	11.2	904	62.7	88.8	56.2
CBD4/PVSK	1856	4.1	14.6	780	56.0	85.4	48.4
CBD6/PVSK	2617	3.1	28.5	493	41.8	71.5	30.8
CBD8/PVSK	4366	1.9	38.9	395	33.0	61.1	20.9

Chapter 4.

Ultrasonic Spray Deposition of TiO_2 Electron Transport Layers for Reproducible and High Efficiency Hybrid Perovskite Solar Cells

Synopsis:

The main drawback of inverted perovskite solar cells is the low PCE compared with conventional counterparts, although the they possess advantages on outstanding stability, negligible hysteresis and easy fabrication way. Nowadays, the rapid development on methodology (e.g. slot die, R2R and spray) and materials (e.g. 2D perovskite and hydrophobic molecule modification) in conventional perovskite solar cells makes them increasingly promising for practical application. Thus, we started to pay attentions on scalable fabricated conventional perovskite solar cells with high performance.

From the viewpoint of the bottom-up fabrication of conventional perovskite solar cells with FTO/ETL/perovskite/HTL/Au architecture, the ETL is the first point to be considered. To date, TiO_2 has been the most commonly used ETL for perovskite solar cells and has been deposited traditionally using an airbrush spray technique. However, this approach yields large distributions of droplet sizes which inherently leads to inhomogeneous nanoscale coatings. To solve this problem, in this article we investigate ultrasonic spray deposition as a facile alternative to the airbrush spray approach. Following detailed structural and electronic characterisation of the deposited layers, we firstly show that ultrasonic deposition results in superior TiO_2 coatings, which consequently enables higher performing devices under optimized conditions that reach 17.4% photoconversion efficiency and, more importantly, yield a 9-fold improvement in terms of device reproducibility. Secondly, through a comparison of diode and solar cell devices, we develop effective benchmarks that predict the effectiveness of the underlying charge transport layer. This enables for the standardisation of the electron transport properties within any batch of solar cells, thus providing a readily accessible pathway towards enhancing reproducibility of fabricated devices.

This paper has been published on Solar Energy (2019, V188, 697-705, 10.1016/j.solener.2019.06.045)

Solar Energy 188 (2019) 697–705

Contents lists available at ScienceDirect

Solar Energy

journal homepage: www.elsevier.com/locate/solener

Ultrasonic spray deposition of TiO_2 electron transport layers for reproducible and high efficiency hybrid perovskite solar cells

Jingsong Sun[a], Alexander R. Pascoe[a], Steffen Meyer[a], Qijie Wu[b], Enrico Della Gaspera[c], Sonia R. Raga[d], Tian Zhang[d], Andrew Nattestad[b], Udo Bach[d], Yi-Bing Cheng[e], Jacek J. Jasieniak[a,*]

[a] ARC Centre of Excellence in Exciton Science, Department of Materials Science and Engineering, Monash University, Clayton, Victoria 3800, Australia
[b] Intelligent Polymer Research Institute (IPRI), Australian Institute for Innovative Materials (AIIM), University of Wollongong, NSW 2522, Australia
[c] School of Science, RMIT University, Melbourne, Victoria 3000, Australia
[d] ARC Centre of Excellence in Exciton Science, Department of Chemical Engineering, Monash University, Clayton, Victoria 3800, Australia
[e] State Key Laboratory of Advanced Technology for Materials Synthesis and Processing, Wuhan University of Technology, Wuhan 430070, China

ARTICLE INFO

Keywords:
TiO_2
Spray-deposition
Electron transport layer
Perovskite
Diode
Solar cell

ABSTRACT

The fabrication of high efficiency perovskite solar cells at larger scales will rely on the optimized deposition conditions of every layer using scalable methodologies. Most current perovskite devices that employ the archetypal TiO_2 hole blocking layer utilise a simple air-brush approach. This approach is not scalable as it results in significant layer inhomogeneity across larger devices areas. To overcome this inherent limitation, in this work we use ultrasonic spray deposition as an alternative approach for the TiO_2 deposition. Focusing on identical reaction chemistries as for air-brush, namely bis(isopropoxide)-bis(acetylacetonate) titanium (IV) based solutions, we find that under optimized conditions smooth TiO_2 layers can be readily deposited over scalable areas on fluorine doped tin oxide. Using these layers at electron transport layers within diodes and perovskite solar cell devices, we develop effective benchmarks that predict the effectiveness of the underlying charge transport layer. This enables for the standardisation of the electron transport properties within any batch of solar cells, thus providing a readily accessible pathway towards enhancing reproducibility of fabricated devices. Under these optimized conditions, methylammonium lead halide photovoltaic devices readily possessing efficiencies of > 16% are achieved. Importantly, the mean batch efficiency of devices fabricated using the ultrasonic spray deposition method is significantly improved and the standard deviation is drastically narrowed. The deposition of an additional *meso*-porous layer is found to lead to further improvements for both of these parameters.

1. Introduction

Hybrid metal halide perovskites have rapidly emerged as a promising material for use in photovoltaics owing to their ease of processing and excellent optoelectronic properties (Correa-Baena et al., 2017a). Leveraging heavily from gradual advances in dye-sensitised, organic and thin-film inorganic solar cell configurations (Snaith, 2013), perovskite solar cell (PSC) efficiencies have improved at an unprecedented rate, increasing from an efficiency of only 3.8% in 2009, as reported by Kojima et al. (Akihiro et al., 2009), to values that already exceed 23% for lab-scale devices (Jeon et al., 2018). This efficiency rivals that of mature solar cells, such as multicrystaline silicon (mc-Si), cadmium telluride (CdTe) and copper-indium-gallium-selenide (CIGS) technologies. While PSC devices are still considered an early-stage technology that is yet to identify a relevant market, one of the chief attributes boasted by PSCs is the solution-based methods commonly used during device fabrication. This attribute affords the potential for mass production, which provides perovskite-based cells with an innate advantage over more established technologies. Nevertheless, PSCs require considerable challenges to be resolved around stability, toxicity and scalability before the technology can be considered as a viable alternative. Important progress has been made to address concerns of device stability (Niu et al., 2015) and toxicity (Espinosa et al., 2015), which are prolific fields in their own right. Here, we focus on addressing a key processing challenge that impacts reproducibility and scalability of PSCs – the deposition of a high quality electron transport layer.

Electron and hole transport layers in PSCs are fundamental towards achieving high efficiency devices as they selectively block holes and

* Corresponding author.
E-mail address: Jacek.Jasieniak@monash.edu (J.J. Jasieniak).

https://doi.org/10.1016/j.solener.2019.06.045
Received 17 April 2019; Received in revised form 13 June 2019; Accepted 19 June 2019
Available online 27 June 2019

electrons, respectively, to reduce interfacial recombination at the electrode interfaces. This has been demonstrated for all high efficiency planar (Docampo et al., 2013; Liu et al., 2013), *meso*-porous (Ball et al., 2013; Kim et al., 2012; Lee et al., 2012) and sensitized (Chung et al., 2012) PSC architectures. Within their "normal superstrate" device configuration, that being where the electron transporting layer (ETL) is deposited on the transparent conductive electrode and the hole transporting layer (HTL) is deposited on the perovskite, almost ubiquitously TiO_2 has been used as the ETL and doped Spiro-OMeTAD (2,2′,7,7′-tetrakis(*N,N*-di-*p*-meth-oxyphenylamine)-9,9-spirobifluorene) as the HTL. Both of these layers have origins in dye-sensitized solar cells (DSSCs) (Bach et al., 1998). The selection of the Spiro-OMeTAD is largely based on its ease of deposition through a low-temperature solution-coating process. Meanwhile, TiO_2 remains the archetypal material owing to its high chemical stability, high optical bandgap of 3.2 eV and appropriate conduction band energy of −4.2 eV vs. vacuum for minimizing voltage losses.

TiO_2 deposition has been demonstrated using spin coating (Ball et al., 2013; Moehl et al., 2014), atomic-layer deposition (Chandiran et al., 2014; Hu et al., 2016), spray pyrolysis (Kavan and Grätzel, 1995; Lee et al., 2012; Supasai et al., 2016), electrodeposition (Kavan et al., 1993; Kim et al., 2015), sputtering (Braga et al., 2013) and thermal oxidation (Ke et al., 2014; Xia et al., 2006). Of these, spray deposition is the most commonly employed approach owing to its simplicity. It involves the deposition of a suitable titanium complex, such as titanium (IV) bis(isopropoxide)-bis (acetylacetonate) ($Ti(acac)_2OiPr_2$) dissolved in isopropanol, onto a heated substrate at ~500 °C, which induces its thermal decomposition to form TiO_2 (Acik et al., 2009). This processing temperature also facilitates crystallization of the TiO_2 into the anatase phase, which provides reduced structural defects and improved electron mobilities compared to its low-temperature processed amorphous state (Conde-Gallardo et al., 2005; Wöbkenberg et al., 2010). The structural, optical and electronic properties of the sprayed TiO_2 films are sensitive to experimental variables, such as the deposition precursor concentration, temperature, deposition rate, spray distance and pattern, and gas pressure (Tachibana et al., 2008).

Conventionally, the spray deposition of TiO_2 for use as a blocking layer in solar cells has been carried out using an airbrush spray technique (Nguyen-Phan et al., 2010). This form of "pressurized" spray, relies on a high pressure carrier gas to atomise a liquid flowing through a nozzle. The particle diameters emerging from these systems and their size distribution are related to the nozzle geometry, the physical properties of the liquid, its flow rate, the air pressure and distance between the nozzle and the substrate that is being coated (Arthur and McDonell, 2017). Typical median droplet sizes of > 50 μm are common, albeit with very broad droplet size distributions due to the inherent atomization process. Importantly, the droplets are carried to the substrate within the gas stream at pressures of 100′s kPa, which causes them to have very high impact velocities with the substrate (10–100′s m/s). Practically, this is beneficial from the point of view of reducing evaporation rates of volatile droplets during the deposition process, particularly when depositing on heated substrates. However, the large distribution in droplet size can make coatings inhomogeneous and the high pressures cause significant overspray, which necessitates high efficiency exhaust systems and increases material waste.

For these reasons, ultrasonic spray deposition systems have started to be harnessed in many applications that require homogeneous thin film coatings, such as protective coatings for steel (Mark and Henry, 1999), transparent electrodes (Bian et al., 2004), and even perovskite solar cells (Tait et al., 2016). Zhou et al. recently used this approach to deposit TiO_2 nanoparticle films at temperatures of < 150 °C and showed that these could serve as ETLs for perovskite solar cells (Zhou et al., 2017). While offering low temperature processing, the use of nanoparticle dispersions did lead to shunting problems, likely due to pin hole formation, resulting in low device performance. This demonstrates that a more robust approach to TiO_2 ETL still likely involves pyrolysis of molecular precursors, such as $Ti(acac)_2OiPr_2$.

Ultrasonic nozzles use a tip vibrating at a frequency f to nebulize a liquid stream into a mist of droplets. The median droplet size in this case is proportional to $f^{-2/3}$, which for typical frequencies of 20–100 kHz gives median droplets of size ~20–100 μm (Lang, 1962). Importantly, these droplets have a narrower size distribution and 10–100 times lower impact velocities as compared to the airbrush spray approach. The lower size distributions can enable more homogeneous coatings to be prepared, which is a very lucrative aspect for the use of ultrasonic systems in thin film coatings, particularly for use as charge transport layers (CTLs) in solar cells. However, for higher temperature depositions, the lower impact velocities may be detrimental towards achieving a homogenous coating compared to the airbrush deposition approach (Filipovic et al., 2014).

In this work, we compare the commonly used airbrush to ultrasonic spray method for the deposition of TiO_2 coating from pyrolsed Ti $(acac)_2OiPr_2$ precursor. These coatings are assessed as ETLs within diode and methyl ammonium lead iodide ($MAPbI_3$) PSCs. It is found that ultrasonic deposition of ETLs provides superior device performance and a signficant improvement in device reproducibility, albeit only under high-pressure deposition conditions.

2. Materials and experimental details

2.1. TiO_2 blocking layer deposition and characterization

Unless otherwise stated, all materials were purchased from either Sigma-Aldrich or Alfa Aesar, and used as received. The home-built spray system comprised a Sono-Tek 120 kHz Accumist ultrasonic spray shaping nozzle mounted to a 3-axis gantry robot, a Sonotek Selectaspray cabinet with a generator sequence controller, and a syringe pump liquid delivery system. Fluorine doped tine oxide (FTO)/glass substrates were cleaned using a three stage sonication process in hellmanex, water and ethanol. The dense TiO_2 blocking layer was formed by the spray pyrolysis of a $Ti(acac)_2OiPr_2$ solution at 500 °C. This solution was formed by diluting $Ti(acac)_2OiPr_2$ in isopropanol (1:19 vol). The sprayed samples were annealing for 10 mins at 500 °C in air after the completion of the spray cycle, before being cooled down to room temperature. For the mesoporous devices, an 18 nm TiO_2 nanoparticle paste (JGC-C&C) was diluted in ethanol (1:8 vol) prior to spin-coating on the dense TiO_2 blocking layer at 8000 rpm for 40 s in air and then annealed at 500 °C for 30 mins.

UV–vis spectroscopy was performed using a PerkinElmer Lambda 950 UV/VIS/NIR spectrophometer. Ellipsometric measurements were carried out on J.A. Woollam M-2000DI Spectroscopic ellipsometer with TiO_2 samples being deposited on polished silicon wafers with a natural oxide layer. Atomic Force Microscopy (AFM) measurements were performed on a Dimension Icon (Veeco).

2.2. Diode fabrication and characterization

Spiro-OMeTAD (2,2′,7,7′-tetrakis(*N,N*-di-*p*-meth-oxyphenylamine)-9,9-spirobifluorene) was purchased from Luminescence Technology Corp. The spiro-OMeTAD solution was formed by mixing 40 mg of spiro-OMeTAD in 500 μL of chlorobenzene, with 7.5 μL lithium bis (trifluoromethylsulphonyl)imide in acetonitrile (500 mg mL^{-1}) and 16.88 μL 4-*tert*-butylpyridine as additives. This spiro-OMeTAD solution was spin-coated on the dense TiO_2 blocking layer at 3000 rpm for 30 s. An 80 nm gold layer was then evaporated onto the devices. The current-voltage response of the diodes were measured with a continuously increased voltage from 0 to 1.5 V in the dark using a Zahner Zennium electrochemical workstation (ECW IM6).

2.3. Solar cell fabrication and characterization

Fabrication of solar cell devices was carried out in a N_2 filled glovebox. The perovskite precursor solution was formed by mixing

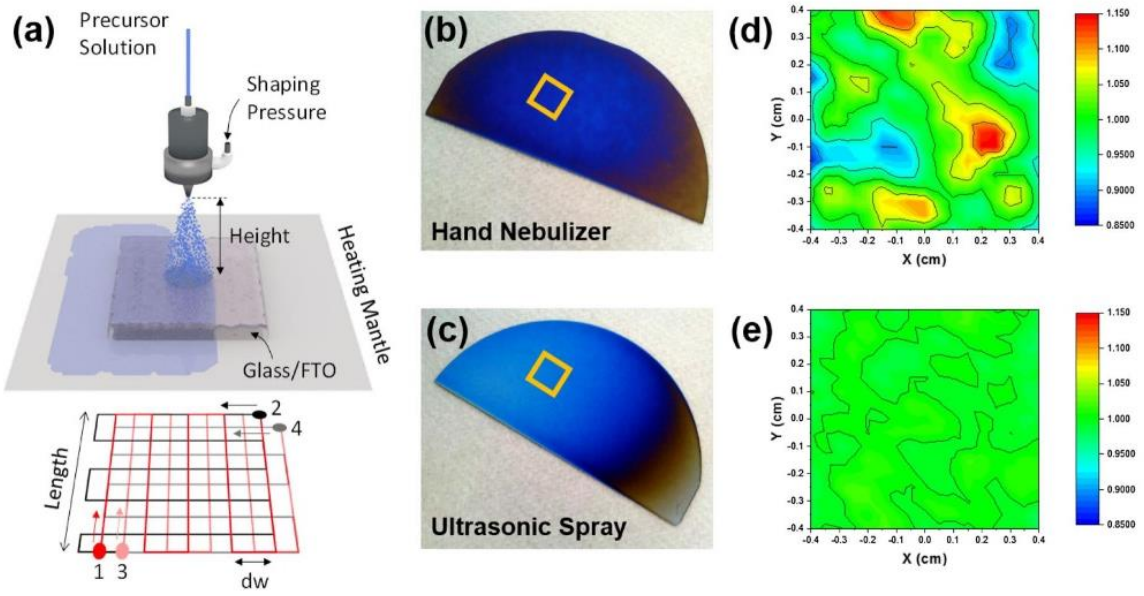

Fig. 1. Schematic diagram of the ultrasonic spray deposition approach used in this work (a). Digital photographs and relative thickness maps derived from spectroscopic ellipsometry of marked areas in the micrographs of TiO_2 sprayed on silicon wafers by a conventional hand nebulizer (b and d) and through ultrasonic spray deposition (c and e).

stoichiometric amounts of CH_3NH_3I and PbI_2 in a combination of dimethyl sulfoxide (DMSO) and *N*-methyl-2-pyrrolidone (NMP) (7:3 vol) to form a (46 wt%) concentration solution. 30 µL of the perovskite precursor solution was applied to the surface of the substrate prior to spin-coating. The films were spin-coated using a two-stage process: 1000 rpm for 5 s using an acceleration of 200 rpm/s, then 6000 rpm for 50 s using an acceleration of 6000 rpm/s. A nitrogen gas flow was introduced after 20 s of the second spin-coating step and sustained for a further 20 s. The perovskite films were then annealed on a hot-plate at 100 °C for a duration of 10 mins. A spiro-OMeTAD solution was spin-coated on the perovskite film at 3000 rpm for 30 s, the same as that deposited on the diode devices. An 80 nm gold layer was then evaporated onto the devices. Current-voltage characterization was performed using a solar simulator (Oriel) fitted with a filtered 1000 W xenon lamp to replicate AM1.5, 1 kW/m^2 conditions. The illumination of the light source was calibrated using a silicon reference cell (Peccell Technologies) with a color filter to minimize the spectral mismatch between the calibration diode and the perovskite solar cell. The J-V response was recorded using a Keithley 2400 source meter. The solar cells were masked with a non-reflective aperture of 0.16 cm^2 that defined the active area of the device. Impedance spectroscopy measurements were performed under 1 sun illumination using a white LED powered by a PP210 potentiostat. A Zahner Zennium electrochemical workstation ECW IM6 was used as a frequency response analyzer.

3. Results and discussion

With the goal of developing a high-quality and reproducible TiO_2 ETL for perovskite solar cells, we have assessed the conventionally used $Ti(acac)_2OiPr_2$: isopropanol solution as a drop-in replacement within an ultrasonic spray deposition system to coat 10 × 10 cm^2 FTO/glass substrates with TiO_2 at 500 °C. To achieve this we have carried out variable deposition cycles within the spray pattern defined in Fig. 1a, with a single spray cycle being defined as the completed deposition across all four offset spray trajectories (labelled in Fig. 1a as 1–4). The optimized conditions at a flow rate of 0.5 mL/minute with a nozzle velocity of 100 mm/s were found to be: length = 12 cm, line spacing (dW) = 1.5 cm, height = 13.5 cm, and nozzle power = 1.5 W. The shaping pressure was controlled between 10 and 200 kPa, with the later being preferred for this particular spray nozzle (*vide infra*). The ultrasonic sprayed TiO_2 film is highly crystalline anatase, as confirmed by glancing angle XRD pattern in Fig. S1.

Fig. 1b and c show the digital photographs of TiO_2 films sprayed on a silicon wafer using a typical hand nebuliser at ~ 350 kPa and our ultrasonic spray system at a shaping pressure of ~ 200 kPa, respectively. For both samples, the spray nozzle was fixed at 13.5 cm above the substrates and 6 mL of spray precursor solution was used to do the coating under static deposition conditions. Noteworthy, the edge inhomogeneities are eliminated in the actual samples used for solar cells by moving the spray head in our outlined pattern and spraying beyond the boundaries of the substrate. Ellipsometric mapping of these samples, as measured over 0.4 × 0.4 cm^2 areas, are shown in Fig. 1d and e, respectively. It is evident from both the optical images and ellipsometric mapping that the ultrasonic process facilitates TiO_2 film deposition of an enhanced homogeneity, particularly at the mm scale. Analysing the ellipsometric maps more closely shows that the TiO_2 deposited by the hand nebulizer results in a mean thickness deviation of up to ± 15%, while for the ultrasonic process it was < ± 5%. This is clear evidence of the superior coating properties offered by the ultrasonic deposition process, and is directly related to the improved droplet distribution.

In addition to homogeneity, the thickness of the TiO_2 needs to be precisely controlled to ensure optimised charge blocking layer characteristics. For simplicity, from hereon we define the TiO_2 layers deposited on the original FTO coated glass at different cycles as T_x, where x denotes the number of TiO_2 deposition cycles. The thickness (t) of these layers was measured by depositing reference samples on a silicon wafer substrate with a native oxide layer and then using spectroscopic ellipsometry (Fig. S2). This approach was chosen because attempts to measure the thickness directly on FTO glass through SEM was deemed inconclusive due to a low contrast between the FTO and TiO_2 layers (Fig. S3). From these measurements the functional correlation between T_x and t under the above deposition conditions was determined to be t (nm) = 5.9 T_x.

The effectiveness of TiO_2 as a blocking layer depends on its hole blocking, electron collection and shunting properties. To analyse the effectiveness of these processes, Au/Spiro-OMeTAD/TiO_2/FTO diodes were fabricated using different thicknesses of ultrasonically sprayed TiO_2. The corresponding J–V curves of these diodes are shown in Fig. 2a. For completeness we have also included the J-V curve of Au/

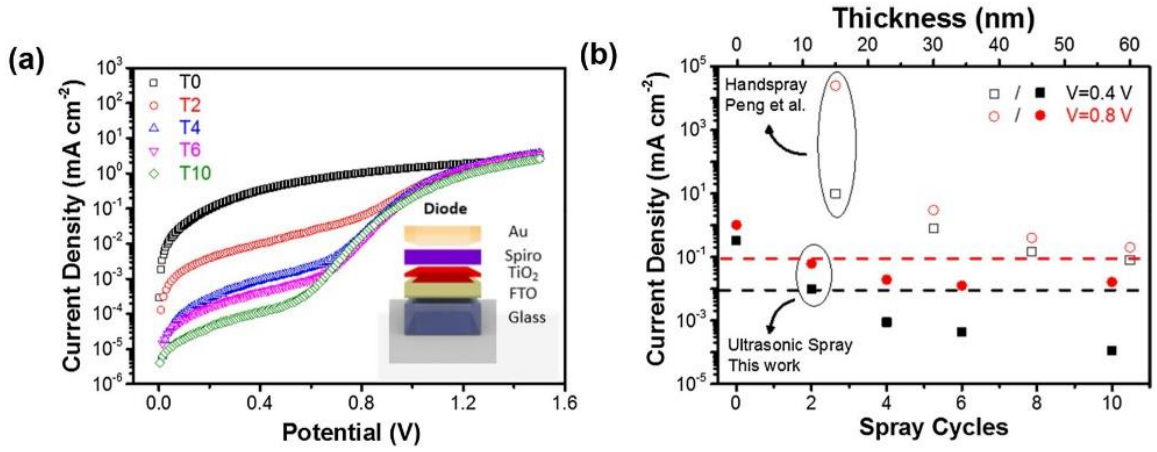

Fig. 2. J-V curves of TiO_2 layers for increased spraying cycles of FTO/TiO_2/Spiro-OMeTED/Au diodes (a) and specific current values at selected voltages of 0.4 and 0.8 V (b). The dashed lines at 0.1 and 0.01 mA cm^{-2} represent the minimum proposed current density requirements at 0.4 and 0.8 V, respectively, for this diode to exhibit sufficient blocking characteristics to be suitable in solar cells, as identified by Peng et al. (2004) .

Spiro-OMeTAD/FTO structure, even though this is not a diode. Consistent with the standard Schockley one-diode formalism, three regimes can be clearly identified: (i) at low voltages ($< \sim 0.3$ V) the devices exhibit Ohmic behavior due to residual shunting, (ii) at intermediate voltages a clear turn-on behavior is seen, which is characteristics of the junction ideality factor, temperature and saturation current, and (iii) at higher voltages the current saturates to series resistance limits. The extracted parameters from fits of the diodes to the Schockley diode formalism are included in Table 1. The ideality factors show a slight variation across the samples, with a general trend of being at ~ 3. This suggests that for all the diodes the carrier recombination is likely to be interface or deep-level defect limited (Kang et al., 2008; Narushima et al., 2003). These trends cannot be reliably compared to solar cells because the interfaces and dominant charge transport mechanisms in such devices are entirely different compared to these diodes. We note that the series resistances extracted here are evidently limited by the electrodes and the rectifying junction, and not reflective of the TiO_2 layers, which should have seen progressive increase with increasing T_x.

Table 1
Fitted devices parameters of TiO_2/Spiro-OMeTAD diodes using a Schokley model.

T_x	R_s (Ω cm^2)	R_{sh} (kΩ cm^2)	J_0 (mA cm^{-2})	n
2	7.97	4	1.22×10^{-5}	3.68
4	8.47	43	1.04×10^{-9}	2.58
6	7.81	115	1.11×10^{-9}	2.72
10	10.67	667	2.86×10^{-9}	2.94

A comparison between the shunt resistances provides the most direct measure of the TiO_2 homogeneity and effectiveness as a charge blocking interface, although it is hard to determine what an appropriate value should be without a qualitative comparison to a complete solar cell. Such a qualitative comparison has been made by Peng and co-workers for dye-sensitised solar cells by simply considering the currents at 0.4 V and 0.8 V for identical diodes made here, but using hand-spray approach for the TiO_2. Those values are plotted in Fig. 2b, with the authors finding a current density of 0.01 mA cm^{-2} (0.1 mA cm^{-2}) at 0.4 V (0.8 V) being sufficiently low to yield good blocking properties. We include the equivalent current densities from our diodes for comparison in this figure. It can be observed that the required current densities are achieved at T_2, which is equivalent to only 12 nm. This represents a TiO_2 film that is 80% thinner than those reported by Peng and co-workers, indicating a higher quality deposition process using the ultrasonic method. Further inspection of the diodes fits indicates that a progressive reduction in J_0 parameter is observed with increasing T_x. This should yield a greater turn-on voltage and, subsequently, higher open circuit voltages in functional solar cells.

To validate these charge blocking properties, planar $MAPbI_3$ PSCs were fabricated using the TiO_2 films as ETLs (Fig. 3a). The resulting photovoltaic parameters are summarized in Fig. 3b. These show

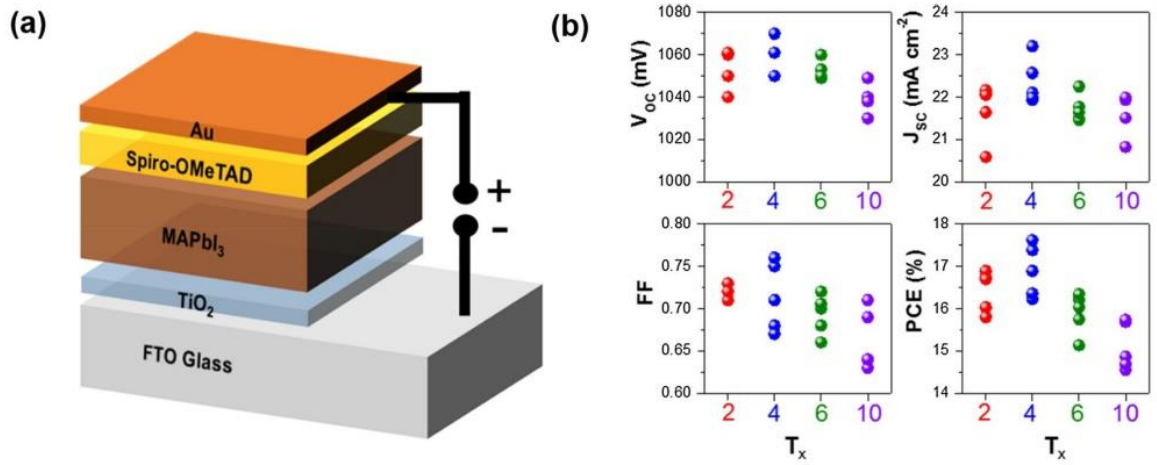

Fig. 3. Schematic of the perovskite solar cells used in this work (a) and a summary of the their parameters from devices fabricated using progressively increased TiO_2 layers (b).

comparable median open circuit voltages (V_{oc}) of ~ 1050 mV and fill factors (FFs) of ~ 0.72 across all T_x. This expected trend arises due to the similar interface chemistry between the TiO_2 ETLs and perovskite layers. Of all the parameters, the short-circuit current density (J_{sc}) shows the largest deviation with a peak value at T_4 of 23.2 mA cm^{-2}. A progressive reduction is observed at higher T_x and at T_2. This trend can be partly understood from the diode measurements, which show that T_4 has a 20-fold greater shunt resistance than T_2. Within the device, for the T_2 sample with a 12-nm TiO_2 film, a low R_{sh} would result in a higher hole surface recombination at the FTO, yielding the lower photocurrent. Meanwhile, at the higher T_x, an enhancement of the electron recombination is expected due to an accumulation of electrons at the interface within the perovskite arising from the poor electron transport properties of TiO_2 (Peng et al., 2004). These factors result in the PSCs with T_4, which have a mean TiO_2 thickness of ~ 24 nm, posssessing the most optimal hole blocking and electron transport properties, thus yielding the highest PCEs. Notably, this correlation allows us to identify that a shunt resistance of ~ 75 kΩ cm^2 for a FTO/TiO_2/Spiro-OMeTAD/Au diode provides a good benchmark for achieving good blocking layer properties in functional solar cells.

To further investigate the performance variation of these devices, electrochemical impedance spectroscopy (EIS) measurements were conducted under illumination. Fig. 4a shows the Nyquist plots for the perovskite device with T_x ETLs at 0.8 V bias under the 1 sun illumination. The equivalent circuit used for fitting the EIS data is shown in Fig. 4b. It consists of a recombination resistance (R_{Rec}) component, a constant phase element (CPE) element and a series resistance (R_s) contribution. We find that the series resistances of T_2 to T_6 devices are comparable at ~ 1.9 Ω cm^2, but that the T_{10} device shows an increased series resistance of 2.8 Ω cm^2 (see Fig. 4a (inset)) This confirms that the TiO_2 layer is indeed having an impact on the total series resistance, but it is signficant only at the larger thicknesses. In Fig. 4b we show the R_{Rec} versus applied voltage. The recombination resistance shows an increase from T_2 to T_4 devices and then subsequently drops for the T_{10} device. As higher R_{Rec} correlates to reduced carrier recombination within a device (Correa-Baena et al., 2017b), the above results confirm that the T_4 devices provide a TiO_2-perovskite interface with the most favourable charge extraction characteristics as well as optimum blocking of the FTO recombination pathways. We summarize the above findings through a schematic of the proposed carrier extraction and recombination mechanisms at the TiO_2-perovskite for different T_x in Fig. 4c.

Noting that PSC exhibit the hysteresis, in Fig. 5a we show typical forward and reverse J-V curves of planar PSC using T_4. The reverse scan shows a PCE of 17.5%, with V_{oc} = 1048 mV, J_{sc} = 23.2 mA cm^{-2} and FF = 0.72, while the forward scan shows a decrease in FF to 0.55, which leads to a lower PCE of 13.1%. The steady-state output of this PSC was measured using a voltage of 850 mV at maximum power output for 300 s, where the efficiency stabilized to ~ 16.3%, as shown in Fig. 5b.

The above PSCs were fabricated using TiO_2 at a nozzle shaping higher pressure of 200 kPa; however, as we now show, this high gas pressure is a very important factor for achieving such high efficiency PSCs. In Fig. 6a and b, digital images of T_4 sprayed TiO_2 on silicon wafer are shown for 10 kPa and 200 kPa shaping pressures, respectively. Close inspection of these images demonstrate that the higher pressure facilitates a slightly more macroscopically homogeneous TiO_2 film. This is further validated through spectroscopic ellipsometry

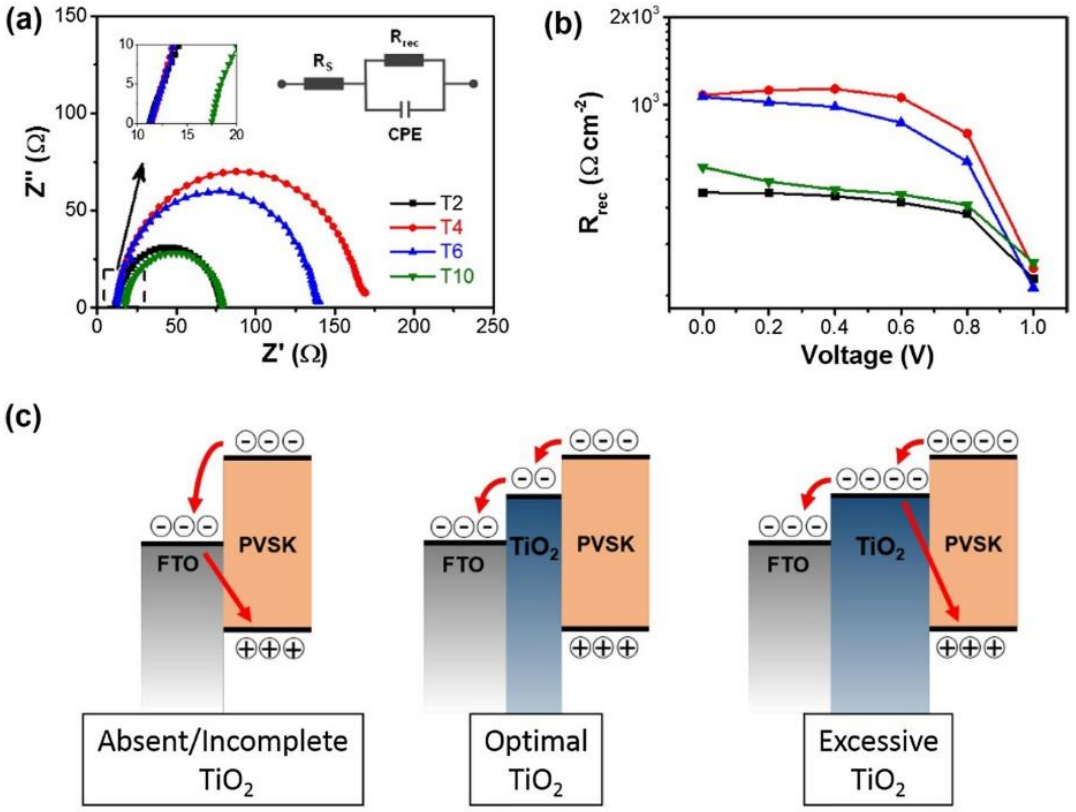

Fig. 4. Nyquist plot of perovskite devices with T_x ETL at a bias of 0.8 V under 1 sun illumination showing the equivalent circuit model within the inset (a). The extracted recombination resistance (R_{rec}) from the equivalent circuit model as a function of the applied voltage at 1 sun illumination (b). Schematic of the proposed carrier extraction and recombination mechanisms at different TiO_2-perovskite interfaces (c).

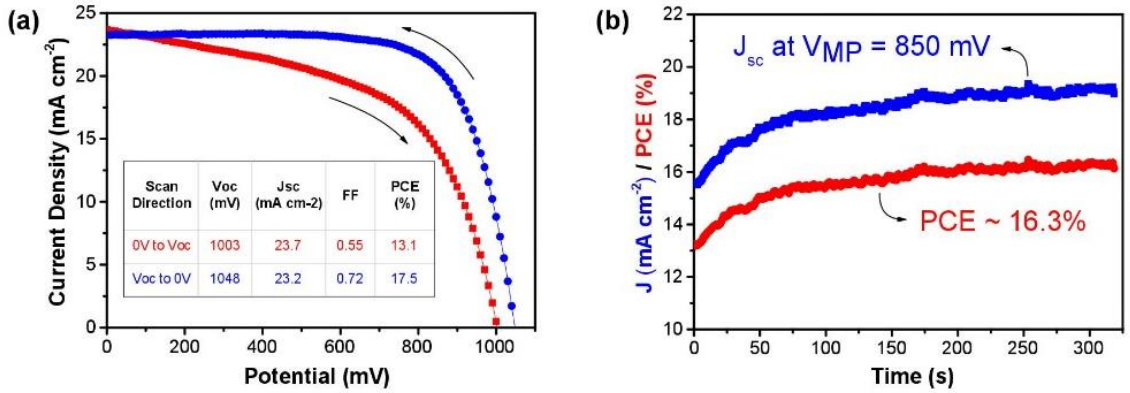

Fig. 5. J-V curves under forward and reverse scan (a) and steady state output curves (b) of perovskite solar cells fabricated using 4 TiO_2 deposition cycles (T_4).

thickness mapping, which shows slightly larger features on the surface of the 10 kPa sample (Fig. 6c) and an overall standard deviation in thickness of 0.7 nm compared to only 0.4 nm for the 200 kPa (Fig. 6d). More prominent structural variations are observed at the microscopic level across these samples, with atomic force microscopy (AFM) topographic images shown in Fig. 6c and d for the 10 kPa and 200 kPa samples, respectively. It is evident that the surface of the 10 kPa sample possesses significant nanoscale perturbations compared to the 200 kPa

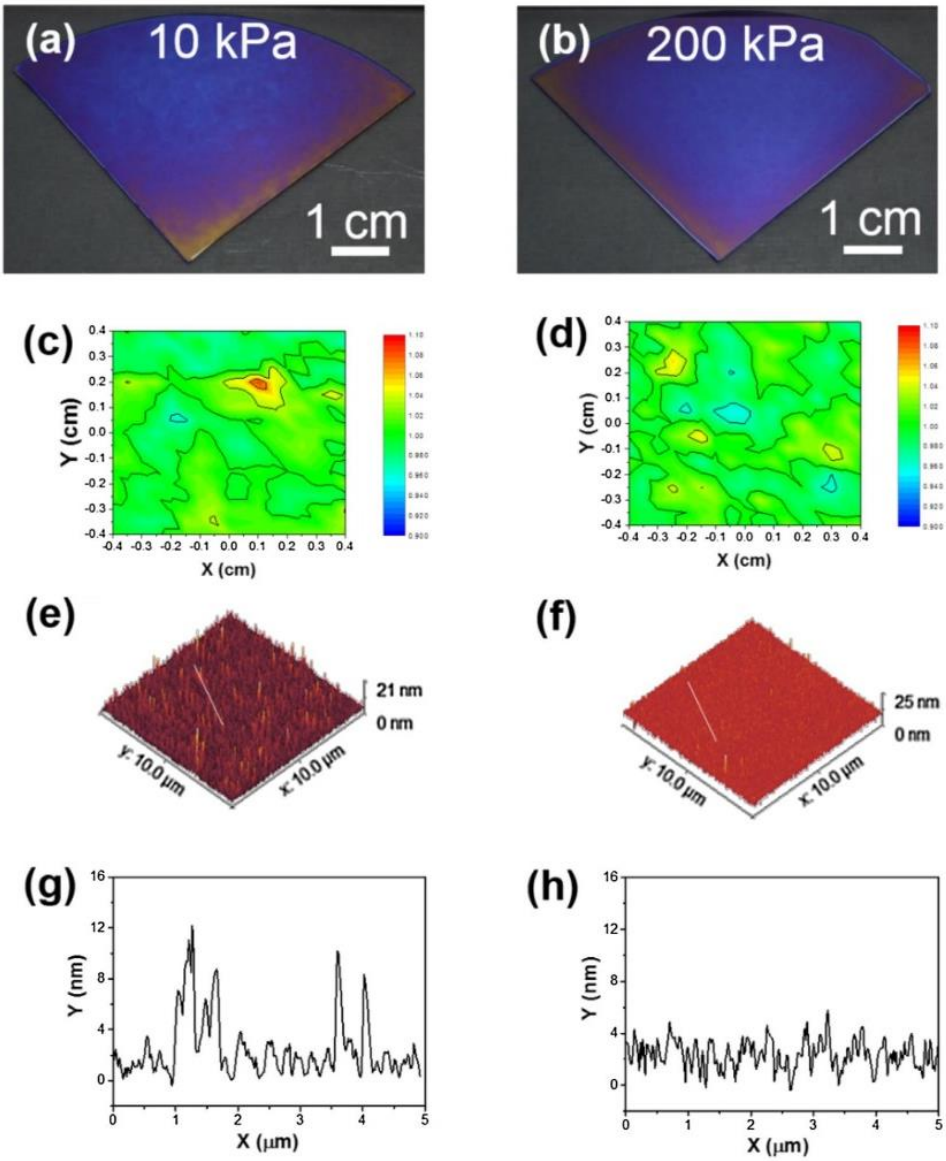

Fig. 6. Digital photographs (a and b), spectroscopic ellipsometer thickness maps relative to the median thickness (c and d),3-dimensional (e and f) and line (g and h) AFM profiles of ultrasonic spray-deposited TiO_2 films on silicon wafers with a 10 kPa (left) and 200 kPa (right) shaping gas pressure, respectively.

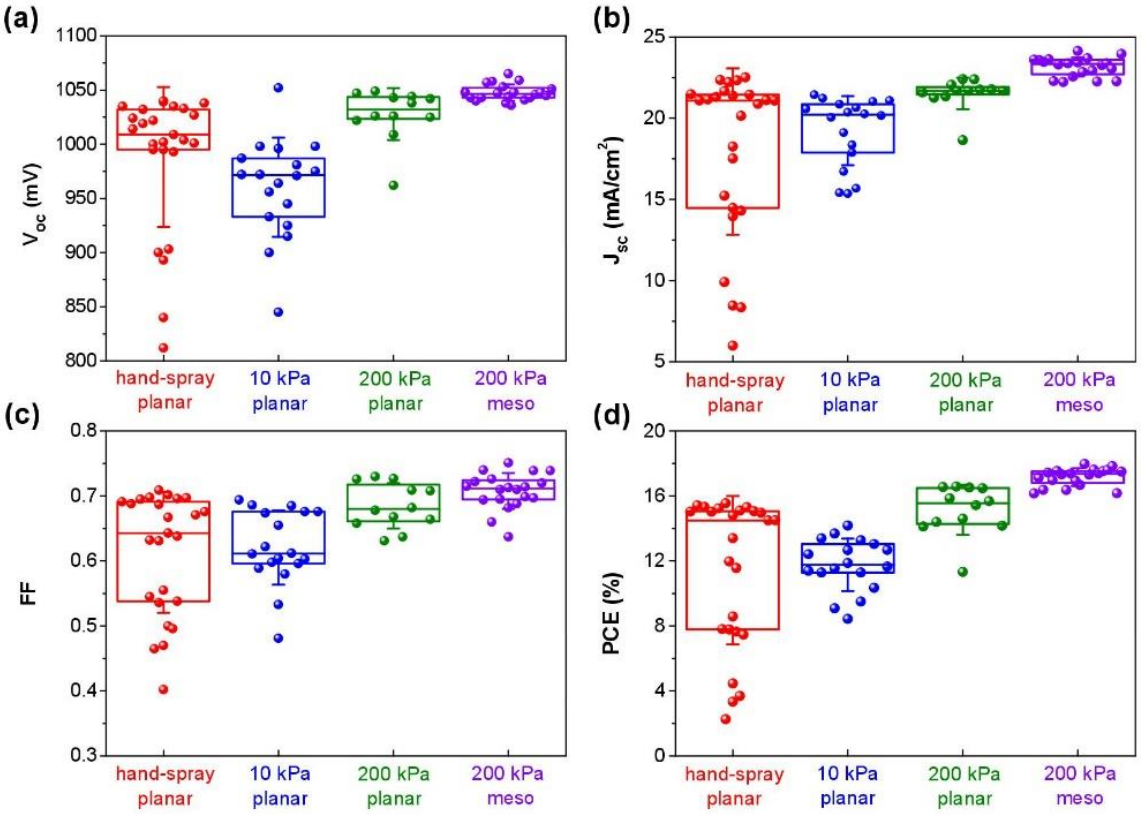

Fig. 7. Summary of the perovskite solar cell V_{oc}, J_{sc}, FF and PCE (represented in a, b, c and d, respectively) using TiO_2 made by hand-spray, ultrasonic spray with low pressure shaping gas, ultrasonic spray with high pressure shaping gas with and without a mesoporous TiO_2 layer.

sample (Fig. 6g and h), which indicates that the mean velocity of droplets (as dictated by the pressure of the nozzle) dictates a variation in the surface structure.

Evidently, the low pressure deposition conditions cause larger TiO_2 coating variations compared to the higher pressure deposition both at the macro and micro levels. This observation is likely to arise directly from the lower droplet and impact velocities, which are critical parameters for depositing volatile droplets onto high-temperature substrates. If the droplets being deposited pre-maturely evaporate to a point where decomposition is occurring during the droplet flight and/or they do not coalescence on the substrate following impact, then an inhomogenous coating will be observed (Ham et al., 2016). Fortunately, the $Ti(acac)_2OiPr_2$ solution thermalizes relatively slowly compared to the carrier solvent (IPA), which makes variations moderate and prevents dry powder deposition under our experimental conditions, but noticeable differences are observed nonetheless because this balance isn't achieved at the lower shaping pressure.

To understand the relative impact of these structural variations using ultrasonic spray deposition to that for TiO_2 deposited through the traditional hand-spray system, we have fabricated batches of PSCs using the entire 100 cm^2 TiO_2 coated FTO/Glass substrates cut to 1.25 × 2 cm^2 sizes. The extracted device characteristics of these samples without any sample discrimination within a batch are shown in Fig. 7. A comparison between the planar device characteristics of hand-spray, 10 kPa and 200 kPa samples clearly indicates the superior performance of the 200 kPa ultrasonic deposited TiO_2 across all device characteristics. Importantly, the hand-spray samples exhibit a relatively high median efficiency of 14.5%, but have a large device performance spread with a standard deviation of 4.6%. In comparison, the 200 kPa sample exhibit a median efficiency of 15.6%, albeit with a drastically reduced standard deviation of 1.5%. This indicates that the hand-spray can provide high quality blocking layers suitable for high-efficiency PSCs, but due to homogeneity problems, there are many poor performing devices. Somewhat surprisingly, the 10 kPa samples showed the lowest mean performance characteristics, but had comparable standard deviations to the 200 kPa. This confirms that the slight differences in macroscopic inhomogeneity of the TiO_2 do not perturb the sample reproducibility over the 100 cm^2 deposition scale; however, the topographic variations at the microscopic scale evidently yield poorer hole blocking properties.

To understand if higher levels of reproducibility and device performance could be achieved, we further deposited ~ 150 nm thick mesoporous layers of TiO_2 on top of 200 kPa sprayed T_4 layers prior to the deposition of the perovskite layers. These layers were characterized using conventional XRD and SEM to validate their mesostructure and anatase phase (see Fig. S4). These were deposited by spin-coating using a commercial ink tailored for this deposition approach. This is consistent with the prospects of manufacturing such devices, for which the *meso*-porous layers would likely be printed, whilst very thin transport layers would in fact be spray deposited. As has been previously suggested, the *meso*-porous scaffold reduces shunting pathways and enhances electron extraction within perovskite devices (Grätzel and Zakeeruddin, 2013). The device characteristics of the mesoporous PSC devices fabricated here are also shown in Fig. 7. It is evident that the presence of the mesoporous layer has a favourable effect on all device characteristics, particularly J_{sc} and FF, with the median efficiency being 17.4%. This represents a 12% relative enhancement compared to the planar device (see in Table 2). Importantly, these enhancements are accompanied by drastic reductions to the absolute standard deviations of all the parameters, with that for efficiency being a remarkable 0.5%.

Table 2
Mean and medium parameters for PSC devices using different TiO_2 ETLs.

Samples	J_{sc} (mA cm^{-2})	V_{oc} (mV)	FF	PCE (%)
Hand-spray	18.0 ± (5.1) 21.1	988 ± (65) 1009	0.61 ± (0.09) 0.64	11.4 ± (4.6) 14.5
Ultrasonic spray (10 kPa)	19.2 ± (2.1) 20.2	960 ± (46) 972	0.62 ± (0.06) 0.61	11.8 ± (1.6) 11.7
Ultrasonic spray (200 kPa, planar)	21.5 ± (1.0) 21.7	1028 ± (14) 1032	0.67 ± (0.03) 0.68	15.1 ± (1.5) 15.6
Ultrasonicspray (200 kPa, meso)	23.2 ± (0.6) 23.3	1048 ± (8) 1047	0.71 ± (0.03) 0.71	17.2 ± (0.6) 17.4

This is direct evidence that the mesoporous layer further assists in creating a more macroscopically homogeneous ETL with more favourable charge extraction properties within this PSC configuration.

4. Conclusions

In this work we have compared the effectiveness of TiO_2 layers deposited through the conventional hand-spray and ultrasonic methods as suitable electron transport layers in perovskite solar cells. It was found that hand-spray deposition of TiO_2 yields coatings with a macroscopic mean thickness deviation of up to ± 15%. This deviation could be significantly reduced to less than ± 5% using ultrasonic deposition. However, this was only achieved when the shaping pressure used during the deposition was high (200 kPa). In comparison, the films deposited at lower pressures (10 kPa) exhibited slightly larger thickness variations and were significantly more inhomogeneous at the microscopic level. These structural variations had a significant effect on the performance of methyl ammonium lead iodide perovskite solar cells, with devices featuring a ~ 24 nm TiO_2 film deposited using the high shaping pressure ultrasonic approach, yielding the highest median efficiency of 15.6%, followed by hand-spray at 14.5%, and finally low shaping pressure ultrasonic method at 11.8%. Importantly, the ultrasonic method yielded devices with a 300% reduction in standard deviation of efficiency compared to the hand-spray, which can be directly correlated to the macroscopic homogeneity of the TiO_2 layers. The inclusion of a mesoporous TiO_2 nanoparticle scaffold onto the high shaping pressure TiO_2 layers was found to enhance the mean efficiency to 17.4% and remarkably provided a further 300% reduction to its standard deviation. These results indicate that the ultrasonic spray method is a suitable approach to fabricating high quality and reproducible TiO_2 electron transporting layers for PSC, provided that high deposition pressures are used. Coupling this deposition approach to additional mesoporous layers provides further efficiency and reproducibility benefits, which are important factors towards larger area perovskite device fabrication.

Author contributions

The manuscript was written through contributions of all authors. All authors have given approval to the final version of the manuscript.

Acknowledgement

JS acknowledges funding support through the Monash Graduate Scholarship and Monash International Postgraduate Research Scholarship programs. JJ acknowledges funding support through the Australian Research Council under the grant CE170100026. AN acknowledges funding support through the Australian Research Council Discovery Early Career Researcher Award (DECRA) DE160100504. The authors acknowledge the use of the facilities at the Monash Centre for Electron Microscopy (MCEM).

Appendix A. Supplementary material

Supplementary data to this article can be found online at https://doi.org/10.1016/j.solener.2019.06.045.

References

Acik, I.O., Madarász, J., Krunks, M., Tonsuaadu, K., Pokol, G., Niinistö, L., 2009. Titanium (IV) aetylacetonate xerogels for processing titania films. J. Therm. Anal. Calorim. 97, 39–45.
Akihiro, K., Kenjiro, T., Yasuo, S., Tsutomu, M., 2009. Organometal halide perovskites as visible-light sensitizers for photovoltaic cells. J. Am. Chem. Soc. 131, 6050–6051.
Arthur, McDonell, V.G., 2017. Atomization and sprays, second edition. CRC Press Second Edition.
Bach, U., Lupo, D., Comte, P., Moser, J.E., Weissortel, F., Salbeck, J., Spreitzer, H., Gratzel, M., 1998. Solid-state dye-sensitized mesoporous TiO2 solar cells with high photon-to-electron conversion efficiencies. Nature 395, 583–585.
Ball, J.M., Lee, M.M., Hey, A., Snaith, H.J., 2013. Low-temperature processed meso-superstructured to thin-film perovskite solar cells. Energy Environ. Sci. 6, 1739–1743.
Bian, J.M., Li, X.M., Gao, X.D., Yu, W.D., Chen, L.D., 2004. Deposition and electrical properties of N-In codopedp-type ZnO films by ultrasonic spray pyrolysis. Appl. Phys. Lett. 84, 541–543.
Braga, A., Baratto, C., Colombi, P., Bontempi, E., Salvinelli, G., Drera, G., Sangaletti, L., 2013. An ultrathin TiO2 blocking layer on Cd stannate as highly efficient front contact for dye-sensitized solar cells. Phys. Chem. Chem. Phys. 15, 16812–16818.
Chandiran, A.K., Yella, A., Mayer, M.T., Gao, P., Nazeeruddin, M.K., Gratzel, M., 2014. Sub-nanometer conformal TiO2 blocking layer for high efficiency solid-state perovskite absorber solar cells. Adv. Mater. 26, 4309–4312.
Chung, I., Lee, B., He, J., Chang, R.P., Kanatzidis, M.G., 2012. All-solid-state dye-sensitized solar cells with high efficiency. Nature 485, 486–489.
Conde-Gallardo, A., Guerrero, M., Castillo, N., Soto, A.B., Fragoso, R., Cabañas-Moreno, J.G., 2005. TiO2 anatase thin films deposited by spray pyrolysis of an aerosol of titanium diisopropoxide. Thin Solid Films 473, 68–73.
Correa-Baena, J.P., Saliba, M., Buonassisi, T., Grätzel, M., Abate, A., Tress, W., Hagfeldt, A., 2017a. Promises and challenges of perovskite solar cells. Science 358, 739–744.
Correa-Baena, J.P., Turren-Cruz, S.H., Tress, W., Hagfeldt, A., Aranda, C., Shooshtari, L., Bisquert, J., Guerrero, A., 2017b. Changes from bulk to surface recombination mechanisms between pristine and cycled perovskite solar cells. ACS Energy Lett. 2 (3), 681–688.
Docampo, P., Ball, J.M., Darwich, M., Eperon, G.E., Snaith, H.J., 2013. Efficient organometal trihalide perovskite planar-heterojunction solar cells on flexible polymer substrates. Nat. Commun. 4, 2761.
Espinosa, N., Serrano-Luján, L., Urbina, A., Krebs, F.C., 2015. Solution and vapour deposited lead perovskite solar cells: ecotoxicity from a life cycle assessment perspective. Sol. Energy Mater. Sol. Cells 137, 303–310.
Filipovic, L., Selberherr, S., Mutinati, G.C., Brunet, E., Steinhauer, S., Köck, A., Teva, J., Kraft, J., Siegert, J., Schrank, F., 2014. Methods of simulating thin film deposition using spray pyrolysis techniques. Microelectr. Eng. 117, 57–66.
Grätzel, C., Zakeeruddin, S.M., 2013. Recent trends in mesoscopic solar cells based on molecular and nanopigment light harvesters. Mater. Today 16, 11–18.
Ham, E., Gielis, S., Bael, M., Hardy, A., 2016. Ultrasonic spray deposition of metal oxide films on high aspect ratio microstructures for three-dimensional all-solid-state Li-ion batteries. ACS Energy Lett. 1, 1184–1188.
Hu, H., Dong, B., Hu, H., Chen, F., Kong, M., Zhang, Q., Luo, T., Zhao, L., Guo, Z., Li, J., Xu, Z., Wang, S., Eder, D., Wan, L., 2016. Atomic layer deposition of TiO2 for a high-efficiency hole-blocking layer in hole-conductor-free perovskite solar cells processed in ambient air. ACS Appl. Mater. Interfaces 8, 17999–18005.
Jeon, N.J., Na, H., Jung, E.H., Yang, T.Y., Lee, Y.G., Kim, G., Shin, H.W., Il Seok, S., Lee, J., Seo, J., 2018. A fluorene-terminated hole-transporting material for highly efficient and stable perovskite solar cells. Nat. Energy 3 (8), 682–689.
Kang, B.S., Ahn, S.E., Lee, M.J., Stefanovich, G., Kim, K.H., Xianyu, W.X., Lee, C.B., Park, Y., Baek, I.G., Park, B.H., 2008. High-current-density CuOx/InZnOx thin-film diodes for cross-point memory applications. Adv. Mater. 20, 3066–3069.
Kavan, L., Grätzel, M., 1995. Highly efficient semiconducting TiO2 photoelectrodes prepared by aerosol pyrolysis. Electrochim. Acta 40, 643–652.
Kavan, L., O'Regan, B., Kay, A., Grätzel, M., 1993. Preparation of TiO2 (anatase) films on electrodes by anodic oxidative hydrolysis of TiCl3. J. Electroanal. Chem. 346, 291–307.
Ke, W., Fang, G., Wang, J., Qin, P., Tao, H., Lei, H., Liu, Q., Dai, X., Zhao, X., 2014. Perovskite solar cell with an efficient TiO(2) compact film. ACS Appl. Mater. Interfaces 6, 15959–15965.
Kim, H.S., Lee, C.R., Im, J.H., Lee, K.B., Moehl, T., Marchioro, A., Moon, S.-J., Humphry-Baker, R., Yum, J.-H., Moser, J.E., Grätzel, M., Park, N.-G., 2012. Lead iodide perovskite sensitized all-solid-state submicron thin film mesoscopic solar cell with efficiency exceeding 9%. Sci. Rep. 2, 591.
Kim, M.C., Kim, B.J., Yoon, J., Lee, J.W., Suh, D., Park, N.G., Choi, M., Jung, H.S., 2015. Electro-spray deposition of a mesoporous TiO2 charge collection layer: toward large scale and continuous production of high efficiency perovskite solar cells. Nanoscale 7, 20725–20733.
Lang, R.J., 1962. Ultrasonic atomization of liquids. J. Acoust. Soc. Am. 34, 6–8.
Lee, M.M., Teuscher, J., Miyasaka, T., Murakami, T.N., Snaith, H.J., 2012. Efficient hybrid solar cells based on meso-superstructured organometal halide perovskites. Science 338, 643–647.
Liu, M., Johnston, M.B., Snaith, H.J., 2013. Efficient planar heterojunction perovskite

solar cells by vapour deposition. Nature 501, 395–398.
Mark, B.S., Henry, C.F., 1999. Ultrasonic deposition of high-selectivity nanoporous carbon membranes. Science 285 (5435), 1902–1905.
Moehl, T., Im, J.H., Lee, Y.H., Domanski, K., Giordano, F., Zakeeruddin, S.M., Dar, M.I., Heiniger, L.P., Nazeeruddin, M.K., Park, N.G., Gratzel, M., 2014. Strong photocurrent amplification in perovskite solar cells with a porous TiO2 blocking layer under reverse bias. J. Phys. Chem. Lett. 5, 3931–3936.
Narushima, S., Mizoguchi, H., Shimizu, K., Ueda, K., Ohta, H., Hirano, M., Kamiya, T., Hosono, H., 2003. A p-type amorphous oxide semiconductor and room temperature fabrication of amorphous oxide p–n heterojunction diodes. Adv. Mater. 15, 1409–1413.
Nguyen-Phan, T.D., Pham, V.H., Cuong, T.V., Hahn, S.H., Kim, E.J., Chung, J.S., Hur, S.H., Shin, E.W., 2010. Fabrication of TiO2 nanostructured films by spray deposition with high photocatalytic activity of methylene blue. Mater. Lett. 64, 1387–1390.
Niu, G., Guo, X., Wang, L., 2015. Review of recent progress in chemical stability of perovskite solar cells. J. Mater. Chem. A 3, 8970–8980.
Peng, B., Jungmann, G., Jäger, C., Haarer, D., Schmidt, H.W., Thelakkat, M., 2004. Systematic investigation of the role of compact TiO2 layer in solid state dye-sensitized TiO2 solar cells. Coord. Chem. Rev. 248, 1479–1489.
Snaith, H.J., 2013. Perovskites: the emergence of a new era for low-cost, high-efficiency solar cells. J. Phys. Chem. Lett. 4, 3623–3630.
Supasai, T., Henjongchom, N., Tang, I.M., Deng, F., Rujisamphan, N., 2016. Compact nanostructured TiO2 deposited by aerosol spray pyrolysis for the hole-blocking layer in a CH3NH3PbI3 perovskite solar cell. Solar Energy 136, 515–524.
Tachibana, Y., Umekita, K., Otsuka, Y., Kuwabata, S., 2008. Performance improvement of CdS quantum dots sensitized TiO2 solar cells by introducing a dense TiO2 blocking layer. J. Phys. D: Appl. Phys. 41, 102002.
Tait, J.G., Manghooli, S., Qiu, W., Rakocevic, L., Kootstra, L., Jaysankar, M., Masse de la Huerta, C.A., Paetzold, U.W., Gehlhaar, R., Cheyns, D., Heremans, P., Poortmans, J., 2016. Rapid composition screening for perovskite photovoltaics via concurrently pumped ultrasonic spray coating. J. Mater. Chem. A 4, 3792–3797.
Wöbkenberg, P.H., Ishwara, T., Nelson, J., Bradley, D.D.C., Haque, S.A., Anthopoulos, T.D., 2010. TiO2 thin-film transistors fabricated by spray pyrolysis. Appl. Phys. Lett. 96, 082116.
Xia, J., Masaki, N., Jiang, K., Yanagida, S., 2006. Deposition of a thin film of TiOx from a titanium metal target as novel blocking layers at conducting glass/TiO2 interfaces in ionic liquid mesoscopic TiO2 dye-sensitized solar cells. J. Phys. Chem. B 110, 25222–25228.
Zhou, P., Li, W., Li, T., Bu, T., Liu, X., Li, J., He, J., Chen, R., Li, K., Zhao, J., Huang, F., 2017. Ultrasonic spray-coating of large-scale TiO2 compact layer for efficient flexible perovskite solar cells. Micromachines 8 (2).

Supplementary Material

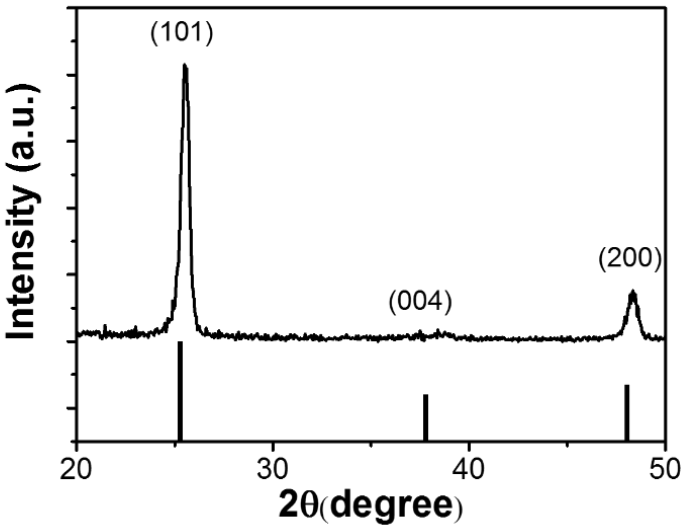

Figure 4S 1 Glancing angle XRD pattern of ultrasonic-sprayed T_8 film on silicon wafer. The incident angle is 0.33º.

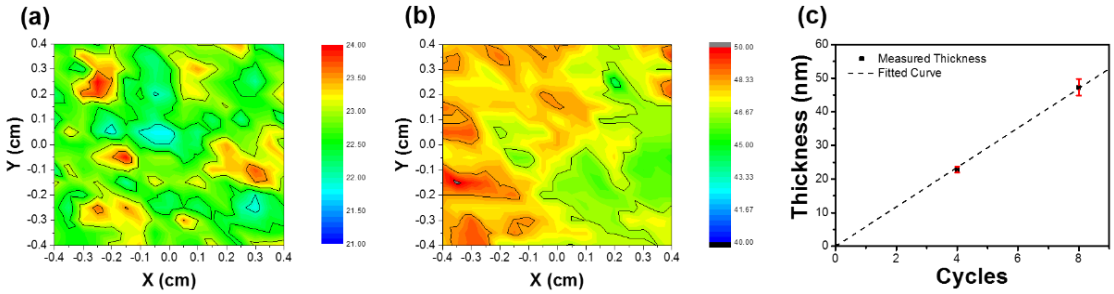

Figure 4S 2 Thickness maps derived from spectroscopic ellipsometry of TiO_2 sprayed on silicon with 4 cycles (a) and 8 cycles (b). A linear correlation with respect to the cycle number and the thickness was determined (c).

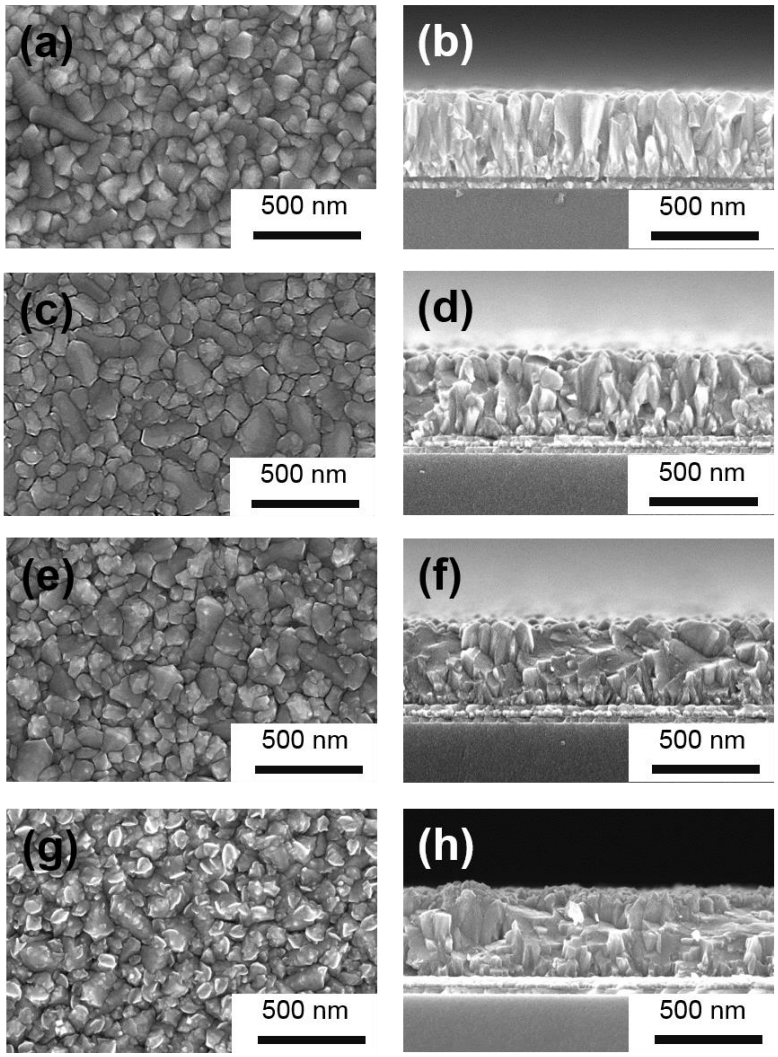

Figure 4S 3 Top-view and cross-section SEM images of TiO_2 sprayed on FTO substrates with 2 (a, b), 4 (c, d), 6 (e, f) and 8 (g, h) cycles, respectively.

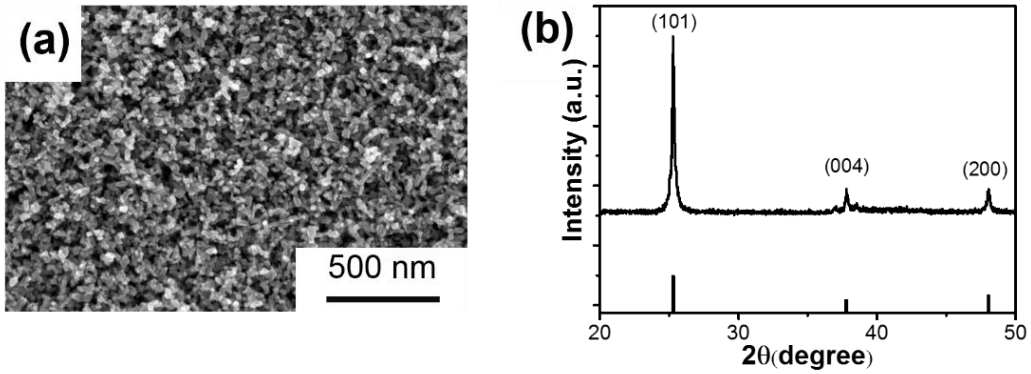

Figure 4S 4 Top-view SEM image with 100k magnification (a) and XRD pattern (b) of calcined mesoporous TiO_2 films on glass, respectively.

Chapter 5.

Enhanced Performance of Perovskite Solar Cells by Micro-Structuring the Mesoporous TiO_2 Layer

Synopsis

Although highly reproducible PSCs have been achieved by using ultrasonic sprayed ETLs (in **Chapter 4**), efficient optimization of the PSC configuration is still key to further improve the device performance. In **Chapter 4**, we showed that a mesoporous TiO_2 layer on top of the compact TiO_2 ETL provides superior PCE (~18%) compared with that of planar devices (~17%). These devices harnessed a spin-coated pristine commercial TiO_2 paste with a calcination at 500 ℃. However, it has been reported that the pristine TiO_2 mesoporous layer in perovskite solar cells suffers from electron transporting problem due to its mediocre conductivity and crystal defects, e.g. oxygen vacancies. Thus, PCEs of mesoporous PSCs are highly dependent on the thickness control, the material modification and surface passivation design of the mesoporous layer. In this work, we report an easily achievable method to develop high-efficiency PSCs by micro-structuring a mesoporous TiO_2 layer formed directly from a TiO_2 nanoparticle dispersion. The micro-structuring is achieved through the controlled crystallization of small molecular additives in the dispersion, which are subsequently thermolyzed in the following coating and calcination. This micro-structure enables for a more efficient charge extraction and less charge recombination, which is shown to result in devices with a higher PCE of ~19% compared to ~18% for the controls. These results highlight the importance of morphology modification of the mesoporous scaffold in PSCs to improve their performance.

5.1 Introduction and Context

To date, most high-performance PSCs are of a mesoscopic conventional configuration, i.e. mesoporous PSCs.[1] As we introduced in **Chapter 1**, the assembly begins with a transparent conductive glass cathode (eg. ITO and FTO) followed by a compact ETL, a mesoporous scaffold, a sequentially deposited perovskite layer, a compact HTL and then an anode electrode. In this efficient architecture, the ETL and HTL selectively block holes and electrons generated in the perovskite absorber, respectively, to reduce interfacial recombination at the electrode interfaces. Initially, planar PSCs were considered to be efficient in terms of radiative efficiency, charge carrier mobilities and photogenerated species lifetimes.[2] However, more recently it has been shown that a mesoporous layer is beneficial for controlling the crystal orientation and grain size of the perovskite material when solution processing techniques are used.[3, 4]

In the pursuit of high-performance PSCs, tremendous research efforts have tended to focus on the optimization of mesoporous TiO_2 layers to improve the charge transport from perovskite to the cathode. Composition modifications of mesoporous layers are one of the most widely used approaches to improve the film conductivity, and thus to enhance their charge transport properties. Additives, such as lithium, aluminum and magnesium,[5] have been used to optimize the mesoporous layer. Among these, the work of Li-doping in TiO_2 mesoporous layer from Graetzel's group has become a typical approach to achieve high performance PSCs.[6] These authors reported that the Li-doped mesoporous TiO_2 layer exhibits superior electronic properties by reducing electronic trap states and enabling faster electron transport. However, this approach requires a secondary calcining at high temperature (500 ℃) after Li modification, which complicates the device fabrication process. Moreover, the Li doping is susceptible to degradation under an ambient atmosphere, requiring the post-treated mesoporous film to be immediately transferred from a hot plate to a nitrogen atmosphere glove box before it cools down to 150 ℃.

Crystal size and thickness of the mesoporous TiO_2 layer has also been reported to having great effects on PSC performance. In mesoporous PSCs, thick mesoporous layers result in enhanced recombination of the injected electrons in TiO_2 conduction band with the hole in the perovskite.[7] In contrast, thin mesoporous layers lead to differences in efficiency between the forward and reverse scans, i.e. hysteresis, due to the imbalanced charge extraction properties.[8, 9] Indeed, research on efficient materials design and thickness manipulation of mesoporous layers have shown optimized benefits towards achieving high-performance device. However, up to now, few works involve the morphologic structuring to achieve efficient and facile modification of the mesoporous layer for high performance PSCs.

In this work, we explore the use of thiourea to structurally modify the mesoporous TiO_2 layer with random micro-level concaves and partially expose underneath compact TiO_2 layer. The micro-structuring is achieved through the crystallization of the additive in the TiO_2 nanoparticle paste dispersion, which are subsequently thermolysed following coating. This unique film structure has a mesoporous scaffold that helps to reduce the interface recombination without significantly sacrificing the electron transport from the perovskite to the ETL. The morphology of the micro-structured layer is well controlled by adjusting the concentration of thiourea in TiO_2 past dispersion. The PSCs using this modified TiO_2 mesoporous layer show an average PCE of ~19% compared to ~18% for the controls. These results highlight that achieving high-performance PSCs relies not only on the nanoscale structure of charge extraction layers, but also on their extended micro-level morphology.

5.2 Experimental Details

5.2.1 Solar Cell Fabrication

Most of the fabrication process were reported in **Chapter 2**. After depositing the compact TiO_2 layer using ultrasonic spray system, the thiourea modified mesoporous layers were fabricated by spin coating the homogeneous TiO_2 nanoparticle paste with different concentration of thiourea. Then the following processes were carried out in a N_2 filled glovebox as discussed in **Section 2.4**. Devices were covered by aluminium foil and stored in a dry-box for 2 days before testing.

5.2.2 Characterization

Characterization of absorption and PL spectra, XRD patterns, SEM images of perovskite films as well as J-V curves, impedance and IPCE spectra of devices were described in **Chapter 2**.

Transient photocurrent (TPC) and transient photovoltage (TPV) decay measurements were performed a pulse 465 nm LED with an interval time of 2 µs. The response of current and voltage of devices were recorded on an Agilent Technologies Infiniivision DSO-X 3032A digital oscilloscope. In TPC measurement, the device was connected to the digital oscilloscope with a 50 Ω termination to achieve a short-circuit condition. In TPV measurements, devices were connected to the digital oscilloscope with a termination of 1 MΩ to achieve open-circuit condition.

5.3 Results and Discussion

5.3.1 Formation of Morphologically Modified Mesoporous TiO_2 Films

The formation mechanism of the micro-structured mesoporous TiO_2 film prepared using a modified thiourea protocol is schematically illustrated in **Figure 5.1**. Briefly, 5 to 20 mg of thiourea is dissolved

in 1 mL of TiO_2 paste (15 wt%) following 5 mins of vertexing the solution to achieve a well dispersed milk white solution. The solution is spin coated on top of an FTO coated glass substrate with a compact TiO_2 ETL on top, which was spray coated as outlined in **Chapter 4**. During the drying process of the mesoporous film, the ethanol evaporates and thiourea crystallizes into microscale crystals. Finally, the sample is annealed in air at 500 ^oC, which intends to eliminate the additives (cellulose and terpineol) in TiO_2 paste, while also decomposes the thiourea to leave microscale vacancies.

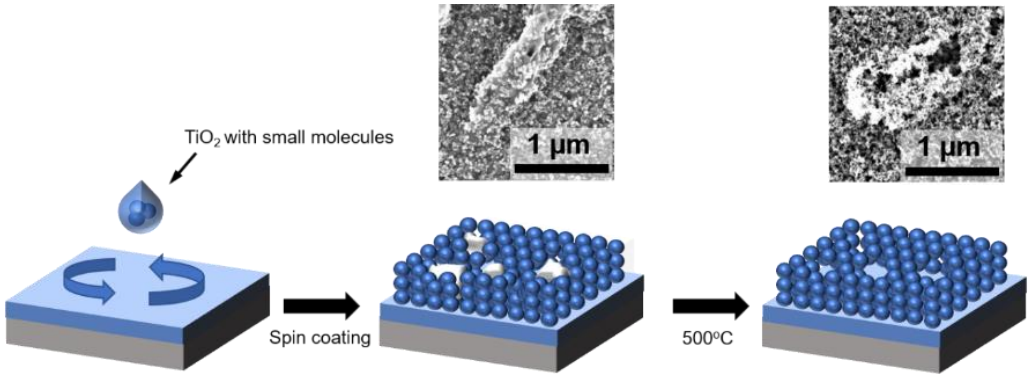

Figure 5.1 Schematic of micro-structured the mesoporous TiO_2 film with inset SEM images recording the morphology transition.

As is shown in **Figure 5.2**, the morphology of the micro-structured TiO_2 mesoporous layer can be manipulated by changing the concentration of thiourea in the TiO_2 solution. For simplicity of notation, here we defined Tx as the mesoporous layer made by diluted TiO_2 paste containing x mg/mL thiourea. As shown in **Figure 5.2A**, the mesoporous layer made with pristine TiO_2 films is consists of a homogenous film of sintered TiO_2 nanoparticles. The addition of 5 mg/mL thiourea, i.e. T5, results in a slightly perturbed surface, which appears to be undulating in its topography although the mesoporous TiO_2 layer still maintains a full coverage of the surface (**Figure 5.2B**). However, as the thiourea is increased to 10 mg/mL, T10, isolated microscale concave features appear on the mesoporous film surface (**Figure 5.2C**). The generated concave features are ~150 nm in depth with distinguished convex edge of 50~100 nm in height, which is verified by atomic force microscope in **Figure 5.3**. A larger concentration of 20 mg/mL thiourea (the saturated concentration of thiourea in the diluted TiO_2 paste solution) leads to even larger concave features that start to overlap with each other (**Figure 5.2D**).

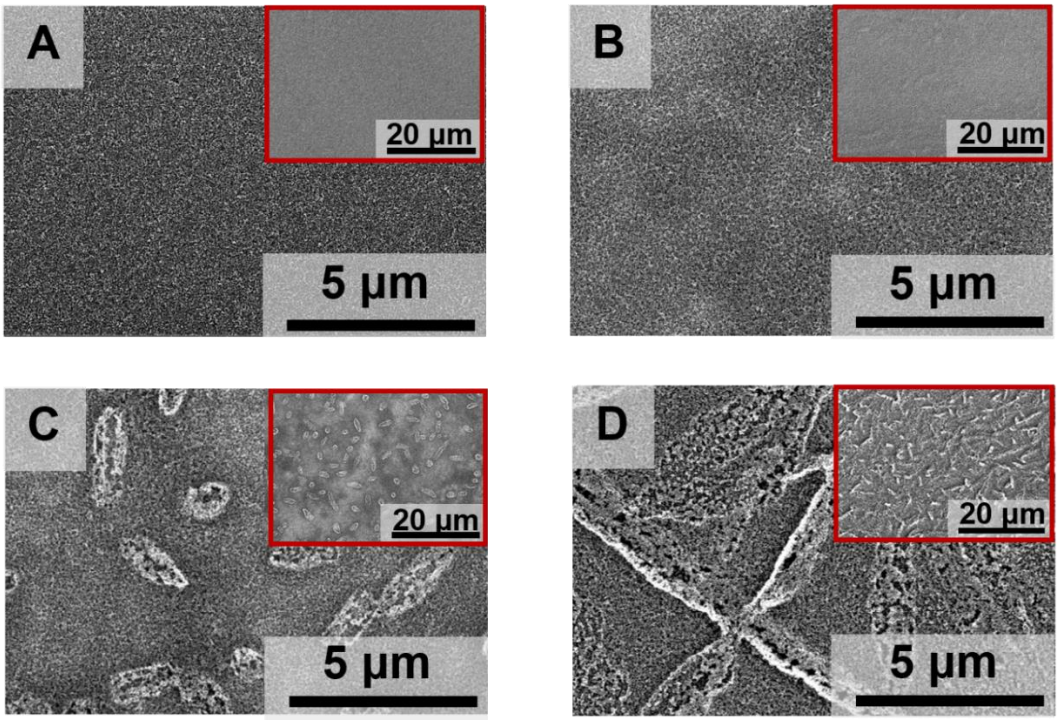

Figure 5.2 SEM images of the films made by pristine diluted TiO_2 paste (A) and diluted TiO_2 paste with 5 mg/mL (B), 10 mg/mL (C) and 20 mg/mL (D) thiourea additive.

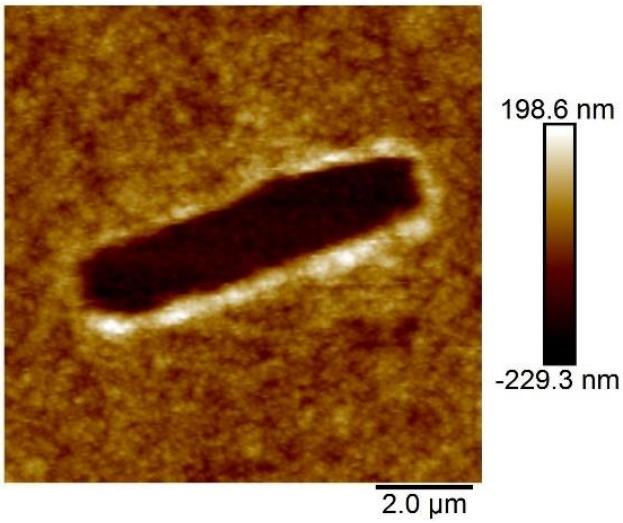

Figure 5.3 AFM image of a concave in T10 film.

To investigate the composition of the TiO_2 mesoporous layers that had been structured using thiourea as an additive, we used XPS to characterize T0 and T10 films. The corresponding survey and high-resolution spectra are shown in **Figure 5.4**, with the elemental proportions of Ti, O, C, S and N being summarized Table 1. Interestingly, from these XPS measurements we observed nearly identical compositions for films prepared both with and without thiourea. This indicates that the thiourea must

thermolyze during calcination under an ambient environment to release the S and N as volatile by-products. To that extent, as illustrated in **Equations 5.1**, it has been previously shown that thiourea decomposes at 180-220 ℃ to generate cyanamide, and thiocyanic acid, both of which possess low-boiling points, and ammonia and hydrogen sulfide gases.[10] Notably, 0.5% sulfur was observed in our samples even for T0, which might be ascribed to the absorption of sulfur-containing compounds in air on TiO_2 nanoparticles.[11, 12]

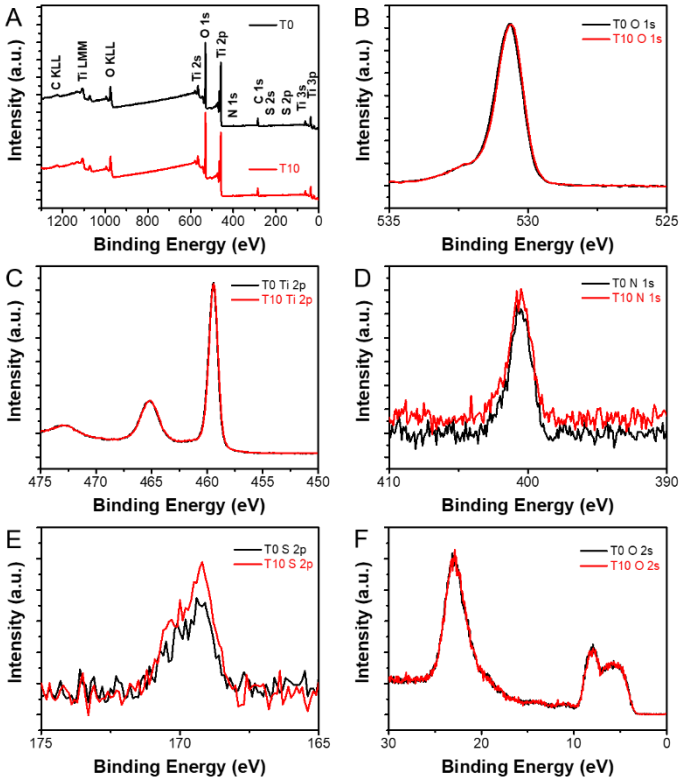

Figure 5.4 XPS spectra of T0 and T10 films: (A) Survey, (B) O 1s, (C) Ti 2p, (d) N 1s, (e) S 2p and (f) O 2s.

Table 5.1 Concentration of Ti, O, C, S and N of the T0 and T10 films

Films	Ti (%)	O (%)	C (%)	S (%)	N (%)
T0	24.9	54.8	18.9	0.5	0.9
T10	24.7	54.7	19.0	0.6	1.0

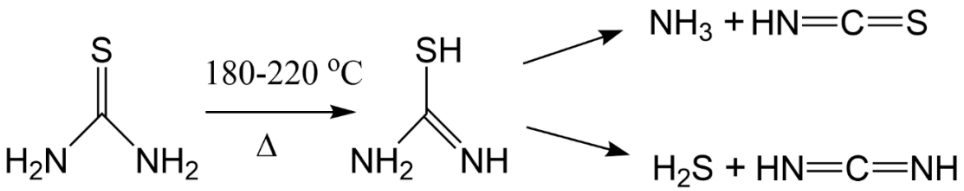

Equation 5.1 The primitive reaction paths for the thermal decomposition of thiourea.

5.3.2 TEM and XRD Analysis

To understand the structural and morphological characteristics of the particles constituting T0 and T10 samples, XRD patterns of the films and TEMs of calcined TiO_2 nanoparticles across these samples were studied and are included in **Figure 5.5**, respectively. The particles were prepared by calcining the dried product from the individual samples at 500 ℃ under air flow. The results show that both samples exhibit almost identical structural characteristics. The XRD spectra exhibit clear signatures of scattering contributions from (101), (103), (004) and (200) planes of anatase at 25.3°, 37.2°,37.8° and 48.0°, respectively. Noteworthy, in both samples, the peak at 37.2° representing (111) plane of rutile impurities can be detected. Scherrer analysis indicates that the average T0 and T10 particle size across these samples is 28.5 nm and 25.1 nm, respectively. The TEM measurements also show similar morphologies of the particles, with particles of 30~50 nm suggesting limited structural variation. From these characterizations we suggest that the inclusion of thiourea does not modify the individual particle lattice or morphology, but instead changes the microscopic characteristics of the films through the formation of the structural perturbation.

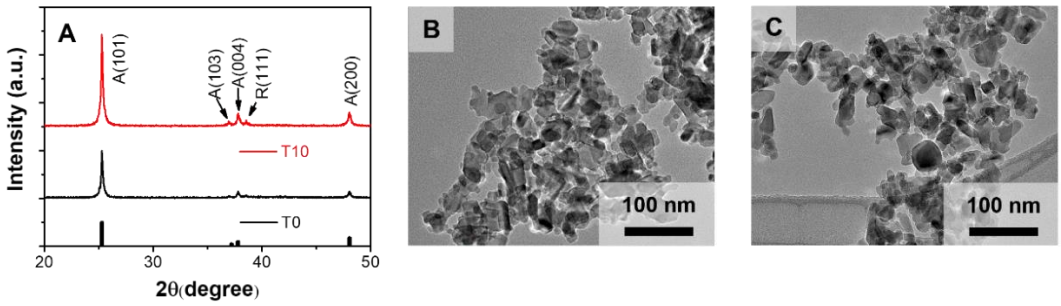

Figure 5.5 XRD patterns (A) and TEM images of T0 (B) and T10 (C) TiO_2 nanoparticles respectively.

5.3.3 Structural Properties of Deposited Perovskites

Mixed cation and anion perovskite ($Cs_{0.05}FA_{0.79}MA_{0.16}PbI_{2.49}Br_{0.51}$) were deposited on top of T0 and T10 films. These films were each ~ 500 nm in film thickness. Despite this, they exhibited vastly different XRD patterns, as seen in **Figure 5.6**. The intensity characteristic peak at 14.8º, which reflects the (101) facet of perovskite, is evidently stronger when the perovskite was grown on the T10 scaffold. This may result from the high wetting property of T10 substrate, which benefits the deposition of perovskite film. A wettable substrate facilitates a completely spread perovskite precursor solution and fully covered perovskite layer after annealing, which finally help to eliminate

pinholes between the interfaces.[13, 14] Noteworthy, it has been reported that non-wetting substrates lead to large perovskite crystal size, a pre-wetting is still required for the perovskite deposition.[16, 15] The structural differences seen through XRD are not evident from the SEM images of the perovskite on the T0 and T10 substrates (see **Figure 5.7**). However, what is observed are mesoscale undulations in the topography. Cross-sectional SEM images of devices in latter section will further show that these undulations arise from the underlying TiO_2 mesoporous scaffold. Evidently, during the annealing of the perovskite, the physical contours of the underlying scaffold must template the growth of the perovskite grains.

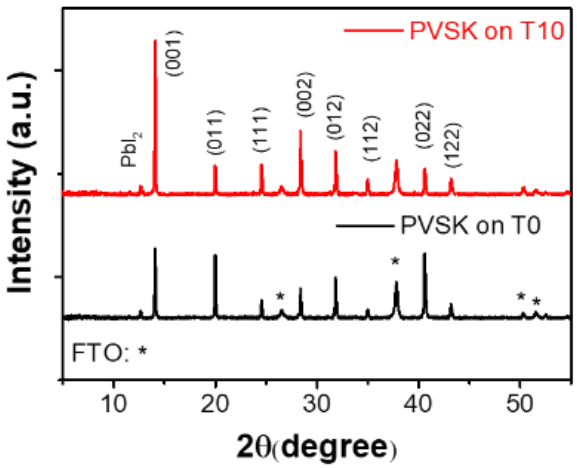

Figure 5.6 XRD pattern of T0 (A) and T10 (B) films.

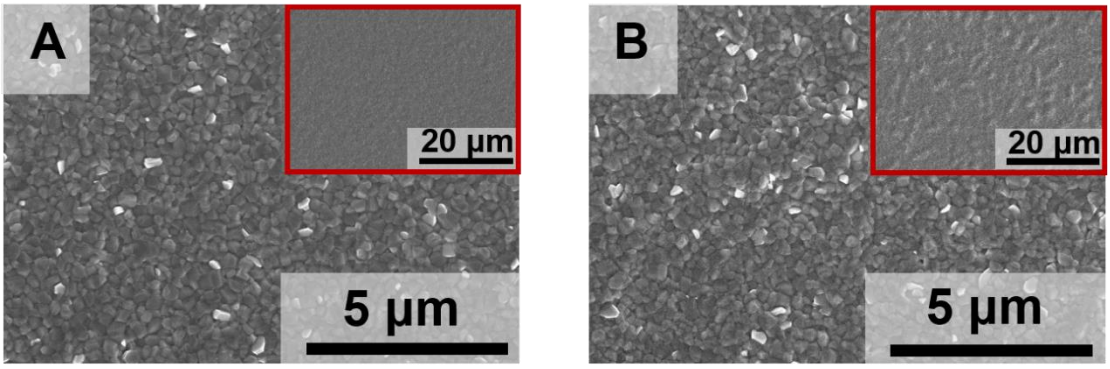

Figure 5.7 Top-view SEM images of T0 (A) and T10 (B) films.

5.3.4 Optical Properties of Deposited Perovskites

Absorptions of the perovskite films on the different mesoporous substrates (T0, T5, T10, T20) are shown in **Figure 5.8A**. Despite exhibiting vastly different structural anisotropy and variations in surface quality, negligibly differences were observed across these samples. This is consistent with all samples exhibiting similar perovskite thicknesses. Furthermore, we used TRPL (**Figure 5.8B**) and

steady-state PL (**Figure 5.8C**) spectroscopy to study the charge transfer kinetics between the perovskite and TiO_2 layers. The PL lifetimes were calculated by **Equation 3.5** and shown in **Table 5.2.** When the perovskite films were deposited on mesoporous TiO_2 layers, their PL lifetimes were dramatically shortened compared with the film on pristine glass. This inherently confirms efficient electron transfer by the mesoporous layers. Notably, the decay lifetimes of perovskite films on both mesoporous layers with and without thiourea were quite similar, suggesting comparable electron transfer quenching. A similar observation can be made when comparing the relative steady-state PL spectra, although the T0 sample in this case does exhibit a slightly higher PL retention. In practise, such subtle changes in PL intensity are within experimental error.

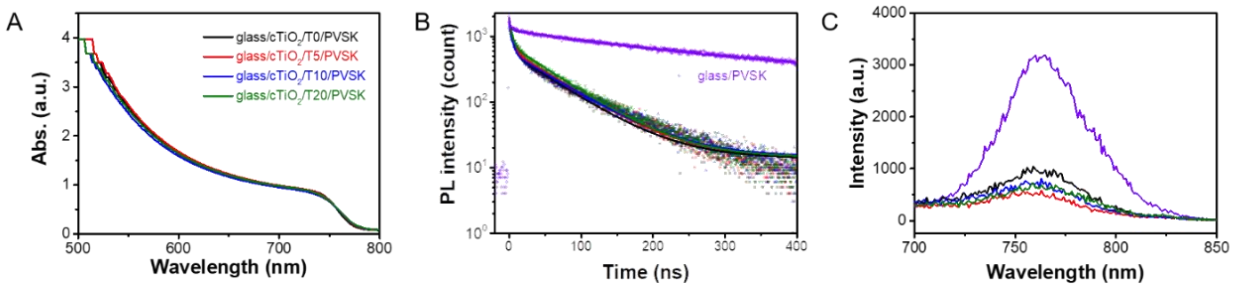

Figure 5.8 Absorption (A), TRPL (B) and steady-state PL (C) spectra of glass/Tx/perovskite films. The light is introduced from glass side.

Table 5.2 Parameters of fitted TRPL spectra.

Sample	A_1	τ_1(ns)	A_2	τ_2(ns)	τ_{avg}(ns)
Perovskite	217	51.3	1021	307	298.3
T0	1064	5.61	504	65.7	56.51
T5	1047	5.33	574	66.4	58.62
T10	1083	4.66	540	67.8	60.12
T20	998	5.74	682	64.1	57.37

The average lifetime $\tau_{avg} = \sum\alpha_i\tau_i$, where $\alpha_i = A_i\tau_i/\sum A_i\tau_i$

5.3.5 Cross-Sectional SEM Analysis of Perovskite Devices

Cross-section SEM images of devices using T0 (A) and T10 (B) mesoporous TiO_2 layer are shown in **Figure 5.9**. It is found that the T0 films exhibits a homogeneously distributed meso-porous layer across the FTO electrode, on which a perovskite film is deposited. Meanwhile, the T10 scaffold clearly shows the micro-structured meso-porous layer on the FTO. The perovskite layer is found to also follow the contour of this meso-porous layer, which results in a perturbed perovskite surface.

Evidently, we can conclude from this analysis that the T10 device can be structurally considered as a hybrid between a planar and a meso-porous device architecture.

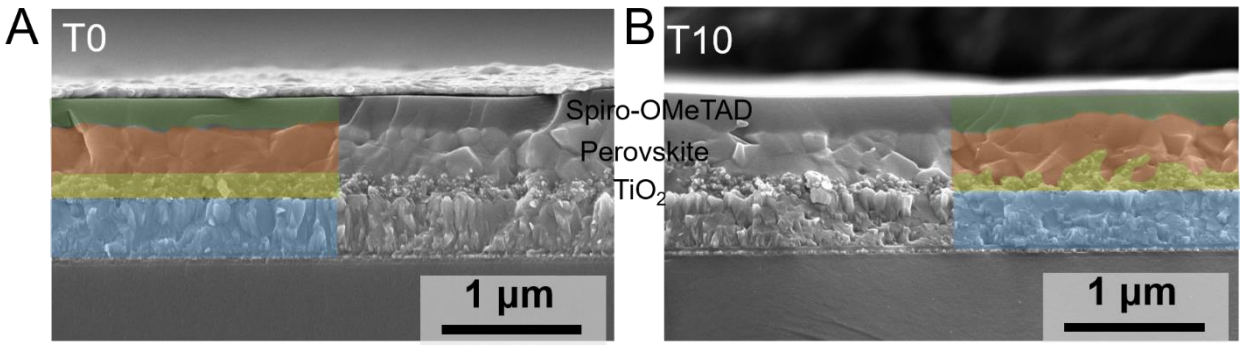

Figure 5.9 Cross-section SEM images of PSCs using T0 (A) and T10 (B) mesoporous TiO_2 layer.

5.3.6 J-V Characteristics of PSCs with Thiourea Modified Mesoporous TiO_2 Layers

To explore the effect of thiourea modification on the device performance, we made devices with thiourea modified mesoporous scaffolds and pristine mesoporous scaffolds as counterparts. The statistical parameters of J_{sc}, V_{oc}, FF and PCE are shown in **Figure 5.10** and summarized in **Table 5.3**. Compared with devices using pristine TiO_2 mesoporous layers (T0), T10 devices showed the biggest enhancement. The average J_{sc} of T10 devices increased from 21.4 mA cm^{-2} to 22.0 mA cm^{-2} and the average V_{oc} increased from 1.10 V to 1.12 V. Thus, although the average FF slightly decreased from 76.6% to 76.2%, on average the PCE of T10 devices was improved from 18.1% to 18.7%. Forward scan (from -0.1 V to1.2 V) and backward scan (from -0.1 V to1.2 V) J-V curves of T0 and T10 devices were achieved by a scan rate of 0.05 V/s, and are included in **Figure 5.11 A**, respectively. The T0 device show a PCE of 18.0% with J_{sc}, V_{oc} and FF of 21.3 mA cm^{-2}, 1.10 V and 76.6%, respectively, while the corresponding parameters of T10 device are 18.9%, 22.1 mA cm^{-2}, 1.12 V and 76.2%, respectively. Both samples show negligible hysteresis, which indicate that the efficient charge transfer between interfaces in devices. The integrated J_{sc} calculated from the IPCE spectra of T0 and T10 devices are 20.6 mA cm^{-2} and 21.3 mA cm^{-2}, respectively (**Figure 5.11 B**), which is consistent with our measured J_{sc} values Notably, further additional of the thiourea to reach T20 devices showed inferior performance, which is mainly ascribed to a reduction in V_{oc} and FF.

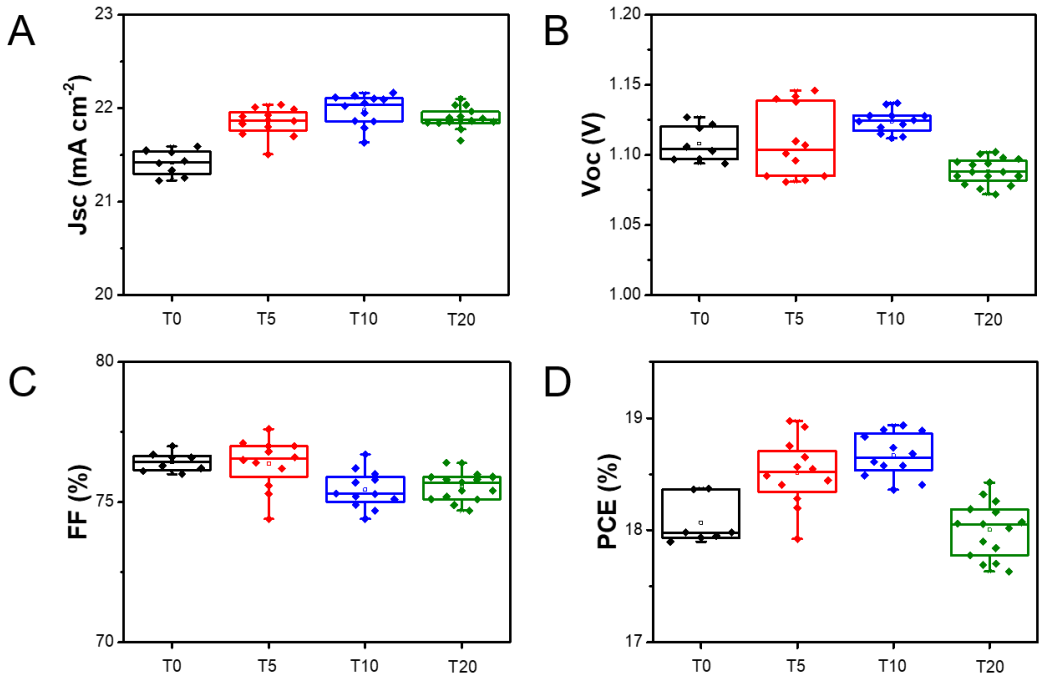

Figure 5.10 Statistic parameters of PSCs using TiO_2 mesoporous layers modified by different concentration of thiourea.

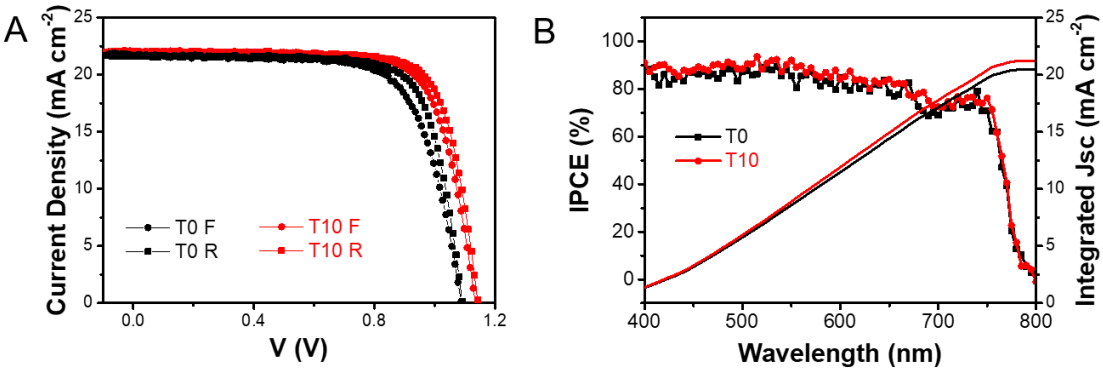

Figure 5.11 J-V curves (A) and IPCE spectra (B) of T0 and T10 PSCs.

Table 5.3 Summarized PSC parameters in **Figure 5.10**.

Sample	**J_{sc} (mA cm^{-2})**	**V_{oc} (V)**	**FF (%)**	**PCE (%)**
T0	21.4±0.2	1.10±0.01	76.4±0.02	18.1±0.2
T5	21.9±0.2	1.10±0.03	76.4±0.04	18.5±0.2
T10	22.0±0.2	1.12±0.01	75.5±0.04	18.7±0.2
T20	21.9±0.2	1.09±0.01	75.5±0.04	18.0±0.2

5.3.7 Transient Photocurrent and Photovoltage Measurements of PSCs with Thiourea Modified Mesoporous TiO_2

To understand the underlying differences that the modification to the TiO_2 mesoporous layer has on the PSCs, charge-carrier dynamics were investigated for the PSC fabricated on T0 and T10 substrates using transient photocurrent (TPC) and transient photovoltage (TPV) at short-circuit and open-circuit conditions, respectively (**Figure 5.12**). For these measurements, the devices were illuminated using a 200 µs square pulse of 525 nm LED light at a power of 20 mW cm^{-2}.[16, 17] From the TPC results we see that the TPC rise and decay times of the T10 device were faster than that of T0 (**Figure 5.12A**). This is suggestive of an imbalance between the electron and hole mobilities and/or the presence of traps in these devices, inherently suggests that shallow traps exist in the TiO_2 mesoporous layer.[18] The constants t_c and t_v are defined as the TPC and TPV decay lifetimes, representing the charge transport and recombination time, respectively.[19] TPC and TPV curves were achieved by measuring the current response at V_{oc} and the voltage response at open-circuit condition triggered by a pulse perturbation with a width of 2 µs. Typically, a fast decay in TPC and TPV indicates a fast charge transport and recombination in devices, respectively. Thus, a perfect PSC should have a fast TPC decay and a slow TPV decay.

The TPC of a T10 device is found to have a t_c of 2.1 µs, which is more than half that of the T0 device at a t_c of 4.8 µs. This suggests that the modification of the mesoporous layer facilitates enhanced carrier extraction from the perovskite to the charge transport layers. Notably, given that the modified ETL caused structural changes to the perovskite and thus, also, modified the ensuing interface with Spiro-OMeTAD, we cannot unequivocally discriminate the precise origin from which this variation arises. Meanwhile, the TPV of the T10 device exhibits a slower t_v of 13.3 µs than that of T0 device at 8.5 µs. This indicates that the T10 device exhibits slower charge recombination compared to the unmodified T10 analogue. As above, while it may be obvious to account for this different in an improved interface at the TiO_2/Perovskite, we cannot unequivocally discriminate the precise origin. In any case, what can be stated is that the modified mesoporous layer caused more efficient carrier extraction and reduced recombination within the PSC compared to the unmodified TiO_2.

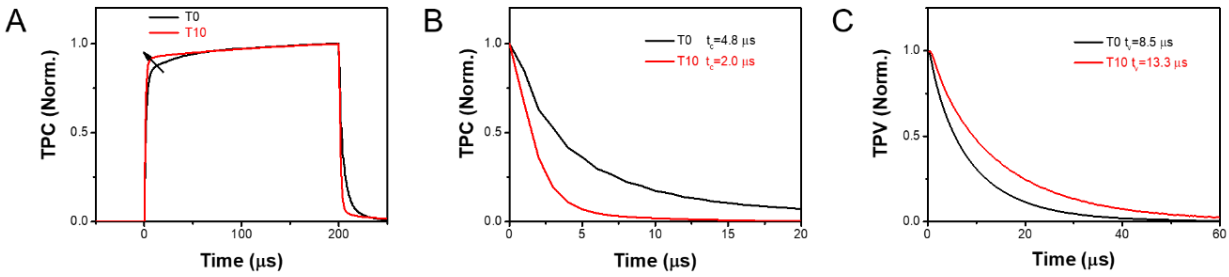

Figure 5.12 Normalized TPC (A) and TPV spectra (B) of T0 and T10 PSCs, respectively at 20 mW cm^{-2}.

5.3.8 Impedance Measurements of PSCs with Thiourea Modified Mesoporous TiO_2 layers

The different TiO_2 films were also investigated by impedance spectroscopy at a 0.8 V bias under 1 sun illumination. This voltage was selectively chosen as it is close the maximum power point of the devices. The equivalent circuit used for fitting the EIS data is shown in **Figure 5.13**, where R_s is the series resistance due to wire and contact resistance, R_1 and R_2 represent the low and high-frequency resistance, respectively,[19] C_g is the high-frequency capacitance, interpreted as the geometric capacitance of the device related to the dielectric properties of the perovskite, and C_s is the low frequency capacitance, which is associated with the surface charge accumulation at perovskite interface. The real impedance intercept (i.e. on the x-axis) of the Nyquist plot represents the contact series resistance of the PSC being measured.[20] As seen in the plots, there is negligible difference among the series resistance of all devices , which is consistence with their comparable FFs. However, the recombination resistance is revealed by the magnitude of the Nyquist plot arcs, i.e. sum of two arcs,[19] which qualitatively shows a favourable increase from T0 to T10 devices and then a subsequent reduction for the T20 device. These results are consistent with the trends observed for V_{oc} measured for the PSCs. As we have noted from the previous section, interpretation of these results from a mechanism perspective is not possible. We consider that the initial increase in recombination resistance may arise from an improved interface between the thiourea modified TiO_2 scaffold and the perovskite layer.

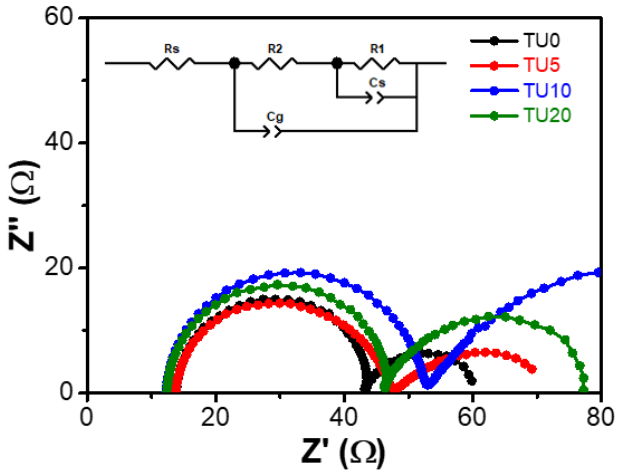

Figure 5.13 Nyquist plots of T0-T20 PSCs 0.8 V under 1 sun illumination with the equivalent circuit inset.

5.3.9 Planar vs Mesoporous PSCs

To understand the role of the mesoporous TiO_2 thickness on the PSC device performance, we fabricated devices using pristine TiO_2 mesoporous layers with different thicknesses by simply spin coating them at 8k revolutions per minute (rpm) and 4k rpm (this being the typical condition in our optimised devices). For comparison, a planar PSC was also made. SEM images of these are shown in **Figure 5.14**, with a clear increase in thickness from ~100 nm to ~170 nm respectively. Across these, the mesoporous film is uniformly deposited on the compact TiO_2 layer.

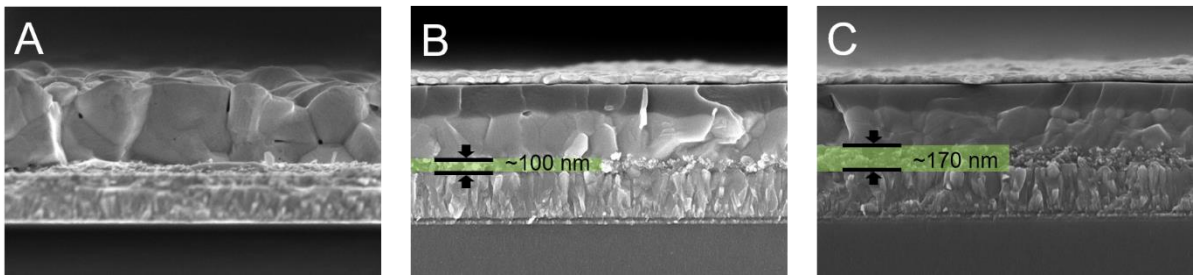

Figure 5.14 Cross-section of planar PSC (A), and mesoporous PCSs using mesoporous layer deposited by 8k rpm (B) and 4k rpm (C).

The J-V curves of the corresponding devices are shown in **Figure 5.15**, with their parameters summarized in **Table 5.4**. The typical mesoporous layer (4k rpm, 170 nm) enables the highest performance across all device characteristics. Meanwhile, the thin mesoporous layer (8k rpm, ~100 nm) leads to a poor V_{oc} and an obvious hysteresis. The planar PSC shows the lowest J_{sc} and V_{oc} with

a large hysteresis. This comparison shows that a sufficiently thickness meso-structure TiO_2 is important to realise low hysteresis and efficient devices.

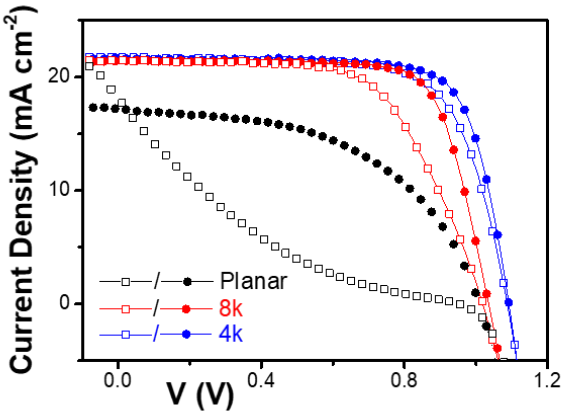

Figure 5.15 J-V curves (A) and Nyquist plots (B) of planar PSC, and mesoporous PSCs with TiO_2 mesoporous layer spin coated by 8k rpm, and 4k rpm.

Table 5.4 Summarized PSC parameters in **Figure 15A**.

Sample	**J_{sc} (mA cm^{-2})**	**V_{oc} (V)**	**FF (%)**	**PCE (%)**	**R_s (Ω cm^2)**	**R_{sh} (Ω cm^2)**
Planar (R)	17.13	1.01	51.9	8.98	11.37	1649
Planar (F)	18.89	0.95	14.2	2.56		
8k rpm(R)	21.38	1.04	75.1	16.61	6.29	3223
8k rpm(F)	21.51	1.02	62.4	13.68		
4k rpm(R)	21.51	1.1	74.5	17.66	5.44	3675
4k rpm(F)	21.51	1.1	73.2	17.31		

Our micro-structured meso-porous layers have an undulating structure, with uneven TiO_2 thicknesses. Despite this, optimised T10 devices achieve enhanced efficiencies compared to the optimal meso-porous layers. Evidently, the undulation of the mesoporous TiO_2 layer results in PSCs with higher PCE due to the reduced charge recombination and improved carrier extraction at the interface between perovskite layer and the mesoporous layer, which cannot be achieved by simply reducing the thickness of the mesoporous layer. Thus, it can be concluded that the performance improvement of thiourea modified mesoporous layer in PSCs is mainly ascribed to the morphology variation more than the thickness variation. This further indicates the importance of morphological modification in interface engineering of PSCs.

5.4 Conclusion

In summary, in this Chapter we have developed a facile modification approach to micro-structure conventionally used mesoporous TiO_2 layers using a thermolysable additive in the form of thiourea. This additive crystallises within the deposited film and during calcination is removed, leaving structural undulations in the mesoporous film. These structural undulations possess some voids and areas of reduced mesoporous layer thickness. Deposition of the perovskites on such modified layers causes less preferential growth compared to the modified mesoporous layers. These microstructural and interfacial changes facilitate PSCs with an enhanced average PCE of 18.7% compared to 18.1% for devices using pristine mesoporous TiO_2 layers. This PCE enhancement arises from an enhanced carrier extraction from the perovskite and an increased recombination resistance. Given the variations in the mesoporous layer and the structure of the perovskite on the different mesoporous layers, we cannot unambiguously assign these enhancements to the TiO_2/perovskite interface. To do so would require further work on identifying the specific role of structural anisotropy and its impact on charge extraction across both ETL and HTL interfaces. None-the-less, the results of this chapter do show that undulating mesoporous layers are not detrimental to the performance of PSCs, and can in fact cause enhanced device characteristics when such layers are optimally engineered. This is an important finding when considering the prospects of large-scale manufacturing, where achieving uniformity may be challenging.

Reference

1. Jeon, N. J.; Na, H.; Jung, E. H.; Yang, T. Y.; Lee, Y. G.; Kim, G.; Shin, H. W.; Il Seok, S.; Lee, J.; Seo, J., A Fluorene-terminated Hole-transporting Material for Highly Efficient and Stable Perovskite Solar Cells. Nature Energy 2018, 3 (8), 682-689.
2. Leijtens, T.; Stranks, S. D.; Eperon, G., E. ; Lindblad, R.; Johansson, E. M. J.; Ian, J. M.; Håkan, R.; Ball, J. M.; Lee, M. M.; Snaith, H. J., Electronic Properties of Meso-Superstructured and Planar Organometal Halide Perovskite Films: Charge Trapping, Photodoping, and Carrier Mobility and Planar Organometal Halide Perovskite Films: Charge Trapping, Photodoping, and Carrier Mobility. ACS Nano 2014, 8, 7147-7155.
3. Ramirez, D.; Alejandro Mejía Escobar, M.; Montoya, J. F.; Jaramillo, F., Understanding the Role of the Mesoporous Layer in the Thermal Crystallization of a Meso-Superstructured Perovskite Solar Cell. The Journal of Physical Chemistry C 2016, 120 (16), 8559-8567.
4. Listorti, A.; Juarez-Perez, E. J.; Frontera, C.; Roiati, V.; Garcia-Andrade, L.; Colella, S.; Rizzo, A.; Ortiz, P.; Mora-Sero, I., Effect of Mesostructured Layer upon Crystalline Properties and Device Performance on Perovskite Solar Cells. Journal of Physical Chemistry Letters 2015, 6 (9), 1628-1637.
5. Rafieh, A. I.; Ekanayake, P.; Wakamiya, A.; Nakajima, H.; Lim, C. M., Enhanced Performance of CH3NH3PbI3-based Perovskite Solar Cells by Tuning the Electrical and Structural Properties of Mesoporous TiO2 Layer via Al and Mg Doping. Solar Energy 2019, 177, 374-381.
6. Giordano, F.; Abate, A.; Baena, J. P. C.; Saliba, M.; Matsui, T.; Im, S. H.; Zakeeruddin, S. M.; Nazeeruddin, M. K.; Hagfeldt, A.; Graetzel, M., Enhanced Electronic Properties in Mesoporous TiO2 via Lithium Doping for High-efficiency Perovskite Solar Cells. Nature Communications 2016, 7, 10379.
7. Huangfu, M.; Shen, Y.; Zhu, G.; Xu, K.; Cao, M.; Gu, F.; Wang, L., Copper Iodide as Inorganic Hole Conductor for Perovskite Solar Cells with Different Thickness of Mesoporous Layer and Hole Transport Layer. Applied Surface Science 2015, 357, 2234-2240.
8. Yin, J.; Cao, J.; He, X.; Yuan, S.; Sun, S.; Li, J.; Zheng, N.; Lin, L., Improved Stability of Perovskite Solar Cells in Ambient Air by Controlling the Mesoporous Layer. Journal of Materials Chemistry A 2015, 3 (32), 16860-16866.
9. Jeon, N. J.; Noh, J. H.; Kim, Y. C.; Yang, W. S.; Ryu, S.; Seok, S. I., Solvent Engineering for High-performance Inorganic-organic Hybrid Perovskite Solar Cells. Nature Materials 2014, 13 (9), 897-903.
10. Wang, Z. D.; Yoshida, M.; George, B., Theoretical Study on the Thermal Decomposition of Thiourea. Computational and Theoretical Chemistry 2013, 1017, 91-98.
11. Huang, W.-F.; Chen, H.-T.; Lin, M. C., Density Functional Theory Study of the Adsorption and Reaction of H2S on TiO2 Rutile. Journal of Physical Chemistry C 2009, 113, 20411–20420.
12. Nanayakkara, C. E.; Pettibone, J.; Grassian, V. H., Sulfur Dioxide Adsorption and Photooxidation on Isotopically-labeled Titanium Dioxide Nanoparticle Surfaces: Roles of Surface Hydroxyl Groups and Adsorbed Water in the Formation and Stability of Adsorbed Sulfite and Sulfate. Physical Chemistry Chemical Physics 2012, 14 (19), 6957-6966.
13. Zhang, S.; Stolterfoht, M.; Armin, A.; Lin, Q.; Zu, F.; Sobus, J.; Jin, H.; Koch, N.; Meredith, P.; Burn, P. L.; Neher, D., Interface Engineering of Solution-Processed Hybrid Organohalide Perovskite Solar Cells. ACS Applied Materials & Interfaces 2018, 10 (25), 21681-21687.
14. Xu, X.; Ma, C.; Cheng, Y.; Xie, Y.-M.; Yi, X.; Gautam, B.; Chen, S.; Li, H.-W.; Lee, C.-S.; So, F.; Tsang, S.-W., Ultraviolet-ozone Surface Modification for Non-wetting Hole Transport Materials Based Inverted Planar Perovskite Solar Cells with Efficiency Exceeding 18%. Journal of Power Sources 2017, 360, 157-165.

15. Bi, C.; Wang, Q.; Shao, Y.; Yuan, Y.; Xiao, Z.; Huang, J., Non-wetting Surface-driven High-aspect-ratio Crystalline Grain Growth for Efficient Hybrid Perovskite Solar Cells. Nature Communications 2015, 6, 7747.
16. O'Regan, B. C.; Barnes, P. R.; Li, X.; Law, C.; Palomares, E.; Marin-Beloqui, J. M., Optoelectronic Studies of Methylammonium Lead Iodide Perovskite Solar Cells with Mesoporous TiO2: Separation of Electronic and Chemical Charge Storage, Understanding Two Recombination Lifetimes, and the Evolution of Band Offsets during J-V Hysteresis. Journal of the American Chemical Society 2015, 137 (15), 5087-5099.
17. Du, T.; Kim, J.; Ngiam, J.; Xu, S.; Barnes, P. R. F.; Durrant, J. R.; McLachlan, M. A., Elucidating the Origins of Subgap Tail States and Open-Circuit Voltage in Methylammonium Lead Triiodide Perovskite Solar Cells. Advanced Functional Materials 2018, 28 (32), 1801808.
18. Li, Z.; Gao, F.; Greenham, N. C.; McNeill, C. R., Comparison of the Operation of Polymer/Fullerene, Polymer/Polymer, and Polymer/Nanocrystal Solar Cells: A Transient Photocurrent and Photovoltage Study. Advanced Functional Materials 2011, 21 (8), 1419-1431.
19. Zarazua, I.; Sidhik, S.; Lopez-Luke, T.; Esparza, D.; De la Rosa, E.; Reyes-Gomez, J.; Mora-Sero, I.; Garcia-Belmonte, G., Operating Mechanisms of Mesoscopic Perovskite Solar Cells through Impedance Spectroscopy and J-V Modeling. The Journal of Physical Chemistry Letters 2017, 8 (24), 6073-6079.
20. Almora, O.; Cho, K. T.; Aghazada, S.; Zimmermann, I.; Matt, G. J.; Brabec, C. J.; Nazeeruddin, M. K.; Garcia-Belmonte, G., Discerning Recombination Mechanisms and Ideality Factors through Impedance Analysis of High-efficiency Perovskite Solar Cells. Nano Energy 2018, 48, 63-72.

Chapter 6.

Bi-Functional Modification of 2D Perovskite Layers using F4TCNQ for Efficient Hybrid Perovskite Solar Cells

Synopsis

In previous chapters we have shown that structurally and chemically optimised ETLs facilitate PSCs with good performance and high reproducibility. However, the traditional architecture on top of the perovskite layer in PSCs, still suffers from problems of charge transfer limitations and stability between the perovskite and HTLs. In this work, we report a facile method to develop high-efficiency PSCs by introducing a molecular additive to modify the 2D-3D perovskite stacking-layered architecture. The modified hybrid perovskite layer is formed via in-situ growth of a 2D perovskite capping layer with a F4TCNQ additive on top of 3D Cs/MA/FA mixed perovskite film. The devices with modified 2D capping layers show improved charge transfer and reduced charge recombination characteristics as compared to pristine 2D perovskite device. The 3D/2D PSCs using this modified 2D perovskite capping layer show the highest steady state PCE of 20.3% compared to 18.2% for the pristine 2D counterpart. In addition to enhancing device performance, the fluorine terminated molecular additive helps to retain the PCE of PSCs in the presence of a thicker 2D perovskite capping layer. This helps to provide an easy way to improve the stability of PSCs via thickening the 2D perovskite capping layers to better protect the 3D perovskite.

The contents presented in this chapter have been modified to a thesis chapter format from a submitted manuscript that is currently under review.

6.1 Introduction

Metal-halide perovskites have become one of the most promising materials for high-performance photovoltaic devices due to their unique optoelectronic properties, such as strong light harvesting capability,[1] long charge carrier diffusion lengths and mobilities,[2] and narrow PL bands with high PL quantum yield.[3] Owing to these advantages, the PCE of PSCs has improved rapidly from 3.8% to ~ 25% in less than ten years.[4-7] These record efficiencies are now on par with those of silicon-based solar cells, and come with major advantages in terms of ease of processing and lower cost, at an equivalent manufacturing scale.[6, 8] However, the underlying problems of metal-halide perovskites in terms of their instability towards moisture and difficulty in controlling crystallisation during solution-processing hindering the further development of PSC technology.[9, 10]

Significant research effort has been focused on improving the PSC performance by means of configuration design,[1, 11, 12] material optimization,[13-15] interface engineering[16, 17] and encapsulation techniques.[18] As we discussed in **Section 1.4.4**, lowering the spatial dimensionality of the perovskite from 3D to 2D by using non-volatile and longer chain organic cations has been reported widely as a promising strategy to simultaneously reduce interfacial defects and improve stability of PSCs.[19, 20] Incorporation of these types of cations induces the formation of layered structures having the general chemical form $(RNH_3)_2A_{n-1}B_nX_{3n+1}$ (n=1,2,3,4…∞),[21] where $A_{n-1}B_nX_{3n+1}$ is the perovskite sheet, RNH_3^+ is a large aliphatic or aromatic alkylammonium spacer cation that isolates the perovskite layers, and *n* is an integer that represents the number of perovskite sheets.[22, 23] In general, structures having smaller values of *n* are considered to be 2D or quasi-2D perovskites, with 3D-like perovskite structure developing with increasing values of *n*. The existence of the larger spacer cations in the 2D sheet structures makes them more hydrophobic than their 3D analogues, facilitating an improved environmental stability,[24] which is conducive to their commercialization.[25] However, the PCE of 2D PSCs is limited due to their high exciton binding energies and poor charge transport properties.[22] In response, hybrid 3D/2D perovskite bilayers have emerged as a promising PSC configuration, with the 3D perovskite dominating the optical absorption and charge transport characteristics and a very thin 2D perovskite capping layer acting to passivate surface defects and protect the 3D perovskite from moisture.[26, 27] It has been shown that the performance of 3D/2D PSCs is strongly influenced by the thickness of the 2D perovskite layer, with PSCs possessing a thicker 2D perovskite capping layer showing improved stability but lower PCEs due to the poor charge transporting properties of the 2D layer.[26, 28]

Herein, we describe the use of additive-engineering as a means for alleviating the charge-transport limitations of the 2D perovskite capping layer in hybrid 3D/2D PSCs. 2,3,5,6-Tetrafluoro-7,7,8,8-tetracyanoquinodimethane (F4TCNQ) is a fluorinated molecular p-type dopant and a strong electron acceptor that is used widely for doping conjugated polymers to enhance their electrical conductivity.[29] Moreover, its use as a perovskite surface modifier has been studied, showing that it effectively passivates the surface states through supramolecular interactions between the F4TCNQ and the surface halide ions.[27] In the present work, we investigate the role of F4TCNQ as an additive for 2D perovskite capping layer and its influence on charge extraction, recombination and device performance within 3D/2D hybrid PSCs. We find that through this approach the PCEs of the resulting devices is significantly improved from 18.1% to over 20%. Importantly, the introduction of F4TCNQ also rendered the performance of hybrid 3D/2D PSCs less sensitive to the thickness of the 2D perovskite capping layer, making this approach a feasible strategy for improving the moisture stability of PSCs through use of a thicker 2D perovskite capping layer.

6.2 Experiment and Characterization

6.2.1 Fabrication of PSC Devices

Depositions of dense TiO_2 blocking layers, mesoporous layers, perovskite layers, Spiro-OMeTAD HTLs and Au electrodes were reported in **Chapter 2**.

Hybrid 3D/2D-architecture perovskite films were fabricated via in-situ crystallization of 2D perovskite on a pre-formed mixed-cation 3D perovskite film comprising caesium, FA and MA.[26] A 5 mg mL^{-1} solution of BAI in IPA was spin-cast onto a $Cs_{0.05}FA_{0.79}MA_{0.16}PbI_{2.49}Br_{0.51}$ 3D perovskite film (**Figure 6.1**). The 3D perovskite film is formulated so as to contain a stoichiometric excess of PbI_2 of around 5 mole%. The F4TCNQ additive was introduced into the 2D capping solution and then spin-cast onto the 3D layer. In this section, we use the notation 2DF# to denote the weight percentage of F4TCNQ relative to BAI in the 2D capping solution, e.g. 2DF5 corresponds to an IPA solution containing 0.25 mg mL^{-1} F4TCNQ and 5 mg mL^{-1} BAI.

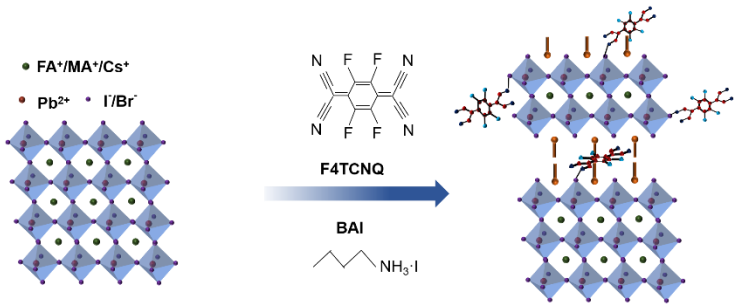

Figure 6.1 The schematic of 3D/2D/F4TCNQ perovskite deposition.

6.2.2 Characterization

Characterization of absorption and PL spectra, XRD patterns, SEM images of perovskite films as well as J-V curves, impedance and IPCE spectra of devices were described in **Chapter 2**.

Grazing-Incidence Wide-Angle X-ray Scattering (GIWAXS) Measurement: In this work we used GIVAXS to analyse the crystallization of the very thin 2D perovskite layers. This measurement was conducted at the SAXS/WAXS beamline of the Australian Synchrotron. 12 keV photons, with a grazing incidence angle of 0.2°, were used and recorded on a Pilatus 1 m detector placed ≈24 cm from the sample position.

Grazing-Angle Reflectance FTIR (GA-FTIR) Measurement: A Bruker Vertex 80v FTIR with a Bruker A562 gold coated integrating sphere was used to characterize the charge states of F4TCNQ in 2D perovskite layers. The angle of incidence was 65°.

6.3 Results and Discussion

6.3.1 Morphology of 3D/2D Perovskite Layers

The top-view SEM images (**Figures 6.2**) show the morphologies of 3D, 3D/2D, 3D/2DF5 and 3D/2DF10 perovskite films, respectively. A clear change in the surface morphology of the 3D perovskite film (**Figure 6.2A**) is observed when the 2D perovskite capping layer is formed (**Figure 6.2B**), with the grain boundaries becoming indistinct and the appearance of a secondary surface layer emerging. These changes are ascribed to the reconstruction of the perovskite on the surface during the formation of the 2D perovskite.[26] The addition of 5% w/w F4TCNQ into the BAI solution (i.e.

2DF5) results in no further change to this surface morphology (**Figure 6.2C**), while evidence of both aggregation of the additive on the surface as well as pin-holes is seen upon further increase in F4TCNQ for 2DF10 (**Figures 6.2D** and **Figure 6.3**).

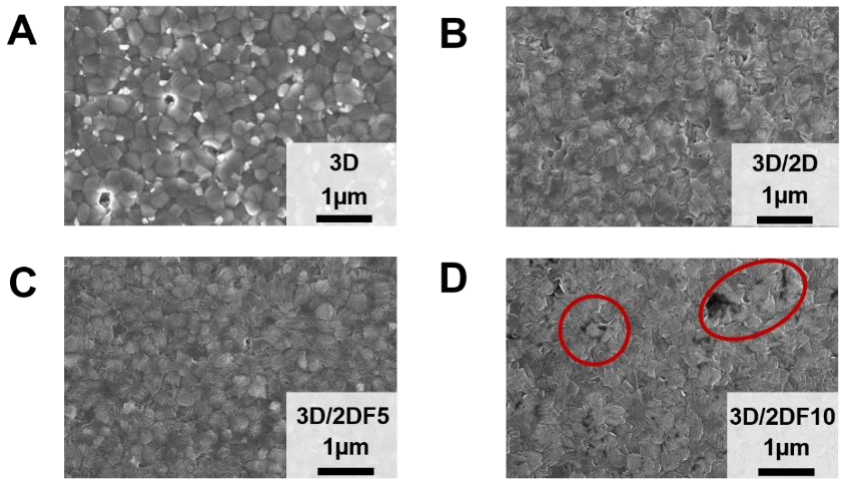

Figure 6.2 Top-view SEM images of 3D (A), 3D/2D (B), 3D/2DF5 (C) and 3D/2DF10 (D) perovskite films.

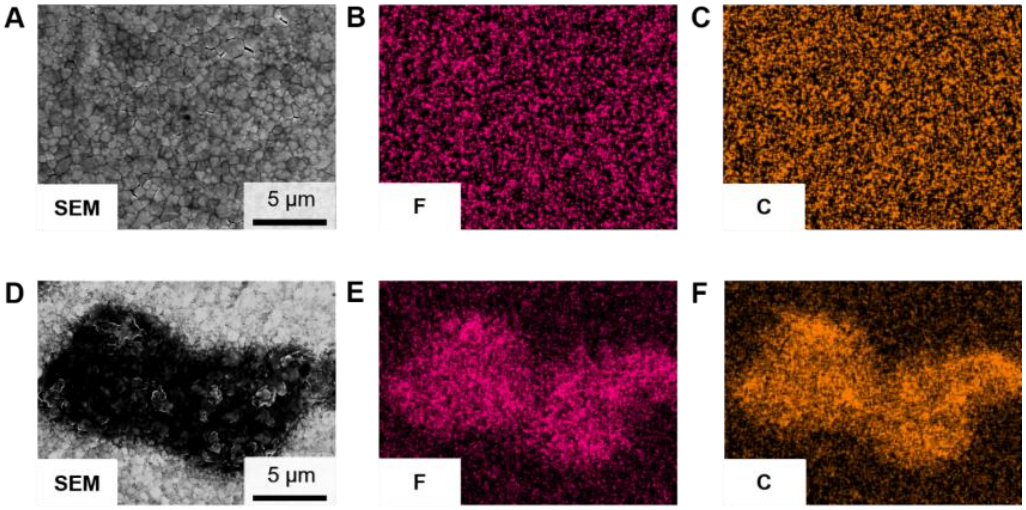

Figure 6.3 Top-view SEM images and F- and C- elements EDX mapping of 3D/2DF5 (A-C) and 3D/2DF10 (D-F) perovskite films.

6.3.2 Composition of 3D/2D Perovskite Layers

XRD patterns included in **Figure 6.4** show that pure 3D perovskite possess the typical polycrystalline structure with a slight excess of PbI_2 as seen by the (100) scattering peak at 12.7°.[30] The formation of new scattering peaks at 9.04° and 13.5° is seen for the 3D/2D films, which are characteristic of the

(040) and (060) planes of a 2D perovskite (n =2).[24] This is accompanied by the disappearance of the PbI_2 peak. This suggests that the formation of the 2D perovskite capping layer arises from the conversion of residual PbI_2 at the surface of the 3D perovskite film. The slight reduction in the intensity of the scattering peaks associated with the 3D perovskite is consistent with its partial conversion in the 2D perovskite formation process. The intensity of the 2D peak at 13.5° appears to increase with increasing F4TCNQ content, suggesting that the F4TCNQ-modified 2D perovskite is textured preferentially to enhanced scattering from the (060) plane,[31, 32] whereas the additive does not significantly change the peak positions of the (110) and (220) planes at 14.1° and 28.4°, respectively, of the underlying 3D perovskite.[33] Thus, it is concluded that the F4TCNQ additive slightly alters the lattice structure of the 2D perovskite capping layer but has essentially no effect on the bulk crystallinity of the underlying 3D perovskite film.

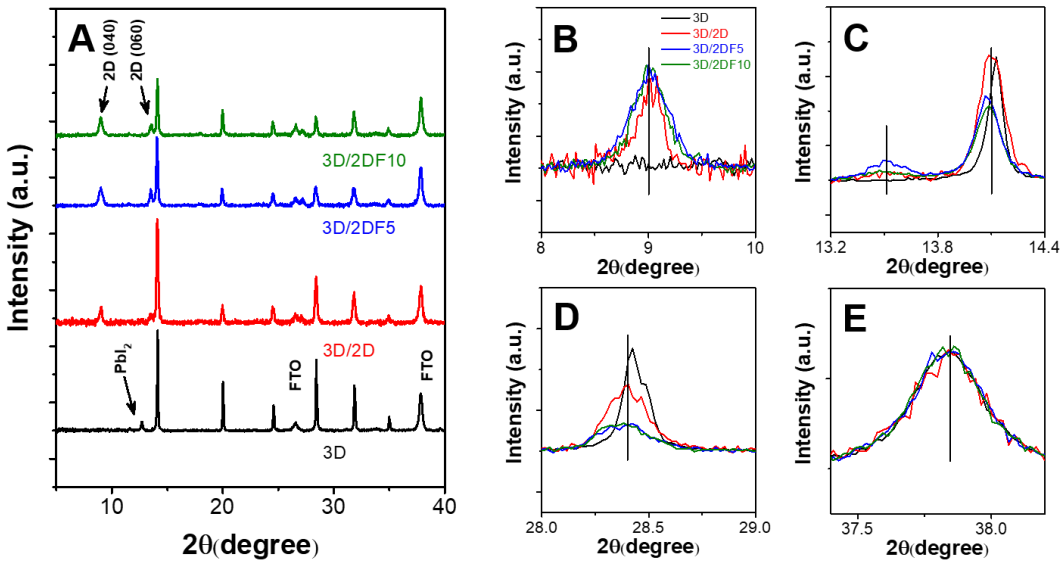

Figure 6.4 XRD patterns of perovskite films 3D, 3D/2D, 3D/2DF5 and 3D/2DF10 perovskite films.

The detailed structure variation of 3D, 3D/2D and 3D/2DF films can be deduced from their 2D GIWAXS patterns in and the corresponding intensity versus q curves in **Figure 6.5**. The characteristic peaks of 2D perovskite at ~ 0.32 $Å^{-1}$, 0.65 $Å^{-1}$ and 1.3 $Å^{-1}$ appear in all 3D/2D perovskite films indicating the formation of 2D perovskite, while the crystal orientation is not changed by F4TCNQ additive **Figure 6.5A-D**. In addition, it is clear that the 2D perovskite characteristic peaks in **Figure 6.5E** are not shifted by F4TCNQ, which demonstrates that the molecule does not intercalate into the 2D perovskite crystalline domains. However, the full width at half maxima (FWHM) of these peaks is broadened with increasing concentration of F4TCNQ added in 2D perovskite layer. This is

indicative that the F4TCNQ reduces the 2D perovskite domain size. Using the simplified Scherrer equation:[34, 35]

$$\mathbf{D} = \frac{2\pi K}{\Delta_q} \qquad \mathbf{(6.1)}$$

where D refers to the mean size of the domains, K is a shape factor (typically 0.8−1, here we use 1) and Δq is the FWHM, the domain sizes of the 2D, 2DF5 and 2DF10 perovskites can be estimated to be 23.3 nm, 18.5 nm and 17.0 nm, respectively.

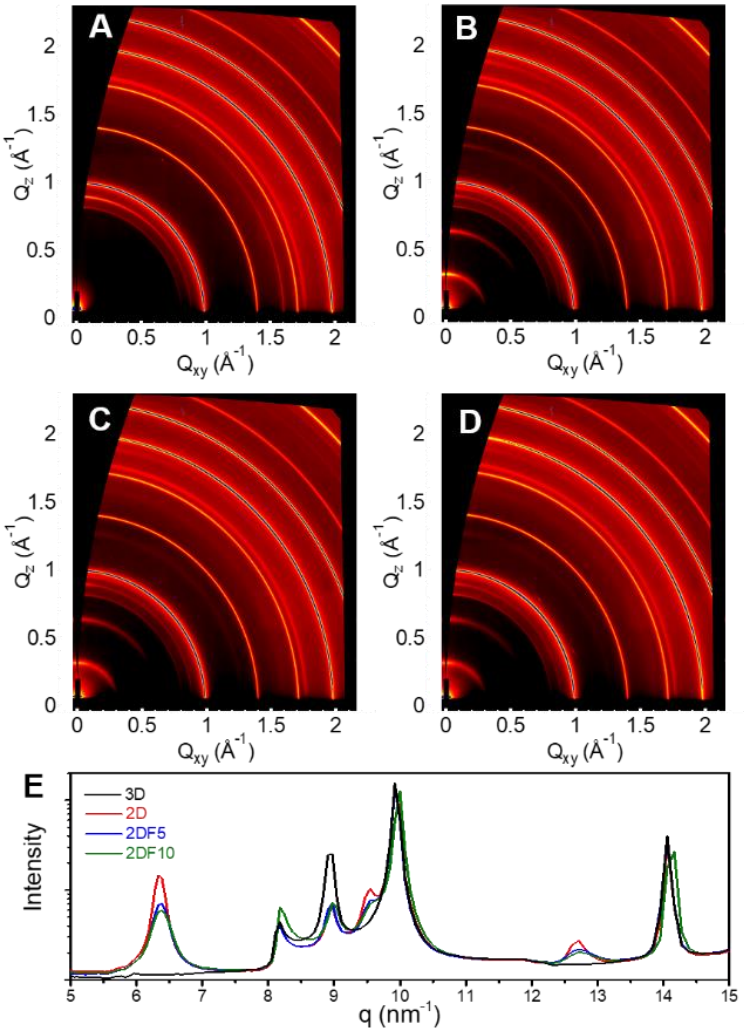

Figure 6.5 2D GIWAXS patterns (A) and intensity vs q curves (B) for the diffraction features obtained from GIWAXS of 3D, 3D/2D, 3D/2DF5 and 3D/2DF10 perovskite films, respectively.

6.3.3 FTIR of 3D/2D Perovskite Layers

The variation domain size of 2D perovskite can be ascribed to the interaction between F4TCNQ and perovskite. GA-FTIR spectra of pristine F4TCNQ, 3D/2D and 3D/2DF5 perovskite films (**Figure**

6.6) were characterized to investigate the charge state of F4TCNQ in perovskite. The cyano-vibrational stretch mode of pristine F4TCNQ at 2227 cm^{-1} shifts to 2217 cm^{-1} and 2195 cm^{-1} when it is in the 2D perovskite film, confirming the interaction (halogen bonding) between F4TCNQ and halogen in perovskite.[36] This enables F4TCNQ to assemble at the surfaces and boundaries of 2D perovskite domains, and likely suppresses their growth and reduce their domain sizes. Notably, according to **Equation 6.2**, the degree of charge transfer (δ) is linearly scale with the frequency shift (Δv) :[37]

$$\delta = \frac{2\Delta v}{v_0}\left[1 - \frac{v_1^2}{v_0^2}\right]^{-1} \quad \textbf{(6.2)}$$

where *v0* and *v1* represent the vibrational frequencies of "free" component and its radical-ion, respectively.

Based on the experimental shift observed here, we can estimate that the degree of charge transfer is about 1 This is consistent with a partial charge transfer, which is more reminiscent of a covalent bond formation. This itself would confirm a more passivating role by the F4-TCNQ.[38]

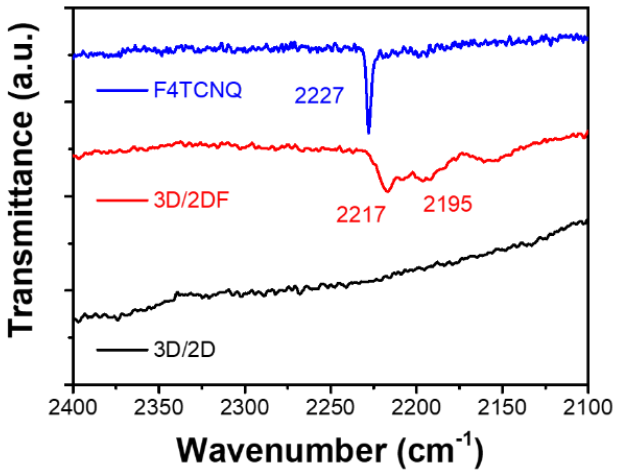

Figure 6.6 GA-FTIR spectra of F4TCNQ, 3D/2D, 3D/2DF5 perovskite films. The glancing angle was used at 65°.

6.3.4 Optical Properties of 3D/2D Perovskite Layers

UV-vis absorption measurements of a pristine 3D perovskite film and 3D/2D perovskite bilayers, with and without F4TCNQ additive, are shown in **Figure 6.7A**. These measurements were made using substantially thinner 3D perovskites layers than those typically used in devices (0.2 mol L^{-1} precursor solution *c.f.* 1.2 mol L^{-1} precursor solution for devices) to amplify the 2D perovskite capping layer absorption compared to that on thicker 3D perovskite films. The absorption band

centred at ~ 550 nm is consistent with the formation of an *n*=2 2D perovskite capping layer.[39] Interestingly, this absorption peak shows a slight red shift after the addition of F4TCNQ in the 2D perovskite films, which implies a narrowing of the bandgap of the 2D perovskite.[31]

To further probe the optical properties of these perovskite layers, steady-state PL and TRPL measurements were conducted. The PL peak of the 3D perovskite layer is located at ~762 nm, with a negligible emission shift being detected for the 3D/2D perovskite layers with and without F4TCNQ (**Figure 6.7B).** This is consistent with their absorption results. TRPL measurements were conducted to examine the charge transport and defect passivation effects of the 2D capping layer on the 3D perovskite films (**Figure 6.7C**). To quantify these characteristics, the PL decay curves were fitted using the following bi-exponential decay function **Euqtion 6.2**, with the best-fit parameter values summarized in **Table 6.1**

$$Y = A_1\, exp\left(\frac{-t}{\tau_1}\right) + A_2\, exp\left(\frac{-t}{\tau_2}\right) + y_0 \qquad \textbf{(6.3)}$$

where A_n and τ_n are the best-fit amplitudes and PL decay times, respectively. Compared with a pristine 3D perovskite film, the longer PL lifetime for 3D/2D perovskite bilayer films, with or without F4TCNQ modification of the 2D layer, is extended from 2.9 μs to more than 3.2 μs. The introduction of the F4TCNQ into the 2D perovskite layer does not significantly alter the lifetime of the longer-lived PL component of 3D/2D perovskite bilayer films. This indicates that the 2D perovskite capping layer, either with or without F4TCNQ modification, reduces non-radiative recombination of the 3D perovskite layer. Meanwhile, the proportion of the very short-lived component that decays within 0.3 μs after excitation increases concomitantly with increasing amount of F4TCNQ. Given that the fast decay component in TRPL of perovskites is typically associate with charge extraction,[40] we attribute the observed trend to an enhanced rate of charge extraction between the 3D perovskite and the 2D perovskite capping layers.

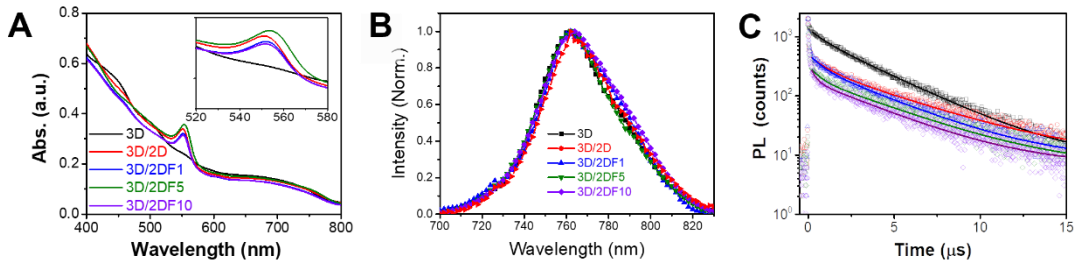

Figure 6.7 UV-vis absorption (A), steady state PL (B) and TRPL spectra (C) of 3D, 3D/2D and 3D/2D (with 1%, 5% and 10% F4TCNQ) perovskite films on glass slides.

Table 6.1 Best-fit parameter values from analysis of PL decay according to **Equation 6.3** for 3D, 3D/2D and 3D/2DF# perovskite films on glass slides.

Sample	A_1	τ_1(ns)	A_2	τ_2(ns)	τ_{avg}(ns) *
3D	23.5	0.43	76.5	2.94	2.83
3D/2D	45.4	0.23	54.6	3.44	3.27
3D/2DF1	53.2	0.22	46.8	3.24	3.02
3D/2DF5	65.9	0.13	34.1	3.38	3.15
3D/2DF10	71.5	0.13	28.5	3.27	2.98

*The average lifetime τ ave $= \sum \alpha i * \tau i^2 \; / \sum \alpha i \; * \tau i$

6.3.5 Device Performance

Having shown that the use of F4TCNQ as an additive within 2D capping layers on 3D perovskites results in changes to the structural, optical and interfacial properties of the system, we investigated the impacts of these changes on PSCs. As shown in **Figure 6.8A**, the solar cell architecture investigated here consisted of fluorine-doped tin oxide (FTO)/TiO_2/m-TiO_2/3D perovskite (with or without 2D perovskite capping layer)/Spiro-OMeTAD/Au configuration. The corresponding energy levels of the individual materials are included in **Figure 6.8B**,[41] with the perovskite levels having been determined from their measured ionization energies (IE) using photoelectron spectroscopy in air, see **Figure 6.9**, and their optical bandgap.[41, 42] Under the assumption that the measured IE approximates the absolute value of the VBM in perovskites, IE = -VBM.[42] These measurements show that the VBM of the 3D $Cs_{0.05}FA_{0.79}MA_{0.16}PbI_{2.49}Br_{0.51}$ perovskite layer decreases from -5.55 eV to -5.45 eV after being capped by a 2D perovskite layer, while the VBM for all F4TCNQ modified samples is within the error of the instrument (±0.05 eV).

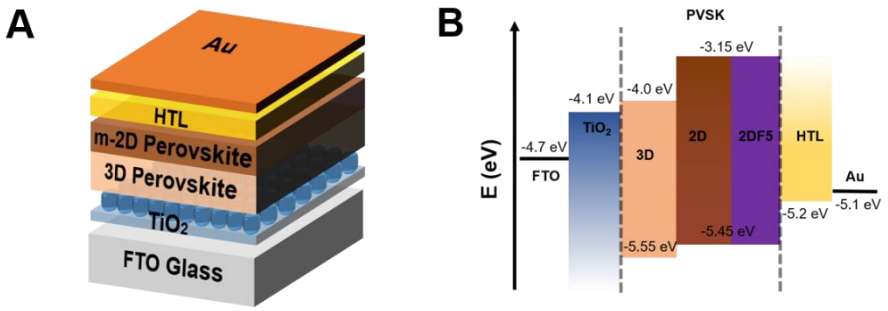

Figure 6.8 Schematics of device architecture (A) and corresponding energy alignment (B) of devices with 2DF layers.

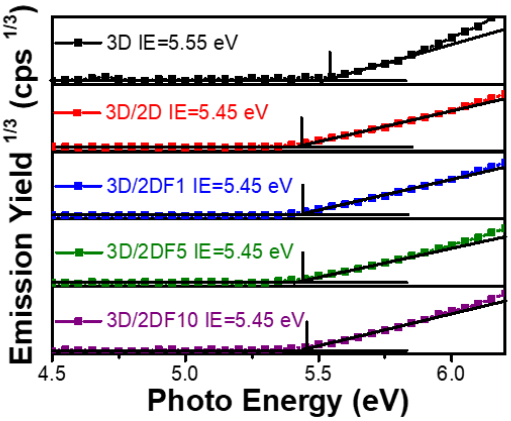

Figure 6.9 PESA spectra of perovskite films with 3D, 3D/2D and 3D/2DF perovskite films on FTO glass with TiO_2 compact and mesoporous layers.

Figure 6.10 shows the J-V characteristics and steady-state PCEs of the PSC devices, respectively. The 3D PSC shows J_{sc} = 21.3 mA cm^{-2}, V_{oc} = 1.10 V, FF = 74.4% and PCE= 17.5% under a reverse-bias scan from 1.2 V to -0.1 V, with the corresponding steady-state PCE stabilising at 17.4% within 300 s. Coating of a pristine 2D perovskite layer on top of the 3D perovskite film improves the PCE to 18.2%, which is attributed to the enhancement in V_{oc} (1.11 V) and FF (76.6%). The improvement of the V_{oc} and FF is attributed to the larger Fermi-level splitting resulting from the reduced non-radiative recombination loss at the interface between the perovskite layer and charge extraction layers.[37] This trend is further supported by the larger dark-current onset voltage for devices with perovskites comprising the 2D layer. Notably, there is no significant improvement in the R_s of the PSCs with 3D/2D layers, but an increase in the R_{sh} value from 612 Ω cm^2 to 869 Ω cm^2 is observed. This is consistent with previous reports, which indicate that J_{sc} does not show obvious improvement in the presence of 2D perovskite layers because their poor conductivity hinders the transport of carriers and reduces the charge collection effectiveness of HTLs.[24, 37]

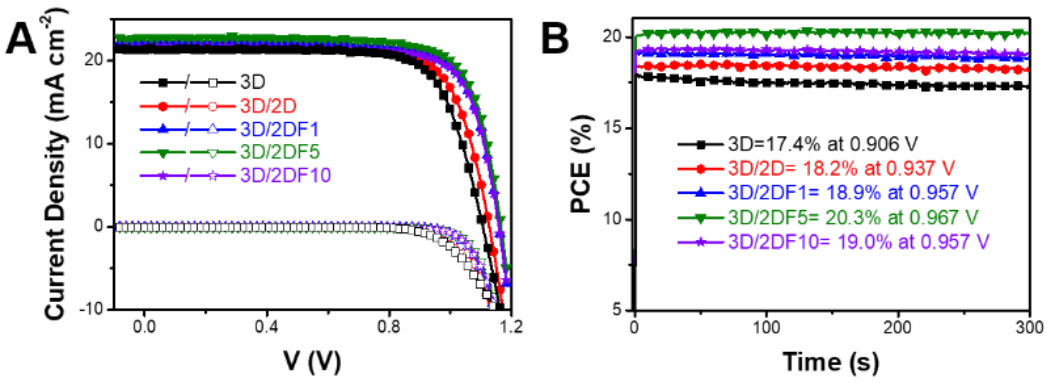

Figure 6.10 Light and dark J-V curves (A) and steady-state PCE characterization (B) of PSCs with 3D, 3D/2D and 3D/2DF (1%, 5% and 10%) perovskite films.

The drawback of pure 2D capping layers is efficiently resolved by the addition of F4TCNQ molecules. For the optimal 5% w/w F4TCNQ sample (3D/2DF5), the R_s reduces significantly from 5.01 Ω cm^2 to 3.70 Ω cm^2, and the R_{sh} further increases to 2,937 Ω cm^2. As a result, the J_{sc}, V_{oc} and PCE of the PSC are dramatically improved to 22.8 mA cm^{-2}, 1.16 V and 20.1%, respectively. Forward and reverse scan J-V curves of these optimised devices, which exhibit negligible hysteresis, as well as IPCE results of 3D/2D and 3D/2DF5 PSCs are shown in **Figure 6.11**. Notably, the devices comprising 3D/2DF10 hybrid perovskite films exhibit slightly lower PCEs compared with 3D/2DF5 PSC. This is attributed to the accumulation of F4TCNQ additives on the perovskite film surface and/or structural variations of the 2D capping layer at the higher F4TCNQ concentrations, as discussed earlier. The distribution of device parameters is shown in **Figure 6.12** and also summarized in **Table 6.2**. The average J_{sc}, V_{oc}, FF and PCE of 3D/2DF5 devices are 22.3 mA cm^{-2}, 1.15 V, 75.5% and 19.4%, respectively, with good reproducibility. These parameters are significantly better than those of 3D/2D PSCs without F4TCNQ additives at 20.8 mA cm^{-2}, 1.11 V, 75.1% and 17.3%, respectively.

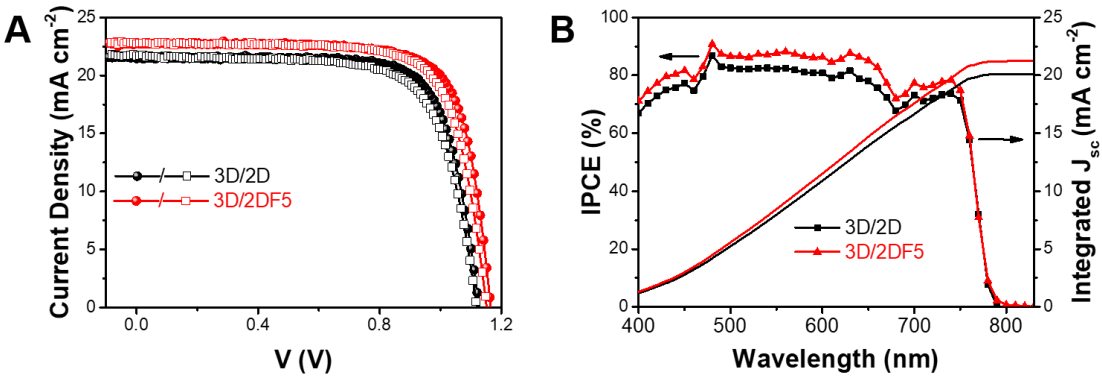

Figure 6.11 Reverse and forward scan of J-V curves (A) and IPCE spectra (B) of PSCs with 3D/2D and 3D/2DF5 hybrid perovskite films.

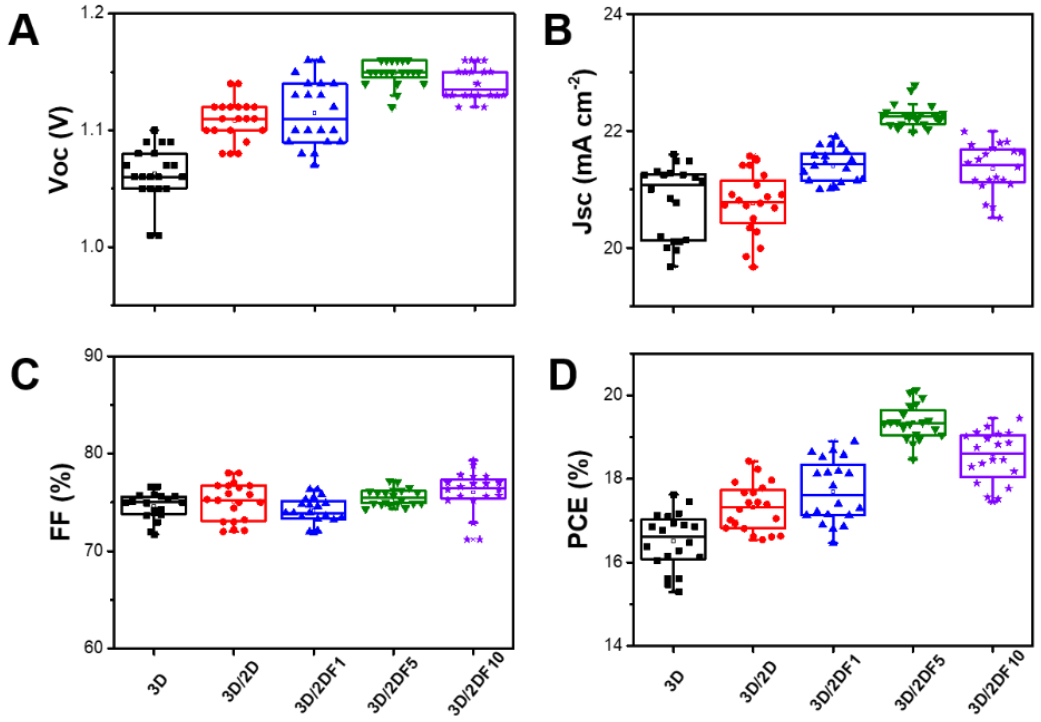

Figure 6.12 Summarized parameters in box chart of 20 samples for devices with 3D, 3D/2D and 3D/2DF (1%, 5% and 10%) perovskite films.

Table 6.2 Summarized parameters of PSCs corresponding to **Figure 6.12**. R_{sh} and R_s are obtained from the slopes of J-V curves at zero and over open circuit potential.

Devices	J_{sc} (mA cm^{-2})	V_{oc} (V)	FF (%)	PCE (%)	R_s (Ω cm^2)	R_{sh} (Ω cm^2)
3D	21.3 [a] (20.8±0.81) [b]	1.10 (1.06±0.04)	74.4 (75.0±3.1)	17.5 (16.5±1.0)	6.68	612
3D/2D	20.9 (20.8±0.8)	1.11 (1.11±0.03)	76.6 (75.1±2.7)	18.2 (17.3±1.1)	5.01	869
3D/2DF1	21.3 (21.4±0.6)	1.15 (1.11±0.05)	76.1 (74.1±2.5)	18.8 (17.7±1.1)	3.72	2160
3D/2DF5	22.8 (22.3±0.5)	1.16 (1.15±0.02)	76.0 (75.5±1.8)	20.1 (19.4±0.7)	3.70	2937
3D/2DF10	21.8 (21.3±0.7)	1.15 (1.14±0.02)	76.6 (76.0±3.3)	19.3 (18.4±1.1)	4.11	1486

[a] Parameters of the best device in each architecture.

[b] Mean values with standard deviation are calculated from 20 independent devices.

6.3.6 Investigation of the Charge Transport Dynamics

To better understand the underlying differences that the 2D perovskite and F4TCNQ have on the PSC characteristics, charge-carrier dynamics were investigated using the TPC technique. For these measurements, the devices were illuminated using a 200 μs square pulse of 525 nm LED light. By conducting TPC measurements at different light intensities, the turn-on and turn-off dynamics[43] and charge trapping and de-trapping characteristics[44] inside the device could be probed. **Figure 6.13** shows the normalized TPC responses of the PCS devices at short circuit condition, with the raw TPC responses of these devices being included in **Figure 6.14**. The results show that the PSCs with 3D and 3D/2D architectures possess a rapid photocurrent component and a much slower secondary process that exhibits a rise time in the 100's μs range. The introduction of the F4TCNQ additive into the 2D capping layer causes a dramatic enhancement of these slower rise-time dynamics to < 20 μs at 20 mW cm^{-2}. This clearly indicates enhanced extraction dynamics for these devices.

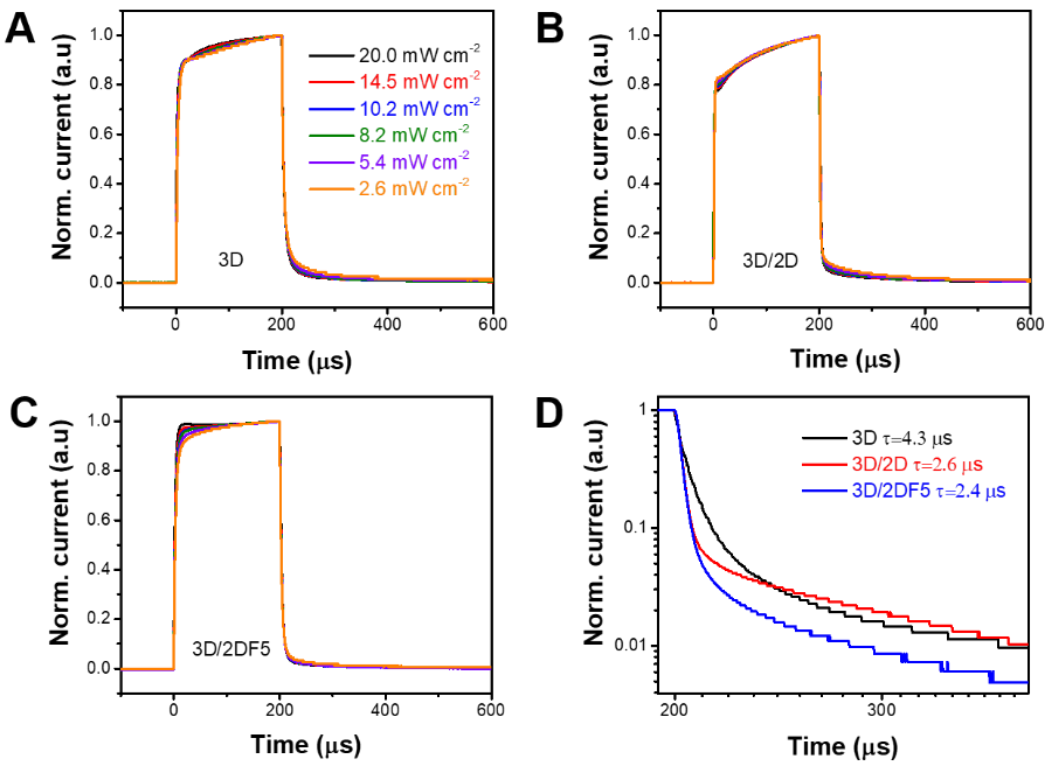

Figure 6.13 Normalized photocurrent decay curves of PSCs with 3D (A), 3D/2D (B) and 3D/2DF5 (C) perovskite films, respectively and the semi-log TPC decay profiles of PSCs at 5.7 mW cm^{-2} (D).

The existence of the slower rise time process in TPC measurements is suggestive of an imbalance between the electron and hole mobilities and/or the presence of traps in these devices.[45] Since we have shown that the 3D structure is unaffected by the inclusion of F4TCNQ in the 2D perovskite layer and that long-lived charge carriers exist in our devices, we can infer that the origin of these differences arises due to extraction differences at the interface between the 3D perovskite layer and the charge extraction layers (i.e. 2DF5/Spiro-OMeTAD) rather than the bulk of the device. It is worth noting that the TPC risetime of the 3D/2DF0 device is slower compared to the 3D or 3D/2DF5 devices. This is direct evidence of retarded charge extraction due to the insulating nature of the pristine 2D layer.[46] We also observe a small change in the risetime in the F4TCNQ 2D layer devices as a function of LED intensity (**Figure 6.14**), with the risetime becoming slower with a decrease in the incident light intensity. This suggests that shallow traps in these devices do exist, but are progressively filled under increasing light, albeit at low intensities.

The turn-off dynamics of the TPC curves consist of an initial fast decay component, which originates from the collection of free charge carriers, and a long-lived photocurrent tail corresponding to the collection of slower mobile carriers (see **Figure 6.14D-F**). It is clear that the fast decay is accelerated

by introducing the 2D perovskite capping layer. Moreover, the magnitude of the initial decay component further increases upon adding F4TCNQ. This indicates that the modified 2D perovskite capping layer improves hole extraction from the perovskite, likely due to a better passivated interface between the 3D and 2D perovskites. Notably, the pristine 2D perovskite capping layer exhibits an enhanced proportion of the long carriers (beyond ~ 250 µs) compared to both the 3D and modified 2D interfaces. This can be ascribed to charge accumulation at 3D/2D interface, again, due to the low intrinsic conductivity of the 2D layer.

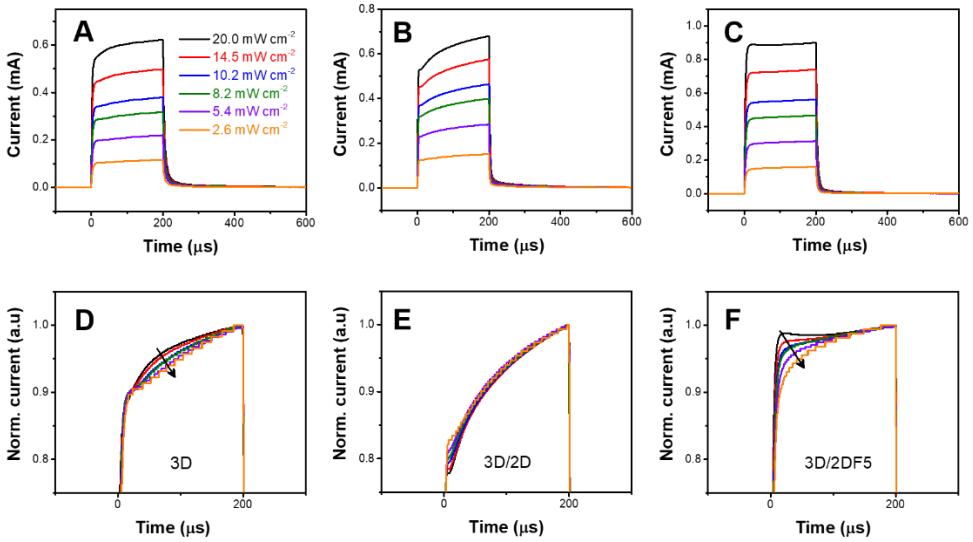

Figure 6.14 Raw TPC curves of PSCs with 3D (A), 3D/2D (B) and 3D/2DF5 (C) perovskite films collected at short-circuit condition under different light intensities. The lower row highlights the turn-on dynamics of the normalized TPC curves.

The recombination and charge-transfer dynamics were further investigated by using impedance spectroscopy measurements under 1-sun illumination at various applied voltages (**Figure 6.15**).[47] These measurements yield the total recombination resistance in the device, which is related directly to the recombination at the interface of the perovskite and the charge extraction process.[48] The analysis is based on fits to the equivalent circuit shown in the **Figure 6.15D** inset, where R_s is the series resistance due to wire and contact resistance, R_1 and R_2 represent the low and high-frequency resistance, respectively, C_g is the high-frequency capacitance, interpreted as the geometric capacitance of the device related to the dielectric properties of the perovskite, and C_s is the low frequency capacitance, which is associated with the surface charge accumulation at perovskite interface.[49] The recombination resistance (R_{rec}) of the PCSs devices was determined as a sum of R1 and R2. Near short-circuit conditions (≤ 0.4 V), the R_{rec} scarcely changes (see **Figure 6.15D**) with an increasing in the applied voltage, suggesting free carrier recombination is less pronounced in this

voltage regime. Although the values of R_{rec} are similar near short-circuit condition across the different devices, the devices with pristine and modified 2D layers do exhibit a slightly higher R_{rec} value compared to pristine 3D perovskite. This suggests that 3D devices have a slightly higher degree of bimolecular recombination near short-circuit condition. This observation also confirms that the shallow traps in the pristine and modified 2D devices observed from the TPC measurements do not have a significant contribution to the free carrier losses.[50] The observed results are also consistent with the PSC device characteristics, where the introduction of the 2D perovskite capping layer improves the J_{sc} and FF values. Meanwhile, for voltages greater than 0.8 V (i.e. beyond the device maximum power-point), the R_{rec} value decreases exponentially with increased applied voltage, indicating a dominant non-radiative (bimolecular) recombination process is occurring in this voltage regime.[47,48] Moreover, the 2DF5 PSC showed larger recombination resistance values as compared to PSCs with either pristine 3D or 3D/2D perovskites. This is indicative that the interfacial recombination process is suppressed by the F4TCNQ additive.

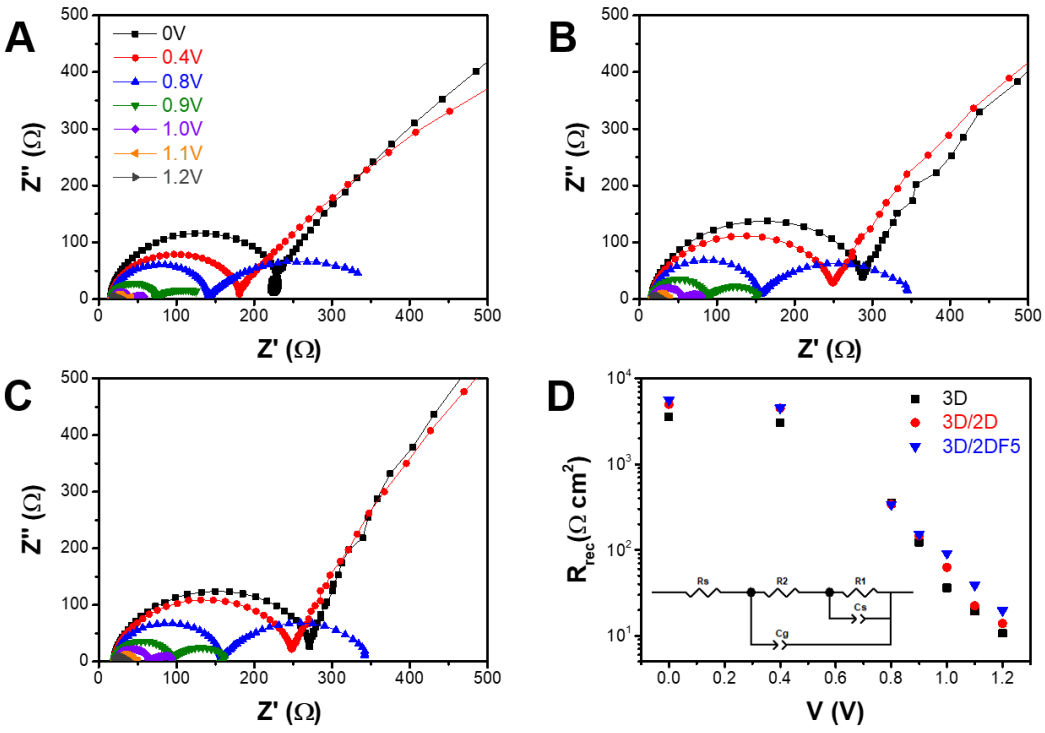

Figure 6.15 Nyquist plot measured at different applied voltages corresponding to the PSCs with 3D (A), 3D/2D (B) and 3D/2DF5 (C) perovskite films, respectively, and calculated recombination resistances, R_{rec}, (D) based on fits to the equivalent circuit shown in the inset.

Based on the above observations, we schematically depict the proposed charge collection mechanisms across the different PCSs used in this study in **Figure 6.16**. For the neat 3D perovskites (**Figure 6.16A**), trap states are more likely to be generated on the surface, which leads to recombination of

charges at this interface (**Figure 6.16B**).[51] Application of a thin 2D perovskite capping layer grown *in situ* (**Figure 6.16C**) passivates the 3D perovskite surface to effectively eliminate surface trap states. This results in efficient charge separation and suppression of non-radiative recombination channels.[26] As a result, devices fabricated using 3D/2D PSCs exhibit an enhanced V_{oc} compared to neat 3D perovskites. However, their J_{sc} and FF parameters do not increase, which likely arises from the poor charge-transport properties of the 2D perovskite capping layer restricting charge extraction (**Figure 6.16D**). Meanwhile, when F4TCNQ additive is introduced into the 2D perovskite layer, it can interact with halide ions within the 2D perovskite sheets and at the 3D/2D surface (**Figure 6.16E**). It has been suggested that this interaction results in an interfacial dipole layer at the 3D perovskite/F4TCNQ interface, which leads to a favourable enhancement of the electric field at the perovskite/HTL interface.[52] Furthermore, the 2D perovskite and F4TCNQ serve as an electron donor and electron acceptor pair, respectively, thus these can form an effective heterojunction which facilitates an enhanced charge-carrier extraction through the 2D layer (**Figure 6.16F**). We ascribe the above-mentioned phenomena collectively to the overall improvements in the performance of the PSC devices in the presence of F4TCNQ.

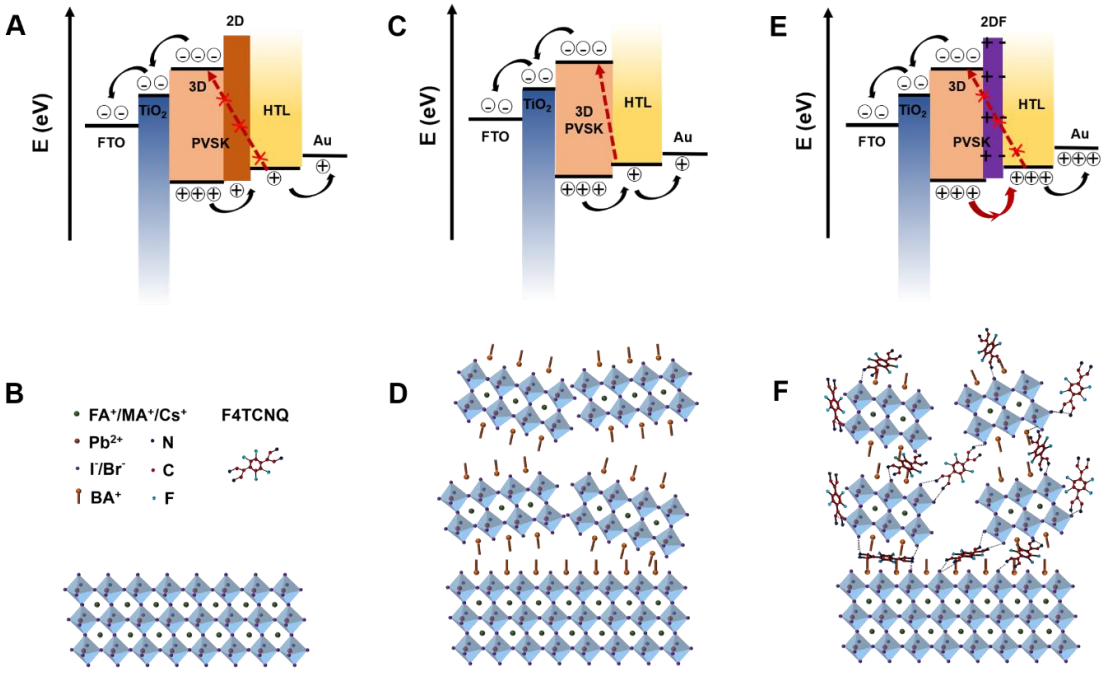

Figure 6.16 Schematic architectures of perovskite films and mechanisms of corresponding PSCs with 3D (A, B), 3D/2D (C, D) and 3D/2DF (E, F) perovskite films, respectively.

6.3.7 Stability Testing of Devices

In addition to maximising efficiency, a key to the future prospects of PSCs is overcoming their operational instability. To this end, here we have measured the stability of the 3D, 3D/2D and 3D/2DF5 PSCs of unsealed devices for 30 days at room temperature and high humidity (~ 60% RH) conditions (**Figure 6.17**). Moreover, in the inset photographs in **Figure 6.17D** we also show the changes in the bare perovskite films exposed to these same testing conditions. It is found that high humidity leads to fast degradation of perovskite, with the PSC of the 3D device degrading to 47% of its original PCE during the testing period. This degradation is mainly reflected in a reduced J_{sc} and FF. The photographs of the 3D perovskite film exhibit changes from a brown to yellow colour, which reflects a decomposition from perovskite to PbI_2, respectively.[26] In comparison, the 2D perovskite layer dramatically improves the PSC stability to 80% of the original PCE after the 30 days, with the F4TCNQ modified 2D layer further improving this stability factor to 85%. Photographs of the 2D-modified perovskite films show that, while becoming slightly opaquer, their dark brown colour remains intact after the testing period. This is clear evidence that these films are more resistant to moisture than 3D perovskites alone. XRD of the various perovskite films after testing verify these visual trends (see **Figure 6.18**), with the 3D perovskite exhibiting approximately 3 times the amount of PbI_2 than the 3D/2DF5 perovskite sample.

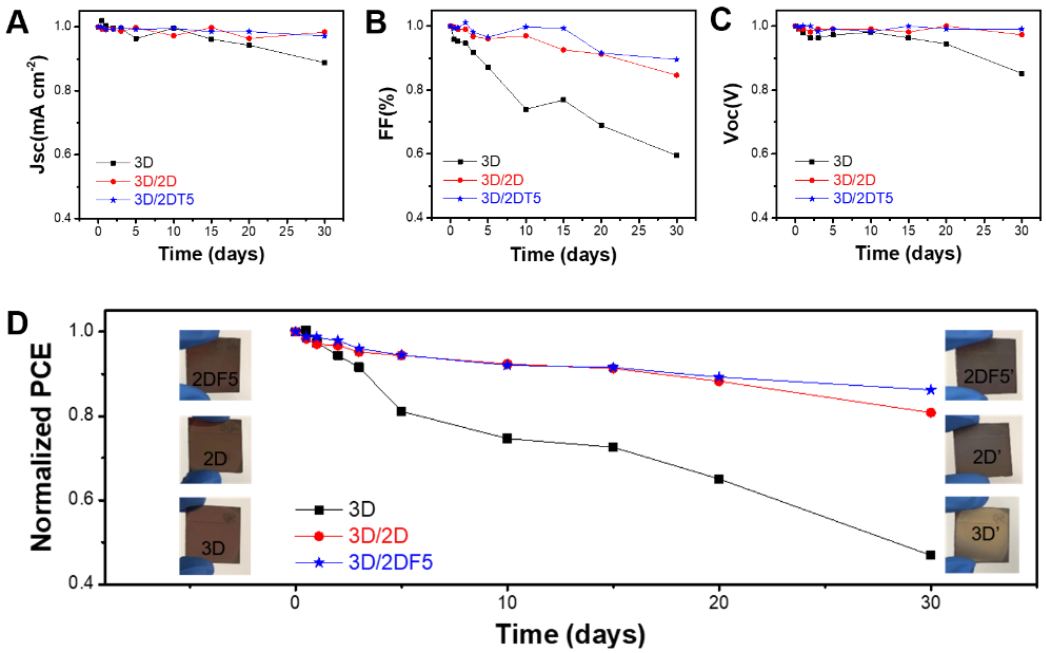

Figure 6.17 (A) Detailed J_{sc}, FF and V_{oc} of PSCs with 3D, 3D/2D and 3D/2DF5 perovskite films. (B) Stabilities test of unencapsulated devices with 3D, 3D/2D and 3D/2DF5 perovskite films under ambient environment with ~60% humidity for 30 days. The photo images inset exhibit corresponding initial (3D, 2D, 2DF5) and final perovskite (3D', 2D', 2DF5') films.

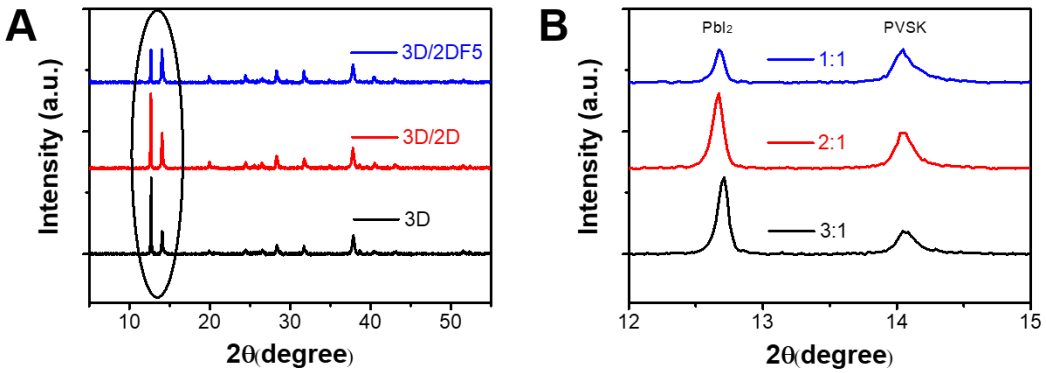

Figure 6.18 XRD patterns of 3D, 3D/2D, 3D/2DF5 perovskite films after being exposed under ambient environment with 60% humidity for 30 days. The ratios in (B) show the intensity ratio of the PbI2 peak and the perovskite peak.

The origins of this moisture-resistance have been probed through contact angle measurements between water droplets and the perovskite films (see **Figure 19**). Compared with the neat 3D perovskite, the pristine 2D perovskite capping layer increases its contact angle from 42.5° to 51.8°, likely owing to the hydrophobic properties of the BA^+ cation forming the 2D structure.[26] Addition of the fluorine-terminated F4TCNQ further increases the contact angle to 56.6°. Evidently, the improved hydrophobicity suppresses the decomposition of the perovskite to PbI_2 under the high humidity environment.[10]

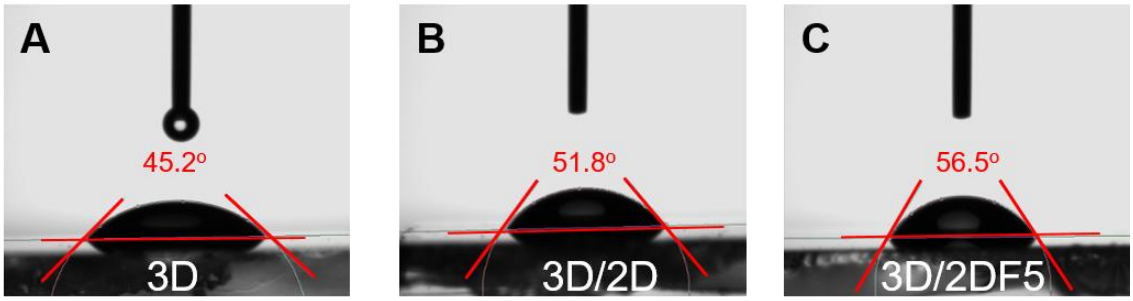

Figure 6.19 Contact angle characterization of corresponding perovskite films.

Given that the poor charge extraction in 3D/2D perovskite layer is improved upon addition of the F4TCNQ additive, it seems reasonable to expect that the performance of the PCE can be retained even when using a thicker 2D layer. To test this postulation, thicker 2D perovskite capping layers were produced by increasing the concentration of BAI in the 2D precursor solution. As the 2D perovskite capping layer is difficult to distinguish from the underlying bulk perovskite absorber layer in cross-sectional SEM, the very thin 2D perovskite layers made by 5mg mL^{-1} BAI solution could not be detected accurately using this approach (**Figure 6.20A, B**). However, we can estimate the

thicknesses of both 2D and 2DF5 perovskite capping layers using 10 mg mL^{-1} BAI solution at ~28 nm (see **Figure 6.20 C, D**). This value is similar to the thickness of the 2D perovskite layer (~30 nm) deposited using 8mg mL^{-1} phenethylammonium iodide in isopropanol as a cation precusor.[26]

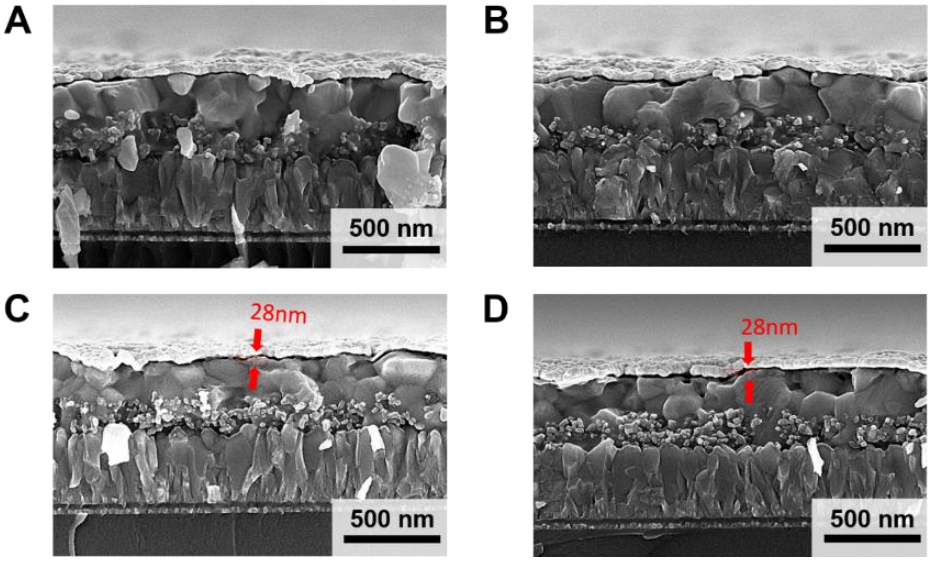

Figure 6.20 Cross-section SEM images of 3D/2D and 3D/2DF5 perovskite films using 5 mg mL^{-1} (A, B) and 10 mg mL^{-1} (C, D) BAI/IPA precursor solution, respectively.

To further verify that the thickness of the 2D perovskite is increased with higher BAI concentration, XRD was used to measure the relative 2D and 3D scattering contributions (**Figure 6.21**). These measurements show that the characteristic peaks representing (040) and (060) of the 2D perovskite using 10mg mL^{-2} BAI solution, either with or without F4TCNQ, are dramatically enhanced compared with films prepared using 5mg mL^{-1} BAI solution (see **Figure 6.4A**). This confirms a higher conversion of 3D perovskite to 2D perovskite when the concentration of BAI is increased from 5 mg mL^{-1} to 10 mg mL^{-1}.

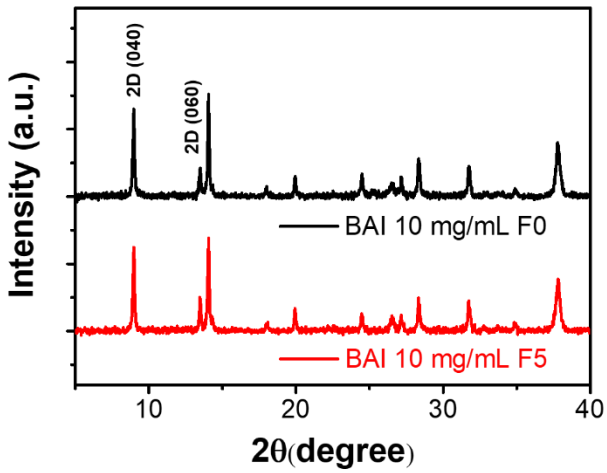

Figure 6.21 XRD patterns of 3D/2D and 3D/2DF5 made by 10 mg mL^{-1} BAI solution.

6.3.8 Impact of 2D Perovskite Thickness

The PSC device fabricated using the 3D/2D perovskite structure based on 10 mg mL^{-1} BAI solution show a comparatively low J_{sc} (20.3 mA cm^{-2}), FF (71.7%) and PCE (16.4%) relative to those prepared using the 5 mg mL^{-1} solution. Meanwhile, the PSC fabricated with an added 5% F4TCNQ in this thick 2D perovskite capping layer configuration, displays a comparatively higher J_{sc} (21.4 mA cm^{-2}), FF (73.1%) and PCE (18.2%) (**Figure 6.22**). This is consistent with the poor charge transport properties of 2D perovskites hindering charge extraction for the unmodified 3D/2D sample,[28] and further evidence of the improved electrical properties of the additive modified 2D perovskite. In addition, the PSCs with the thicker 2D perovskite layer further result in better stability than those made by 5 mg mL^{-1} BAI solution. As shown in **Figure 6.17**, the 5% F4TCNQ modified device retains almost 90% of its PCE after 30 days of exposure to ~60% humidity. Thus, this facile strategy of F4TCNQ addition to the 2D perovskite layer paves an efficient way to simultaneously improve the stability and performance of PSCs.

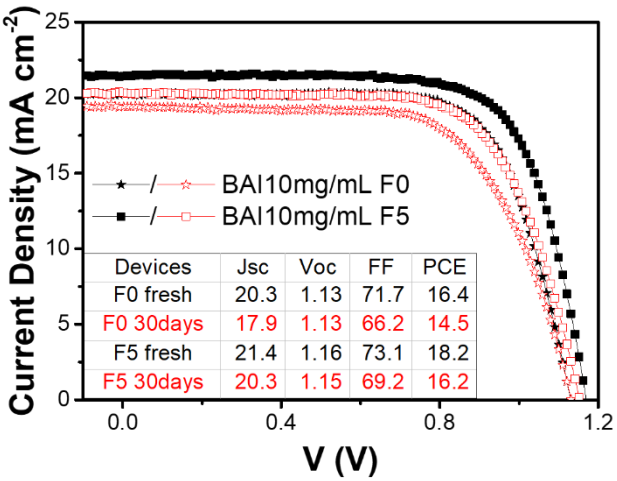

Figure 6.22 Reverse scanned J-V curves of fresh and 30 days later of PSCs with 3D/2D and 3D/2DF5 made by 10 mg mL^{-1} BAI solution, respectively. The PSCs were stored in ambient air with ~60% humidity.

6.4 Conclusions

In this study we have developed a unique and facile interfacial engineering approach that has enabled the performance and stability of 3D/2D perovskite solar cells to be improved. The hydrophobic molecular additive F4TCNQ was used to modify the 2D perovskite capping layer without altering the 3D perovskite crystal properties. The strong electron-acceptor characteristic of F4TCNQ enables it to form supramolecular interaction with halide ions in the perovskite, which helps reduce the degree of interfacial non-radiative recombination and improve charge extraction characteristics from the bulk

perovskite to the 2D perovskite layer. These enhancements result in PSCs with 2D perovskite capping layers modified with F4TCNQ exhibiting device efficiencies of >20%, which represents a relative increase compared to neat 3D and 3D/2D perovskite structures by 24% and 13%, respectively. In addition to the improvement in the charge transport properties, the long-term stability of PSCs with F4TCNQ was also dramatically enhanced. Importantly, the improved charge transporting properties enabled by the F4TCNQ additive made the PSC efficiency less sensitive to the thickness of the 2D perovskite capping layer. Thus, implementing a thicker 2D capping layer helped to provide a facile but effective strategy to further improve the stability of PSCs without significantly compromising on device efficiency. It is envisaged that the universal nature of this facile 2D layer modification lends itself to be adopted in other perovskite-based optoelectronics, where achieving high efficiency and maximising stability are also paramount. A key aspect of the current work is that the devices developed harness doped Spiro-OMeTAD as a hole-transport layer. Given that F4TCNQ is a known p-dopant, the assessment of undoped polymers as hole-transport layer provides an interesting future work direction that may both accentuate the role of interfacial doping, but also further improve on the stability of the fabricated devices.

References:

1. Lee, M. M.; Teuscher, J.; Miyasaka, T.; Murakami, T. N.; Snaith, H. J., Efficient Hybrid Solar Cells Based on Meso-superstructured Organometal Halide Perovskites. Science 2012, 338, 643-647.
2. Shi, D.; Adinolfi, V.; Comin, R.; Yuan, M.; Alarousu, E.; Buin, A.; Chen, Y.; Hoogland, S.; Rothenberger, A.; Katsiev, K.; Losovyj, Y.; Zhang, X.; Dowben, P. A.; Mohammed, O. F.; Sargent, E. H.; Bakr, O. M., Low Trap-state Density and Long Carrier Diffusion in Organolead Trihalide Perovskite Single Crystals. Science 2015, 347 (6221), 519-522.
3. Sutter-Fella, C. M.; Li, Y.; Amani, M.; Ager, J. W.; Toma, F. M.; Yablonovitch, E.; Sharp, I. D.; Javey, A., High Photoluminescence Quantum Yield in Band Gap Tunable Bromide Containing Mixed Halide Perovskites. Nano Letters 2016, 16 (1), 800-806.
4. NREL Efficiency chart https://www.nrel.gov/pv/cell-efficiency. (accessed April, 17).
5. Lee, M. M.; Teuscher, J.; Miyasaka, T.; Murakami, T. N.; Snaith, H. J., Efficient Hybrid Solar Cells Based on Meso-Superstructured Organometal Halide Perovskites. Science 2012, 338 (6107), 643-647.
6. Kojima, A.; Teshima, K.; Shirai, Y.; Miyasaka, T., Organometal Halide Perovskites as Visible-Light Sensitizers for Photovoltaic Cells. Journal of the American Chemical Society 2009, 131, 6050-6051.
7. Jung, E. H.; Jeon, N. J.; Park, E. Y.; Moon, C. S.; Shin, T. J.; Yang, T. Y.; Noh, J. H.; Seo, J., Efficient, Stable and Scalable Perovskite Solar Cells Using Poly(3-hexylthiophene). Nature 2019, 567 (7749), 511-515.
8. Qi, J.; Y. Zhao; X. Zhang; X. Yang; Y. Chen; Z. Chu; Q. Ye; X. Li; Z. Yin; You, J., Surface Passivation of Perovskite Film for Efficient Solar Cells. Nature Photonics 2019, 13 (7), 460–466.
9. Chen, B.; Rudd, P. N.; Yang, S.; Yuan, Y.; Huang, J., Imperfections and Their Passivation in Halide Perovskite Solar Cells. Chemical Society Reviews 2019, 48, 3842-3867.
10. Niu, G.; Guo, X.; Wang, L., Review of Recent Progress in Chemical Stability of Perovskite Solar Cells. Journal of Materials Chemistry A 2015, 3, 8970-8980.
11. Chen, W.; Wu, Y.; Yue, Y.; Liu, J.; Zhang, W.; Yang, X.; Chen, H.; Bi, E.; Ashraful, I.; Grätzel, M.; Han, L., Efficient and Stable Large-area Perovskite Solar Cells with Inorganic Charge Extraction Layers. Science 2015, 350 (6263), 944-948.
12. Liu, T.; Chen, K.; Hu, Q.; Zhu, R.; Gong, Q., Inverted Perovskite Solar Cells: Progresses and Perspectives. Advanced Energy Materials 2016, 6 (17), 1600457.
13. McMeekin, D. P.; Sadoughi, G.; Rehman, W.; Eperon, G. E.; Saliba, M.; Hörantner, M. T.; Haghighirad, A.; Sakai, N.; Korte, L.; Rech, B.; Johnston, M. B.; Herz, L. M.; Snaith, H. J., A Mixed-cation Lead Mixed-halide Perovskite Absorber for Tandem Solar Cells. Science 2016, 351 (6269), 151-155.
14. Giordano, F.; Abate, A.; Baena, J. P. C.; Saliba, M.; Matsui, T.; Im, S. H.; Zakeeruddin, S. M.; Nazeeruddin, M. K.; Hagfeldt, A.; Graetzel, M., Enhanced Electronic Properties in Mesoporous TiO2 via Lithium Doping for High-efficiency Perovskite Solar Cells. Nature Communications 2016, 7, 10379.
15. Wu, W. Q.; Wang, Q.; Fang, Y.; Shao, Y.; Tang, S.; Deng, Y.; Lu, H.; Liu, Y.; Li, T.; Yang, Z.; Gruverman, A.; Huang, J., Molecular Doping Enabled Scalable Blading of Efficient Hole-transport-layer-free Perovskite Solar Cells. Nature Communications 2018, 9 (1), 1625.
16. Zhou, H.; Chen, Q.; Li, G.; Luo, S.; Song, T. B.; Duan, H. S.; Hong, Z.; You, J.; Liu, Y.; Yang, Y., Interface Engineering of Highly Efficient Perovskite Solar Cells. Science 2014, 345 (6196), 542-546.
17. Chen, J.; Seo, J. Y.; Park, N. G., Simultaneous Improvement of Photovoltaic Performance and Stability by In Situ Formation of 2D Perovskite at (FAPbI3)0.88(CsPbBr3)0.12/CuSCN Interface. Advanced Energy Materials 2018, 8 (12), 1702714.

18. Cheacharoen, R.; Rolston, N.; Harwood, D.; Bush, K. A.; Dauskardt, R. H.; McGehee, M. D., Design and Understanding of Encapsulated Perovskite Solar Cells to Withstand Temperature Cycling. Energy & Environment Science 2018, 11 (1), 144-150.
19. Grancini, G.; Roldan-Carmona, C.; Zimmermann, I.; Mosconi, E.; Lee, X.; Martineau, D.; Narbey, S.; Oswald, F.; Angelis, F. D.; Graetzel, M.; Nazeeruddin, M. K., One-Year Stable Perovskite Solar Cells by 2D/3D Interface Engineering. Nature Communications 2017, 8, 15684.
20. Cao, D. H.; Stoumpos, C. C.; Farha, O. K.; Hupp, J. T.; Kanatzidis, M. G., 2D Homologous Perovskites as Light-Absorbing Materials for Solar Cell Applications. Journal of the American Chemical Society 2015, 137 (24), 7843-7850.
21. David, B. M., Synthesis, Structure, and Properties of Organic-Inorganic Perovskites and Related Materials. John Wiley & Sons, Inc.: 1999; Vol. 48, p 246.
22. Yan, J.; Qiu, W.; Wu, G.; Heremans, P.; Chen, H., Recent Progress in 2D/quasi-2D Layered Metal Halide Perovskites for Solar Cells. Journal of Materials Chemistry A 2018, 6 (24), 11063-11077.
23. Lu, J.; Jiang, L.; Li, W.; Li, F.; Pai, N. K.; Scully, A. D.; Tsai, C. M.; Bach, U.; Simonov, A. N.; Cheng, Y. B.; Spiccia, L., Diammonium and Monoammonium Mixed-Organic-Cation Perovskites for High Performance Solar Cells with Improved Stability. Advanced Energy Materials 2017, 7 (18), 1700444.
24. Li, J.; Wang, J.; Zhang, Y.; Wang, H.; Lin, G.; Xiong, X.; Zhou, W.; Luo, H.; Li, D., Fabrication of Single Phase 2D Homologous Perovskite Microplates by Mechanical Exfoliation. 2D Materials 2018, 5 (2), 021001.
25. Meng, L.; You, J.; Yang, Y., Addressing the Stability Issue of Perovskite Solar Cells for Commercial Applications. Nature Communications 2018, 9 (1), 5265.
26. Chen, P.; Bai, Y.; Wang, S.; Lyu, M.; Yun, J.; Wang, L., In Situ Growth of 2D Perovskite Capping Layer for Stable and Efficient Perovskite Solar Cells. Advanced Functional Materials 2018, 28 (17), 1706923.
27. Cho, Y.; Soufiani, A. M.; Yun, J. S.; Kim, J.; Lee, D. S.; Seidel, J.; Deng, X.; Green, M. A.; Huang, S.; Ho-Baillie, A. W. Y., Mixed 3D-2D Passivation Treatment for Mixed-Cation Lead Mixed-Halide Perovskite Solar Cells for Higher Efficiency and Better Stability. Advanced Energy Materials 2018, 8 (20), 1703392.
28. Tsai, H.; Asadpour, R.; Blancon, J. C.; Stoumpos, C. C.; Even, J.; Ajayan, P. M.; Kanatzidis, M. G.; Alam, M. A.; Mohite, A. D.; Nie, W., Design Principles for Electronic Charge Transport in Solution-processed Vertically Stacked 2D Perovskite Quantum Wells. Nature Communications 2018, 9 (1), 2130.
29. Yan, H.; Manion, J.; Yuan, M.; Garcia de Arquer, F.; McKeown, G.; Beaupre, S.; Leclerc, M.; Sargent, E.; Seferos, D., Increasing Polymer Solar Cell Fill Factor by Trap-Filling with F4-TCNQ at Parts Per Thousand Concentration. Advanced Materials 2016, 28 (30), 6491-6496.
30. Burschka, J.; Pellet, N.; Moon, S. J.; Humphry-Baker, R.; Gao, P.; Nazeeruddin, M. K.; Gratzel, M., Sequential Deposition as a Route to High-performance Perovskite-sensitized Solar Cells. Nature 2013, 499 (7458), 316-319.
31. Blancon, J. C.; Tsai, H.; Nie, W.; Stoumpos, C. C.; Pedesseau, L.; Katan, C.; Kepenekian, M.; Soe, C. M. M.; Appavoo, K.; Sfeir, M. Y.; Tretiak, S.; Ajayan, P. M.; Kanatzidis, M. G.; Even, J.; Crochet, J. J.; Mohite, A. D., Extremely Efficient Internal Exciton Dissociation through Edge States in Layered 2D Perovskites. Science 2017, 355 (6331), 1288-1292.
32. Chang, Y. H.; Lin, J. C.; Chen, Y. C.; Kuo, T. R.; Wang, D. Y., Facile Synthesis of Two-dimensional Ruddlesden-Popper perovskite Quantum Dots with Fine-tunable Optical Properties. Nanoscale Research Letter 2018, 13 (1), 247.
33. Tan, H.; Jain, A.; Voznyy, O.; Lan, X.; Pelayo, F.; Fan, J.; Quintero-Bermudez, R.; Yuan, M.; Zhang, B.; Zhao, Y.; Fan, F.; Li, P.; Quan, L.; Zhao, Y.; Lu, Z.; Yang, Z.; Hoogland,

S.; Sargent, E., Efficient and Stable Solution-processed Planar Perovskite Solar Cells via Contact Passivation. Science 2017, 355, 722-726.
34. Rivnay, J.; Mannsfeld, S. C.; Miller, C. E.; Salleo, A.; Toney, M. F., Quantitative Determination of Organic Semiconductor Microstructure from the Molecular to Device Scale. Chemical Reviews 2012, 112 (10), 5488-5519.
35. Wu, T.; Yang, Y.; Zou, Y.; Wang, Y.; Wu, C.; Han, Y.; Song, T.; Zhang, Q.; Gao, X.; Sun, B., Nanoplatelet Modulation in 2D/3D Perovskite Targeting Efficient Light-emitting Diodes. Nanoscale 2018, 10 (41), 19322-19329.
36. Liu, C.; Huang, Z.; Hu, X.; Meng, X.; Huang, L.; Xiong, J.; Tan, L.; Chen, Y., Grain Boundary Modification via F4TCNQ To Reduce Defects of Perovskite Solar Cells with Excellent Device Performance. ACS Applied Materials & Interfaces 2018, 10 (2), 1909-1916.
37. Kampar, E.; Neilands, O., Degree of Charge Transfer in Donor–Acceptor Systems of the π–π Type. Russian Chemical Reviews 1986, 55, 334-342.
38. Mendez, H.; Heimel, G.; Winkler, S.; Frisch, J.; Opitz, A.; Sauer, K.; Wegner, B.; Oehzelt, M.; Rothel, C.; Duhm, S.; Tobbens, D.; Koch, N.; Salzmann, I., Charge-transfer Crystallites as Molecular Electrical Dopants. Nature Communications 2015, 6, 8560.
39. Lin, Y.; Bai, Y.; Fang, Y.; Chen, Z.; Yang, S.; Zheng, X.; Tang, S.; Liu, Y.; Zhao, J.; Huang, J., Enhanced Thermal Stability in Perovskite Solar Cells by Assembling 2D/3D Stacking Structures. The Journal of Physical Chemistry Letters 2018, 9 (3), 654-658.
40. Zhao, L.; Lin, Y. L.; Kim, H.; Giebink, N. C.; Rand, B. P., Donor/Acceptor Charge-Transfer States at Two-Dimensional Metal Halide Perovskite and Organic Semiconductor Interfaces. ACS Energy Letters 2018, 3 (11), 2708-2712.
41. Jeon, N. J.; Na, H.; Jung, E. H.; Yang, T. Y.; Lee, Y. G.; Kim, G.; Shin, H. W.; Il Seok, S.; Lee, J.; Seo, J., A Fluorene-terminated Hole-transporting Material for Highly Efficient and Stable Perovskite Solar Cells. Nature Energy 2018, 3 (8), 682-689.
42. Jasieniak, J.; Califano, M.; Watkins, S. E., Size-Dependent Valence and Conduction Band-Edge Energies of Semiconductor Nanocrystals. ACS Nano 2011, 5 (7), 5888–5902.
43. O'Regan, B. C.; Barnes, P. R.; Li, X.; Law, C.; Palomares, E.; Marin-Beloqui, J. M., Optoelectronic Studies of Methylammonium Lead Iodide Perovskite Solar Cells with Mesoporous TiO2: Separation of Electronic and Chemical Charge Storage, Understanding Two Recombination Lifetimes, and the Evolution of Band Offsets during J-V Hysteresis. Journal of the American Chemical Society 2015, 137 (15), 5087-5099.
44. Du, T.; Kim, J.; Ngiam, J.; Xu, S.; Barnes, P. R. F.; Durrant, J. R.; McLachlan, M. A., Elucidating the Origins of Subgap Tail States and Open-Circuit Voltage in Methylammonium Lead Triiodide Perovskite Solar Cells. Advanced Functional Materials 2018, 28 (32), 1801808.
45. Li, Z.; Gao, F.; Greenham, N. C.; McNeill, C. R., Comparison of the Operation of Polymer/Fullerene, Polymer/Polymer, and Polymer/Nanocrystal Solar Cells: A Transient Photocurrent and Photovoltage Study. Advanced Functional Materials 2011, 21 (8), 1419-1431.
46. Zhang, X.; Ren, X.; Liu, B.; Munir, R.; Zhu, X.; Yang, D.; Li, J.; Liu, Y.; Smilgies, D. M.; Li, R.; Yang, Z.; Niu, T.; Wang, X.; Amassian, A.; Zhao, K.; Liu, S., Stable High Efficiency two-dimensional Perovskite Solar Cells via Cesium Doping. Energy & Environmental Science. 2017, 10 (10), 2095-2102.
47. Zarazua, I.; Sidhik, S.; Lopez-Luke, T.; Esparza, D.; De la Rosa, E.; Reyes-Gomez, J.; Mora-Sero, I.; Garcia-Belmonte, G., Operating Mechanisms of Mesoscopic Perovskite Solar Cells through Impedance Spectroscopy and J-V Modeling. The Journal of Physical Chemistry Letters 2017, 8 (24), 6073-6079.
48. Zarazua, I.; Han, G.; Boix, P. P.; Mhaisalkar, S.; Fabregat-Santiago, F.; Mora-Sero, I.; Bisquert, J.; Garcia-Belmonte, G., Surface Recombination and Collection Efficiency in Perovskite Solar Cells from Impedance Analysis. Journal of Physical Chemistry Letters 2016, 7 (24), 5105-5113.

49. Almora, O.; Cho, K. T.; Aghazada, S.; Zimmermann, I.; Matt, G. J.; Brabec, C. J.; Nazeeruddin, M. K.; Garcia-Belmonte, G., Discerning Recombination Mechanisms and Ideality Factors through Impedance Analysis of High-efficiency Perovskite Solar Cells. Nano Energy 2018, 48, 63-72.
50. Park, N. G.; Grätzel, M.; Miyasaka, T., Organic-Inorganic Halide Perovskite Photovoltaics: From Fundamentals to Device Architectures. Springer: 2016; Vol. Cham.
51. Simpson, M. J.; Doughty, B.; Yang, B.; Xiao, K.; Ma, Y. Z., Imaging Electronic Trap States in Perovskite Thin Films with Combined Fluorescence and Femtosecond Transient Absorption Microscopy. The Journal of Physical Chemistry Letters 2016, 7 (9), 1725-1731.
52. Song, D.; Wei, D.; Cui, P.; Li, M.; Duan, Z.; Wang, T.; Ji, J.; Li, Y.; Mbengue, J. M.; Li, Y.; He, Y.; Trevor, M.; Park, N. G., Dual Function Interfacial Layer for Highly Efficient and Stable Lead Halide Perovskite Solar Cells. Journal of Materials Chemistry A 2016, 4 (16), 6091-6097.

Chapter 7. Conclusions and Outlook

7.1 Conclusions

Metal halide perovskites have rapidly emerged as an exciting and promising photovoltaic material. While their progress in terms of efficiency has been unprecedented, with efficiencies now reaching over 25%, many of the fundamental aspects underlying these efficiency gains remain unelucidated. Critical to the operation of such devices are the charge transporting layers and the extraction of charges from the absorber material. This thesis is focussed on understanding the interplay between structure and property of charge transporting materials and interfaces towards achieving PSCs with high PCE, stability and scalability.

NiO is the most widely adopted inorganic hole transporting material owing to its high bandgap and appropriate energy level structure. Normally, NiO HTLs in inverted PSCs are fabricated via sol-gel, particle ink, sputter and spray deposition, which form uniform planar NiO films. However, their poor interfacial properties with perovskites results in low device fill factors and hinders their use in high performance PSCs. To resolve the poor contact issue between the NiO HTL and the perovskite layer, in **Chapter 3** we designed a mesoporous NiO scaffold that completely covered the FTO electrode was grown by a facile chemical bath deposition process. Compared with normal planar NiO HTLs, this mesoporous NiO HTL dramatically improved the light harvesting and charge transporting efficiencies of PSCs to increase their fill factors up to record values of 85% and PCEs up to 16.7%. Although high fill factors were achieved in inverted PSCs using the chemical bath processed NiO in the above study, the PCEs of the devices were still inferior compared with conventional PSCs. In addition, following rapid developments in methodology (e.g. slot die, R2R and spray) and materials (e.g. 2D perovskite and hydrophobic molecule modification) for conventional PSCs, the conventional configuration was considered to be more promising for practical application and future scaling.

Towards these goals, we established an ultrasonic spray system for programmable spray of uniform TiO_2 ETLs. TiO_2 is the most commonly used ETM in conventional PSCs and has been conventionally deposited via spin-coating and/or airbrush spray. However, the spin-coating is not an appropriate approach for scalable fabrication of large devices. Meanwhile, airbrush spray is a low-cost approach but yields large distributions of droplets size, and thus leads to inhomogeneous film formation. In **Chapter 4**, we reported an alternative deposition method, namely ultrasonic spray, to fabricate TiO_2

films as ETLs in conventional PSCs. This deposition approach was shown to result in superior TiO_2 coatings, which consequently enabled higher performing devices under optimized conditions that could reach 17.4% photoconversion efficiency and, more importantly, yield a 9-fold improvement in terms of device reproducibility. In addition, through a comparison of diode and solar cell devices, we developed effective benchmarks that predicted the effectiveness of the underlying charge transport layer.

After the optimization of sprayed TiO_2 ETLs, we found that a mesoporous layer could further improve the reproducibility and device PCE. The mesoporous layer was made by spin-coating pristine commercial TiO_2 paste with a calcination at a high temperature. However, TiO_2 mesoporous layer in perovskite solar cells suffer from electron transporting problem due to their mediocre conductivity and the crystal defects. In **Chapter 5**, we introduced a facile method to morphological modify the mesoporous layer from a TiO_2 nanoparticle dispersion. The micro-structuring was achieved through the controlled crystallization of thiourea during deposition, which was subsequently thermolyzed during calcination. This micro-structured mesoporous layer facilitated charge extraction and less charge recombination between the perovskite and the mesoporous TiO_2 layer. Thus, device PCEs were improved by 5% compared to the control, achieving more than 19%.

Through progressive optimisation of the underlying CTLs, it was evident that the morphology of the CTLs plays a significant role in device operation and stability. Having optimised this for a number of different CTLs, we turned our attention to the architecture on top of the perovskite in **Chapter 6**, which involves the interface between the perovskite layer and the HTL. Normally, perovskites are sensitive to moisture due to the hygroscopic property of its small amino cations. Lowering the spatial dimensionality of the perovskite from 3D to 2D by using non-volatile and longer chain organic cations has been reported widely as a promising strategy to simultaneously reduce interfacial defects and improve stability of PSCs. However, the high exciton binding energies and poor charge transport properties of the 2D perovskite has limited their device PCE to date. In our research, we showed that a 3D/2D bilayer structured device could be used to improve the device performance compared to near 3D devices, although large charge recombination and poor charge extraction between the HTL and the perovskite layer hindered further efficiency gains. To overcome this, we introduced F4TCNQ as a modifier to effectively passivate surface states of the 3D/2D perovskite layer through supramolecular interactions between the F4TCNQ and the surface halide ions in the perovskite. This approach improved the PCEs of the resulting devices from 18.1% (3D/2D PSCs) to over 20% (3D/2DF5 PSCs). In addition, the additive made the performance of hybrid 3D/2D PSCs less sensitive

to the thickness of the 2D perovskite capping layer, making this approach a feasible strategy for improving the moisture stability of PSCs through the use of a thicker 2D perovskite capping layer.

7.2 Outlook

We have achieved conventional PSCs with PCEs exceeding 20% and stabilities of >1 month under 65% humidity to 85% PCE through the judicious design and optimization of the PSC architecture from the viewpoints of materials, fabrication process, interface engineering and charge dynamics. However, although possessing low-cost and easy fabrication processing, the overall performance of PSCs is still inferior compared with Si solar cells. Moreover, to realize the practical application of such devices, it will be also important to address scalability, durability and sustainability challenges in the future.

Scalability: While the ultrasonic spray system for scalable fabrication of TiO_2 ETLs underneath of perovskite layers is a suitable methodology, other layers, including the perovskite, the top charge transporting layer and electrode, are unlikely to be deposited using this approach. Owing to the need for such layers to be deposited with precise control of thickness and composition, roll-to-roll approaches, such as gravure or slot-die coating, can be considered as suitable methods for ensuring high throughput and low capex manufacturing. Given the chemical and structural instability of metal halide perovskites, achieving control of solution and interface chemistry will be paramount towards developing such methods successfully. However, while the notion of low-cost printing of PSCs has an allure, it is still difficult to state whether solution processing will ultimately be used for all the layers or any layers in the future for such devices. Fully evaporated devices have been demonstrated,[1] and while efforts in such areas are small compared to solution approaches, further work is required to compare fully printed PSCs to those made by vacuum approaches in terms of efficiency and scalability.

Durability: Stability is among the biggest problems for future use of PSCs. The potential solutions to this issue can be considered from two aspects: device material selection and encapsulation technology. Within the device architecture, stable charge transporting materials and electrodes should be used to protect the perovskite layer from moisture. As an example, Spiro-OMeTAD is not a suitable candidate in going forward as an HTL as far as stability is concerned. In this thesis we have largely focussed on charge transport layer development for the bottom electrode on glass, which can be exposed to appreciable temperatures for processing. Developing alternative, low-cost and durable charge transport layers that can be deposited at low temperature remains an on-going challenge,

particularly those that are doped sufficiently to be used within practical printing thickness ranges of 100's nm. In addition, the electrodes themselves are equally important to achieve durability, although they have been less considered. Perfect barrier properties for metals are achieved at micron scale thicknesses, while the commonly used thin metal layers used as top electrodes are of the order of 100 nm. Developing tailored electrode structures that can reduce oxygen and water ingress presents an opportunity for further progress. Beyond direct protection routes, developing more stable perovskite compositions will also be important in going forward. This may be achieved through simple mixtures with appropriate stabilizing polymers, such as PEO,[2] or through structurally engineered layers, such as for polystyrene,[3] PbS quantum dots,[4] and benzenethiol modification layer[5] Each of these strategies will need to be developed in conjunction with encapsulation of the completed PSCs. Up to now, glass-on-glass encapsulation that typically uses a UV or thermally curable polymer have been the most predominantly used. However, further exploring more durable, lower cost and/or lower ingress solutions needs to happen to ensure PSC can ultimately scale.

Sustainability: The sustainability of perovskites is widely debated in terms of environmental issues owing to the toxicity of the lead and tin salts and hazardous solvents used during the fabrication process. At a high level, to mitigate the risks around toxicity, robust encapsulation technology and recycling procedures are required to prevent leaching of Pb^{2+} into the environment. However, a more sustainable long-term solution needs to be in avoiding the use of toxic metals within the composition all together. There are many alternative systems currently being explored, including $AgBiS_2$[6] and low-toxicity lead-free perovskite solar cells.[7] Unfortunately, none of these have emerged with remotely comparable performance characteristics to that of the lead halide perovskites. Greater efforts in computational materials discovery coupled to combinatorial materials exploration systems will likely be needed if new photovoltaic candidates are to be discovered in a timely way.

7.3 Final Remark

In only 10 years the PCEs of PSCs in the lab have almost matched those of Si solar cells. This remarkable progress is a sign of the enormous potential of this emerging technology. Yes, major efforts are needed to overcome factors like stability, durability and sustainability, but through continual and steady progress, even at a partial rate to what has been occurring to date, it is more than likely that the perovskite solar cells will be commercialised and play an important role in providing affordable and clean electricity for our planet.

References

1. Matteocci, F.; Cinà, L.; Lamanna, E.; Cacovich, S.; Divitini, G.; Midgley, P. A.; Ducati, C.; Carlo, A. D., Encapsulation for Long-term Stability Enhancement of Perovskite Solar Cells. Nano Energy 2016, 30, 162-172.
2. Kim, M.; Motti, S. G.; Sorrentino, R.; Petrozza, A., Enhanced Solar Cell Stability by Hygroscopic Polymer Passivation of Metal Halide Perovskite Thin Film. Energy & Environmental Science 2018, 11 (9), 2609-2619.
3. Wang, Q.; Dong, Q.; Li, T.; Gruverman, A.; Huang, J., Thin Insulating Tunneling Contacts for Efficient and Water-Resistant Perovskite Solar Cells. Advanced Materials 2016, 28 (31), 6734-6739.
4. Zheng, X.; Lei, H.; Yang, G.; Ke, W.; Chen, Z.; Chen, C.; Ma, J.; Guo, Q.; Yao, F.; Zhang, Q.; Xu, H.; Fang, G., Enhancing Efficiency and Stability of Perovskite Solar Cells via a High Mobility P-type PbS Buffer Layer. Nano Energy 2017, 38, 1-11.
5. Lu, J.; Lin, X.; Jiao, X.; Gengenbach, T.; Scully, A. D.; Jiang, L.; Tan, B.; Sun, J.; Li, B.; Pai, N.; Bach, U.; Simonov, A. N.; Cheng, Y.-B., Interfacial Benzenethiol Modification Facilitates Charge Transfer and Improves Stability of cm-sized Metal Halide Perovskite Solar Cells with up to 20% Efficiency. Energy & Environmental Science 2018, 11 (7), 1880-1889.
6. Bernechea, M.; Miller, N. C.; Xercavins, G.; So, D.; Stavrinadis, A.; Konstantatos, G., Solution-processed Solar Cells based on Environmentally Friendly AgBiS2 Nanocrystals. Nature Photonics 2016, 10 (8), 521-525.
7. Ke, W.; Kanatzidis, M. G., Prospects for Low-toxicity Lead-free Perovskite Solar Cells. Nature Communications 2019, 10 (1), 965.